UNIVERSIDAD AUTÓNOMA DE BAJA CALIFORNIA

INSTITUTO DE INGENIERÍA

MAESTRÍA Y DOCTORADO EN CIENCIAS E INGENIERÍA

“Preparation and characterization of highly selective palladium catalysts supported on various carbon nanostructures for aerobic ethanol oxidation to acetic acid”

TESIS PARA OBTENER EL GRADO DE:
DOCTOR EN INGENIERÍA

PRESENTA
Rubén Castro Contreras

Dr. Mario Alberto Curiel Álvarez
DIRECTOR

Dr. Benjamín Valdez Salas
CODIRECTOR

Mexicali, B. C. **Junio 2018**

Mario Alberto Curiel Álvarez PhD, researcher-professor for Institute of Engineering-Autonomous University of Baja California, Benjamin Valdez Salas PhD, researcher-professor for Institute of Engineering-Autonomous University of Baja California, and Professor Philippe SERP, research-professor for Laboratoire de Chimie de Coordination-École Nationale Supérieure des Ingénieurs en Arts Chimiques Et Technologiques, certify that PhD thesis entitled: **"Preparation and characterization of highly selective palladium catalysts supported on various carbon nanostructures for aerobic ethanol oxidation to acetic acid"**, has been performed by Ruben Castro Contreras under their supervision in the Laboratoire de Chimie de Coordination and Institute of Engineering.

Mario Alberto Curiel Álvarez PhD

Benjamín Valdez Salas PhD

Professor Philippe SERP

Institutional seals

For the LORD gives wisdom, and from his mouth comes knowledge and understanding.

Proverbs 2:6

DEDICATION

This PhD manuscript is dedicated to my beloved parents who have always been a source of inspiration, proud and force to carry out my higher studies and to confront the life with encourage, enthusiasm and fear of God.

ACKNOWLEDGEMENTS

I, Ruben Castro Contreras would like to thank:

My God who has given unconditional support.

The director of Institute of Engineering – Gisela Montero Alpírez PhD who has approved my international and national research stays.

My jury – Mario Alberto Curiel Álvarez PhD, Roumen Koytchev Zlatev PhD, Nicola Radnev Nedev PhD, Mónica Carrillo Beltrán PhD, and Benjamin Valdez Salas PhD who have taken part and deliberated in my PhD defense.

I sincerely thank a number of people, who have been very important pieces to conclude my PhD research work. Some, however, deserve special mention:

My family who has provided physical and spiritual support.

My mexican supervisors – Mario Alberto Curiel Alvarez PhD and Benjamin Valdez Salas PhD who have given academic, administrative, and financial support.

My french supervisor – Professor Philippe SERP who has provided academic, experimental, administrative, and financial support.

All ENSIACET people who have given technical and scientific support in catalysis side, for example:

Idaline CHANTEPERDRIX (Batch reactor and TitroLine KF trace titrator)

Laurent ROPIQUET (GC and BET)

All LCC people who have provided technical and scientific support in characterization side, for example:

Alain MOREAU (ICP-AES)

Isabelle BORGET (Elemental analysis)

Stephanie SEYRAC (TGA)

Sonia MALLET LADEIRA (XRPD)

Corinne ROUTABOUL (IR and Raman)

Vincent COLLIÈRE (SEM and TEM)

I also thank:

My friend - Bruno MACHADO who has given academic, experimental, technical, and scientific (XPS) support.

CONACYT who has provided financial support for 4 years.

All my mexican and french friends who have spent real time.

ABSTRACT

Modern industrial chemistry is based on catalytic processes. Approximately 80 % of all catalytic processes require heterogeneous catalysts. Zero emission plants, green chemistry, and sustainable development have become a major driving force in technological innovation. Green chemistry prevents pollution through better process design than by managing emissions and wastes. Catalysis is one of the fundamental pillars of green chemistry, the design of chemical products and processes that reduce or eliminate the use and generation of hazardous substances. The design and application of new catalysts and catalytic systems are simultaneously achieving the dual goals of environmental protection and economic benefit. Among the most important chemicals currently used, acetic acid is one of them. Acetic acid is produced both synthetically and by bacterial fermentation. The biological route accounts for only about 10 % of world production, about 75 % accounts by methanol carbonylation, and alternative methods account for the rest. Acetic acid is widely used as solvent in many industrial processes, manufacture of daily products, film industry, food additive, and testing blood in clinical laboratories. Thus, the acetic acid becomes a significant product for chemical, food, textile, cosmetic, agrochemical, and film industries due to its excellent physicochemical properties. Oxidation of alcohols to aldehydes, ketones or carboxylic acids is widely employed in heterogeneous catalysis. Among the most important alcohols for chemical industry, ethanol is one of them. An important application of ethanol is as reactant into oxidation reaction to acetic acid.

Nowadays, silica, carbon, clay, zeolites, metal oxides, and other mesoporous materials are being used as inorganic solid supports. But, the quest of new materials as catalyst supports continues being an important topic for catalysis community. Carbon is currently used as catalyst support due to its unique physicochemical properties such as porosity, high surface area, acidic and basic media resistance, electrical conductivity, thermal resistance, and inertness. Carbon has also become a promising material in catalysis compared to the catalyst supports already used. Many carbon materials frequently used as catalyst supports due to their physicochemical properties and catalytic performances are activated carbon, carbon black, and graphite, which are suitable carbon materials to prepare supported metal catalysts for catalyzed chemical reactions. Activated carbon, carbon black, and graphite are not only the carbon materials used as catalyst supports, but also different carbon nanostructures which are synthesized by chemical methods. These carbon nanostructures such as graphene (G), multi-walled carbon nanotubes (CNT), carbon nanofibers (CNF), and fibrous carbon (FC) have unique physicochemical properties. It is well known that the incorporation of functional groups, heteroatoms, or thermal treatment modifies the surface chemistry of such support. The use of palladium-group metals as active phase on carbon supports has showed high activity and selectivity towards the main product for oxidation reactions. Therefore, we propose to prepare highly selective palladium catalysts supported on carbon nanostructures for aerobic ethanol oxidation to acetic acid. Besides, the synthesis of carbon nanostructures, the preparation method of palladium catalysts, and the results of aerobic ethanol oxidation to acetic acid are presented.

ABBREVIATIONS

H_2	Hydrogen
H_2O_2	Hydrogen peroxide
H_2O	Water
O_2	Oxygen
CO_2	Carbon dioxide
CO	Carbon monoxide
NO_x	Nitrogen oxides
SO_x	Sulphur oxides
VOCs	Volatile organic compounds
AcOH	Acetic acid
AcH	Acetaldehyde
C_2H_4	Ethylene
C_2H_3N	Acetonitrile
C_4H_4S	Thiophene
HCl	Hydrochloric acid
H_2SO_4	Sulfuric acid
HNO_3	Nitric acid
G	Graphene
C-CVD	Catalytic-chemical vapor deposition
-COOH	Carboxylic acid functional group
-OH	Alcohol functional group
HT	High temperature
TOF	Turnover frequency
TON	Turnover number
SEM	Scanning electron microscopy
TEM	Transmission electron microscopy
STEM	Scanning transmission electron microscopy
LRTEM	Low resolution transmission electron microscopy
HRTEM	High resolution transmission electron microscopy
EELS	Electron energy loss spectroscopy
EFTEM	Energy filtered transmission electron microscopy
EDX	Energy dispersive X-ray
TGA	Thermogravimetric analysis
BET	Brunauer, Emmett and Teller
XRPD	X-ray powder diffraction
IR	Infrared
XPS	X-ray photoelectron spectroscopy
ICP-AES	Inductively coupled plasma-atomic emission spectroscopy

DP	Diffraction patterns
CHNS	Carbon, hydrogen, nitrogen, and sulphur
TCD	Thermal conductivity detector
STP	Standard temperature and pressure
CCD	Charge-coupled device
CNT	Multi-walled carbon nanotubes
CNT-COOH	Functionalized multi-walled carbon nanotubes
CNT$_{HT}$	High temperature treated multi-walled carbon nanotubes
CNT-COOH HT	High temperature treated functionalized multi-walled carbon nanotubes
N-CNT	Nitrogen doped multi-walled carbon nanotubes
N-CNT$_{HT}$	High temperature treated nitrogen doped multi-walled carbon nanotubes
S-CNT	Sulphur doped multi-walled carbon nanotubes
S-CNT$_{HT}$	High temperature treated sulphur doped multi-walled carbon nanotubes
FLG	Few layer graphene
FLG-COOH	Functionalized few layer graphene
FLG$_{HT}$	High temperature treated few layer graphene
FLG-COOH HT	High temperature treated functionalized few layer graphene
CNF	Carbon nanofibers
CNF-COOH	Functionalized carbon nanofibers
CNF$_{HT}$	High temperature treated carbon nanofibers
CNF-COOH HT	High temperature treated functionalized carbon nanofibers
sCNF	Small carbon nanofibers
sCNF-COOH	Functionalized small carbon nanofibers
sCNF$_{HT}$	High temperature treated small carbon nanofibers
sCNF-COOH HT	High temperature treated functionalized small carbon nanofibers
FC	Fibrous carbon
FC-COOH	Functionalized fibrous carbon
FC$_{HT}$	High temperature treated fibrous carbon
FC-COOH HT	High temperature treated functionalized fibrous carbon
Pd	Palladium
Ni	Nickel
Pt	Platinum
Au	Gold
Co	Cobalt
Ru	Ruthenium
KBr	Potassium bromide
Al_2O_3	Alumina
SiO_2-Al_2O_3	Silica-alumina
FID	Flame ionization detector
DFT	Density functional theory

LIST OF FIGURES

Page

Chapter I Introduction

Chapter II Theoretical framework

Chapter IV Results

Chapter V Discussion

Chapter VI Catalytic tests

LIST OF TABLES

Page

Chapter I Introduction

Chapter II Theoretical framework

Chapter III Methodology

Chapter IV Results

LIST OF SCHEMES

Page

INDEX

CHAPTER I

Introduction

1.1 Introduction

Catalysis is the key to chemical transformations. Most industrial syntheses and nearly all biological reactions require catalysts. Furthermore, catalysis is the most important technology in environmental protection.

The term "catalysis" was introduced as early as 1836 by Berzelius in order to explain various decomposition and transformation reactions. He assumed that catalysts possess special powers that can influence the affinity of chemical substances.

A definition that is still valid today is due to Ostwald (1895): "A catalyst accelerates a chemical reaction without affecting the position of the equilibrium." [1]

There are many different types of catalysts (see Figure 1.1). They range from the proton, H^+, through Lewis acids, various metals, organometallic complexes, organic and inorganic polymers and all the way to enzymes. [2]

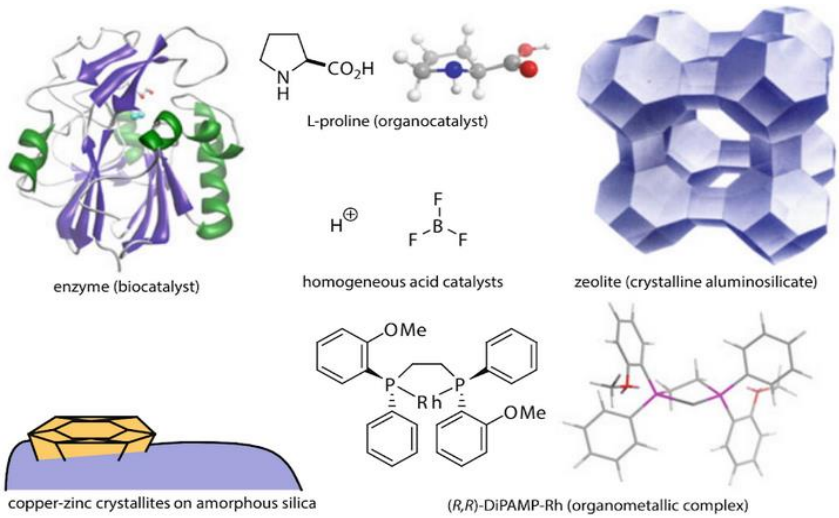

Figure 1.1 Different types of catalysts.

To clearly understand the structural order of this Chapter I: Introduction, the main issues are summarized in Table 1.1.

Table 1.1 Main issues of Chapter I.

Issues
1.2 Catalysis: The heart of the industrial processes
1.3 Acetic acid as an important product for human use
1.4 Commonly employed catalysts for oxidation reactions.
1.5 Carbon as a promising material in supported catalysis
1.6 Frequently used carbon materials as catalyst supports
1.7 New carbon materials as catalyst supports
1.8 Support surface activation
1.9 Carbon materials compared to conventional oxides
1.10 Effect of active phase on the support surface
1.11 Palladium-group metals as active phase
1.12 Motivation
1.13 Problem identification
1.14 Aims
1.15 Summary
1.16 References

1.2 Catalysis: The heart of the industrial processes

Modern industrial chemistry is based on catalytic processes. Approximately 80 % of all catalytic processes require heterogeneous catalysts, 15 % homogeneous catalysts, and 5 % biocatalysts. [3] The traditional area in which catalysts have been used for over 100 years is the chemical industry. Nowadays, other important areas have emerged to be treated by using catalysts. The catalyst market can be devided into four main areas (see Figure 1.2):

1. Environmental catalysts
2. Chemistry catalysts
3. Petroleum refining catalysts
4. Polymerization catalysts

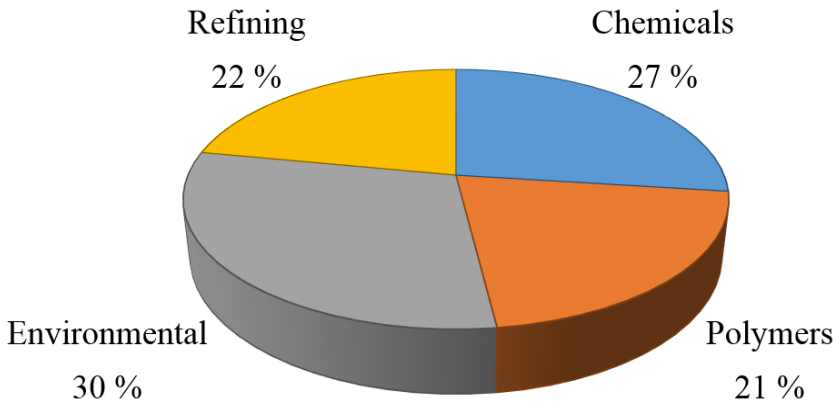

Figure 1.2 Worldwide catalyst market according to application. [4]

In future, companies will choose more catalytic routes since these are mostly shorter and lead to cheaper processes than non-catalytic processes.

Heterogeneous catalysts are used on a large scale in the following areas:

- Production of organic and inorganic chemicals
- Crude oil refining and petrochemistry
- Environmental protection
- Energy conversion processes

Fine or speciality chemicals, unlike the traditional products, have complex chemical structures and properties that justify a high selling price.

In high added value products, where relatively small quantities of products are manufactured, factors such as catalyst costs, separation of product from catalyst and reactants, recycling and regeneration of catalysts, etc., assume reduced significance relative to that in the manufacture of chemicals. This is because these costs can be more readily absorbed in the relatively high value of the products.

Whereas in bulk chemicals manufacture the choice of oxidant is largely restricted to molecular oxygen, the economics of fine chemicals production allow a broader choice of oxidants such as H_2O_2 or other peroxides. Increasingly stringent environmental constraints are making the industrial use of classical stoichiometric oxidants such as dichromate, permanganate, and manganese dioxide prohibitive.

There is a general trend toward substitution of such antiquated technologies by catalytic methods that do not generate aqueous effluents containing large quantities of inorganic salts (see Scheme 1.1). [5]

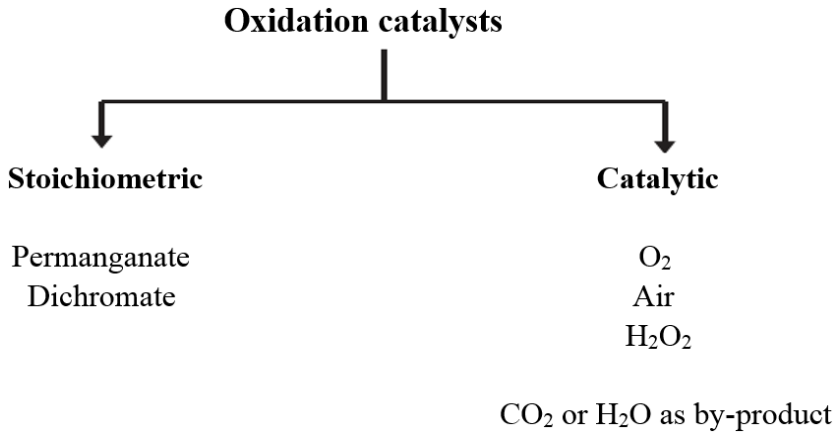

Scheme 1.1 Comparison of stoichiometric and catalytic routes for oxidation processes.

Zero emission plants, environmentally benign or green chemistry, and sustainable development have become a major driving force in technological innovation. The major aim of successful developing fine chemicals is, to design more precision into organic synthesis.

As noted above, a prime cause of waste generation is the use of stoichiometric inorganic reagents. Hence, the solution is simple: replacement of antiquated stoichiometric methodologies with cleaner catalytic alternatives, *e.g.*, catalytic hydrogenations, catalytic oxidations with O_2 or H_2O_2 and catalytic carbonylations.

Traffic and industry are the most important sources of air pollution. They are responsible for the emission of CO, nitrogen oxides (NO_x), sulfur oxides (SO_x), and all sorts of volatile organic compounds (VOCs). Therefore, environmental catalysts are necessary for cleaning flue gases.

Green chemistry, also called sustainable chemistry, prevents pollution through better process design than by managing emissions and wastes.

Catalysis is one of the fundamental pillars of green chemistry, the design of chemical products and processes that reduce or eliminate the use and generation of hazardous substances. The design and application of new catalysts and catalytic systems are simultaneously achieving the dual goals of environmental protection and economic benefit. [6]

Catalysis offers numerous green chemistry benefits including:

- Lower energy requirements
- Catalytic versus stoichiometric amounts of materials
- Increased selectivity
- Decreased use of processing and separation agents
- Allows for the use of less toxic materials

Heterogeneous catalysis, in particular, addresses the goals of green chemistry by providing the ease of separation of product and catalyst, thereby eliminating the need for separation through distillation or extraction.

1.3 Acetic acid as an important product for human use

Acetic acid, also known as ethanoic acid, is an organic chemical compound. It is one of the simplest carboxylic acids and has the chemical formula $C_2H_4O_2$. This acid is an important chemical reagent and acidity regulator.

Acetic acid is produced both synthetically and by bacterial fermentation. Today, the biological route accounts for only about 10 % of world production, about 75 % accounts by methanol carbonylation, and alternative methods account for the rest. [7]

Total worldwide production of virgin acetic acid is estimated at 5 Mt/a (million metric tons per year), approximately half of which is produced in the United States.

European production stands at approximately 1 Mt/a and is declining, and 0.7 Mt/a is produced in Japan. Another 1.5 Mt are recycled each year, bringing the total world market to 6.5 Mt/a. [8]

Acetic acid is widely used for different applications such as:

- Solvent in many industrial processes
- In manufacture of daily products such as perfumes, synthetic fibers, inks, dyes, pesticides, and wood glues.
- Testing blood in clinical laboratories
- Film industry
- Food additive

Thus, the acetic acid becomes a significant product for chemical, food, textile, cosmetic, agrochemical, and film industries due to its excellent physicochemical properties.

1.4 Commonly employed catalysts for oxidation reactions

Oxidation of alcohols to aldehydes, ketones or carboxylic acids is widely employed in heterogeneous catalysis. Furthermore, oxidation reactions may be considered as the heart of chemical synthesis. However, the indiscriminate uses of corrosive chemicals in this endeavor are threating to the ecosystems, public health, and terrestrial, aquatic, and aerial flora and fauna. Heterogeneous catalysts minimize the use of chemicals in industries and thus are friendly and green to the environment. The green chemistry approaches must meet health and environmental safeties and use vary little chemicals reducing both cost and time. [9]

Catalytic approaches might be considered as green since specific chemical transformation could be achieved within very short time with the addition of very little catalysts, significantly reducing production cost as well as health and environmental risks. [10, 11]

Heterogeneous catalysis is considered to be a better choice for the synthesis of commodity materials. [12-14] Nowadays, silica, carbon, clay, zeolites, metal oxides, and other mesoporous materials are being used as inorganic solid supports. [15, 16] Supported materials can be obtained as complexes with transition metals by heterogenization process. [17] Various support materials along with their major features are showed in Table 1.2.

Table 1.2 Major features, advantages, and disadvantages of commonly used support materials.

Support materials	Features	Advantages	Disadvantages	References
Alumina	Hardness Resistant to abrasion and chemical attack High thermal conductivity	Thermally stable Well-ordered pore Narrow pore size	Difficult to control the hydrolysis rate of aluminum precursors	[18]
Silica	Tendency to form large networks Found in nature and living organisms Hardness	High efficiency High selectivity Highly stable	Low compatibility Formation of aggregates/agglomerates	[19]
Zeolite	Microporous Inertness Excellent electron conductivity	Highly effective Less or no corrosion High thermo stability	Irreversible adsorption Impossibility of using microporosity Difficult to exploit the shape selectivity	[20, 21]
Carbon	Nonmetallic Tetravalent Porous structure	Large surface area Excellent electron conductivity Thermal stability	High temperature physical activation Expensive Emission of greenhouse gasses during pyrolysis	[22,23]

In heterogeneous catalysis reactions, the catalysts and reactants exist in different phases. In reality, the vast majority of heterogeneous catalysts are solids and the vast majority of reactants are gases or liquids. [24]

A phase separation catalysis reaction greatly helps in reactant, product, and catalyst separation at the end of the reaction. Heterogeneous catalysts are also easier to prepare and handle. Many heterogeneous catalysts widely employed for oxidation of alcohols are presented in Table 1.3.

Table 1.3 The most commonly used catalysts for oxidation of alcohols.

Catalyst	Method of preparation	Major application	Reference
Au/CuO	Coprecipitation	Alcohol oxidation	[25]
Microstructured Au/Ni-fiber	Incipient impregnating	Alcohol oxidation	[26]
Silica-supported Au-Cu alloy	-	Alcohol oxidation	[27]
Gold nanoparticles supported on MgO	Deposition - precipitation	Alcohol oxidation	[28]
Metal-organic framework supported gold nanoparticles	Colloidal deposition	Alcohol oxidation	[29]
Au/TiO_2	Deposition - precipitation	Alcohol oxidation	[30]
Gold	Deposition - precipitation	Alcohol oxidation	[31]
MCM-48 molecular sieve modified with $SnCl_2$	Post - synthesis modification	Alcohol oxidation	[32]
Supported gold	Deposition - precipitation	Alcohol oxidation	[33]
Gold	-	Alcohol oxidation	[34]
Au/C	Immobilization	Alcohol oxidation	[35]

Among the most important alcohols for chemical industry, ethanol is one of them. An important application of ethanol is as reactant into oxidation reaction to acetic acid. In this reaction, acetic acid as main product and acetaldehyde, ethyl acetate, and carbon dioxide as by-products, they are commonly obtained. Thus, acetic acid from ethanol oxidation using molecular oxygen or air as oxidizing agent, moderate reaction conditions and a heterogeneous catalyst becomes an interesting route due to its low operation costs, no toxic by-products, and abundant reactants compared to the traditional routes.

Table 1.4 shows other heterogeneous catalysts, which are employed for ethanol oxidation to acetic acid. It is seen that reaction conditions are very important for ethanol oxidation to acetic acid, being the acetic acid yield affected by both kind of catalyst and reaction temperature.

Table 1.4 Heterogeneous catalysts employed for direct ethanol oxidation to acetic acid.

Catalyst	Atmosphere	Temperature (°C)	Product/Yield (%)	Reference
PdO/ZrO_2	Oxidant	175	Acetaldehyde/8 Acetic acid/10 Ethyl acetate/11	[36]
$PdO/ZrO_2 + ZrO_2$	Oxidant	175	Acetaldehyde/10 Acetic acid/1 Ethyl acetate/26	[36]
$TiPd_{0.03}PO_x$	Oxidant	200	Acetic acid/36 Ethyl acetate/45	[37]
Pd/Zeolite Y	Oxidant	110	Acetic acid/6 Ethyl acetate/41	[38]
Au/ZnO	Oxidant	180	Acetaldehyde/74 Acetic acid/15 Ethyl acetate/2	[39]
Au/ZnO	Oxidant	220	Acetaldehyde/44 Acetic acid/46 Ethyl acetate/6	[39]
Au/CuO	Oxidant	160	Acetaldehyde/80 Acetic acid/4	[39]
Au/TiO_2 Au/Al_2O_3 Au/ZnO	Oxidant	150	Acetic acid/90	[40]
$Au/MgAl_2O_4$	Oxidant	180	Acetic acid/83	[41]

For some presented heterogeneous catalysts high acetic acid yields were achieved, but not for all cases. This is particularly true for some gold catalysts. However, it is important to note that Pd catalysts are cheaper.

1.5 Carbon as a promising material in supported catalysis

The quest of new materials as catalyst supports continues being an important topic for the catalysis community.

Currently, carbon (see Figure 1.3) is used as catalyst support due to its unique physicochemical properties such as porosity, high surface area, acidic and basic media resistance, electrical conductivity, thermal resistance, and inertness. Carbon has also become a promising material in catalysis compared to oxide catalyst supports already used. The most important parameters for the catalyst manufacturer and the user of a catalyst are porosity, pore size distribution, metal particle size distribution, attrition resistance, metal oxidation state, and active surface area, which determine a vast part of the catalytic response of catalyst in the chemical reaction. [42] According to that, highly porous materials as carbon materials provide easy access of the reactants to the catalytically active sites and thus exhibit higher catalytic activity. Furthermore, the pore size distribution plays an important role on the catalytic performance, for it not only determines the active surface area available for the deposition of highly dispersed, catalytically active metal particles, but also controls the access of substrate molecules to these supported metallic particles. The metal particle size distribution also plays an important role with respect to the catalytic performance. Thus, an increase in the active surface area of the support with decreasing metal particle size generally leads to higher catalytic activity. This may be achieved by both the pretreatment of the support under oxidizing conditions [43, 44] and the technique of metal deposition on the support. These pretreatments and deposition techniques can be applied to catalyst supports such as carbon.

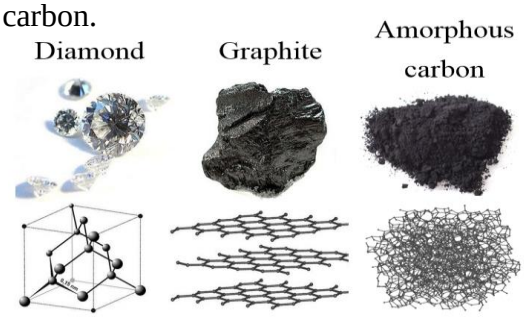

Figure 1.3 Allotropes of carbon.

1.6 Frequently used carbon materials as catalyst supports

Many carbon materials frequently used as catalyst supports due to their physicochemical properties and catalytic performances are activated carbon, carbon black, and graphite, which are suitable carbon materials to prepare supported metal catalysts for catalyzed chemical reactions.

1.6.1 Activated carbon

Activated carbon is manufactured from suitable precursors in two ways: chemical activation and physical activation (see Figure 1.4). Chemically activated carbons are manufactured by the simultaneous carbonization and activation of the raw material at 600-800 °C. Physically activated carbons are manufactured from a precarbonized material, which is obtained by thermal decomposition of a carbonaceous precursor at 600-800 °C in the absence or under controlled admission of air. [45] The activation step is usually performed in the presence of steam and/or carbon dioxide at 800-1100 ^{o}C. Wood, coal, lignite, coconut shell and peat are the most important raw materials for the production of activated carbon. The final products show different properties, such as pore structure and active surface area, depending on the nature of the precursor, the nature of the activating agent and the conditions of the activation process.

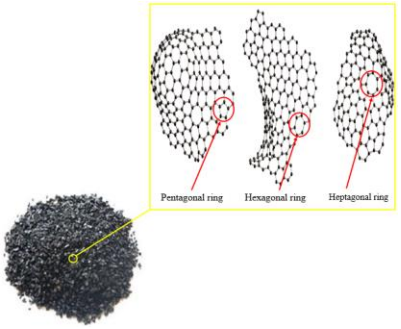

Figure 1.4 Activated carbon and its structure.

1.6.2 Carbon black

Carbon blacks are manufactured by the pyrolysis of hydrocarbons such as natural gas or oil fractions from petroleum processing. [46] Graphitized carbon black has a high surface area and it is obtained by recrystallization of the spherical carbon black particles at 2500-3000 °C (see Figure 1.5a). The degree of graphitization is determined by the process temperature. Carbon black particles possess the core-shell feature. The core units arrange randomly due to their small sizes. In contrast, the shell units are connected approximately in a concentric fashion, and this tendency is slightly more pronounced for larger shell units (see Figure 1.5c) than the one (see Figure 1.5b). The unique feature observed from carbon black surfaces has a flake-like arrangement of graphite layers whose edges are characteristic of the growth of formation systems. The deposition of these flakes during formation process results in approximately spherical carbon particles. The flake-like morphology of carbon black surfaces is rationally reproduced by the hexagonal graphite sheets. Graphite sheets are partially covered with each other, resulting in the surface grain pattern formed by the interconnected flake's edges (see Figures 1.5d-e). [47]

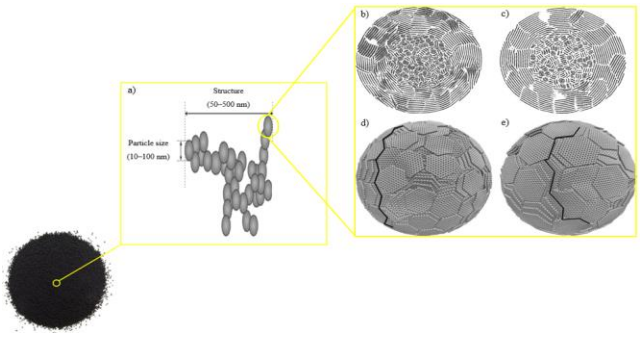

Figure 1.5 Carbon black: a) its structure, b) carbon black particles with shell units d = 2.7 nm, c) carbon black particles with shell units d = 3.7 nm, d) surface morphology of carbon black particles with shell units d = 2.7 nm, and e) surface morphology of carbon black particles with shell units d = 3.7 nm. The dark lines are drawn to highlight the grain pattern on the carbon black surface. The radii of these carbon black particles are 20 nm and the densities are 2 g/cm^3.

1.6.3 Graphite

In contrast to activated carbon and carbon black, graphite is a highly crystalline material composed of stacked planes of aromatic rings 0.335 nm apart (see Figure 1.6). The electronic character of the stacked aromatic systems makes it possible for definite atoms or molecules to slip between the layers, either accepting or donating electrons to bond with the carbon system, a process referred to as intercalation. [48, 49]

Furthermore, this material is characterized by relatively low surface area of only 10-50 m^2/g. Nevertheless, for some applications such graphite is indeed used as support material. However, high surface area graphite (HSAG) is available from graphitized material by a special grinding process. Surface areas of 100-300 m^2/g make this graphite an interesting support material for precious metal catalysts. [50-53]

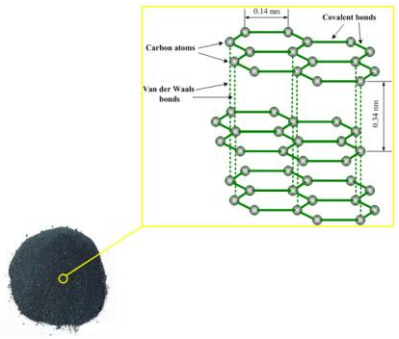

Figure 1.6 Graphite and its structure.

1.7 New carbon materials as catalyst supports

Activated carbon, carbon black, and graphite are not the only carbon materials used as catalyst supports. Thanks to the discovery of different carbon structures by chemical methods, [54] they are currently used as catalyst supports due to their excellent physicochemical properties. These carbon structures such as graphene (G), multi-walled carbon nanotubes (CNT), carbon nanofibers (CNF), and fibrous carbon (FC) have totally changed the research approach in heterogeneous catalysis. [55]

1.7.1 Graphene

The use of graphite as catalyst support also allowed paying attention on its unit structure called graphene (see Figure 1.7). Thus, graphene as catalyst support became a promising carbon material in catalysis as those already mentioned above (see section 1.6).

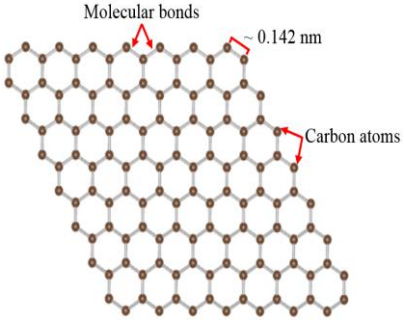

Figure 1.7 A graphene sheet.

1.7.2 Carbon nanotubes

Carbon nanotubes can be classified by the amount of rolled-up graphene layers, *e.g.*, single-walled carbon nanotubes and multi-walled carbon nanotubes (see Figure 1.8). Carbon nanotubes synthesized by chemical vapor deposition (CVD) are usually covered on their outer surface with a layer of amorphous carbon, which is probably formed during the cooling step of the synthesis. [56] Besides, it is known that the capillarity is reduced when the inner cavity of the tube decreases. [57] The wide nanotube cavities appeared to be more preferentially filled compared to the narrower cavities. In small cavities, the van der Waals repulsion forces are significantly higher than that of capillarity, and thus inhibit the penetration of the solution inside the tube channel. It is well noting that the absence of metallic particles on the outer surface of the tube when the metal active phase is attached that is due to many factors such as hydrophobic character of the outer surface, relatively large inner cavity, and the relatively low metal precursor, which affect dispersion and distribution of active phase. But, it is not observed on the region near the tube tip. [58]

The relatively high interaction between the deposited metal and the inner wall of the carbon nanotubes could come from the electronic modification of the graphene planes due to the presence of curvature. As already mentioned, the presence of structural defects on the tube wall could also induced anchorage of the active phase particles on the wall surface. The nature of the metal precursor salt has almost no detected effect on the final dispersion state of the metallic particles, but if the solvent when a wetness impregnation method is used. The curvature of the channel could also induce modification on the molecular adsorption on the metallic phase, which in turn modifies the catalytic activity or selectivity of the reaction products.

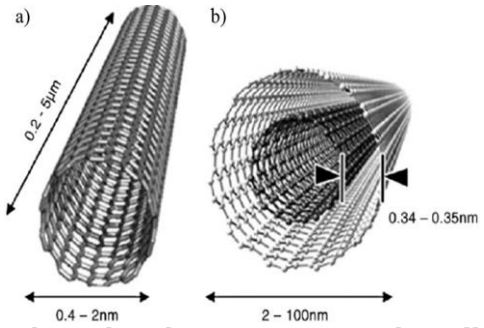

Figure 1.8 Carbon nanotube and its dimensions. a) single-walled and b) multi-walled.

1.7.3 Carbon nanofibers

Carbon nanofibers have no cavity compared to carbon nanotubes. Carbon nanofibers with a diameter between 10-200 nm are grown from decomposition of carbon containing gases, *e.g.*, methane, carbon monoxide, and ethylene on metal particles of similar sizes. [59] Carbon atoms are generated on the free metal surface, diffuse through the particle and are converted into a graphite-based fiber by segregation. By a proper choice of the synthesis conditions such as temperature, gas and metal used the morphology of the fiber can either be of the fishbone (exposed edge planes) or the parallel type (exposed basal planes) (see Figure 1.9).

Potentially these carbon structures have unique properties to be used as catalyst supports. They have a high surface area from 10 to 200 m^2/g and do neither possess micropores nor impurities, *e.g.*, inorganic matter. [48, 60, 61] A major disadvantage to the application of carbon nanofibers for catalytic purposes was their limited availability and high production costs. However, recently these drawbacks have been overcome due to the development of fluidized bed technology for large-scale production. [61, 62] It should be noted that the yield is a result of both the growth rate and longevity of the growth.

On the other hand, very large particles would be inactive because carbon diffusion through these particles is too sluggish. Therefore, a suitable particle size of metal precursor it helps to increase the carbon nanofibers yield. Carbon nanofibers have a number of characteristics that make them materials of promise as catalyst supports. Carbon nanofibers are chemically stable for corrosive attack in acidic and basic environments; this can be a serious advantage in certain liquid phase operations. Carbon nanofibers are also inert and withstand most organic solvents. Carbon nanofibers are also stable toward sintering, for high-temperature gas reactions, unlike oxide supports. However, carbon nanofibers are prone to reactions in the presence of oxygen and hydrogen. It is important to note that carbon nanofibers are also conductive. [63] Thermal conductivity may be advantageous in strongly exothermic or endothermic reactions where heat transfer may become limiting.

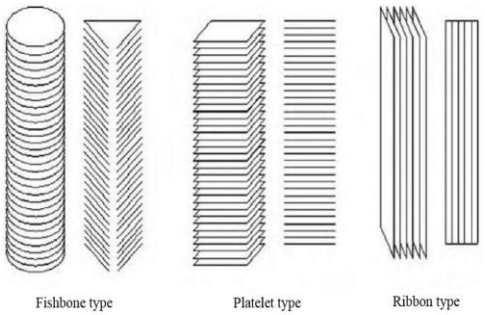

Figure 1.9 Types of carbon nanofibers.

1.8 Support surface activation

Currently, it is well known that the incorporation of functional groups, elements, or pretreatments to carbon materials are carried out before, in or after synthesis to enhance their surface chemistry.

1.8.1 Oxidation method

The incorporation of functional groups such as carboxylic groups, phenolic groups, lactonic groups, and etheric groups on the carbon surface through an oxidative method changes the acid/base and redox properties and decreases the hydrophobic character of the carbon material (see Figure 1.10). [45] Furthermore, these surface functionalities are assumed as anchoring sites to immobilize the metallic particles [64-66] and enhance the wettability of the carbon material for polar solvents (*e.g.*, water). However, it is essential to carry out the oxidation in a controlled manner so as not to destroy the carbon materials. When this oxidation method is carried out in liquid phase that can be controlled much better; it proceeds more homogeneously than in gas phase. [67] The defect sites present in each carbon structure enhance the oxidation. [67-70]

In general, oxidation with concentrated acids results in the formation of hydroxyl and carbonyl groups, whereas oxidation with hydrogen peroxide results in the formation of carboxyl groups. The choice of oxidant also depends on the nature of other phases that may be present together with the carbon materials (*e.g.*, metal or oxide layers). In the case of pure carbon material aggregates, oxidative treatments in acids, *e.g.*, nitric acid, can be used. This also helps to remove any residual metal such as iron, nickel, cobalt, or copper, which was used to form the carbon materials. [71, 72]

On the other hand, the oxygen containing surface groups can be divided in acidic, neutral and basic. This implies that the carbon surface may have different amounts and types of oxygen surface groups and, consequently, both negatively and positively charged surface sites. When preparing a supported catalyst, one needs not only physically accessible sites but also chemical reactivity toward the metal precursor.

The electrostatic repulsion between the charged surface and the ionic catalyst precursor may be stronger than the non-specific dispersion forces of attraction. The catalyst dispersion is optimal when the entire carbon surface is accessible, *e.g.*, when there is an electrostatic attraction between the positively charged surface and the catalyst precursor anions or vice versa. [73] Carboxyl, quinone and lactone groups are acidic. Because of their negative charge they enhance the interaction between the carbon surface and a positively charged metal precursor. Furthermore, they decrease the hydrophobic character of the carbon, thus, making the surface more accessible for the solution of the metal precursor. [73, 74-76] Phenols, carbonyls and ethers are weakly acidic to neutral. These oxygen groups increase the interaction of the metal precursor or the metal particle with the support, thus, minimizing sintering. [76]

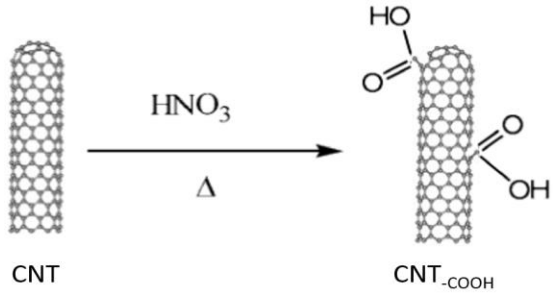

Figure 1.10 Oxidation method (-COOH) applied to multi-walled carbon nanotubes (CNT).

1.8.2 Doping of heteroatoms

Doping of heteroatoms such as nitrogen, sulphur, or phosphorus also play an important role in the surface chemistry of the carbon material (see Figure 1.11).

But, the identification of surface heteroatom species is a delicate art and requires much experience. [77-79] When ammonia or acetonitrile are used as nitrogen source for doping the carbon surface, it is known that pyridine- and pyrrole-like functions are created at the edges of the carbon material. [73, 80-86] Sulphur also plays an important role in changing the catalytic properties of carbon support when it is used as heteroatom in the doping process. [87, 88] Therefore, heteroatoms located at defect sites alter the electronic properties of carbon supports. [89, 90] Specifically, the electronic perturbations caused by nitrogen and sulphur can be significant as inert carbons became catalytically active as a result of the doping process.

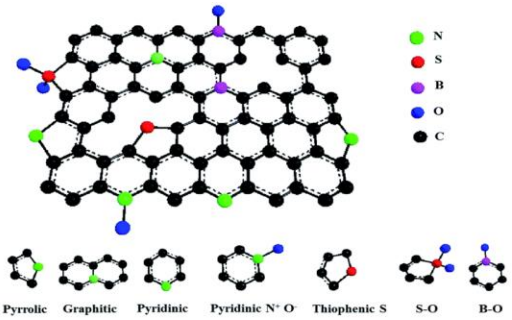

Figure 1.11 Possible groups obtained by doping of heteroatoms in a graphene (G) sheet. [91]

1.8.3 Thermal treatment

A thermal treatment may also improve the carbon surface removing impurities (*e.g.*, amorphous carbon) and/or change its chemical activity, for example by selective removal of functional groups (see Figure 1.12).

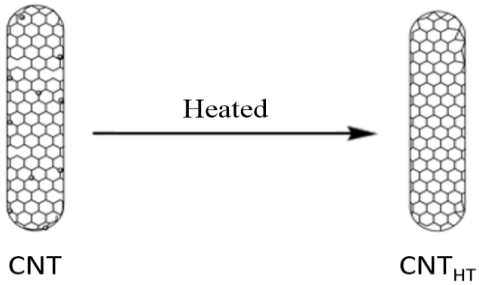

Figure 1.12 Multi-walled carbon nanotubes (CNT) modified by a high temperature (HT) treatment.

1.9 Carbon materials compared to conventional oxides

It should be mentioned that carbon materials are typically considered inert catalyst supports compared to conventional oxides as they lack Lewis acid sites and present only weak Brønsted acid-base properties. According to that, on the carbon surface at least three types of adsorption occur: weak (basal plane), strong (edge plane) and very strong or irreversible (pores). Carbon materials as catalyst supports represent an obvious alternative to oxides to study electronic metal-support interactions and eliminate the challenges associated with atom migration and metal encapsulation. [92]

1.10 Effect of active phase on support surface

The preparation of supported catalysts generally involve contacting a (porous) pre-shaped support with most often an solution of a suitable precursor of the active component which, in one of the subsequent preparation steps, is converted into the active component. Only when a sufficiently high interaction between the two exists at this stage of the procedure, the wished distribution and high dispersion of the active component can be achieved. With poor interactions notably during removal of the solvent, *e.g.*, during drying, an unwanted re-distribution may occur leading to broad particle size distribution of the active component. [48] The interaction between the solvated precursors and the support surface as modified by the solvent is generally of an electrostatic nature.

Generally speaking, dispersions tend to be relatively low in microporous carbons [93, 94] while higher dispersions can be obtained when mesopores are present. [94]

1.11 Palladium-group metals as active phase

The use of palladium-group metals as active phase on carbon supports has showed high activity and selectivity towards the main product for hydrogenation, oxidation, hydrodehalogenation, decarbonylation, and debenzylation reactions (see Figure 1.13). [95-97] Therefore, the catalytic activity of palladium catalyst supported on carbon strongly depends on the physicochemical properties of palladium particles and carbon such as size and dispersion of loaded palladium particles and surface chemistry of the carbon support. [98] Hence, an effective control of these properties can be reached by modifying surface functional groups on carbon supports [99, 100] or by the use of carbon with well-defined structures such as mesoporous carbons, [101, 102] carbon nanotubes, [103, 104] carbon nanofibers, and/or graphene layers. As already mentioned, the properties of carbon supports are modified by surface functional groups, thus these carbon supports arise to be more chemically actives and allow increasing the number of anchoring sites, ensuring a great palladium dispersion on the support. [105] These anchoring sites can be destroyed during a treatment (*e.g.*, thermal), but the number of the remaining ones could still be sufficient to bind the palladium metal on carbon support treated.

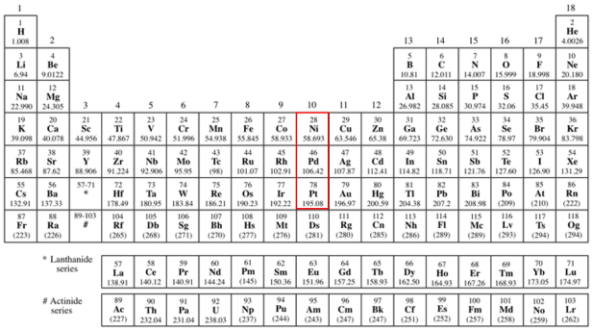

Figure 1.13 Palladium-group metals (located into the red rectangle).

1.12 Motivation

The use of catalysis, together with green chemistry and sustainable development, allow achieving the desired target without adverse implications in large- and small-scale chemical processes, keeping a cleaner environment, lower costs, and stable public relationship. According to that, the preparation and characterization of highly selective supported catalysts for selected chemical reaction is the main goal of this PhD thesis.

1.13 Problem identification

The need to carry out cleaner large-scale chemical reactions decreasing costs, energy, wastes, hazardous chemicals, and toxic solvents is only achieved by using supported metal catalysts with higher performances compared to the catalysts commonly employed. A clean environment, stable public health, suitable growth of flora and fauna, and a social, economic and environmental coexistence will become the result of a catalyzed chemical reaction.

1.14 Aims

According to Introduction, we propose to resolve the problem previously described applying the following aims:

- **General**

Preparation and characterization of highly selective supported metal catalysts for aerobic ethanol oxidation to acetic acid.

- **Specific**

1. Synthesis of carbon nanostructures such as few layer graphene, carbon nanotubes, doped carbon nanotubes, carbon nanofibers, and fibrous carbon by the catalytic-chemical vapor deposition technique.
2. Detailed characterization of the carbon nanostructures.
3. The use of palladium metal as active phase.
4. Preparation of palladium catalysts supported on various carbon nanostructures by the wetness impregnation method.
5. Detailed characterization of the palladium catalysts.
6. Palladium catalysts employed in the aerobic ethanol oxidation to acetic acid.

1.15 Summary

Catalysis continues being the main key for all industrial process. In particular, oxidation of alcohols mainly ethanol oxidation to acetic acid is considered as an interesting catalyzed chemical reaction by supported metal catalysts. Metals such as palladium and gold are often employed for ethanol oxidation. Carbon materials such as graphene, carbon nanotubes, and carbon nanofibers have become suitable catalyst supports due to their well-defined nanostructures and unique physicochemical properties. Thus, palladium catalysts supported on carbon materials will be considered as those heterogeneous catalysts employed for ethanol oxidation reaction to acetic acid as will be discussed in this PhD thesis.

1.16 References

[1] J. Hagen, Industrial Catalysis: A Practical Approach, Chapter 1: Introduction, Second Edition, Wiley-VCH, Weinheim (**2006**) ISBN: 3-527-31144-0.

[2] G. Rothenberg, Catalysis: Concepts and Green Applications, Chapter 1: Introduction, Second Edition, Wiley-VCH, Weinheim (**2017**) ISBN: 978-3-527-34305-8.

[3] J. Weitkamp, R. Gläser, Katalyse In: Winnacker and Küchler, Chemische Technik Prozesse und Produkte. Wiley-VCH, Weinheim (**2004**).

[4] Frost and Sullivan, Advanced Catalysts, Global Overview of Technological Developments, D (**2004**) 282.

[5] R. A. Sheldon, Fine chemicals by catalytic oxidation CHEMTECH SEPT. (**1991**) 566.

[6] S. K. Ritter, Green Chemistry Report, Chemical & Eng. News 80, 47, (**2002**) 19.

[7] https://doi.org/10.1002/14356007.a01_045.pub3.

[8] "Production report." Chem. Eng. News (**2005**) 67–76.

[9] G. Centi, S. Perathoner, "Catalysis and sustainable (green) chemistry," Catalysis Today, 77, 4 (**2003**) 287–297.

[10] J. H. Clark, D. J. Macquarrie, "Heterogeneous catalysis in liquid phase transformations of importance in the industrial preparation of fine chemicals," Organic Process Research & Development, 1, 2 (**1997**) 149–162.

[11] Y. Wang, X. Wang, M. Antonietti, "Polymeric graphitic carbon nitride as a heterogeneous organocatalyst: from photochemistry to multipurpose catalysis to sustainable chemistry," Angewandte Chemie International Edition, 51, 1 (**2012**) 68–89.

[12] P. Sudarsanam, L. Katta, G. Thrimurthulu, B. M. Reddy, "Vapor phase synthesis of cyclopentanone over nanostructured ceria-zirconia solid solution catalysts," Journal of Industrial and Engineering Chemistry, 19, 5 (**2013**) 1517–1524.

[13] A. Kajbafvala, H. Ghorbani, A. Paravar, J. P. Samberg, E. Kajbafvala, S. K. Sadrnezhaad, "Effects of morphology on photocatalytic performance of Zinc oxide nanostructures synthesized by rapid microwave irradiation methods," Superlattices and Microstructures, 51, 4 (**2012**) 512–522.

[14] K.-H. Kim, S.-K. Ihm, "Heterogeneous catalytic wet air oxidation of refractory organic pollutants in industrial wastewaters: a review," Journal of Hazardous Materials, 186, 1 (**2011**) 16–34.

[15] A. Corma, H. García, F. X. Llabrés I Xamena, "Engineering metal organic frameworks for heterogeneous catalysis," Chemical Reviews, 110, 8 (**2010**) 4606–4655.

[16] A. Kajbafvala, S. Zanganeh, E. Kajbafvala, H. R. Zargar, M. R. Bayati, S. K. Sadrnezhaad, "Microwave-assisted synthesis of narcis-like zinc oxide nanostructures," Journal of Alloys and Compounds, 497, 1-2 (**2010**) 325–329.

[17] M. Yoon, R. Srirambalaji, K. Kim, "Homochiral metal-organic frameworks for asymmetric heterogeneous catalysis," Chemical Reviews, 112, 2 (**2012**) 1196–1231.

[18] P. Kim, Y. Kim, H. Kim, I. K. Song, J. Yi, "Synthesis and characterization of mesoporous alumina for use as a catalyst support in the hydrodechlorination of 1,2-dichloropropane: effect of preparation condition of mesoporous alumina," Journal of Molecular Catalysis A: Chemical, 219, 1 (**2004**) 87–95.

[19] I. Mora-Barrantes, A. Rodríguez, L. Ibarra, L. González, J. L. Valentín, "Overcoming the disadvantages of fumed silica as filler in elastomer composites," Journal of Materials Chemistry, 21, 20 (**2011**) 7381–7392.

[20] G. Perot, M. Guisnet, "Advantages and disadvantages of zeolites as catalysts in organic chemistry,"Journal of Molecular Catalysis, 61, 2 (**1990**) 173–196.

[21] A. Nezamzadeh-Ejhieh, S. Khorsandi, "Photocatalytic degradation of 4-nitrophenol with ZnO supported nano-clinoptilolite zeolite," Journal of Industrial and Engineering Chemistry, 20, 3 (**2014**) 937–946.

[22] A.-N. A. El-Hendawy, "Surface and adsorptive properties of carbons prepared from biomass," Applied Surface Science, 252, 2 (**2005**) 287–295.

[23] Z. Z. Chowdhury, S. B. A. Hamid, R. Das et al., "Preparation of carbonaceous adsorbents from lignocellulosic biomass and their use in removal of contaminants from aqueous solution," BioResources, 8, 4 (**2013**) 6523–6555.

[24] D. Cole-Hamilton, R. Tooze, "Homogeneous catalysis—advantages and problems," in Catalyst Separation, Recovery and Recycling, Springer (**2006**) 1-8.

[25] H. Wang, W. Fan, Y. He, J. Wang, J. N. Kondo, T. Tatsumi, "Selective oxidation of alcohols to aldehydes/ketones over copper oxide-supported gold catalysts," Journal of Catalysis 299 (**2013**) 10–19.

[26] G. Zhao, M. Deng, Y. Jiang, H. Hu, J. Huang, Y. Lu, "Microstructured Au/Ni-fiber catalyst: Galvanic reaction preparation and catalytic performance for low-temperature gas-phase alcohol oxidation,"Journal of Catalysis 301 (**2013**) 46–53.

[27] W. Li, A. Wang, X. Liu, T. Zhang, "Silica-supported Au-Cu alloy nanoparticles as an efficient catalyst for selective oxidation of alcohols," Applied Catalysis A: General 433-434 (**2012**) 146–151.

[28] V. V. Costa, M. Estrada, Y. Demidova et al., "Gold nanoparticles supported on magnesium oxide as catalysts for the aerobic oxidation of alcohols under alkali-free conditions," Journal of Catalysis 292 (**2012**) 148–156.

[29] H. Liu, Y. Liu, Y. Li, Z. Tang, H. Jiang, "Metal-organic framework supported gold nanoparticles as a highly active heterogeneous catalyst for aerobic oxidation of alcohols," Journal of Physical Chemistry C, 114, 31 (**2010**) 13362–13369.

[30] X. Yang, X. Wang, C. Liang et al., "Aerobic oxidation of alcohols over Au/TiO_2: an insight on the promotion effect of water on the catalytic activity of Au/TiO_2," Catalysis Communications, 9, 13 (**2008**) 2278–2281.

[31] H. Li, B. Guan, W. Wang et al., "Aerobic oxidation of alcohol in aqueous solution catalyzed by gold,"Tetrahedron, 63, 35 (**2007**) 8430–8434.

[32] S. Endud, K.-L. Wong, "Mesoporous silica MCM-48 molecular sieve modified with $SnCl_2$ in alkaline medium for selective oxidation of alcohol," Microporous and Mesoporous Materials, 101, 1-2 (**2007**) 256–263.

[33] T. Hayashi, T. Inagaki, N. Itayama, H. Baba, "Selective oxidation of alcohol over supported gold catalysts: methyl glycolate formation from ethylene glycol and methanol," Catalysis Today, 117, 1–3 (**2006**) 210–213.

[34] B. Guan, D. Xing, G. Cai et al., "Highly selective aerobic oxidation of alcohol catalyzed by a Gold(I) complex with an anionic ligand," Journal of the American Chemical Society, 127, 51 (**2005**) 18004–18005.

[35] L. Prati, F. Porta, "Oxidation of alcohols and sugars using Au/C catalysts: part 1. Alcohols," Applied Catalysis A: General, 291, 1-2 (**2005**) 199–203.

[36] A. B. Gaspar, F. G. Barbosa, S. Letichevsky, L. G. Appel, Appl. Catal., A 380 (**2010**) 113.

[37] P. R. Blum, J. B. Hazen, M. F. Lemanski, USPTO US5334751A, ed., The Standard Oil Company: USA (**1994**).

[38] T. Y. Yan, J.–R. Chang, USPTO US6399812 B1, Ed., T. Y. Yan J.-R. Chang: USA (**2002**).

[39] T. Takei, N. Iguchi, M. Haruta, New J. Chem. 35 (**2011**) 2227.

[40] S. M. Tembe, G. Patrick, M. S. Scurrell, Gold Bull. 42 (**2009**) 321.

[41] N. F. Zheng, G. D. Stucky, J. Am. Chem. Soc. 128 (**2006**) 14278.

[42] D. S. Cameron, S. J. Cooper, I. L. Dodgson, B. Harrison, J. W. Jenkins, Catal. Today 7 (**1990**) 113.

[43] R. Burmeister, B. Despeyroux, K. Deller, K. Seibold, P. Albers, Stud. Surf. Sci. Catal 78 (**1993**) 361.

[44] P. Albers, R. Burmeister, K. Deller, B. Despeyroux, German Patent DE 4308101, to Degussa AG (**1994**).

[45] J. Günther, TELMA (Hannover) 20 (**1990**) 157.

[46] O. Wohler F. von Sturm, E. Wege, H. von Kienle, M. Voll, P. Kleinschmit, in: W. Gerhartz (Ed.), Ullmann's Encyclopedia of Industrial Chemistry, vol. A5, VCH, Weinheim (**1986**) 95.

[47] S. Ban, K. Malek, C. Huang, Z. Liu, Carbon 49 (**2011**) 3362-3370.

[48] R. A. van Santen, P. W. N. M. van Leeuwen, J. A. Moulijn, B. A. Averill (Eds.), Study of Surface Science Catalysis 123 (**1999**) (Chapters 9 and 10).

[49] R. L. Augustine, Heterogeneous Catalysis for the Synthetic Chemist, Marcel Dekker, New York (**1996**) (Chapter 13).

[50] P. Gallezot, S. Chaumet, A. Perrard, P. Isnard, J. Catal. 168 (**1997**) 104.

[51] D. Richard, P. Gallezot, D. Neibecker, I. Tkatchenko, Catal. Today 6 (**1989**) 171.

[52] D. Richard, P. Fouilloux, P. Gallezot, in: M. J. Phillips, M. Ternan (Eds.), Proc. 9th Int Congr. Catal. 3 (**1998**) 1074.

[53] A. Giroir-Fendler, D. Richard, P. Gallezot, Stud. Surf. Sci. Catal. 41 (**1998**) 171.

[54] S. Iijima, Nature 354 (**1991**) 56-58.

[55] http://dx.doi.org/10.1039/9781782622567.

[56] C. Emmenegger, J. M. Bonard, Ph. Mauron, P. Sudan, A. Lepora, B. Groberty, A. Zuttel, L. Schalapbach, Carbon 41 (**2003**) 539.

[57] M. Ajayan, O. Stephan, Ph. Redlich, C. Colliex, Nature 375 (**1995**) 564.

[58] J. P. Tessonnier, L. Pesant, G. Ehret, M. J. Ledoux, C. Pham-Huu, Applied Catalysis A: General 288 (**2005**) 203-210.

[59] D. Chen, K. O. Christensen, E. Ochoa-Fernandez, Z. Yu, B. Totdal, N. Latorre, A. Monzon, A. Holmen, Synthesis of Carbon Nanofibers: Effects of Ni crystal size during Methane Decomposition. J. Catal. 229 (**2005**) 82.

[60] M. S. Hoogenraad, Ph.D thesis, Utrecht University (**1995**) (Chapters 2 and 7).

[61] K. P. de Jong, J. W. Geus, Catal. Rev. Sci. Eng. 42 (**2000**) 481.

[62] V. N. Parmon, G. G. Kuvshinov, V. A. Sadykov, V. A. Sobyanin, Stud. Surf. Sci. Catal. 119 (**1998**) 677.

[63] N. M. A. Rodriguez, Review of Catalytically Grown Carbon Nanofibers, J. Mater. Res. 8 (**1993**) 3233.

[64] T. D. Tran, S. H. Langer, Electrochim. Acta 38 (**1993**) 1551.

[65] A. Giroir-Fendler, D. Richard, P. Gallezot, Faraday Discuss. 92 (**1992**) 69.

[66] D. Richard, P. Gallezot, Stud. Surf. Sci. Catal. 31 (**1987**) 71.

[67] H. Ago, T. Kugler, F. Cacialli, W. R. Salaneck, M. S. P. Shaffer, A. H. Windle, R. H. Friend, Work Functions and Surface Functional Groups of Multiwall Carbon Nanotubes. J. Phys. Chem. B 103 (**1999**) 8116.

[68] H. Hiura, T. W. Ebbesen, K. Tanigaki, Opening and Purification of Carbon Nanotubes in High Yields. Adv. Mater. 7 (**1995**) 275.

[69] M. S. P. Shaffer, X. Fan, A. H. Windle, Dispersion and Packing of Carbon Nanotubes. Carbon 36 (**1998**) 1603.

[70] D. B. Mawhinney, V. Naumenko, A. Kuznetsova, J. T. Yates, J. Liu, R. E. Smalley, Surface Defect Site Density on Single Walled Carbon Nanotubes by Titration. Chem. Phys. Lett. 324 (**2000**) 213.

[71] H. Darmstadt, L. Summchen, J. M. Ting, U. Roland, S. Kaliaguine, C. Roy, Effects of Surface Treatment on the Bulk Chemistry and Structure of Vapor Grown Carbon Fibers. Carbon 35 (**1997**) 1581.

[72] TT. G. Ros, A. J. van Dillen, J. W. Geus, D. C. Koningsberger, Surface Oxidation of Carbon Nanofibers. Chem.-Eur. J. 8 (**2002**) 1151.

[73] F. Rodriguez-Reinoso, Carbon 36 (**1998**) 159.

[74] G. Ertl, H. Knözinger, J. Weitkamp (Eds.), Preparation of Solid Catalysts, Wikey, Weinhein, (**1999**) (Chapters 3 and 4).

[75] S. V. Gurevich, P. A. Simonov, A. S. Lisitsyn, V. A. Likholobov, E. M. Moroz, A. L. Chuvilin V. N. Kolomiichuk, React. Kinet. Catal. Lett. 41 (**1990**) 211.

[76] C. Prado-Burguete, A. Linares-Solano, F. Rodriguez-Reinoso, C. Salinas-Martinez de Lecea, J. Catal. 115 (**1989**) 98.

[77] R. C. Bansal, J.-B. Donnet, F. Stoeckli, Active Carbon, Marcel Dekker, New York (**1988**).

[78] H. P. Boehm, in: C. Morterra, A. Zecchina, G. Costa (Eds.), Structure and Reactivity of Surfaces, Elsevier, Amsterdam (**1989**) 145.

[79] H. P. Boehm, Carbon 32 (**1994**) 759.

[80] B. Stöhr, H. P. Boehm, R. Schlögl Carbon, 29, 6 (**1991)** 707-20.

[81] J. R. Pels, F. Kapteijn, J. A. Moulijn, Q. Zhu, K. M. Thomas, Carbon, 33, 11 (**1995**) 1641-53.

[82] R. J. J. Jansen, Ph.D thesis, Delft University (**1994**) (Chapter 1).

[83] H. P. Boehm, Carbon 32 (**1994**) 759.

[84] B. Stöhr, H. P. Boehm, R. Schlögl, Carbon, 29, 6 (**1991**) 707-20.

[85] J. R. Pels, F. Kapteijn, J. A. Moulijn, Q. Zhu, K. M. Thomas, Carbon, 33, 11 (**1995**) 1641-53.

[86] A. Benyounes, M. Kacimi, M. Ziyad, P. Serp, Chinese Journal of Catalysis 35 (**2014**) 970-978.

[87] V. Meeyoo, J. H. Lee, D. L. Trimm, N. W. Cant Catal. Today 44 (**1998**) 67.

[88] T.-C. Yu, H. Shaw, Appl. Catal. B 18 (**1998**) 105.

[89] Y. Zheng et al. Hydrogen evolution by a metal-free electrocatalyst. Nat. Commun. 5 (**2014**) 3783.

[90] Y. Ito, W. Cong, T. Fujita, Z. Tang & M. Chen, High catalytic activity of nitrogen and sulfur co-doped nanoporous graphene in the hydrogen evolution reaction. Angew. Chem. Int. Ed. 54 (**2015**) 2131-2136.

[91] C. R. Raj, A. Samanta, S. H. Noh, S. Mondal, T. Okajima, T. Ohsaka, Emerging new generation electrocatalysts for the oxygen reduction reaction. J. Mater. Chem. A, 4 (**2016**) 11156-11178.

[92] E. Auer, A. Freund, J. Pietsch & T. Tacke, Carbons as supports for industrial precious metal catalysts. Appl. Catal. A 173 (**1998**) 259–271.

[93] F. Rodriguez-Reinoso, I. Rodriguez-Ramos, C. Moreno-Castilla, A. Guerrero-Ruiz, J. D. Lopez-Gonzalez, J Catal, 99, 1 (**1986**) 171-83.

[94] C. Prado-Burguete, A. Linares-Solano, F. Rodriguez-Reinoso, C. Salinas-Martínez de Lecea, J Catal, 115, 1 (**1989**) 98-106.

[95] DEGUSSA AG, Precious Metal Powder Catalysts.

[96] P. N. Rylander, Hydrogenation Methods, Academic Press, London (**1985**).

[97] M. Freifelder, Practical Catalytic Hydrogenation, Wiley, New York (**1971**).

[98] K. Kohler, R. G. Heidenreich, J. G. Krauter, E. Pietsch, J. Chem. A Eur. J 8 (**2002**) 622.

[99] J. Li, M. J. Vergne, E. D. Mowles, W. H. Zhong, D. M. Hercules, C. M. Lukehart, Carbon 43 (**2005**) 2883.

[100] Z. Li, W. Yan, S. Dai, Langmuir 21 (**2005**) 11999.

[101] H. Yang, D. Zhao, J. Mater. Chem. 15 (**2005**) 1217.

[102] R. Ryoo, S. H. Joo, M. Kruk, M. Jaroniec, Adv. Mater. 13 (**2001**) 677.

[103] S. Iijima, T. Ichihashi, Nature 354 (**1991**) 56.

[104] J. L. Bahr, J. M. Tour, J. Mater. Chem. 12 (**2002**) 1952.

[105] D. J. Suh, T.-J. Park, S.-K. Ihm, Carbon 31 (**1993**) 427.

CHAPTER II

Theoretical Framework

2.1 Introduction

In heterogeneous catalysis, the synthesis of carbon nanomaterials, the catalyst preparation method, and the catalytic process into the chemical reaction are three very important steps to consider when activity, selectivity and stability of a catalyst must be achieved. Atomic and/or molecular level knowledge about what is happening during the synthesis, preparation and reaction must completely be understood to achieve the desired goal. Furthermore, advanced characterization techniques become a necessary complement to clearly understand the catalytic processes.

To clearly understand the structural order of this Chapter II: Theoretical Framework, the main issues are summarized in Table 2.1.

Table 2.1 Main issues of Chapter II.

Issues
2.2 Growth methods of carbon nanotubes
2.3 Production of heterogeneous catalysts
2.4 Catalyst and its properties
2.5 Effect of physical adsorption on the catalyst
2.6 Individual steps in a heterogeneous catalytic reaction
2.7 Electron transfer between substrate and catalyst
2.8 Metals
2.9 Energetic aspects of catalytic activity
2.10 Catalyst performance
2.11 Catalyst deactivation and regeneration
2.12 Characterization of catalyst supports and metal catalysts
2.13 Summary
2.14 References

2.2 Growth methods of carbon nanotubes (CNT)

There are three main methods to produce carbon nanotubes: [1]

- Arc discharge method. This method creates CNT through arc-vaporization of two carbon rods placed end to end, separated by approximately 1 mm, in an enclosure that is usually filled with inert gas at low pressure.

- Laser vaporization method. In this method, CNT are prepared by laser vaporization of graphite rods with a 50:50 catalyst mixture of cobalt and nickel at 1200°C in flowing argon, followed by heat treatment in vacuum at 1000°C to remove the C_{60} and other fullerenes.

- Catalytic-chemical vapor deposition (C-CVD) method. This process consists in the decomposition of a hydrocarbon vapor into carbon and hydrogen on a catalytic surface at high temperature (600-1200 °C).

Depending upon the strength of the interaction between the catalyst metal and the substrate upon which it is deposited, two different growth models have been proposed (see Figure 2.1). [2] In each case, carbon is extracted from the hydrocarbon feedstock gas and diffuses through the catalyst particle before taking its place in the forming nanotube. The growth model when there is weak interaction between the catalyst particle and the substrate is known as “tip growth”, as the catalyst particle stays at the tip of the nanotube. The model when there is strong interaction is known as “base growth”, as the catalyst particle remains anchored to the substrate at the base of the nanotube.

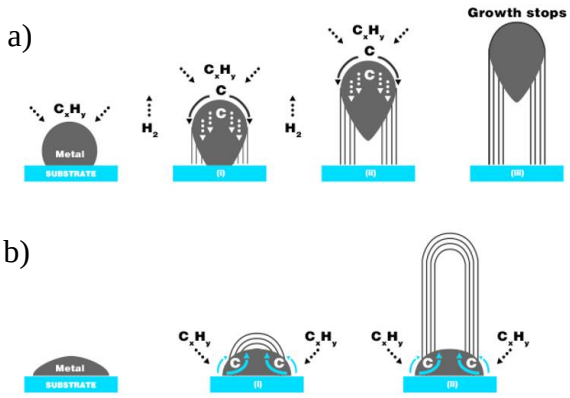

Figure 2.1 Widely accepted growth mechanisms for multi-walled carbon nanotubes (CNT) by catalytic-chemical vapor deposition (C-CVD) technique using a supported metal catalyst. a) tip-growth model and b) base-growth model.

In contrast to Figure 2.1, Figure 2.2 shows the growth mechanism for multi-walled carbon nanotubes (CNT) by catalytic-chemical vapor deposition (C-CVD) technique using an unsupported catalyst. In this case, carbon is extracted from the hydrocarbon feedstock gas and diffuses through the catalyst particle everywhere before taking its place in the forming nanotube.

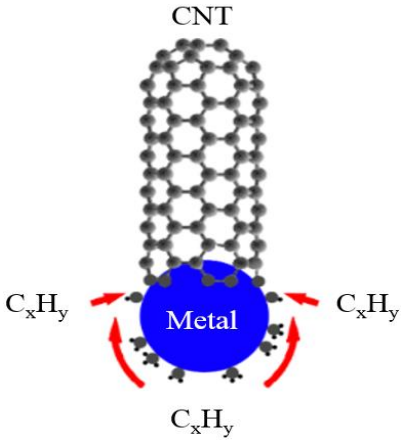

Figure 2.2 Growth mechanism for multi-walled carbon nanotubes (CNT) by catalytic-chemical vapor deposition (C-CVD) technique using an unsupported catalyst. Figure redrawn with modifications from [3].

2.3 Production of heterogeneous catalysts

Depending on their structure and method of production, catalysts can be divided into three main groups: [4]

- Bulk catalysts
- Impregnated catalysts
- Shell catalysts

One of the best-known methods for producing catalysts is the impregnation of a porous support material with solutions of active components. [5, 6]

In the impregnation process, active components with thermally unstable anions (*e.g.*, nitrates, acetates, carbonates, hydroxides) are used. The support is immersed in a solution of the active component under precisely defined conditions (concentration, mixing, temperature, time). Depending on the production conditions, selective adsorption of the active component occurs on the surface or in the interior of the support. The result is nonuniform distribution.

To achieve the best possible impregnation, the air in the pores of the support is removed by evacuation, or the support is treated with gases such as CO_2 or NH_3 prior to impregnation. After impregnation, the catalyst is dried and calcined.

For large-scale manufacture the so-called incipient wetness impregnation (also called pore volume, or dry or capillary impregnation) is the most advantageous method. In this approach the support is brought into contact with a solution the volume of which corresponds to the total pore volume of the solid and which contains the appropriate amount of precursor compound. The principle of this method is shown in Figure 2.3.

If catalysts with high loadings of the active compounds are to be made, limited solubility of the precursor compound may cause problems, and multiple impregnations may have to be applied. With incipient wetness impregnation, even precursor compounds that do not interact with the support can be deposited when the solvent is removed during a subsequent drying procedure.

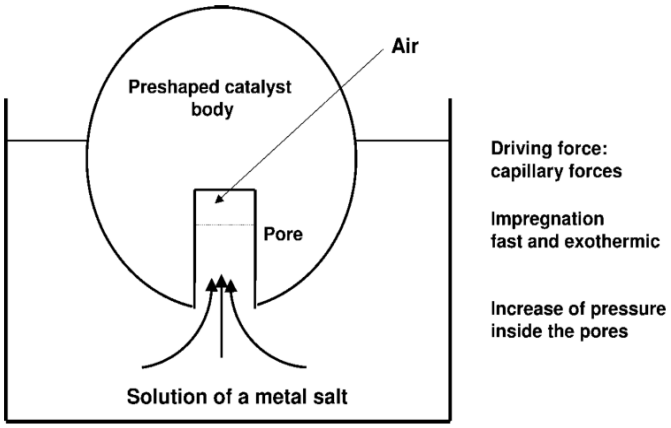

Figure 2.3 Principle of catalyst preparation by incipient wetness impregnation.

2.4 Catalyst and its properties

It is now known that the catalyst is involved in chemical bonding with the reactants during the catalytic process. Thus catalysis is a cyclic process: the reactants are bound to one form of the catalyst, and the products are released from another, regenerating the initial state (see Scheme 2.1). [7] The intermediate catalyst complexes are in most of the cases highly reactive and difficult to detect.

In theory, an ideal catalyst would not be consumed during the reaction, but this is not the case in practice. Owing to competing reactions, the catalyst undergoes chemical changes, and its activity becomes lower (catalyst deactivation). Thus catalysts must be regenerated or eventually replaced.

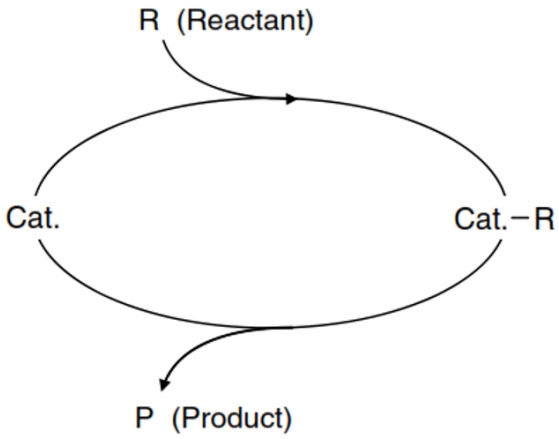

Scheme 2.1 Catalytic cycle.

Numerous organic intermediate products, required for the production of plastics, synthetic fibers, pharmaceuticals, dyes, resins, and pigments, can only be produced by catalytic processes.

Most of the processes involved in crude-oil processing and petrochemistry, such as purification stages, refining, and chemical transformations, require catalysts. Environmental protection measures such as automobile exhaust control and purification of off-gases from power stations and industrial plant would be inconceivable without catalysts. [8]

The suitability of a catalyst for an industrial process depends mainly on the following three properties: [9, 10]

- Activity
- Selectivity
- Stability (deactivation behavior)

Activity is a measure of how fast one or more reactions proceed in the presence of the catalyst.

The turnover frequency (TOF) quantifies the specific activity of a catalytic center for a specific reaction under defined reaction conditions by the number of molecular reactions or catalytic cycles occurring at the center per unit time. For a heterogeneous catalyst, the TOF can be calculated employing the following equations: [11]

$$\text{TOF } (\text{min}^{-1}) = \frac{\text{Total feed (mol min}^{-1})}{\text{Metal loading (mol)}} \times \text{Conversion}$$

$$\text{Conversion} = \frac{\text{n}(\text{A}_{\text{in}}) - \text{n}(\text{A}_{\text{out}})}{\text{n}(\text{A}_{\text{in}})} \times 100$$

where,

$n(A_{in})$ = Input moles of reactant "A"

$n(A_{out})$ = Output moles of reactant "A"

The turnover number (TON) specifies the maximum use that can be made of a catalyst for a specific reaction under defined conditions by a number of molecular reactions or reaction cycles occurring at the reactive center up to the decay of activity. The relationship between TOF and TON is: [12]

$$\text{TON} = \text{TOF } (min^{-1}) \times \text{Lifetime of the catalyst (min)}$$

The selectivity of a reaction is the fraction of the starting material that is converted to the desired product. It is expressed by the ratio of the amount of desired product to the reacted quantity of a reaction partner A and therefore gives information about the course of the reaction. The selectivity of the reaction depends strongly on the catalyst and the reaction conditions. In addition to the desired reaction, parallel and sequential reactions can also occur (see Scheme 2.2):

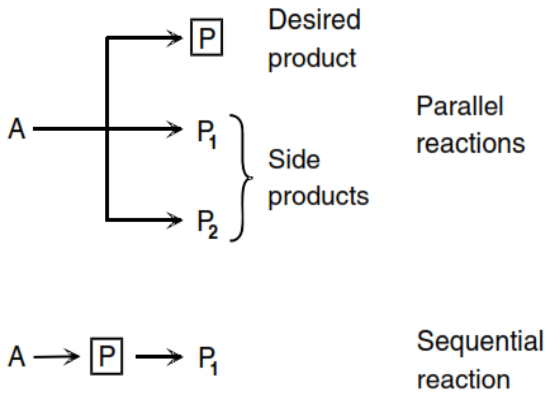

Scheme 2.2 Parallel and sequential reactions.

Thus, the product selectivity can be calculated using the following equations: [11]

$$\text{Product selectivity} = \frac{\text{Product yield}}{\text{Conversion}} \times 100$$

$$\text{Product yield} = \frac{\text{Fraction of A converted to product}}{A_{in}} \times 100$$

$$\text{Conversion} = \frac{n(A_{in}) - n(A_{out})}{n(A_{in})} \times 100$$

where,

A = reactant "A"

A_{in} = Input of reactant "A"

$n(A_{in})$ = Input moles of reactant "A"

$n(A_{out})$ = Output moles of reactant "A"

The chemical, thermal, and mechanical stability of a catalyst determines its lifetime in industrial reactors. Catalyst stability is influenced by numerous factors, including decomposition, coking, and poisoning. Catalyst deactivation can be followed by measuring activity or selectivity as a function of time.

Catalysts that lose activity during a process can often be regenerated before they ultimately have to be replaced. The total catalyst lifetime is of crucial importance for the economics of a process. Today the efficient use of raw materials and energy is of major importance, and it is often preferable to optimize existing processes than to develop new ones. For various reasons, the target quantities should be given the following order of priority:

Selectivity > Stability > Activity

2.5 Effect of physical adsorption on the catalyst

In any gas/solid catalytic system, the reactant must first be adsorbed on the catalyst surface. This is why surface characterization is so important. Studying the adsorption of various molecules under controlled conditions yields information regarding the catalyst surface area, pore volume, and pore size distribution. [13] The key factor here is accessibility. There are two types of adsorption. In physical adsorption, or physisorption, the molecules are attached to the surface through Van der Waals interactions. Conversely, chemical adsorption, or chemisorption, involves the breaking and creation of chemical bonds. Both adsorption types are used in characterization studies. Physisorption is used for determining the total surface area and pore volume, usually at temperatures that are close to the boiling point of the adsorbate. Nitrogen adsorption at 77 K is normally used.

Conversely, chemisorption is used for measuring specific chemical entities (such as Brønsted acid sites) on the surface. It is also used to determine the active surface area.

The total surface area of a solid is related to the volume of gas that is adsorbed on this surface at a given temperature and pressure. An adsorption isotherm is a graph, which shows how the amount adsorbed depends on the equilibrium pressure of the gas, at constant temperature. There are six main types of isotherms (see Figure 2.4). Type I isotherms are typical for adsorption on microporous materials, such as molecular sieves and some activated carbons. Type II isotherms describe a multilayer adsorption on a nonporous or macroporous material. Isotherm types III and V are related to no monolayer formation, so the incoming molecule is adsorbed preferentially on another adsorbed molecule, rather than on an "empty" site, for example, when H_2O is adsorbed on a hydrophobic material. For heterogeneous catalysis applications, the most important materials are those with type IV isotherms (monolayer formation followed by filling of mesopores). [14] The type IV isotherm, in which the initial region is closely related to type II, tends to level off at high relative pressure. The initial part of the type IV isotherm is attributed to the monolayer-multilayer adsorption, because it follows the same path as the corresponding part of a type II isotherm obtained with the given adsorptive on the same surface area of the adsorbent in a non-porous form. [15] It exhibits a hysteresis loop, the lower branch of which represents measurements obtained by progressive addition of gas of the adsorbent, and the upper branch represents measurements by progressive withdrawal. The hysteresis loop is associated with the filling and emptying of the mesopores by capillary condensation. Type IV isotherms are common, but the exact shape of the hysteresis loop varies from one system to another. [16]

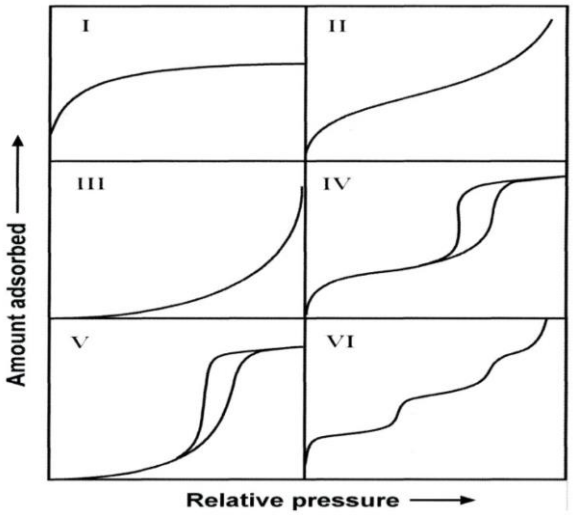

Figure 2.4 The six types of adsorption isotherms.

2.6 Individual steps in a heterogeneous catalytic reaction

Heterogeneously catalyzed reactions are composed of purely chemical and purely physical reaction steps. For the catalytic process to take place, the starting materials must be transported to the catalyst. Thus, apart from the actual chemical reaction, diffusion, adsorption, and desorption processes are of importance for the progress of the overall reaction. In a catalytic gas reaction on a porous catalyst, the reaction steps are (see Figure 2.5): [17, 18]

1) Diffusion of the starting materials through the boundary layer to the catalyst surface.
2) Diffusion of the starting materials into the pores (pore diffusion).
3) Adsorption of the reactants on the inner surface of the pores.
4) Chemical reaction on the catalyst surface.
5) Desorption of the products from the catalyst surface.
6) Diffusion of the products out of the pores.
7) Diffusion of the products away from catalyst through the boundary layer and into the gas phase.

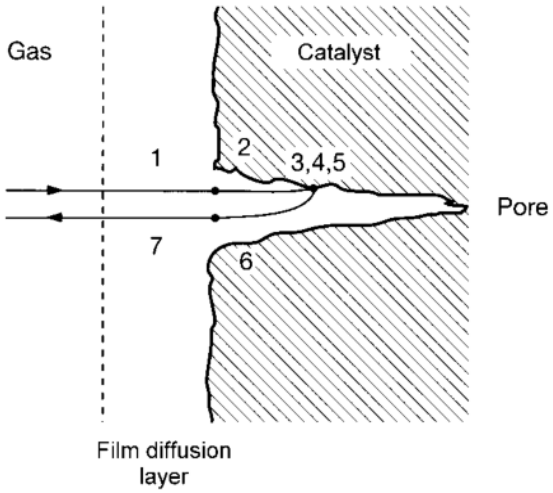

Figure 2.5 Individual steps of a heterogeneously catalyzed gas-phase reaction.

In heterogeneous catalysis chemisorption of the reactants and products on the catalyst surface is of central importance, so that the actual chemical reaction (step 4) cannot be considered independently from steps 3 and 5.

2.7 Electron transfer between substrate and catalyst

The following classification is relative to the substrate:

- Acceptor reactions: Electrons flow from catalyst to substrate; the adsorbate acts as an acceptor (examples: starting materials with high electron affinity; reactions in which oxygen is mobilized).

- Donor reactions: Electrons flow from substrate to catalyst (examples: substrates that readily release electrons, *i.e.*, reducing agents with low ionization energies; reactions in which H_2 or CO is mobilized.

This classification is schematically shown in Figure 2.6.

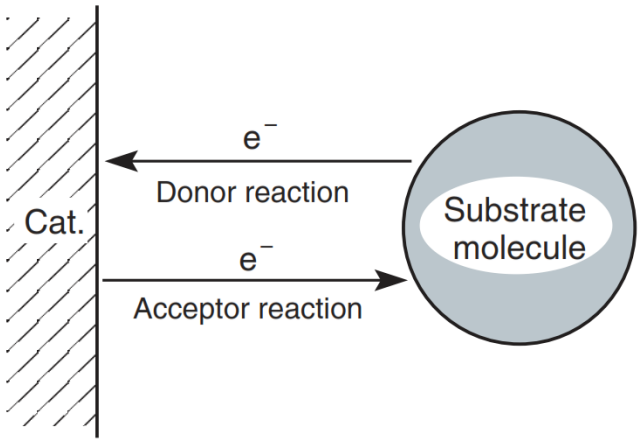

Figure 2.6 Electron transfer between catalyst and substrate.

2.8 Metals

For metals and metal alloys in particular, relationships have been sought between collective properties and catalytic behavior. The metallic state was generally described by the simple band model or the Pauling valence structure theory.

In metals the valence shell is formed by the s or d band. The main-group elements with their s bands are typical electron donors and form strong bonds with electron acceptors such as sulfur or oxygen; stable sulfides and oxides are formed. These metals are therefore not suitable as catalysts. In contrast the transition metals with their d bands are excellent catalysts. It is noteworthy that both hydrogenation and oxidation reactions can be carried out with d-block elements.

Metals normally have a relatively narrow d band. The catalytic properties are strongly influenced by the occupational density of the electrons in this band. In many cases, a direct relationship has been found between the catalytic activity of transition metals and the electronic properties of the unfilled d bands. This is shown by the general trend of the rate of adsorption along the transition metal rows. [19, 20]

The bonding in a transition metal is partially due to unpaired electrons in bonding d orbitals. The contribution of these *d* electrons to the valence bonding was termed "percentage of *d* character" of the metallic bonding by Pauling, who made a distinction between three types of *d* orbitals in transition metals:

- Bonding *d* orbitals involved in covalent dsp hybrid bonds
- Metallic (free) *d* orbitals
- Atomic *d* orbitals

2.9 Energetic aspects of catalytic activity [4, 21]

Chemisorption and associated energetic aspects play a crucial role in understanding heterogeneous catalysis. [22] The active centers on the catalyst surface are probably the result of free valences or electron defects, which weaken the bonds in the adsorbed molecules to such an extent that a reaction can readily occur. The course of a heterogeneously catalyzed reaction is compared to that of an uncatalyzed reaction in Figure 2.7.

In this figure, the three elementary steps on the catalyst surface are depicted qualitatively together with the corresponding energies. For the catalyzed reaction a distinction should be made between the apparent activation energy, starting from the ground state of the gaseous molecule, and the true activation energy, relative to the chemisorbed state. The latter, also known as catalytic activation energy, is more important. Sometimes the product or intermediates being formed may be so strongly bound on the surface that its desorption or further reaction is hindered. In this case the catalyst is poisoned by the product and becomes inactive.

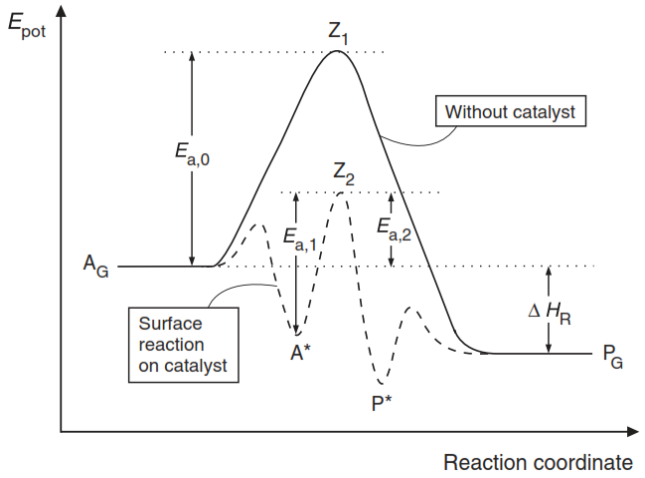

Figure 2.7 Course of a heterogeneously catalyzed gas-phase reaction $A_G \rightarrow P_G$.

where,

$E_{a,0}$ = Activation energy of the homogeneous uncatalyzed gas-phase reaction

$E_{a,1}$ = True activation energy

$E_{a,2}$ = Apparent activation energy of the catalyzed reaction

Z_1 = Transition state of the gas-phase reaction

Z_2 = Transition state of the surface reaction

ΔH_R = Reaction enthalpy

2.10 Catalyst performance

2.10.1 Factors that affect the catalyst performance

It is obvious that a good catalyst should possess high activity. A high activity allows relatively small reactor volumes, short reaction times, and operation under mild conditions. High selectivity is often more important than high activity. Furthermore, a catalyst should maintain its activity and selectivity over a period of time, *i.e.*, it should have sufficient stability.

Catalysts are developed for specific processes, *e.g.*, for a specific reaction in a specific reactor under specific reaction conditions. Therefore, there are many requirements for an industrial catalyst:

- High activity
- High selectivity
- Sufficient stability
- Possibilities for regeneration
- Reproducible production method
- Sufficient thermal stability against sintering
- High compressive strength
- High resistance against mechanical stress

The catalytic performance can be affected by many influences such as:

- Active phase
- Support
- Environment of the reaction
- Promoters
- Inhibitors

The properties of a catalyst can be manipulated by any process that alters the properties of its surface, since the nature of the individual sites at the surface is responsible for the activity, selectivity, and stability of the catalyst.

The most important reasons to use supported catalysts in industry are:

- Costs. The catalytically active components of supported catalysts are often expensive metals. Since this active component is applied in a highly dispersed form, the metal represents only a small fraction of the total catalyst mass.
- Activity. The high activity leads to fast reaction rates, short reaction times, and maximum throughput.
- Selectivity. The selectivity facilitates the following: maximum yield, elimination of side products, and lowering of purification costs.
- Regenerability. It helps keep process costs low.

2.10.1.1 Promoters [23]

Promoters are substances that are themselves not catalytically active but increase the activity of catalysts. There are four types of promoters:

- Structure promoters. They increase the selectivity by influencing the catalyst surface such that the number of possible reactions for the adsorbed molecules decreases and a favored reaction path dominates.
- Electronic promoters. They become dispersed in the active phase and influence its electronic character and therefore the chemical binding of the adsorbate.

- Textural promoters. They inhibit the growth of catalyst particles to form larger, less active structures during the reaction.
- Catalyst-poison-resistant promoters. They protect the active phase against poisoning by impurities.

2.10.1.2 Inhibitors

An inhibitor is a substance that reduces the rate of a catalytic reaction, often as a result of bonding chemically to the catalyst.

2.11 Catalyst deactivation and regeneration [24]

Catalysts have only a limited lifetime. Some lose their activity after a few minutes, others last for more than ten years. The maintenance of catalyst activity for as long as possible is of major economic importance in industry. A decline in activity during the process can be the result of various physical and chemical factors such as:

- Blocking of the catalytically active sites
- Loss of catalytically active sites due to chemical, thermal, or mechanical processes.

The course of the activity of an industrial catalyst with time can be described as shown in Figure 2.8:

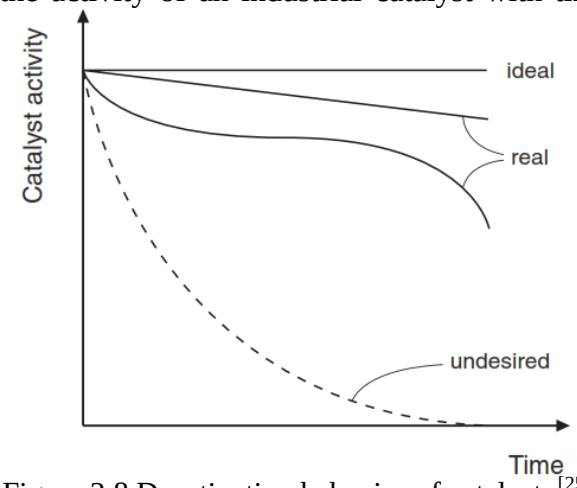

Figure 2.8 Deactivation behavior of catalyst. [25]

The four most common causes of catalyst deactivation are (see Figure 2.9): [26]

- Poisoning of the catalyst
- Deposits on the catalyst surface that block the active centers and change the pore structure
- Thermal processes and sintering of the catalyst lead to a loss of active surface area
- Catalyst losses by evaporation of components

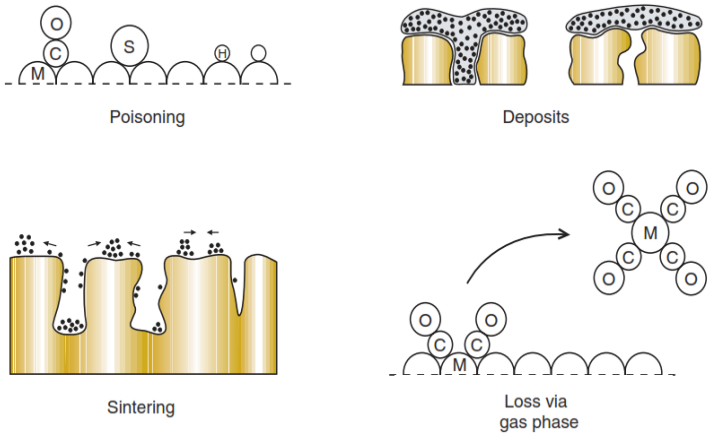

Figure 2.9 Mechanisms of catalyst deactivation (M = metal). [4]

The catalyst activity varies with time as shown in Figure 2.10. The activity decreases with increasing operating time in a manner that depends on the reaction conditions and the deactivation kinetics. The loss of activity can be gradual or very rapid.

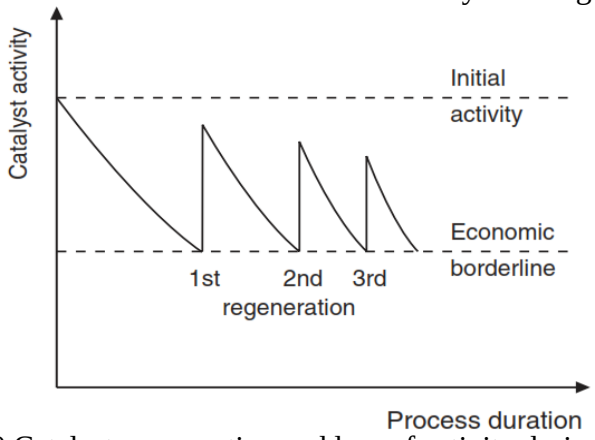

Figure 2.10 Catalyst regeneration and loss of activity during a process.

2.12 Characterization of catalyst supports and metal catalysts

Characterization of nanostructured materials is driven by the need to have qualitative and quantitative information, which serve as the basis for comparison and selection of nanostructured materials, such as, in our case, multi-walled carbon nanotubes, doped multi-walled carbon nanotubes, few layer graphene, carbon nanofibers, and fibrous carbon for specific applications. Such data are also useful for modeling the behavior and performance of such carbon nanomaterials. Besides, characterization provides feedback for use in the design and preparation of carbon nanomaterials. The characteristics often measured are density, abrasion resistance, surface area, average pore size, pore size distribution, pore shape, pore volume, and the surface chemistry of the carbon.

2.12.1 Characterization techniques

Currently, advanced characterization techniques are a useful tool in the nanotechnology field. They provide very important information about the sample measured. In the preparation method, the knowledge of many characteristics from sample allows carrying out a controlled preparation that is known by using advanced characterization techniques such as scanning electron microscopy (SEM), transmission electron microscopy (TEM), high resolution transmission electron microscopy (HRTEM), elemental analysis (microanalysis), thermogravimetric analysis (TGA), physisorption (BET surface area), Raman spectroscopy (Raman), X-ray powder diffraction (XRPD), infrared spectroscopy (IR), X-ray photoelectron spectroscopy (XPS), and inductively coupled plasma-atomic emission spectroscopy (ICP-AES).

2.12.1.1 Scanning electron microscopy (SEM)

SEM is one version of the electron microscopy which uses a beam of electrons to scan the surface of a sample and makes possible the direct observation of its surface features at the micro and submicro levels.

The main features of a scanning electron microscope are an electron source which provides the electrons that interact with the sample to be examined, an arrangement of metal apertures, magnetic lenses and scanning coils or deflector plates that confine, focus and turn the beam of electrons into a thin and focused monochromatic beam which is accelerated towards the sample and which irradiates the sample in a raster fashion as shown in Figure 2.11. [27, 28]

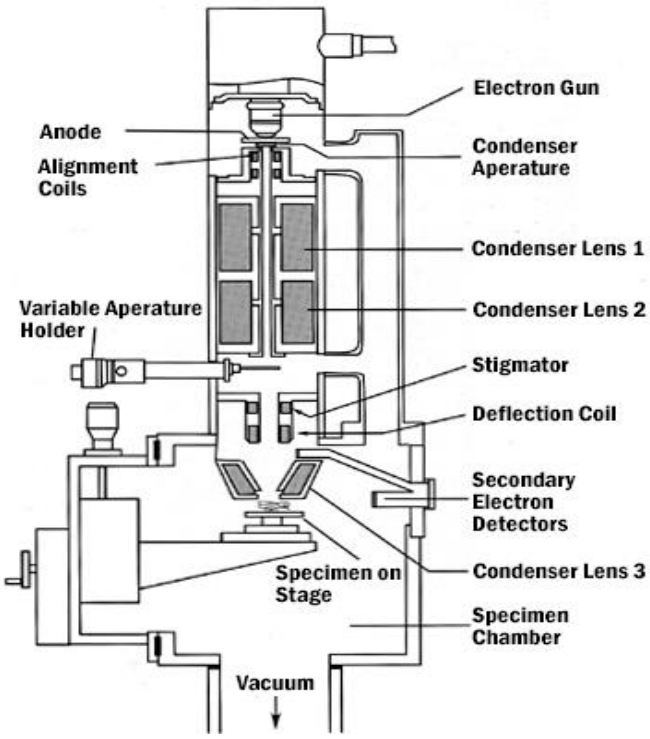

Figure 2.11 Schematic diagram of a scanning electron microscope.

The interaction of the electrons with the sample initiates a number of reactions inside the sample, which results in the generation of signals, which give information about the sample. The SEM imaging process involves four main steps. These include sample preparation, sample scanning process, image formation and image analysis.

The SEM can yield information about the topography (surface features of an object), morphology (shape and size of the particles making up the surface of an object), composition (the elements that the object is composed of and the relative amounts of these) and crystallographic information (how the atoms are arranged in the object). This ability makes the SEM a hugely useful instrument for the study of nanostructured materials. SEM micrographs have a large depth of field that yields a pseudo three-dimensional appearance useful for understanding the surface structure of a sample. [29]

2.12.1.2 Transmission electron microscopy (TEM)

TEM is an imaging technique where a beam of electrons is focused onto a sample, causing an enlarged version to appear on a fluorescent screen to be then registered by a digital camera. [30]

The transmission electron microscope is a very powerful tool for material science. A high energy beam of electrons is shone through a very thin sample, and the interactions between the electrons and the atoms can be used to observe features such as the crystal structure and features in the structure like dislocations and grain boundaries. Chemical analysis can also be performed. [31]

The main components of a transmission electron microscope are an electron source, a thermionic gun, an electron beam, electromagnetic lenses, a vacuum chamber, condensers, a sample stage, and a fluorescent screen as shown in Figure 2.12.

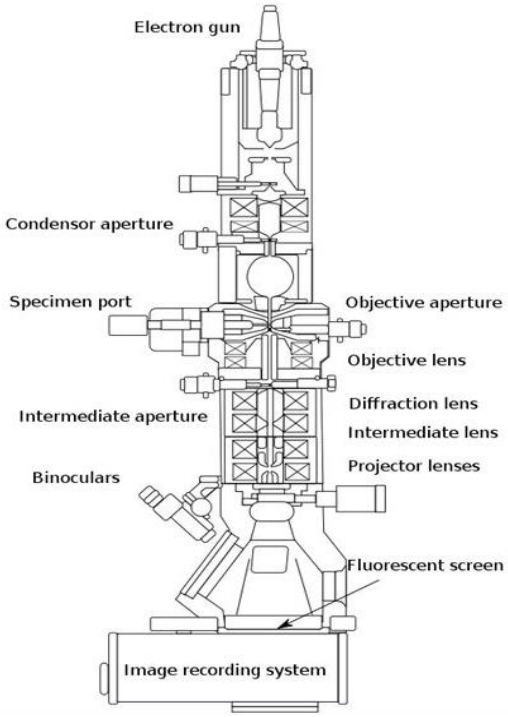

Figure 2.12 Schematic diagram of a transmission electron microscope.

Air needs to be pumped out of the vacuum chamber, creating a space where electrons are able to move. The electrons then pass through multiple electromagnetic lenses. These solenoids are tubes with coil wrapped around them. The beam passes through the solenoids, down the column, makes contact with the screen where the electrons are converted to light and form an image. The image can be manipulated by adjusting the voltage of the gun to accelerate or decrease the speed of electrons as well as changing the electromagnetic wavelength *via* the solenoids. The coils focus images onto a screen or photographic plate.

During transmission, the speed of electrons directly correlates to electron wavelength; the faster electrons move, the shorter wavelength and the greater the quality and detail of the image.

In the image, the lighter areas represent the places where a greater number of electrons were able to pass through the sample and the darker areas reflect the dense areas of the sample. These differences provide information on the structure, texture, shape, and size of the sample.

2.12.1.3 High-resolution transmission electron microscopy (HRTEM)

The most important benefit of HRTEM applied to problems in materials science is its ability to provide real-space images of the local structure of thin samples with an atomic resolution. The widespread availability of field-emission electron sources for transmission electron microscopy/scanning transmission electron microscopy (TEM/STEM) instrumentation has been one of the most important advances in instrumentation. For HRTEM, field-emission sources have provided an increase in image resolution and have promoted the development of computational techniques that further extend image resolution and image interpretability. [32]

The electron column consists of an electron gun and set of 5 or more electromagnetic lenses operating in vacuum. It is convenient to divide the TEM into three components: the illumination system, the objective lens/stage, and the imaging system.

The illumination system comprises the gun and the condenser lenses and its role is to take the electrons from the source and transfer them to the sample. The objective lens and the sample holder/stage system is the heart of the TEM. Here is where all of the beam-sample interactions take place and the two fundamental TEM operations occur, namely, the creation of the various images and diffraction patterns (DP) that are subsequently magnified for viewing and recording. The imaging system uses several lenses to magnify the image or the DP produced by the objective lens and to focus these on the viewing screen or computer display via a detector, or TV camera as shown in Figure 2.13.

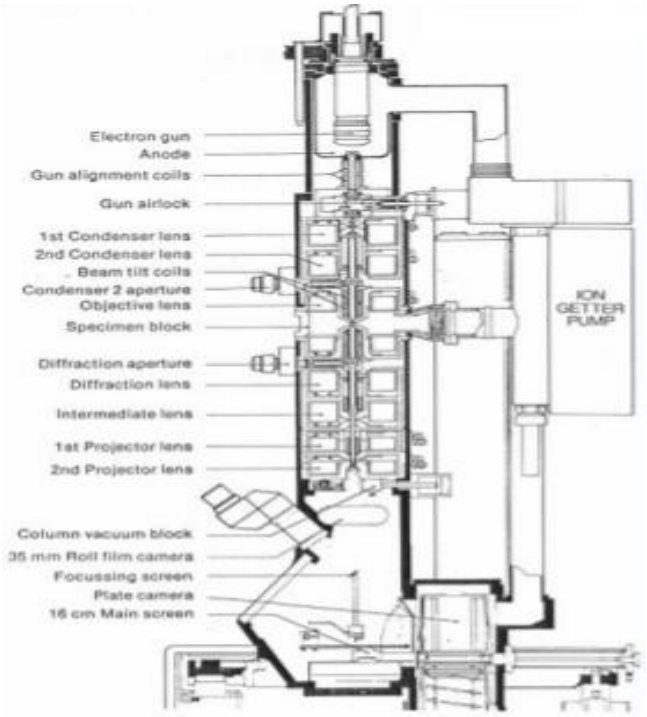

Figure 2.13 Schematic diagram of a high-resolution transmission electron microscope.

The TEM sample is placed in front of the objective lens in the form of a thin foil, thin section, or fine particles transparent for the electron beam. The objective lens forms an image of the electron density distribution at the exit surface of the sample based on the electron optical principles.

A diffraction pattern is formed in the back focal plane of the objective lens and the recombination of the diffracted beams forms an image in the image plane of the objective lens. The diffraction, projection, and intermediate lenses below the objective lens are used to focus and magnify either the diffraction pattern or the image onto a fluorescent screen, which converts the electrons into visible light signal. Because of its high resolution, it is a valuable tool to study nanoscale properties of crystalline material such as semiconductors and metals. TEM imaging can be combined with several material analysis techniques as electron energy loss spectroscopy (EELS), energy filtered TEM (EFTEM), and energy dispersive X-ray (EDX).

HRTEM provides a direct evidence in the local structure and its irregularities at the atomic scale. Furthermore, a structure analysis of crystalline and amorphous materials, characterization of the real structure, especially of structure defects, analysis of internal interface structure, phase analysis, detection of superstructures, detection of order-disorder phenomena, structure investigation of non-stoichiometric compounds, investigation of dynamic processes, imaging of single atoms and atom clusters, detection of point defects, and point defect agglomerates can be performed. [33]

2.12.1.4 Elemental analysis (microanalysis)

Microanalysis is a process where a sample of some material is analyzed for its elemental and sometimes isotopic composition. Elemental analysis can be qualitative and quantitative.

The CHNS elemental analyzer is a proven instrument for the rapid determination of carbon, hydrogen, nitrogen, or sulphur content in organic and other types of materials.

The main components of an elemental analyzer are a furnace (up to 1100 °C), a reactor (combustion chamber, for CHNS determination), a gas chromatographic column, a thermal conductivity detector (TCD), adsorption filters, and an autosampler as shown in Figure 2.14.

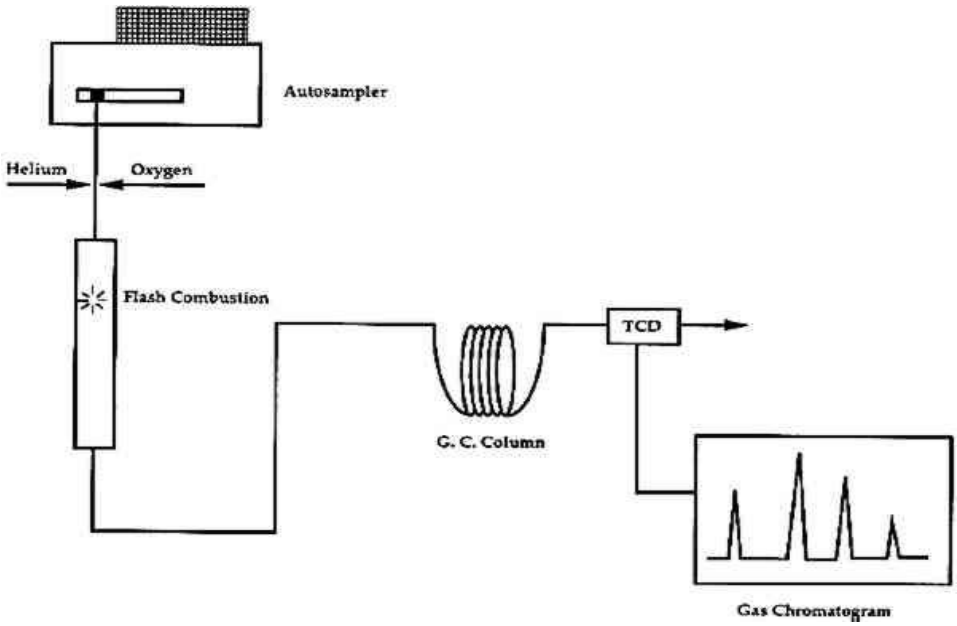

Figure 2.14 Schematic diagram of an elemental analyzer.

The analytical method is based on the complete and instantaneous oxidation of the sample by “flash combustion”, which converts all organic and inorganic substances into combustion products. The resulting combustion gases pass through a reduction furnace and are swept into the chromatographic column by the carrier gas (helium), where they are separated and detected by a thermal conductivity detector (TCD), which gives an output signal proportional to the concentration of the individual components of the mixture.

The organic elemental analysis determines the percentage (%) composition of carbon, hydrogen, nitrogen, and sulphur contained in organic, inorganic, and polymeric materials and in substances of different nature and origin (*e.g.*, solid or liquid samples).

2.12.1.5 Thermogravimetric analysis (TGA)

TGA is a technique in which the mass of a substance is monitored as a function of temperature or time as the sample is subjected to a controlled temperature program in a controlled atmosphere.

The main components of a thermogravimetric analyzer are a furnace, a balance, an autosampler, and a thermocouple as shown in Figure 2.15.

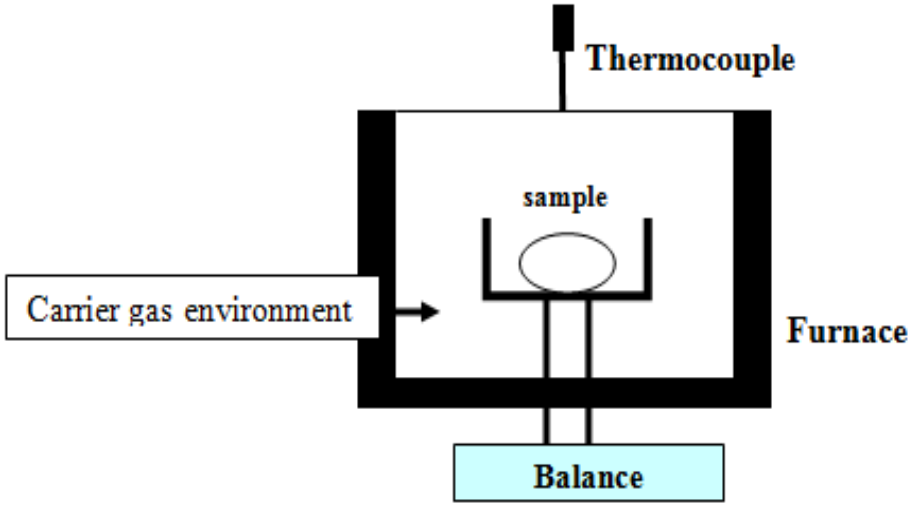

Figure 2.15 Schematic diagram of a thermogravimetric analyzer.

A TGA consists of a sample pan that is supported by a balance. That pan resides in a furnace and is heated or cooled during the experiment. The sample mass is monitored during the experiment. A sample purge gas controls the sample environment. This gas may be inert or reactive, and flows over the sample and exits through an exhaust.

TGA can quantify loss of water, pyrolysis, oxidation, decomposition, amount of metallic catalytic residue remaining on carbon nanotubes, and weight % ash. All these quantifiable applications are usually done upon heating, but there are some experiments where information may be obtained upon cooling.

2.12.1.6 Physisorption (BET surface area)

The BET surface area and the pore size distribution are fundamental parameters for the characterization of solids. Properties such as porosity, strength, hardness, permeability, separation selectivity, corrosion, and thermal stress resistance can be directly correlated to the porous structure of a material. These properties can be easily investigated by the physisorption technique.

The basic components of physical adsorption analyzer are an analysis manifold of accurately known volume and temperature, a vacuum system with valve to manifold, a source of adsorptive gas (typically, N_2) with valve to manifold, a pressure transducer and temperature sensor, a sample tube connected to analysis manifold, and a liquid nitrogen bath as shown in Figure 2.16.

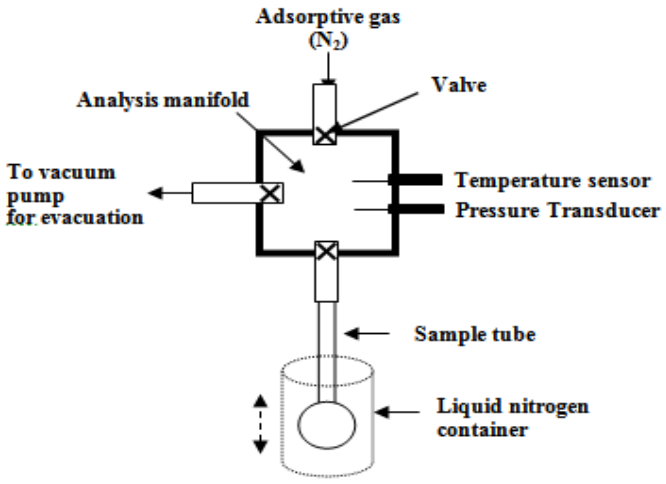

Figure 2.16 Schematic diagram of a physical adsorption analyzer.

Determination of internal surface area is based on adsorption and condensation of N_2 at liquid N_2 temperature, 77K. Initially, the sample is evacuated at 293-523 K (120-250°C) followed by cooling to 77 K by liquid N_2. Then gradually the partial pressure of nitrogen above the sample is increased. Some quantity of gas will be adsorbed by the sample and removed from the gas phase. After stabilization, the equilibrated pressure is recorded and amount of nitrogen adsorbed at each equilibrated pressure is noted. The isotherm, volume adsorbed as function of relative pressure P/P_0, is plotted from the data. The pressure over the sample is gradually increased, until pressure reaches near saturation pressure, by when the complete adsorption isotherm is obtained. The desorption isotherm is measured by a step-wise reduction in pressure until a low pressure over the sample is achieved. Although the volumes are adsorbed at different conditions, the values are reported at STP conditions.

Thus, the BET surface area, pore volume, and pore size distribution of a solid can be known through a physical adsorption analysis.

2.12.1.7 Raman spectroscopy (Raman)

Raman is a spectroscopic technique based on inelastic scattering of monochromatic light, usually from a laser source. Inelastic scattering means that the frequency of photons in monochromatic light changes upon interaction with a sample. Photons of the laser light are absorbed by the sample and then reemitted. Frequency of the reemitted photons is shifted up or down in comparison with original monochromatic frequency, which is called the Raman effect.

A Raman spectrometer typically consists of four main components: an excitation source (laser), a sample illumination system and light collection optics, a wavelength selector (filter or spectrophotometer), and a detector (photodiode array) as shown in Figure 2.17.

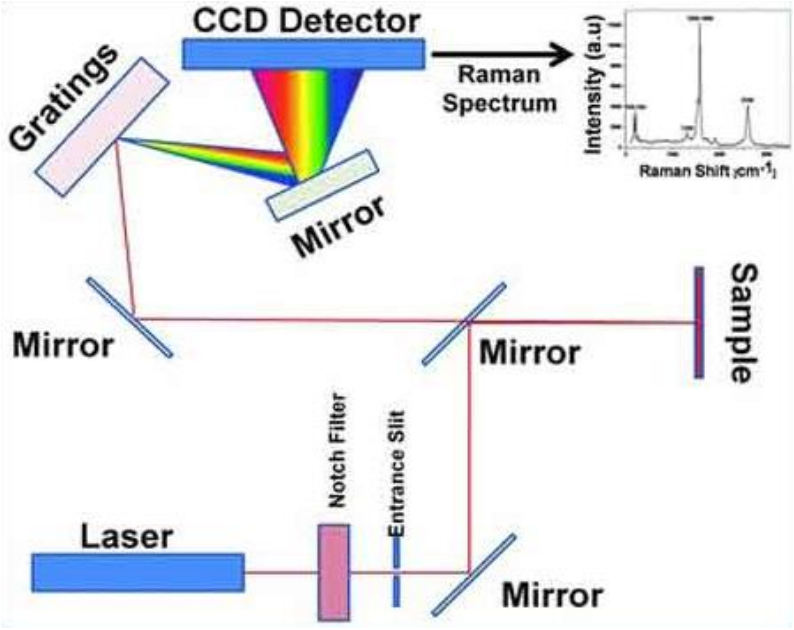

Figure 2.17 Schematic diagram of a Raman spectrometer.

Raman spectroscopy uses a laser light source to irradiate a sample, and generates an infinitesimal amount of Raman scattered light, which is detected as a Raman spectrum using a CCD camera.

The Raman spectroscopy provides information about vibrational, rotational and other low frequency transitions in molecules. It is particularly useful for the characterization of carbon nanomaterials.

2.12.1.8 X-ray diffraction (XRD)

XRD is one of the most potential characterization tools and a non-destructive technique for characterizing both organic and inorganic crystalline materials.

The main components of an X-ray diffractometer are: i) an X-ray tube (source of X-rays), ii) incident-beam optics (condition of the X-ray beam before it hits the sample), iii) a goniometer (platform that holds and moves the sample, and detector), iv) a sample and sample holder, receiving-side optics (condition of the X-ray beam after it has encountered the sample), and v) a detector (count the number of X-rays scattered by the sample) as shown in Figure 2.18.

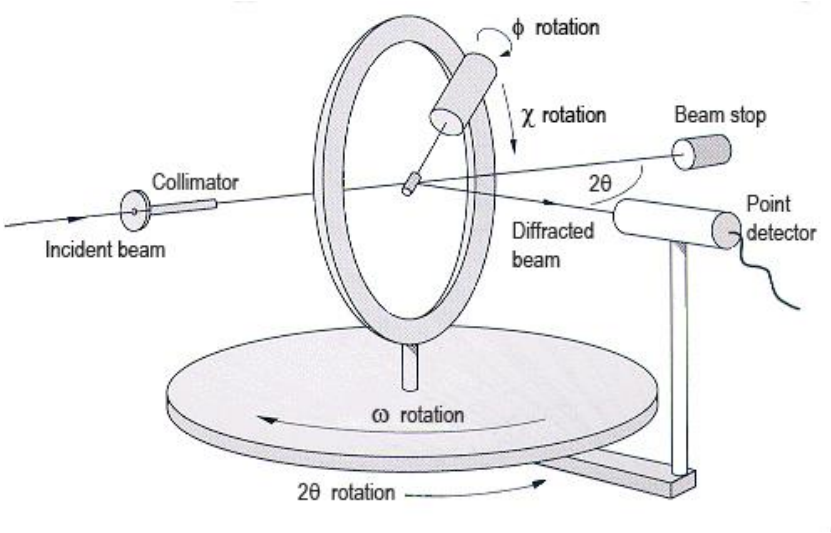

Figure 2.18 Schematic diagram of an X-ray diffractometer.

An X-ray diffractometer produces waves at a known frequency, which is determined by their source. The source is often X-rays, because they are the only kind of energy with the correct frequency for inter-atomic-scale diffraction. However, electrons and neutrons are also common sources, with their frequency determined by their *de Broglie wavelength*. When these waves reach the sample, the atoms of the sample act just like a diffraction grating, producing bright spots at particular angles.

By measuring the angle where these bright spots occur, the spacing of the diffraction grating can be determined by the *Bragg's law*, as illustrated in the following equation:

$$n \lambda = 2 d \sin(\Theta)$$

where,

n = Order of diffraction (whole number)

λ = The wavelength of the rays

d = The spacing between layers of atoms

Θ = The angle between the incident rays and the surface of the crystal

The XRD analysis shows the kinds of materials that compose a solid (qualitative analysis), the quantity of materials that compose the solid (quantitative analysis), the quantity of materials that are crystallized (crystallinity), the amount of stress present in the solid (residual stress), the size of crystallites that compose the solid (crystallite size), and the average orientation of crystallites that compose the solids (texture). The crystallite size can be calculated by applying the Scherrer formula, as illustrated in the following equation:

$$L = \frac{K \lambda}{d \cos(\Theta)}$$

where,

L = Mean crystallite size (nm)

K = Scherrer constant

λ = Wavelength (Å) in the case of Cu Kα1

d = Full width at half maximum (rad)

Θ = Theta angle (°)

2.12.1.9 Infrared spectroscopy (IR)

IR is a technique based on the vibrations of the atoms of a molecule. An infrared spectrum is commonly obtained by passing infrared radiation through a sample and determining what fraction of the incident radiation is absorbed at a particular energy. The energy at which any peak in an absorption spectrum appears corresponding to the frequency of a vibration from a sample molecule.

An infrared spectrometer consists of three basic components: a radiation source, a monochromator, and a detector as shown in Figure 2.19.

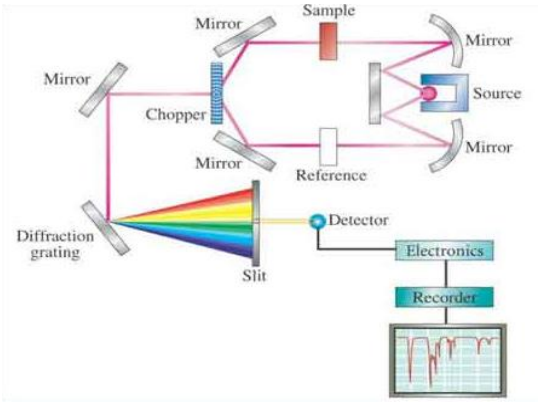

Figure 2.19 Schematic diagram of the infrared spectrometer.

The infrared radiation from the source by reflecting to a flat mirror passes through the sample and reference monochromator then through the sample. The beams are reflected on a rotating mirror, which alternates passing the sample and reference beams to the dispersing element and finally to detector to give the spectrum.

An infrared analysis allows the identification of all types of organic and many types of inorganic compounds, determination of functional groups in organic materials, determination of the molecular composition of surfaces, identification of chromatographic effluents, quantitative determination of compounds in mixtures, determination of molecular conformation, and determination of molecular orientation. [34]

2.12.1.10 X-ray photoelectron spectroscopy (XPS)

XPS is a powerful research tool for surface chemical analysis. It is a versatile technique to study physical and chemical phenomena occurring at surfaces of materials ranging from metals, oxides, semiconductors, glasses, ceramics, polymers, composites and biomaterials. [35]

The main components of an X-ray photoelectron spectrometer are an electron energy analyzer, an X-ray source, a sample, an electron gun, and a detector as shown in Figure 2.20.

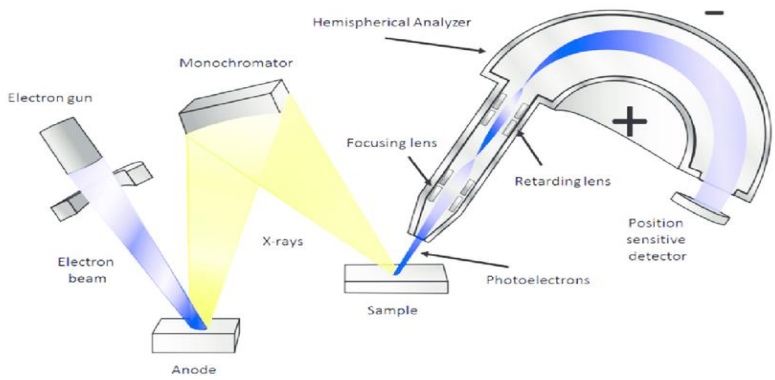

Figure 2.20 Schematic diagram of an XPS system.

XPS spectra are obtained by irradiating a material with a beam of X-rays while simultaneously measuring the kinetic energy and number of electrons that escape from the top 0 to 10 nm of the material being analyzed.

XPS is used to determine: i) the elements present and the quantity of these elements within the top 1-12 nm of the sample surface, ii) any contamination on the surface or in the bulk of the sample, iii) the empirical formula of a material that is free of excessive surface contamination, and iv) the chemical state identification of one or more of the elements in the sample. XPS also gives information on local bonding of atoms, the binding energy of one or more electronic states, the thickness of one or more thin layers (1–8 nm) of different materials within the top 12 nm of the surface, and the density of electronic states.

2.12.1.11 Inductively coupled plasma-atomic emission spectroscopy (ICP-AES)

AES is one of the oldest spectroscopy techniques. In atomic emission spectroscopy, the atomic spectra emitted by a sample are used for the determination of its qualitative or quantitative elemental composition.

In principle, atomic emission spectroscopy can be used for the multi-element analysis of materials in gaseous, liquid, powdered, or solid physical form. Because of its high detection power and the increasing variety of excitation sources available, atomic emission spectroscopy is the most universally used method for multi-element analysis. Atomic emission spectroscopy could involve the dissolution of 1 g of a powdered sample, nebulization into an inductively coupled plasma (ICP), dispersion by a spectrometer with a grating of 1-metre focal length, photo-electric detection, and data processing by a computer to provide quantitative results. [36]

The main components of an ICP-AES equipment are an oscillator, a coupling unit, an induction coil, a plasma torch, an outer gas, an intermediate plasma gas, and an injection gas as shown in Figure 2.21.

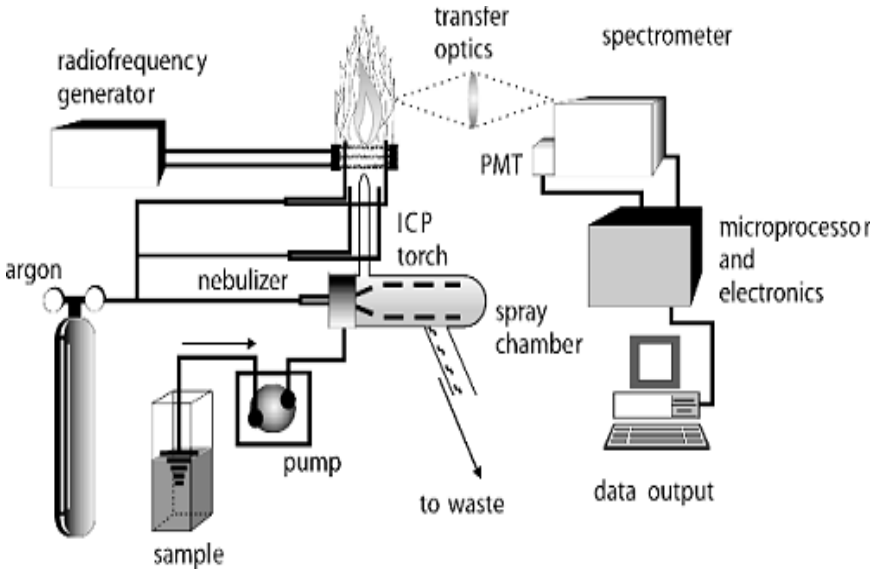

Figure 2.21 Schematic diagram of an ICP-AES equipment.

Atomic emission spectroscopy is based on the principle that excited atoms and ions emit radiation of a characteristic wavelength when electrons return to lower-energy orbitals. Excitation causes one or more electrons to be raised to higher energy levels, and the atom is then in an excited state. When the source of energy is removed, the atom returns to its lowest possible energy state. [37]

An ICP-AES analysis determines the metals present in the sample and the weight percentage (wt%) of each one. Thus, this technique has a detection capability of <1 ppb.

2.13 Summary

As that mentioned in section 2.2, we will use the catalytic-chemical vapor deposition (C-CVD) technique to synthesize our carbon nanomaterials, which will be employed as catalyst supports. Furthermore, the palladium metal will be used as active phase to prepare all catalysts by the wetness impregnation method. Thus, we expect to obtain highly active and selective palladium catalysts for aerobic ethanol oxidation to acetic acid. Besides, the best catalyst will be selected to evaluate its catalytic stability through recycling tests.

2.14 References

[1] M. Wilson, Nanotechnology: Basic Science and Emerging Technologies (**2002**).
[2] R. T. Baker, Carbon 27 (**1989**) 315.
[3] Y. B. Chen, J. Zhang, Carbon 49 (**2011**) 3316-3324.
[4] G. Emig, Chemie in unserer Zeit 21 (**1987**) 128.
[5] M. Kotter, L. Riekert, Chem. Eng. Fundam. 2, 1 (**1982**) 19.
[6] M. Kotter, Chem. Ing. Tech. 55 (**1983**) 179.
[7] Kirk-Othmer, Encyclopedia of Chemical Technology, Homogeneous Catalysis, J. Wiley, New York, 5 (**1992**) 324.

[8] J. A. Godfrey, R. A. Searles, Chemie-Technik, 10, 12 (**1981**) 1271.

[9] J. Hagen, Chemische Reaktionstechnik-Eine Einführung mit Übungen, VCH, Weinheim (**1992**).

[10] W. D. Mroβ, Umschau 7 (**1985**) 423.

[11] A. Benyounes, M. Kacimi, M. Ziyad, P. Serp, Chinese Journal of Catalysis 35 (**2014**) 970-978.

[12] G. Ertl, H. Knözinger, J. Weitkamp, Eds., Handbook of Heterogeneous Catalysis, VCH, Weinheim (**1997**).

[13] K. Meyer, P. Lorenz, B. Böhl-Kuhn, P. Klobes, Porous solids and their characterization. Methods of investigation and application, Cryst. Res. Technol. 29 (**1994**) 903.

[14] G. Rothenberg, Catalysis: Concepts and Green Applications, Wiley-VCH, Weinheim, Chapter 4 (**2008**) ISBN: 978-3-527-31824-7.

[15] IUPAC Commission on Colloid and Surface Chemistry Including Catalysis, Pure Appl. Chem. 57 (**1985**) 603.

[16] F. Rouquerol, J. Rouquerol, K. Sing, Adsorption by Powders and Porous Solids, Academic Press, London (**1999**).

[17] G. C. Bond, Homogeneous Catalysis-Principles and Applications, Oxford Science Publ., Clarendon Press, Oxford. (Short introduction to heterogeneous catalysis) (**1987**).

[18] J. Hagen, Chemische Reaktionstechnik-Eine Einführung mit Übungen, VCH, Weinheim (**1992**).

[19] P. Nordlander, S. Holloway, J. K. Nørskov, Surface Science, 136 (**1984**) 59-81.

[20] A. J. Medford, A. Vojvodic, J. S. Hummelshøj, J. Voss, F. Abild-Pedersen, F. Studt, T. Bligaard, A. Nilsson, J. K. Nørskov , Journal of Catalysis, 328 (2015) 36-42.

[21] E. G. Schlosser, Heterogene Katalyse, Verlag Chemie, Weinheim (**1972**).

[22] G. Ertl, Angew. Chem. 102 (**1990**) 1258.

[23] R. A. van Santen, Surf. Sci. 251/252 (**1991**) 6.

[24] B. Delmon, G. Froment, Catalyst Deactivation. Elsevier, Amsterdam (**1980**).

[25] W. Hölderich, M. Schwarzmann, W. D. Mroβ, Erzmetall 39, 6 (**1986**) 293.

[26] J. T. Richardson, Principles of Catalyst Development, Plenum Press, New York-London (**1989**).

[27] J. Goldstein, D. E. Newbury, D. C. Joy, C. E. Lyman, P. Echlin, E. Lifshin, L. Sawyer, and J. R. Michael, Scanning Electron Microscopy and X-Ray Microanalysis, Kluwer Academic/Plenum Publishers, New York (**2003**) ISBN: 978-0-306-47292-3.

[28] L. Reimer, Scanning Electron Microscopy: Physics of Image Formation and Microanalysis, Springer-Verlag, New York (**1998**) ISBN: 3-540-63976-4.

[29] O.-W. Achaw, Scanning Electron Microscopy, Chapter 24: A Study of the Porosity of Activated Carbons Using the Scanning Electron Microscope, Ghana (**2012**) ISBN: 978-953-51-0092-8.

[30] H. Ma, K.-J. Shieh, T. X. Qiao, Nature and Science 4(3) (**2006**) 14-22.

[31] D. B. Williams and C. B. Carter, Transmission Electron Microscopy, Plenum (**1996**) ISBN: 978-0-387-76500-6.

[32] D. W. Tuggle, L. W. Swanson, J. Vac. Sci. Technol. B 3 (**1985**) 220.

[33] W. Neumann, R. Hillebrand, P. Werner, Electron Microscopy in Solid State Physics, Elsevier, Amsterdam (**1987**) 97-142.

[34] C.-P. Sherman Hsu. Handbook of Instrumental Techniques for Analytical Chemistry, Chapter 15: Infrared Spectroscopy (**1997**) ISBN-13: 9780131773387.

[35] A.W. Wren, F.R. Laffir, N.P. Mellot, M.R. Towler, X-Ray Photoelectron Spectroscopy, Chapter 1: X-ray Photoelectron Spectroscopy: Studies from Industrial and Bioactive Glass to Biomaterials, New York (**2011**) ISBN: 978-1-61728-240-9.

[36] G. L. Moore, Introduction to Inductively Coupled Plasma Atomic Emission Spectrometry, Chapter 1: Principles and history of atomic emission spectroscopy (**1989**) ISBN: 978-0-444-43029-8.

[37] G. L. Moore, Introduction to Inductively Coupled Plasma Atomic Emission Spectrometry, Chapter 6: Inductively Coupled Plasma Atomic Emission Spectrometry (**1989**) ISBN: 978-0-444-43029-8.

CHAPTER III

Methodology

3.1 Introduction

As mentioned in the literature, the catalytic-chemical vapor deposition (C-CVD) technique is the method of choice in heterogeneous catalysis for preparing carbon supports such as few layer graphene (FLG), multi-walled carbon nanotubes (CNT), carbon nanofibers (CNF), and fibrous carbon (FC). [1, 2] This process involved the thermal decomposition of hydrocarbon vapor in the presence of a metal catalyst. [3] In this work, all carbon supports were synthesized by C-CVD into a fluidized bed reactor using ethylene (C_2H_4) as a carbon source, acetonitrile (C_2H_3N) as a carbon and nitrogen source, or thiophene (C_4H_4S) as a carbon and sulphur source. The carbon supports were prepared using various metal oxide catalysts such as $AlCoFeO_4$ for CNT, $NiFe_2O_4$ and $CoFe_2O_4$ for FLG and CNF, and $Cu_{0.1}Ni_{0.9}Co_2O_4$ for FC. These metal oxide catalysts were prepared in our laboratory using the same method for all them. For a long time, the production of carbon supports synthesized by C-CVD has employed supported catalysts, [4] but now we propose the use of unsupported catalysts as those mentioned above. The use of unsupported catalysts as starting materials to synthesize carbon materials is a new way in catalysis to produce these carbon materials. These unsupported catalysts allow preparing carbon nanomaterials with high yield and well-shaped carbon structures, thus becoming promising starting materials in heterogeneous catalysis. These well-shaped carbon structures such as FLG, CNT, CNF, and FC synthesized by C-CVD using unsupported catalysts have allowed exploring new preparation ways of metal catalysts supported on these carbon structures to be compared to metal catalysts supported on metal oxides commercially used in the industry.

To clearly understand the structural order of this Chapter III: Methodology, the main issues are summarized in Table 3.1.

Table 3.1 Main issues of Chapter III.

Issues
3.2 Catalytic-chemical vapor deposition (C-CVD) technique
3.3 Reactants
3.4 Unsupported catalysts used as starting materials to prepare carbon supports
3.5 Supported catalyst used as starting material to prepare carbon supports
3.6 Preparation of carbon supports
3.7 Activation of carbon support surface by chemical methods
3.8 Commercial silica-alumina and alumina used as catalyst supports
3.9 Preparation of palladium catalysts
3.10 Summary
3.11 References

3.2 Catalytic-chemical vapor deposition (C-CVD) technique

3.2.1 Small scale reactor

The experiments were carried out in a vertical fluidized bed reactor equipped with a temperature controller, flow controllers, and doping system as shown in Figure 3.1.

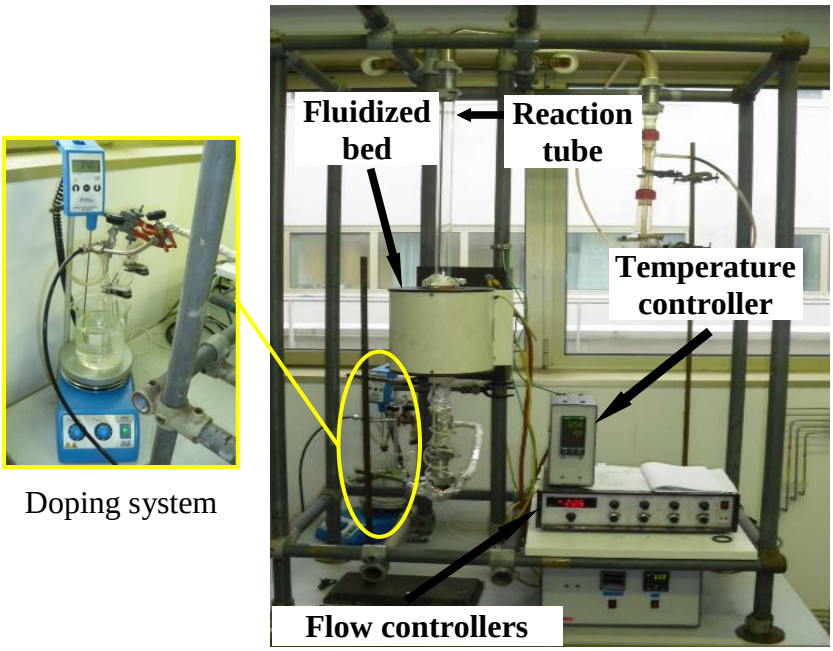

Figure 3.1 Fluidized bed reactor

The synthesis of carbon nanomaterials from thermal decomposition of a hydrocarbon vapor in presence of a metal catalyst was carried out in a quartz tube (2.5 cm internal diameter and 100 cm height), which has a quartz fritted glass (2.5 cm diameter and 0.4 cm height) at half height maximum as shown in Figure 3.2.

Figure 3.2 Quartz tubes with quartz fritted glasses.

3.2.2 Large scale reactor

The experiments were also carried out in a larger vertical fluidized bed reactor equipped with a temperature controller and flow controllers as shown in Figure 3.3.

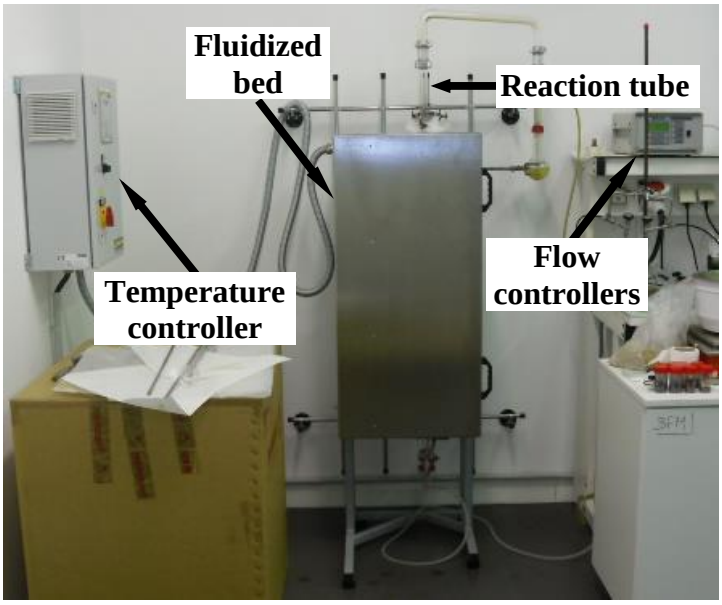

Figure 3.3 Fluidized bed reactor

In that case, the synthesis was also carried out in a quartz tube, which has a quartz fritted glass at half height maximum as shown in Figure 3.4.

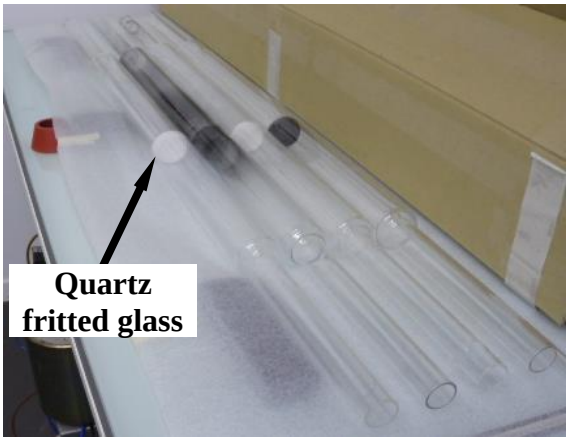

Figure 3.4 Quartz tubes with quartz fritted glasses

3.3 Reactants

Many reactants were purchased from Sigma-Aldrich such as aluminum nitrate nonahydrate (>98%, AlN_3O_9 $9H_2O$), cobalt (II) nitrate hexahydrate (99%, CoN_2O_6 $6H_2O$), iron (III) nitrate nonahydrate (>98%, FeN_3O_9 $9H_2O$), nickel (II) nitrate hexahydrate (>99%, NiN_2O_6 $6H_2O$), copper (II) nitrate trihydrate (>99%, CuN_2O_6 $3H_2O$), citric acid (99%, $C_6H_8O_7$), bis(cyclopentadienyl)nickel(II) ($C_{10}H_{10}Ni$), alumina (>99%, Al_2O_3), silica-alumina catalyst support (grade 135, SiO_2-Al_2O_3), acetonitrile (>99%, C_2H_3N), thiophene (>99%, C_4H_4S), ammonium hydroxide solution (~25% NH_3 basis, H_5NO), acetone (>99.5%, C_3H_6O), and palladium (II) nitrate dihydrate (~40% Pd basis, PdN_2O_6 $2H_2O$). Nitrogen (99.999%, N_2), hydrogen (99.999% H_2), and ethylene (99.999%, C_2H_4) were purchased from Air Liquide.

3.4 Unsupported catalysts used as starting materials to prepare carbon supports

3.4.1 Catalyst preparation method

As already mentioned above, all unsupported catalysts were prepared using the same method. To prepare 1 g of metal oxide catalyst, the desired amount of metal precursors and 3 g of citric acid were placed in 30 mL of water. Then, the solution was stirred for 10 min and a concentrated ammonium hydroxide solution (NH_4OH) was slowly adding until a 6.5 pH value was reached. The slightly acidic solution was newly stirred for 30 additional min. Then, the solution was placed into an oven at 100 °C overnight. The resulting solid was then placed into an oven at 200 °C for 2 h under air. The new resulting solid was crushed until a fine powder was obtained. This resulting fine powder was placed into an oven at 400 °C for 5 h under air.

3.4.1.1 $AlCoFeO_4$ catalyst

The $AlCoFeO_4$ catalyst is a metal oxide catalyst, which has often been used to prepare carbon materials due to its high performance. It produces multi-walled carbon nanotubes. The presence of aluminum, cobalt and iron metals as active phases in its chemical structure allow the formation of multi-walled carbon nanotubes.

3.4.1.2 $NiFe_2O_4$ catalyst

The $NiFe_2O_4$ catalyst is a metal oxide catalyst, which has often been used to prepare carbon materials due to its high performance. It produces few layer graphene and carbon nanofibers. The presence of nickel and iron metals as active phases in its chemical structure allow the formation of few layer graphene and carbon nanofibers.

3.4.1.3 $CoFe_2O_4$ catalyst

The $CoFe_2O_4$ catalyst is a metal oxide catalyst, which has often been used to prepare carbon materials due to its high performance. It produces few layer graphene and carbon nanofibers. The presence of cobalt and iron metals as active phases in its chemical structure allow the formation of few layer graphene and carbon nanofibers.

3.4.1.4 $Cu_{0.1}Ni_{0.9}Co_2O_4$ catalyst

The $Cu_{0.1}Ni_{0.9}Co_2O_4$ catalyst is a metal oxide catalyst, which has often been used to prepare carbon materials due to its high performance. It produces fibrous carbon. The presence of copper, nickel, and cobalt metals as active phases in its chemical structure allow the formation of fibrous carbon.

3.5 Supported catalyst used as starting material to prepare carbon supports

3.5.1 Catalyst preparation method

A wetness impregnation method was used to prepare a nickel catalyst supported on alumina. The desired amount of bis(cyclopentadienyl)nickel(II) ($C_{10}H_{10}Ni$) was added to a diethyl ether solution (500 mL) containing 10 g of alumina (Al_2O_3), so as to introduce 10 wt% of the metal phase. The obtained solution was magnetically stirred at room temperature for 3 h. The resulting solution was then placed in a rotating evaporator to remove the solvent from solution. The resulting solid was then dried under vacuum for 15 h. Finally, the catalyst was reduced in a horizontal tube oven under a nitrogen (300 mL min^{-1} N_2) and hydrogen (300 mL min^{-1} H_2) flow at 450 °C for 2 h.

3.5.1.1 10%Ni/Al_2O_3 catalyst

The 10%Ni/Al_2O_3 catalyst was also used as a starting material to prepare carbon nanomaterials due to its high performance. It produces carbon nanofibers with small diameters. These carbon nanofibers present different characteristics compared to the carbon nanofibers produced with the $NiFe_2O_4$ and $CoFe_2O_4$ catalysts. The presence of nickel metal as active phase in its chemical structure allow the formation of small carbon nanofibers.

3.6 Preparation of carbon supports

3.6.1 Preparation and purification method

3.6.1.1 Few layer graphene (FLG)

FLG was prepared using the $CoFe_2O_4$ catalyst. The synthesis of FLG was carried out in 2 steps.

In the first step, 0.25 g of $CoFe_2O_4$ catalyst were reduced in the fluidized bed under a nitrogen (225 mL min^{-1} N_2) and hydrogen (150 mL min^{-1} H_2) flow at 650 °C. In the second step, the ethylene flow was adjusted at 225 mL min^{-1} for 30 min. The formula $\xi = g_{carbon}/g_{catalyst}$ provides the performance obtained after synthesis. Therefore, the performance for raw few layer graphene was $\xi = 5.5$.

In the purification method, the raw FLG was purified by hydrochloric acid (HCl, 37 wt%) treatment at room temperature overnight. [1] The acidic solution was filtered and then washed with distilled water until a 6.5 pH value.

The resulting solid was dried in an oven at 80 °C overnight. The resulting solid (FLG) was manually crushed and recovered to be used as catalyst support.

3.6.1.2 Multi-walled carbon nanotubes (CNT)

CNT were prepared using the $AlCoFeO_4$ catalyst. The synthesis of CNT was carried out in 2 steps.

In the first step, 0.1 g of $AlCoFeO_4$ catalyst were reduced in the fluidized bed under a nitrogen (225 mL min^{-1} N_2) and hydrogen (150 mL min^{-1} H_2) flow at 650 °C. In the second step, the ethylene flow was adjusted at 225 mL min^{-1} for 30 min. [5] Therefore, the performance for raw multi-walled carbon nanotubes was $\xi = 28.5$.

In the purification method, the raw CNT were purified by aqueous solution (50 vol% H_2SO_4) under a reflux system using an oil bath at 140 °C for 3 h. [6] The acidic solution was filtered and then washed with distilled water until a 6.5 pH value was reached. The resulting solid was dried in an oven at 80 °C overnight. The resulting solid was then crushed in a ball milling for 3 min. The resulting powder solid (CNT) was recovered and used as catalyst support.

3.6.1.3 Carbon nanofibers (CNF)

CNF were prepared using the $CoFe_2O_4$ catalyst. The synthesis of CNF was carried out in 2 steps.

In the first step, 0.25 g of $CoFe_2O_4$ catalyst were reduced in the fluidized bed under a nitrogen (225 mL min^{-1} N_2) and hydrogen (150 mL min^{-1} H_2) flow at 450 °C. In the second step, the ethylene flow was adjusted at 225 mL min^{-1} for 30 min. The performance for raw carbon nanofibers was $\xi = 2.95$.

In the purification method, the raw CNF were purified by hydrochloric acid (HCl, 37 wt%) treatment at room temperature overnight. [1] The acidic solution was filtered and then washed with distilled water until a 6.5 pH value was reached. The resulting solid was dried in an oven at 80 °C overnight. The resulting solid (CNF) was manually crushed and recovered to be used as catalyst support.

3.6.1.4 Small carbon nanofibers (sCNF)

sCNF were prepared using the 10%Ni/Al_2O_3 catalyst. The synthesis of sCNF was carried out in 2 steps.

In the first step, 2 g of 10%Ni/Al_2O_3 catalyst were reduced in the fluidized bed under a nitrogen (160 mL min^{-1} N_2) and hydrogen (120 mL min^{-1} H_2) flow at 650 °C. In the second step, the ethylene flow was adjusted at 60 mL min^{-1} for 1 h. The performance for raw small carbon nanofibers was $\xi = 1.8$. The presence of nickel (Ni) metal mainly allowed the formation of well-shaped carbon materials such as small carbon nanofibers.

In the purification method, the raw sCNF were purified by aqueous solution (50 vol% H_2SO_4) under a reflux system using an oil bath at 140 °C for 3 h. The acidic solution was filtered and then washed with distilled water until a 6.5 pH value was reached. The resulting solid was dried in an oven at 80 °C overnight. The resulting solid (sCNF) was manually crushed and recovered to be used as catalyst support.

3.6.1.5 Fibrous carbon (FC)

FC was prepared using the $Cu_{0.1}Ni_{0.9}Co_2O_4$ catalyst. The synthesis of FC was carried out in 2 steps. In the first step, 0.1 g of $Cu_{0.1}Ni_{0.9}Co_2O_4$ catalyst were reduced in the fluidized bed under a nitrogen (18 L h^{-1} N_2) and hydrogen (18 L h^{-1} H_2) flow at 675 °C. In the second step, the nitrogen and hydrogen flow were adjusted at 12 L h^{-1} and 45 L h^{-1}, respectively. Besides, the ethylene flow was also adjusted at 60 L h^{-1} for 20 min. The performance for raw fibrous carbon was $\xi = 100$.

In the purification method, the raw FC was purified by hydrochloric acid (HCl, 37 wt%) treatment at room temperature overnight. The acidic solution was filtered and then washed with distilled water until a 6.5 pH value was reached. The resulting solid was dried in an oven at 80 °C overnight. The resulting solid (FC) was manually crushed and recovered to be used as catalyst support.

3.7 Activation of carbon support surface by chemical methods

As already known, the surface chemistry of a catalyst support can be improved by heteroatom doping, oxidation method and/or thermal treatment. [2, 7] Doping with heteroatoms assures a high loading and dispersion of the active phase.

The incorporation of oxygen-containing functional groups on carbon support surface increases the amount of anchoring sites everywhere. [7] A high temperature treatment removes impurities (*e.g.*, amorphous carbon) and decreases the grade of structural disorder. Therefore, the surface chemistry of carbon supports has been modified by at least a chemical method mentioned above before using them as catalyst supports.

3.7.1 Functionalization (-COOH), High temperature treatment (HT), and High temperature treated functionalization (-COOH HT)

3.7.1.1 Multi-walled carbon nanotubes (CNT, CNT_{-COOH}, CNT_{HT}, and $CNT_{-COOH\ HT}$)

A portion of purified CNT was functionalized by nitric acid (HNO_3, 65 wt%) treatment under a reflux system at 140 °C for 3 h. [7] The acidic solution was filtered and then washed with distilled water until a 6.5 pH value was reached. The resulting solid was dried in an oven at 80 °C overnight. The resulting solid was crushed in a ball milling for 3 min. The resulting powder solid (CNT_{-COOH}) was recovered and used as catalyst support.

Another portion of purified CNT was treated in a horizontal tube oven under a nitrogen flow at 1000 °C for 1 h. The resulting solid (CNT_{HT}) was recovered and used as catalyst support.

A portion of CNT_{-COOH} was then treated in a horizontal tube oven under a nitrogen flow at 1000 °C for 1 h. The resulting solid ($CNT_{-COOH\ HT}$) was recovered and used as catalyst support.

Thus, purified multi-walled carbon nanotubes (CNT), functionalized multi-walled carbon nanotubes (CNT_{-COOH}), high temperature treated multi-walled carbon nanotubes (CNT_{HT}), and high temperature treated functionalized multi-walled carbon nanotubes ($CNT_{-COOH\ HT}$) have been produced to be used as catalyst supports.

3.7.1.2 Few Layer Graphene (FLG, FLG_{-COOH}, FLG_{HT}, and $FLG_{-COOH\ HT}$)

A portion of purified FLG was functionalized by nitric acid (HNO_3, 65 wt%) treatment under a reflux system at 140 °C for 3 h. The acidic solution was filtered and then washed with distilled water until a 6.5 pH value was reached. The resulting solid was dried in an oven at 80 °C overnight. The resulting solid (FLG_{-COOH}) was manually crushed and recovered to be used as catalyst support.

Another portion of purified FLG was treated in a horizontal tube oven under a nitrogen flow at 1000 °C for 1 h. The resulting solid (FLG_{HT}) was recovered and used as catalyst support.

A portion of FLG_{-COOH} was then treated in a horizontal tube oven under a nitrogen flow at 1000 °C for 1 h. The resulting solid ($FLG_{-COOH\ HT}$) was recovered and used as catalyst support.

Thus, purified few layer graphene (FLG), functionalized few layer graphene (FLG_{-COOH}), high temperature treated few layer graphene (FLG_{HT}), and high temperature treated functionalized few layer graphene ($FLG_{-COOH\ HT}$) have been produced to be used as catalyst supports.

3.7.1.3 Carbon nanofibers (CNF, CNF_{-COOH}, CNF_{HT}, and $CNF_{-COOH\ HT}$)

A portion of purified CNF was functionalized by nitric acid (HNO_3, 65 wt%) treatment under a reflux system at 80 °C for 3 h. The acidic solution was filtered and then washed with distilled water until a 6.5 pH value was reached. The resulting solid was dried in an oven at 80 °C overnight. The resulting solid (CNF_{-COOH}) was manually crushed and recovered to be used as catalyst support.

Another portion of purified CNF was treated in a horizontal tube oven under a nitrogen flow at 1000 °C for 1 h. The resulting solid (CNF_{HT}) was recovered and used as catalyst support.

A portion of CNF_{-COOH} was then treated in a horizontal tube oven under a nitrogen flow at 1000 °C for 1 h. The resulting solid ($CNF_{-COOH\ HT}$) was recovered and used as catalyst support.

Thus, purified carbon nanofibers (CNF), functionalized carbon nanofibers (CNF_{-COOH}), high temperature treated carbon nanofibers (CNF_{HT}), and high temperature treated functionalized carbon nanofibers ($CNF_{-COOH\ HT}$) have been produced to be used as catalyst supports.

3.7.1.4 Small carbon nanofibers (sCNF, $sCNF_{-COOH}$, $sCNF_{HT}$, and $sCNF_{-COOH\ HT}$)

A portion of purified sCNF was functionalized by nitric acid (HNO_3, 65 wt%) treatment under a reflux system at 80 °C for 3 h. The acidic solution was filtered and then washed with distilled water until a 6.5 pH value was reached. The resulting solid was dried in an oven at 80 °C overnight. The resulting solid ($sCNF_{-COOH}$) was manually crushed and recovered to be used as catalyst support.

Another portion of purified sCNF was treated in a horizontal tube oven under a nitrogen flow at 1000 °C for 1 h. The resulting solid ($sCNF_{HT}$) was recovered and used as catalyst support.

A portion of $sCNF_{-COOH}$ was then treated in a horizontal tube oven under a nitrogen flow at 1000 °C for 1 h. The resulting solid ($sCNF_{-COOH\ HT}$) was recovered and used as catalyst support.

Thus, purified small carbon nanofibers (sCNF), functionalized small carbon nanofibers ($sCNF_{-COOH}$), high temperature treated small carbon nanofibers ($sCNF_{HT}$), and high temperature treated functionalized small carbon nanofibers ($sCNF_{-COOH\ HT}$) have been produced to be used as catalyst supports.

3.7.1.5 Fibrous carbon (FC, FC_{-COOH}, FC_{HT}, and $FC_{-COOH\ HT}$)

A portion of purified FC was functionalized by nitric acid (HNO_3, 65 wt%) treatment under a reflux system at 140 °C for 3 h. The acidic solution was filtered and then washed with distilled water until a 6.5 pH value was reached. The resulting solid was dried in an oven at 80 °C overnight. The resulting solid (FC_{-COOH}) was manually crushed and recovered to be used as catalyst support.

Another portion of purified FC was treated in a horizontal tube oven under a nitrogen flow at 1000 °C for 1 h. The resulting solid (FC_{HT}) was recovered and used as catalyst support.

A portion of FC_{-COOH} was then treated in a horizontal tube oven under a nitrogen flow at 1000 °C for 1 h. The resulting solid ($FC_{-COOH\ HT}$) was recovered and used as catalyst support.

Thus, purified fibrous carbon (FC), functionalized fibrous carbon (FC_{-COOH}), high temperature treated fibrous carbon (FC_{HT}), and high temperature treated functionalized fibrous carbon ($FC_{-COOH\ HT}$) have been produced to be used as catalyst supports.

3.7.2 Doping of heteroatoms

As already known, doping is a technique currently used to modify the surface chemistry of catalyst supports. The incorporation of heteroatoms (*e.g.*, nitrogen or sulphur) in the carbon structure has allowed higher interaction between support and metal due to an electronic exchange from metal to support. [8] Therefore, the surface chemistry of multi-walled carbon nanotubes has been modified by doping of heteroatoms before using them as catalyst supports.

3.7.2.1 Doped multi-walled carbon nanotubes (X-CNT, where X = N or S)

3.7.2.1.1 Preparation and purification method

3.7.2.1.1.1 Nitrogen doped multi-walled carbon nanotubes (N-CNT)

N-CNT were prepared using the $AlCoFeO_4$ catalyst. The synthesis of N-CNT was carried out in 2 steps.

In the first step, 0.1 g of $AlCoFeO_4$ catalyst were reduced in the fluidized bed reactor under a nitrogen (225 mL min^{-1} N_2) and hydrogen (150 mL min^{-1} H_2) flow at 650 $^{\circ}C$. In the second step, the nitrogen (225 mL min^{-1} N_2) and hydrogen (150 mL min^{-1} H_2) flow was followed by an acetonitrile flow to the catalyst for 30 min. [2] Therefore, the performance for raw nitrogen doped multi-walled carbon nanotubes was $\xi = 7$.

In the purification method, the raw N-CNT were purified by aqueous solution (50 vol% H_2SO_4) under a reflux system at 140 °C for 3 h. The acidic solution was filtered and then washed with distilled water until a 6.5 pH value was reached. The resulting solid was dried in an oven at 80 °C overnight. The resulting solid was then crushed in a ball milling for 3 min. The resulting powder solid was recovered and used as catalyst support.

3.7.2.1.1.2 Sulphur$_1$ doped multi-walled carbon nanotubes (S_1-CNT)

S_1-CNT were prepared using the $AlCoFeO_4$ catalyst. The synthesis of S_1-CNT was carried out in 2 steps.

In the first step, 0.25 g of $AlCoFeO_4$ catalyst were reduced in the fluidized bed reactor under a nitrogen (225 mL min^{-1} N_2) and hydrogen (150 mL min^{-1} H_2) flow at 750 $^{\circ}$C. In the second step, the nitrogen (225 mL min^{-1} N_2) and hydrogen (150 mL min^{-1} H_2) flow was followed by a thiophene flow to the catalyst for 30 min. Therefore, the performance for raw sulphur$_1$ doped multi-walled carbon nanotubes was $\xi = 2.3$.

In the purification method, the raw S_1-CNT were purified by aqueous solution (50 vol% H_2SO_4) under a reflux system at 140 °C for 3 h. The acidic solution was filtered and then washed with distilled water until a 6.5 pH value was reached. The resulting solid was dried in an oven at 80 °C overnight. The resulting solid was then crushed in a ball milling for 3 min. The resulting powder solid was recovered and used as catalyst support.

3.7.2.1.1.3 Sulphur$_2$ doped multi-walled carbon nanotubes (S_2-CNT)

S_2-CNT were prepared using the $AlCoFeO_4$ catalyst. The synthesis of S_2-CNT was carried out in 3 steps.

In the first step, 0.25 g of $AlCoFeO_4$ catalyst were reduced in the fluidized bed reactor under a nitrogen (225 mL min^{-1} N_2) and hydrogen (150 mL min^{-1} H_2) flow at 750 $^{\circ}C$. In the second step, the ethylene flow was adjusted at 225 mL min^{-1} for 3 min. In the third step, the ethylene flow was newly adjusted at 0 mL min^{-1} and the nitrogen (225 mL min^{-1} N_2) and hydrogen (150 mL min^{-1} H_2) flow was followed by a thiophene flow to the remaining catalyst for 27 min. [9] Therefore, the performance for sulphur$_2$ doped multi-walled carbon nanotubes was $\xi = 3.6$.

In the purification method, the raw S_2-CNT were purified by aqueous solution (50 vol% H_2SO_4) under a reflux system at 140 °C for 3 h. The acidic solution was filtered and then washed with distilled water until a 6.5 pH value was reached. The resulting solid was dried in an oven at 80 °C overnight. The resulting solid was then crushed in a ball milling for 3 min. The resulting powder solid was recovered and used as catalyst support.

3.7.2.2 High temperature treated doped multi-walled carbon nanotubes

3.7.2.2.1 Nitrogen doped multi-walled carbon nanotubes (N-CNT and N-CNT$_{HT}$)

A portion of purified N-CNT was treated in a horizontal tube oven under a nitrogen flow at 1000 °C for 1 h. The resulting solid (N-CNT$_{HT}$) was recovered and used as catalyst support.

Thus, purified nitrogen doped multi-walled carbon nanotubes (N-CNT) and high temperature treated nitrogen doped multi-walled carbon nanotubes (N-CNT$_{HT}$) were produced to be used as catalyst supports.

3.7.2.2.2 Sulphur$_1$ doped multi-walled carbon nanotubes (S_1-CNT and S_1-CNT$_{HT}$)

A portion of purified S_1-CNT was treated in a horizontal tube oven under a nitrogen flow at 1000 °C for 1 h. The resulting solid (S_1-CNT$_{HT}$) was recovered and used as catalyst support.

Thus, purified sulphur doped multi-walled carbon nanotubes (S_1-CNT) and high temperature treated sulphur doped multi-walled carbon nanotubes (S_1-CNT$_{HT}$) were produced to be used as catalyst supports.

3.7.2.2.3 Sulphur$_2$ doped multi-walled carbon nanotubes (S_2-CNT and S_2-CNT$_{HT}$)

A portion of purified S_2-CNT was treated in a horizontal tube oven under a nitrogen flow at 1000 °C for 1 h. The resulting solid (S_2-CNT$_{HT}$) was recovered and used as catalyst support.

Thus, purified sulphur doped multi-walled carbon nanotubes (S_2-CNT) and high temperature treated sulphur doped multi-walled carbon nanotubes (S_2-CNT$_{HT}$) were produced to be used as catalyst supports.

3.8 Commercial silica-alumina and alumina used as catalyst supports

As already known, silica, alumina, or mixed are often used as catalyst supports in many catalytic processes due to their unique physicochemical properties. Thus, many supported catalysts involve the use of metal oxides as support.

Thus, silica, alumina or mixed silica-alumina are catalyst supports in heterogeneous catalysis. We used commercial silica-alumina as support in a palladium catalyst to be compared to the palladium catalysts supported on carbon nanomaterials.

3.9 Preparation of palladium catalysts

As mentioned in the literature, the use of palladium-group metal catalysts supported on carbon have shown high activity and selectivity in oxidation and hydrogenation reactions. [10, 11, 12] According to that, we suggest to use palladium (Pd) metal as active phase supported on our carbon nanomaterials.

3.9.1 Wetness impregnation method

A wetness impregnation method was used to prepare the palladium catalysts supported on carbon nanomaterials. The desired amount of palladium (II) nitrate dihydrate [$Pd(NO_3)_2.2H_2O$] was added to an acetone solution (100 mL) containing 1 g of carbon nanomaterial, so as to introduce 2 wt% of the metallic phase. The solution was then sonicated at room temperature for 1 h and magnetically stirred at room temperature overnight. The solution was then filtered and washed with acetone. The resulting solid was then dried in an oven at 120 °C overnight. Finally, the catalyst was reduced in a horizontal tube oven under a nitrogen and hydrogen flow (20 vol% H_2) at 300 °C for 2 h. [9] All palladium catalysts are shown in Figure 3.5.

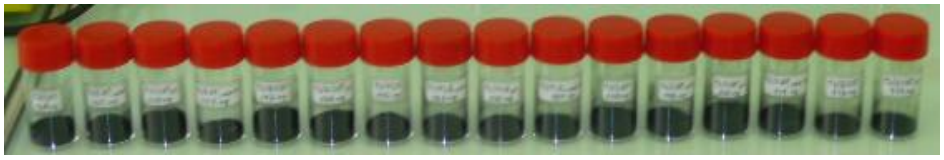

Figure 3.5 Palladium catalysts supported on carbon nanomaterials.

3.10 Summary

A controlled preparation of carbon supports and their surface activation through doping of heteroatoms, functionalization and/or thermal treatment have been performed to produce catalyst supports. In the preparation of palladium catalysts, the preparation method play an important role to assure the immobilization of active phase on the support.

Finally, all characterization analyses of the unsupported catalysts, carbon supports, commercial supports, and palladium catalysts were carried out using the following characterization techniques: TEM micrographs were taken with a JEOL JEM 1011 microscope operating at 100 kV. HRTEM micrographs were obtained using a JEOL JEM-ARM200F Cold FEG microscope operating at 200 kV with a point resolution of > 1.9°A. The elemental analysis results were obtained using a CHNS Perkin-Elmer elemental analyzer. The thermograms were acquired in a temperature range from 30 to 1000 °C at 10 °C min^{-1} under air atmosphere using a TG/DTA Shimadzu. The Brunauer-Emmett-Teller (BET) analyses by N_2 adsorption isotherms at 77 K (QuantaChrome instrument) were performed to give the specific surface area, pore volume, and pore diameter. Raman spectra were measured in a micro Raman spectrometer HR 800 Jobin Yvon Horiba using a laser of 532 nm wavelength as an excitation source. XRPD spectra were measured at room temperature with a Panalytical X'PERT PRO diffractometer, employing Cu Kα radiation (λ = 1.54 Å) and a parabolic MPD-mirror for Cu radiation. The diffractograms were acquired in 2θ range from 5° to 90°, using a continuous scan mode with an acquisition step size of 0.0170° and a counting time of 299.72 s. IR spectra were acquired with a Thermo Scientific Nicolet 6700 FT-IR spectrometer equipped with a DLaTGS (deuterated L-alanine doped triglycine sulfate) detector, using a KBr pellet, a resolution of 4 cm^{-1}, and 16 scans.

XPS spectra were obtained with an XPS K-alpha ThermoScientific apparatus, which operated with a non chromatized Mg K source (1253.6 eV). Palladium particle size distribution was determined using the ImageJ software on at least 250 particles. The palladium percentage results were measured using an iCAP 6300 ICP spectrometer.

3.11 References

[1] R. R. Bacsa, I. Cameán, A. Ramos, A. B. Garcia, V. Tishkova, W. S. Bacsa, J. R. Gallagher, J. T. Miller, H. Navas, V. Jourdain, M. Girleanu, O. Ersen, P. Serp, Carbon 89 (**2015**) 350-360.

[2] A. Benyounes, M. Kacimi, M. Ziyad, P. Serp, Chinese Journal of Catalysis 35 (**2014**).

[3] M. Kumar, Y. Ando, Journal of Nanoscience and Nanotechnology 10 (**2010**) 3739-3758.

[4] R. Philippe, B. Caussat, A. Falqui, Y. Kihn, P. Kalck, S. Bordère, D. Plee, P. Gaillard, D. Bernard, P. Serp, Journal of Catalysis 263 (**2009**) 345-358.

[5] M. Corrias, B. Caussat, A. Ayral, J. Durand, Y. Kihn, P. Kalck, P. Serp, Chem Eng Sci, **2003**, 58(19):4475.

[6] B. F. Machado, A. Marchionni, R. R. Bacsa, M. Bellini, J. Beausoleil, W. Oberhauser, F. Vizza, P. Serp, Journal of Energy Chemistry 22 (**2013**) 296-304.

[7] A. Solhy, B. F. Machado, J. Beausoleil, Y. Kihn, F. Gonçalves, M. F. R. Pereira, J. J. M. Órfão, J. L. Figueiredo, J. L. Faria, P. Serp, Carbon, **2008**, 46(9):1194.

[8] C. R. Raj, A. Samanta, S. H. Noh, S. Mondal, T. Okajima, T. Ohsaka, Emerging new generation electrocatalysts for the oxygen reduction reaction. J. Mater. Chem. A, 4 (**2016**) 11156-11178.

[9] S. Louisia, R. Castro Contreras, M. Heitzmann, M. R. Axet, P.-A. Jacques, P. Serp, Catalysis Communications 109 (**2018**) 65-70.

[10] DEGUSSA AG, Precious Metal Powder Catalysts.

[11] P. N. Rylander, Hydrogenation Methods, Academic Press, London (**1985**) 970-978.

[12] M. Freifelder, Practical Catalytic Hydrogenation, Wiley, New York (**1971**).

CHAPTER IV

Results

4.1 Introduction

In the nanotechnology field, advanced characterization techniques such as SEM, TEM, HRTEM, microanalysis, TGA, BET, Raman, XRPD, IR, XPS, and ICP-AES have become fundamental unit for the technological research and development. Currently, heterogeneous catalysis is mainly focused in the preparation of catalysts with improved characteristics and properties. This is only achieved by using characterization techniques, which provide specific information from the catalyst. Thus, the catalyst behavior can clearly be understood through this specific information. In this Chapter IV, the characterization results of carbon supports and palladium catalysts are presented.

To clearly understand the structural order of this Chapter IV: Results, the main issues are summarized in Table 4.1.

Table 4.1 Main issues of Chapter IV.

Issues
4.2 Characterization results of unsupported catalysts, carbon supports, and commercial supports
4.3 Characterization results of palladium catalysts
4.4 Summary
4.5 References

4.2 Characterization results of unsupported catalysts, carbon supports, and commercial support

4.2.1 Unsupported catalysts characterized by SEM, ICP-AES, and BET

4.2.1.1 Results obtained by SEM

The SEM micrographs of $AlCoFeO_4$, $NiFe_2O_4$, $CoFe_2O_4$, and $Cu_{0.1}Ni_{0.9}Co_2O_4$ catalysts have showed a heterogeneous morphology for all them, forming flakes with different sizes as shown in Figure 4.1.

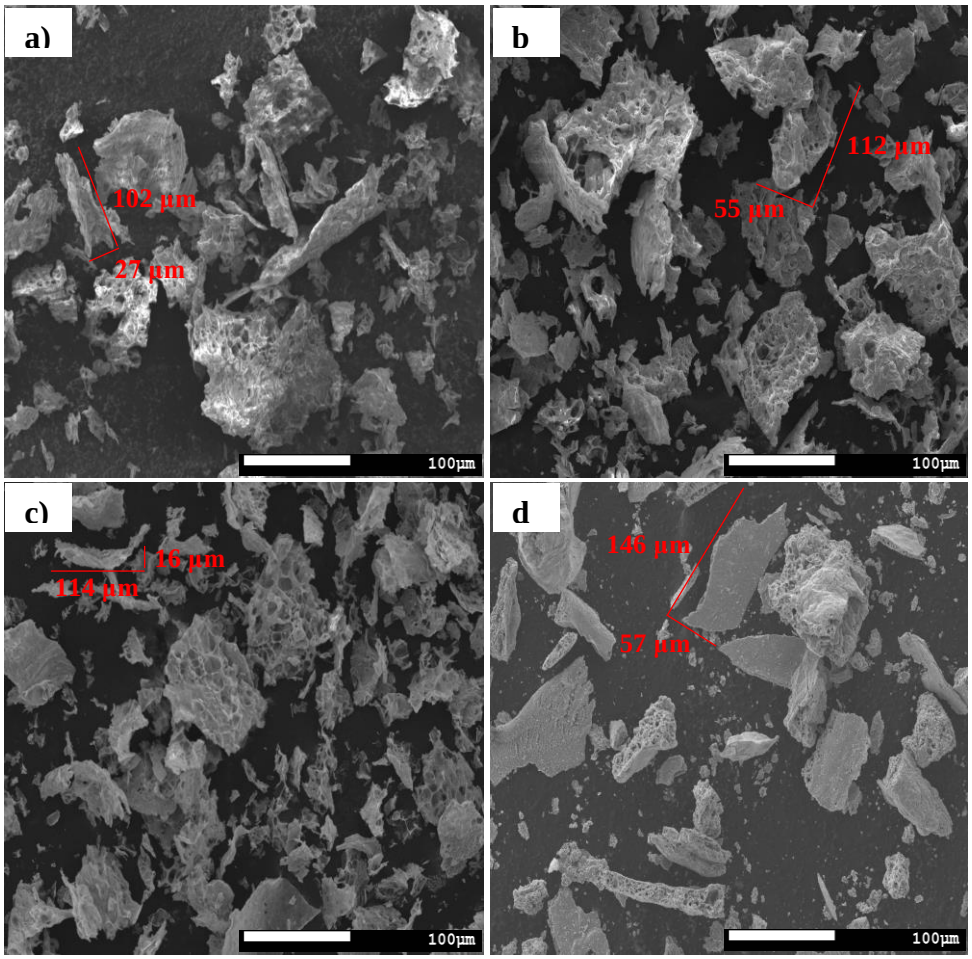

Figure 4.1 SEM micrographs of unsupported catalysts. a) $AlCoFeO_4$, b) $NiFe_2O_4$, c) $CoFe_2O_4$ and d) $Cu_{0.1}Ni_{0.9}Co_2O_4$.

Furthermore, the contrasting analysis performed on a flake in each unsupported catalyst has displayed no difference in chemical composition around surface for all them as shown in Figure 4.2.

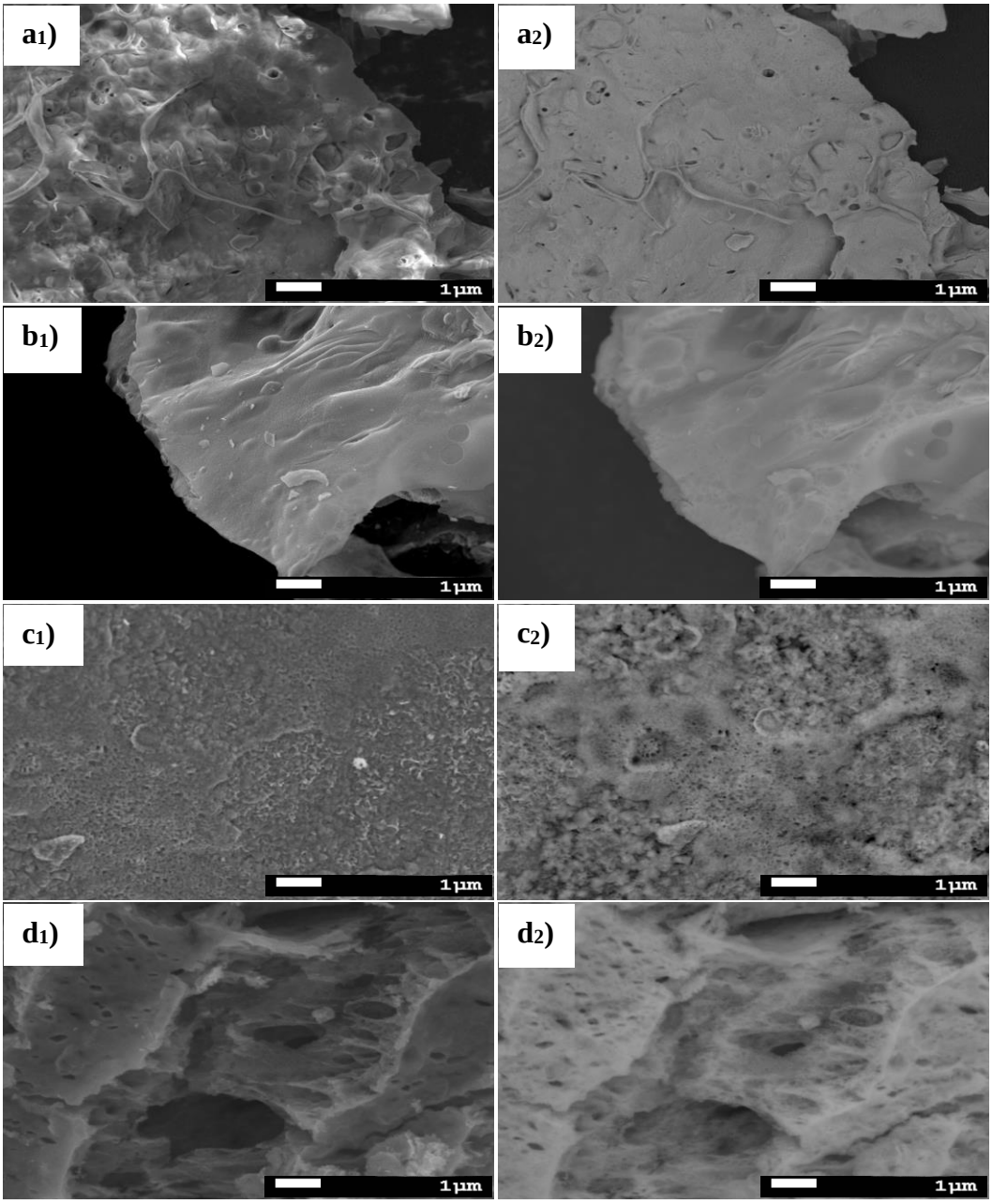

Figure 4.2 Contrasting analyses (a_2, b_2, c_2, and d_2) of unsupported catalysts. a_1-a_2) $AlCoFeO_4$, b_1-b_2) $NiFe_2O_4$, c_1-c_2) $CoFe_2O_4$ and d_1-d_2) $Cu_{0.1}Ni_{0.9}Co_2O_4$.

Finally, the EDX spectra of unsupported catalysts have indeed presented the chemical composition and the mass percentage of each element according to their chemical formulas as shown in Figure 4.3.

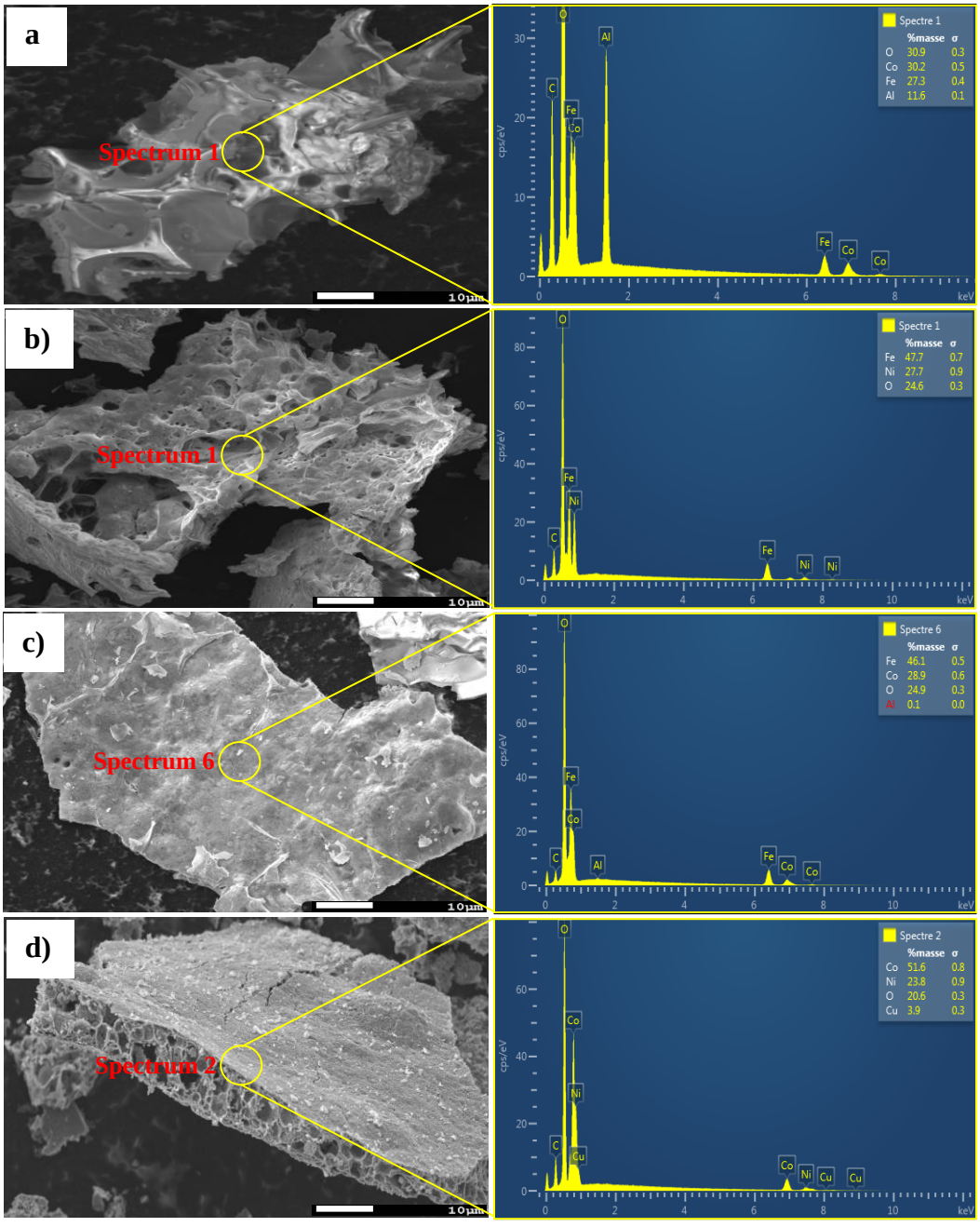

Figure 4.3 EDX spectra of unsupported catalysts. a) $AlCoFeO_4$, b) $NiFe_2O_4$, c) $CoFe_2O_4$ and d) $Cu_{0.1}Ni_{0.9}Co_2O_4$.

4.2.1.2 Results obtained by ICP-AES

The ICP-AES results of unsupported catalysts are summarized in Table 4.2.

Table 4.2 ICP-AES results of unsupported catalysts.

Catalyst	Element	Theoretical %	Experimental %
$AlCoFeO_4$	Al	13.11	11.70
	Co	28.64	27.75
	Fe	27.14	25.70
$NiFe_2O_4$	Ni	25.04	25.42
	Fe	47.65	49.14
$CoFe_2O_4$	Co	25.12	26.36
	Fe	47.60	49.16
$Cu_{0.1}Ni_{0.9}Co_2O_4$	Cu	2.64	2.97
	Ni	21.91	22.50
	Co	48.90	51.56

4.2.1.3 Results obtained by BET

The BET results of unsupported catalysts are summarized in Table 4.3. They exposed medium to low surface areas, small pore volumes, and mesopores in their structures.

Table 4.3 BET results of unsupported catalysts.

Catalyst	BET surface area ($m^2 g^{-1}$)	Pore volume ($cm^3 g^{-1}$)	Pore diameter (nm)
$AlCoFeO_4$	91	0.3	12.9
$NiFe_2O_4$	30	0.1	17.8
$CoFe_2O_4$	19	0.1	26.3
$Cu_{0.1}Ni_{0.9}Co_2O_4$	28	0.2	35.1

4.2.2 FLG, FLG$_{-COOH}$, FLG$_{HT}$, and FLG$_{-COOH\ HT}$ characterized by TEM, HRTEM, microanalysis, TGA, BET, Raman, XRPD, IR, and XPS

4.2.2.1 Results obtained by TEM

The TEM micrographs of few layer graphene have showed the same morphological pattern (stacked graphene layers) no matter their preparation methods as shown in Figure 4.4.

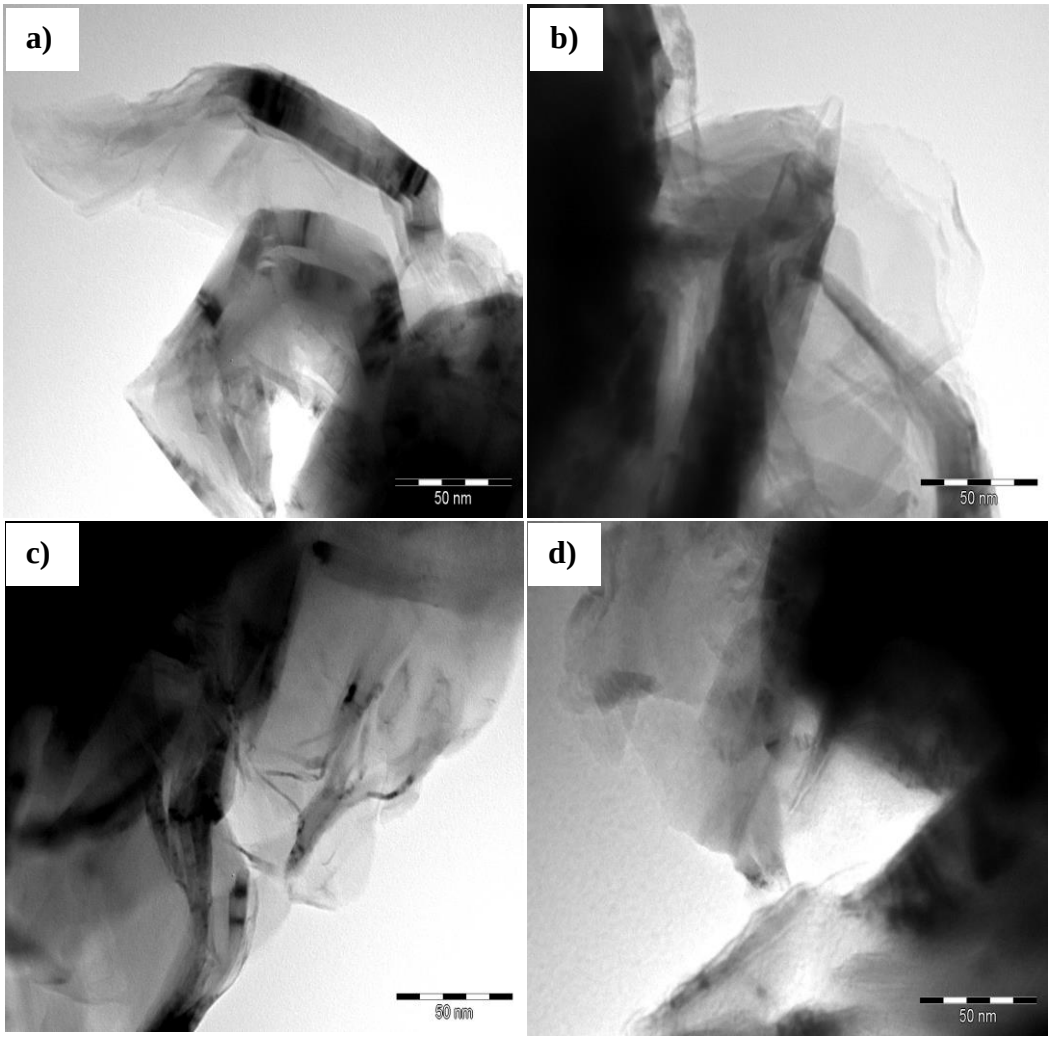

Figure 4.4 TEM micrographs of few layer graphene. a) FLG, b) FLG$_{-COOH}$, c) FLG$_{HT}$, and d) FLG$_{-COOH\ HT}$.

4.2.2.2 Results obtained by HRTEM

The HRTEM micrograph of FLG support has clearly displayed the flat graphene layers as shown in Figure 4.5.

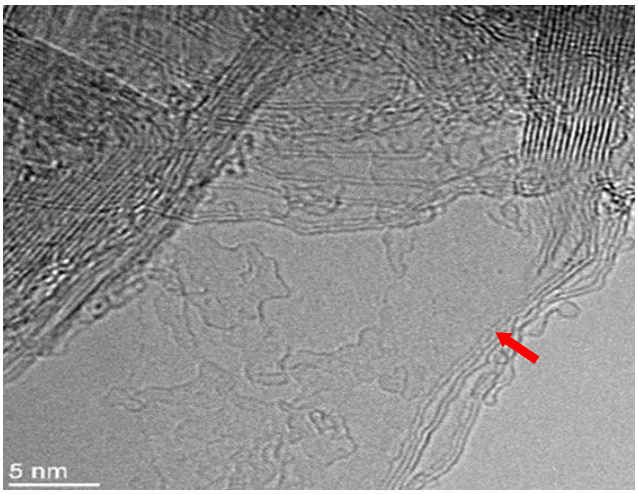

Figure 4.5 HRTEM micrograph of FLG support.

4.2.2.3 Results obtained by microanalysis

The microanalysis results of few layer graphene have presented carbon percentage up to 97 % as summarized in Table 4.4.

Table 4.4 Microanalysis results of few layer graphene.

Support	Elements			
	C%	H%	N%	S%
FLG	98.8	0	0	0
FLG_{-COOH}	97.1	0	0	0
FLG_{HT}	98.6	0	0	0
$FLG_{-COOH\ HT}$	98.7	0	0	0

4.2.2.4 Results obtained by TGA

The TGA results of few layer graphene have revealed a similar tendency in their decomposition temperatures and purities up to 96 % as shown in Figure 4.6.

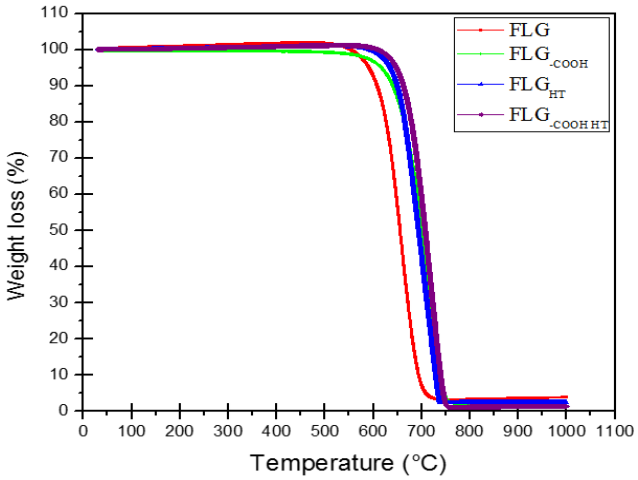

Figure 4.6 TGA analyses of few layer graphene.

4.2.2.5 Results obtained by BET

The BET results of few layer graphene are summarized in Table 4.5. Low surface areas, small pore volumes, and mesopores in their structures have been measured.

Table 4.5 BET results of few layer graphene.

Support	BET surface area ($m^2 g^{-1}$)	Pore volume ($cm^3 g^{-1}$)	Pore diameter (nm)
FLG	36	0.2	24.9
FLG_{-COOH}	50	0.2	16.8
FLG_{HT}	74	0.3	16.2
$FLG_{-COOH\ HT}$	71	0.3	15.3

4.2.2.6 Results obtained by Raman

The Raman spectra of few layer graphene exhibited a structural order acceptable as shown in Figure 4.7.

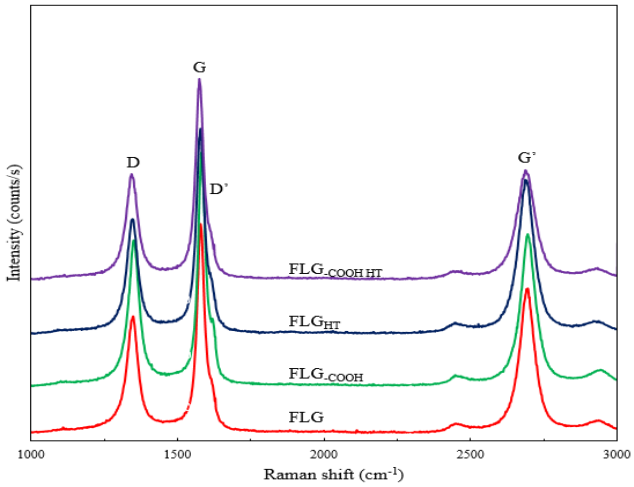

Figure 4.7 Raman spectra of few layer graphene.

4.2.2.7 Results obtained by XRPD

The XRD diffractograms of few layer graphene have indicated a similar crystallinity for carbon no matter their preparation methods as shown in Figure 4.8.

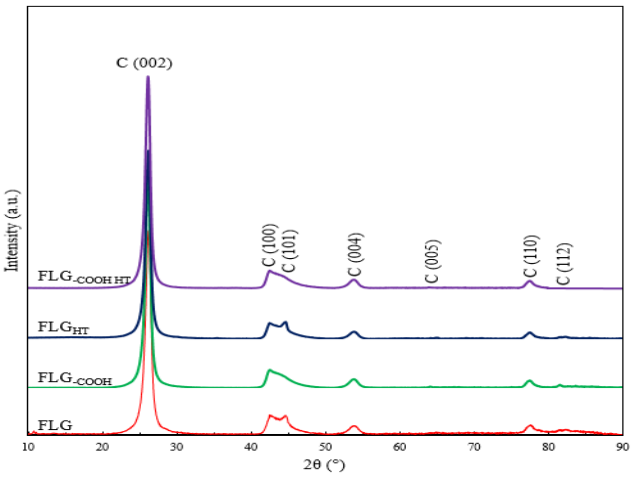

Figure 4.8 XRD diffractograms of few layer graphene.

4.2.2.8 Results obtained by IR

The IR spectra of few layer graphene have shown for those treated supports the carbonyl group from carboxylic acid functional groups as shown in Figure 4.9.

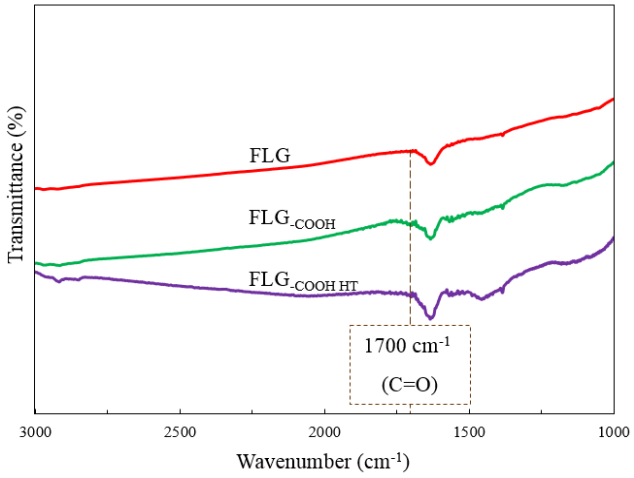

Figure 4.9 IR spectra of few layer graphene.

4.2.2.9 Results obtained by XPS

The XPS spectra of few layer graphene presented a chemical composition equal to 100 % and the sp^3/sp^2 ratio for all them are summarized in Table 4.6.

Table 4.6 Chemical composition and sp^3/sp^2 ratio from XPS spectra for few layer graphene.

Support	Elements				sp^3/sp^2
	C%	O%	N%	S%	ratio
FLG	99.1	0.9	0.0	0.0	0.3
FLG_{-COOH}	96.2	3.8	0.0	0.0	0.3
FLG_{HT}	99.2	0.8	0.0	0.0	0.3
$FLG_{-COOH\ HT}$	99.0	1.0	0.0	0.0	0.3

4.2.3 CNT, CNT$_{-COOH}$, CNT$_{HT}$, and CNT$_{-COOH\ HT}$ characterized by TEM, HRTEM, microanalysis, TGA, BET, Raman, XRPD, IR, and XPS

4.2.3.1 Results obtained by TEM

The TEM micrographs of multi-walled carbon nanotubes have shown morphological damages after nitric acid oxidation as shown in Figure 4.10.

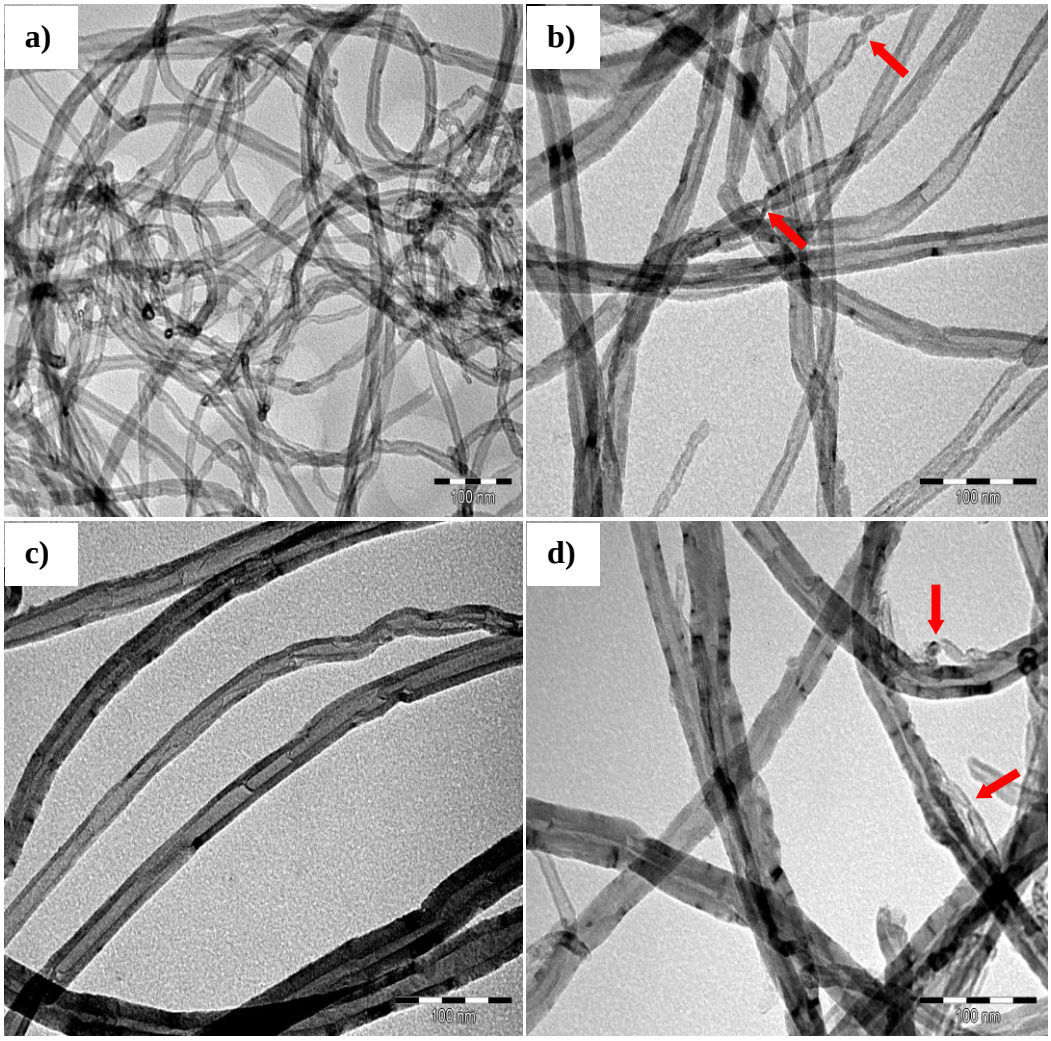

Figure 4.10 TEM micrographs of multi-walled carbon nanotubes. a) CNT, b) CNT$_{-COOH}$, c) CNT$_{HT}$, and d) CNT$_{-COOH\ HT}$.

4.2.3.2 Results obtained by HRTEM

The HRTEM micrograph has clearly displayed the multi-walled carbon tube structures as shown in Figure 4.11.

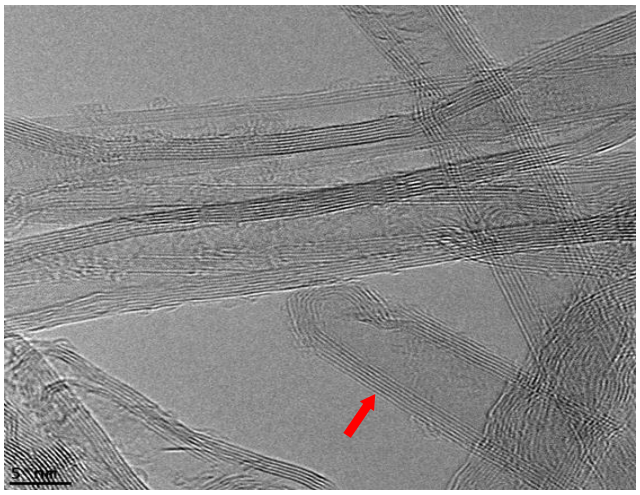

Figure 4.11 HRTEM micrograph of CNT support.

4.2.3.3 Results obtained by microanalysis

The microanalysis results of multi-walled carbon nanotubes presented carbon percentage up to 90 % as summarized in Table 4.7.

Table 4.7 Microanalysis results of multi-walled carbon nanotubes.

Support	Elements			
	C%	H%	N%	S%
CNT	92.3	0	0	0
CNT_{-COOH}	90.4	0	0	0
CNT_{HT}	96.2	0	0	0
$CNT_{-COOH\ HT}$	97.6	0	0	0

4.2.3.4 Results obtained by TGA

The TGA results of multi-walled carbon nanotubes have revealed a similar tendency in their decomposition temperatures and purities up to 93 % as shown in Figure 4.12.

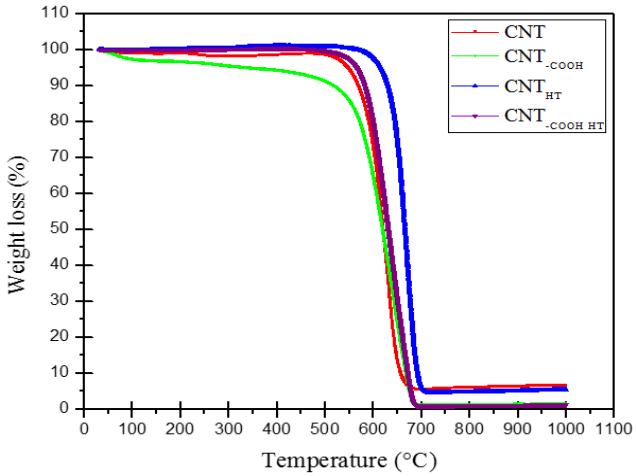

Figure 4.12 TGA analyses of multi-walled carbon nanotubes.

4.2.3.5 Results obtained by BET

The BET results of multi-walled carbon nanotubes show high surface areas, medium pore volumes, and mesopores in their structures as summarized in Table 4.8.

Table 4.8 BET results of multi-walled carbon nanotubes.

Support	BET surface area ($m^2\ g^{-1}$)	Pore volume ($cm^3\ g^{-1}$)	Pore diameter (nm)
CNT	152	2.6	68.6
CNT_{-COOH}	220	1.2	22.2
CNT_{HT}	166	2.7	65.4
$CNT_{-COOH\ HT}$	251	1.4	23.1

4.2.3.6 Results obtained by Raman

The Raman spectra of multi-walled carbon nanotubes exhibited a structural order relatively acceptable as shown in Figure 4.13.

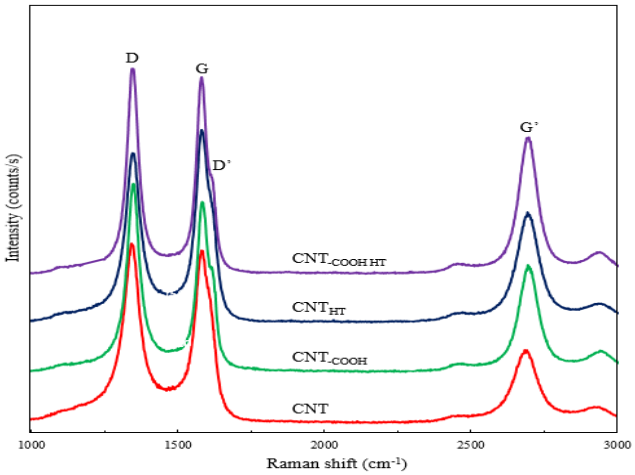

Figure 4.13 Raman spectra of multi-walled carbon nanotubes.

4.2.3.7 Results obtained by XRPD

The XRD diffractograms of multi-walled carbon nanotubes have indicated a define crystallinity no matter their preparation methods as shown in Figure 4.14.

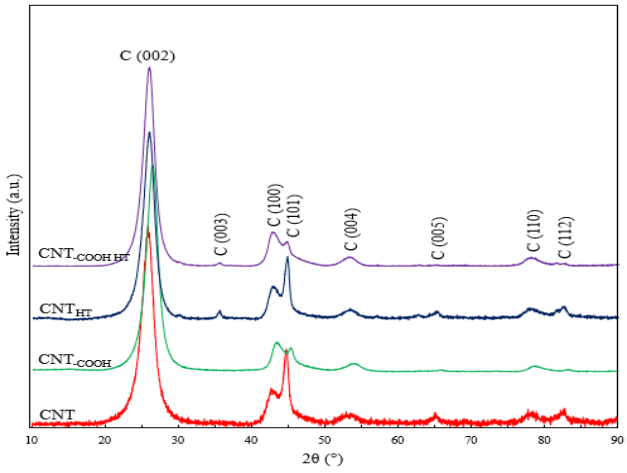

Figure 4.14 XRD diffractograms of multi-walled carbon nanotubes.

4.2.3.8 Results obtained by IR

The IR spectra of multi-walled carbon nanotubes have showed for those treated supports the carbonyl group from carboxylic acid groups as shown in Figure 4.15.

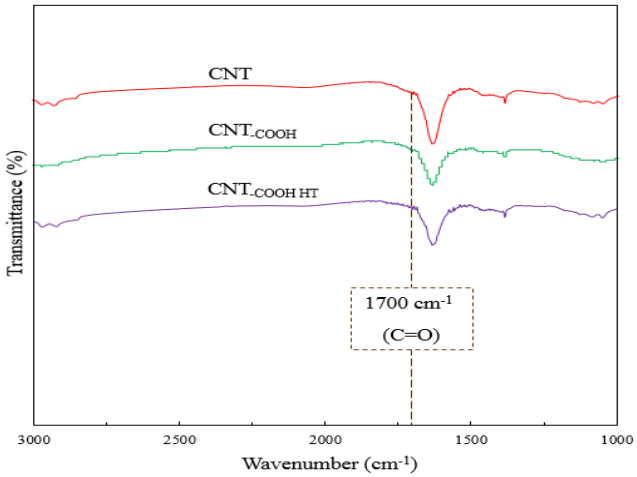

Figure 4.15 IR spectra of multi-walled carbon nanotubes.

4.2.3.9 Results obtained by XPS

The XPS spectra of multi-walled carbon nanotubes have presented the chemical composition equal to 100 % and the sp^3/sp^2 ratio for all them as summarized in Table 4.9.

Table 4.9 Chemical composition and sp^3/sp^2 ratio from XPS spectra for multi-walled carbon nanotubes.

Support	Elements				sp^3/sp^2 ratio
	C%	O%	N%	S%	
CNT	99.2	0.8	0.0	0.0	0.4
CNT_{-COOH}	94.3	5.7	0.0	0.0	0.5
CNT_{HT}	99.8	0.3	0.0	0.0	0.4
$CNT_{-COOH\ HT}$	99.2	0.8	0.0	0.0	0.4

4.2.4 N-CNT and N-CNT$_{HT}$ characterized by TEM, HRTEM, microanalysis, TGA, BET, Raman, XRPD, IR, and XPS

4.2.4.1 Results obtained by TEM

The TEM micrographs of nitrogen doped multi-walled carbon nanotubes have indeed showed unique characteristics due to nitrogen doping as shown in Figure 4.16.

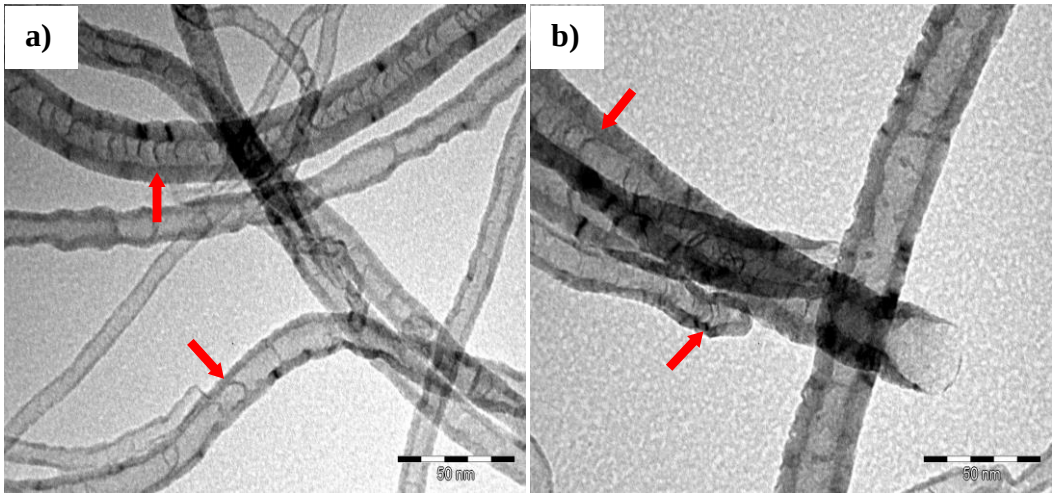

Figure 4.16 TEM micrographs of nitrogen doped multi-walled carbon nanotubes. a) N-CNT and b) N-CNT$_{HT}$.

4.2.4.2 Results obtained by HRTEM

The HRTEM micrograph of N-CNT support has clearly displayed its structural difference compared to pristine CNT support as shown in Figure 4.17.

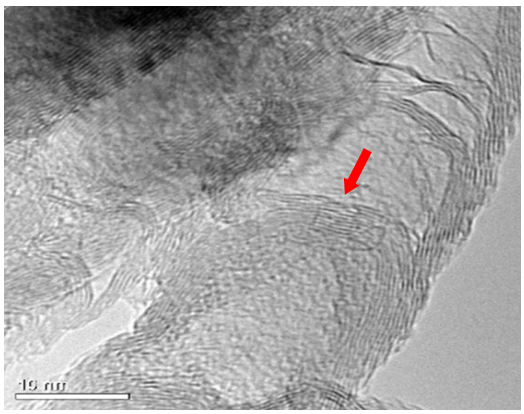

Figure 4.17 HRTEM micrograph of N-CNT support.

4.2.4.3 Results obtained by microanalysis

The microanalysis results of nitrogen doped multi-walled carbon nanotubes have presented carbon and nitrogen percentages up to 92% and 1% respectively as summarized in Table 4.10.

Table 4.10 Microanalysis results of nitrogen doped multi-walled carbon nanotubes.

Support	Elements			
	C%	H%	N%	S%
N-CNT	92.3	0	2.95	0
$N\text{-}CNT_{HT}$	95.6	0	1.65	0

4.2.4.4 Results obtained by TGA

The TGA results of nitrogen doped multi-walled carbon nanotubes have revealed a similar tendency in their decomposition temperatures and purities up to 92 % as shown in Figure 4.18.

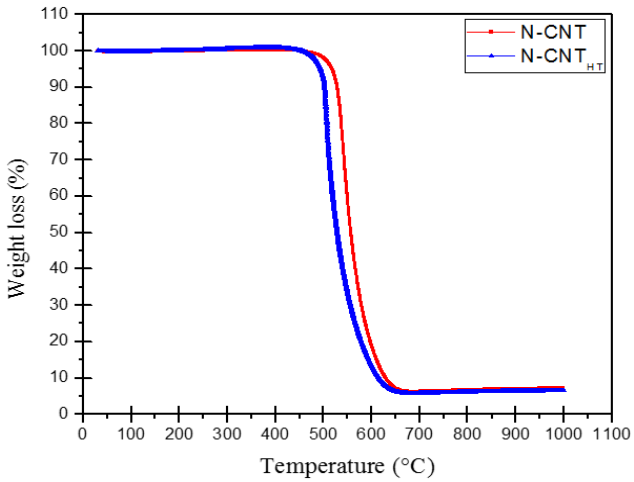

Figure 4.18 TGA analyses of nitrogen doped multi-walled carbon nanotubes.

4.2.4.5 Results obtained by BET

The BET results of nitrogen doped multi-walled carbon nanotubes have exposed high surface areas, large pore volumes, and macropores in their structures as summarized in Table 4.11.

Table 4.11 BET results of nitrogen doped multi-walled carbon nanotube supports.

Support	BET surface area ($m^2\ g^{-1}$)	Pore volume ($cm^3\ g^{-1}$)	Pore diameter (nm)
N-CNT	183	2.7	59.7
$N\text{-}CNT_{HT}$	168	2.5	58.9

4.2.4.6 Results obtained by Raman

The Raman spectra of nitrogen doped multi-walled carbon nanotubes exhibited a structural order almost acceptable as shown in Figure 4.19.

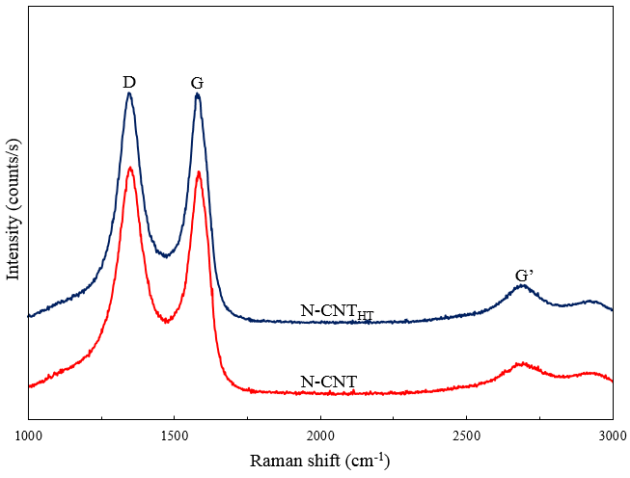

Figure 4.19 Raman spectra of nitrogen doped multi-walled carbon nanotubes.

4.2.4.7 Results obtained by XRPD

The XRD diffractograms of nitrogen doped multi-walled carbon nanotubes have indicated a define crystallinity no matter their preparation methods as shown in Figure 4.20.

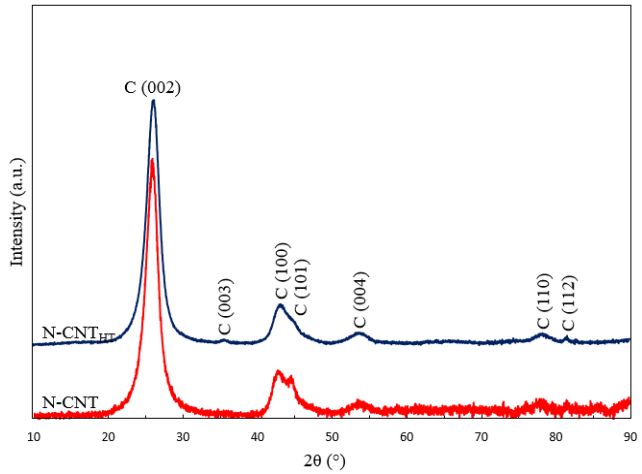

Figure 4.20 XRD diffractograms of nitrogen doped multi-walled carbon nanotubes.

4.2.4.8 Results obtained by IR

The IR spectrum of nitrogen doped multi-walled carbon nanotubes have clearly showed a C-N stretching from amine groups as shown in Figure 4.21.

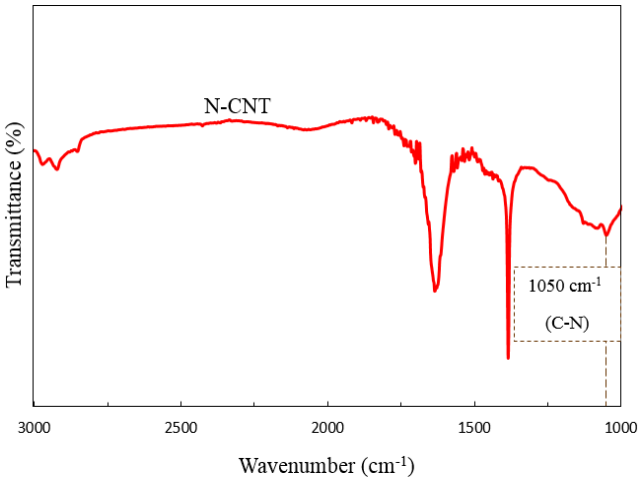

Figure 4.21 IR spectrum of nitrogen doped multi-walled carbon nanotubes.

4.2.4.9 Results obtained by XPS

The XPS spectra of nitrogen doped multi-walled carbon nanotubes have presented two results:

1. The chemical composition equal to 100 % and the sp^3/sp^2 ratio for all them as summarized in Table 4.12.

Table 4.12 Chemical composition and sp^3/sp^2 ratio from XPS spectra for nitrogen doped multi-walled carbon nanotubes.

Support	**Elements**				**sp^3/sp^2 ratio**
	C%	**O%**	**N%**	**S%**	
N-CNT	96.7	1.7	1.7	0.0	0.5
$N\text{-}CNT_{HT}$	97.7	0.8	1.5	0.0	0.5

2. Nitrogen species formed in nitrogen doped multi-walled carbon nanotubes.

At least three types of nitrogen species were found in nitrogen doped multi-walled carbon nanotubes: pyridinic, pyrrolic, N-oxide, and quaternary nitrogen. Nitrogen peak deconvolution indicated the presence of 29% pyridinic nitrogen, 31% of pyrrolic nitrogen, 12% of quaternary nitrogen, and 28% of nitrogen oxides. [1]

4.2.5 S_1-CNT and S_1-CNT_{HT} characterized by TEM, microanalysis, TGA, BET, Raman, XRPD, IR, and XPS

4.2.5.1 Results obtained by TEM

The TEM micrographs of sulphur$_1$ doped multi-walled carbon nanotubes have indeed showed unique characteristics due to sulphur doping as shown in Figure 4.22.

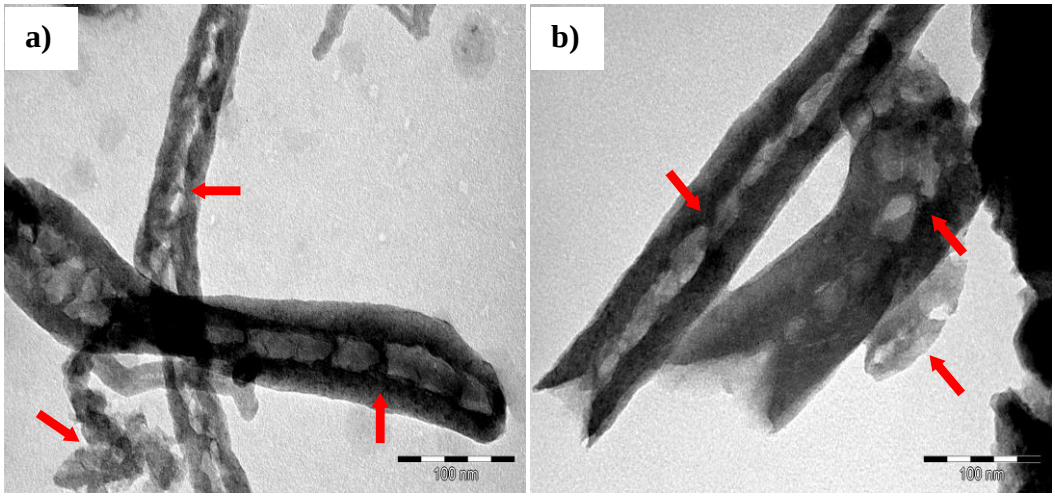

Figure 4.22 TEM micrographs of sulphur$_1$ doped multi-walled carbon nanotubes. a) S_1-CNT and b) S_1-CNT_{HT}.

4.2.5.2 Results obtained by microanalysis

The Microanalysis results of sulphur$_1$ doped multi-walled carbon nanotubes have presented carbon and sulphur percentages up to 64% and 9% respectively as summarized in Table 4.13.

Table 4.13 Microanalysis results of sulphur$_1$ doped multi-walled carbon nanotubes.

Support	Elements			
	C%	H%	N%	S%
S_1-CNT	64.1	0	0	12.3
S_1-CNT_{HT}	67.1	0	0	9.55

4.2.5.3 Results obtained by TGA

The TGA results of sulphur$_1$ doped multi-walled carbon nanotubes have revealed a similar tendency in their decomposition temperatures and purities up to 65 % as shown in Figure 4.23.

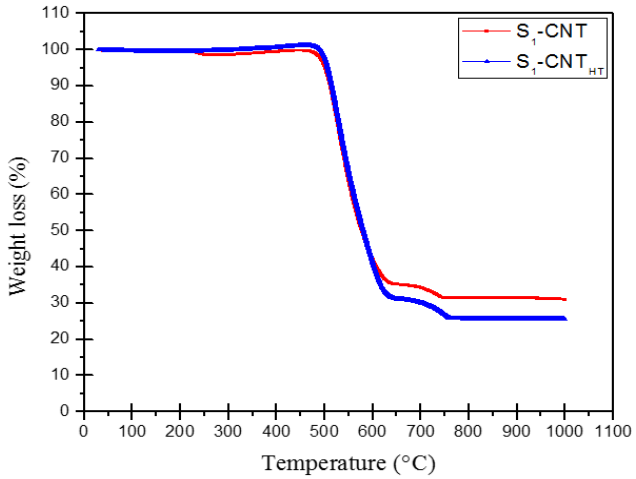

Figure 4.23 TGA analyses of sulphur$_1$ doped multi-walled carbon nanotubes.

4.2.5.4 Results obtained by BET

The BET results of sulphur$_1$ doped multi-walled carbon nanotubes have exposed low surface areas, large pore volumes, and macropores in their structures as summarized in Table 4.14.

Table 4.14 BET results of sulphur$_1$ doped multi-walled carbon nanotubes.

Support	BET surface area ($m^2\ g^{-1}$)	Pore volume ($cm^3\ g^{-1}$)	Pore diameter (nm)
S_1-CNT	48	4.2	349.7
S_1-CNT_{HT}	79	0.4	18.3

4.2.5.5 Results obtained by Raman

The Raman spectra of sulphur$_1$ doped multi-walled carbon nanotubes exhibited a high structural disorder as shown in Figure 4.24.

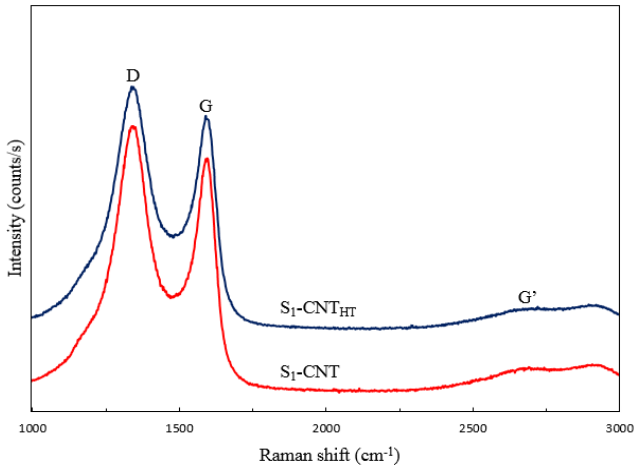

Figure 4.24 Raman spectra of sulphur$_1$ doped multi-walled carbon nanotubes.

4.2.5.6 Results obtained by XRPD

The XRD diffractograms of sulphur$_1$ doped multi-walled carbon nanotubes have indicated presence of metal traces from catalyst as shown in Figure 4.25.

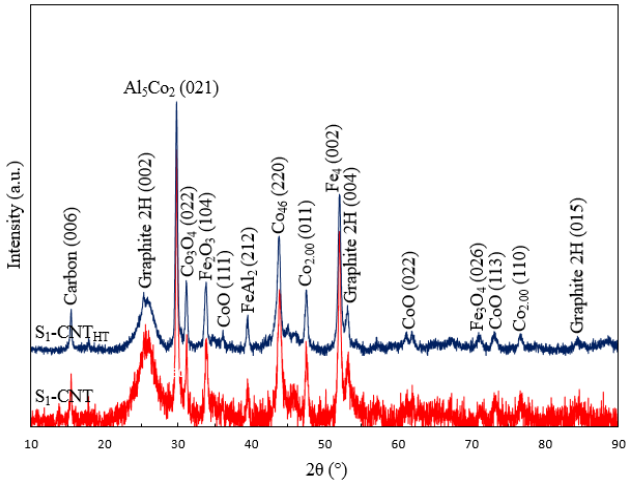

Figure 4.25 XRD diffractograms of sulphur$_1$ doped multi-walled carbon nanotubes.

4.2.5.7 Results obtained by IR

The IR spectrum of sulphur$_1$ doped multi-walled carbon nanotubes have clearly showed a C=S stretching and an S=O stretching from thiocarbonyl and sulfoxide compounds respectively as shown in Figure 4.26.

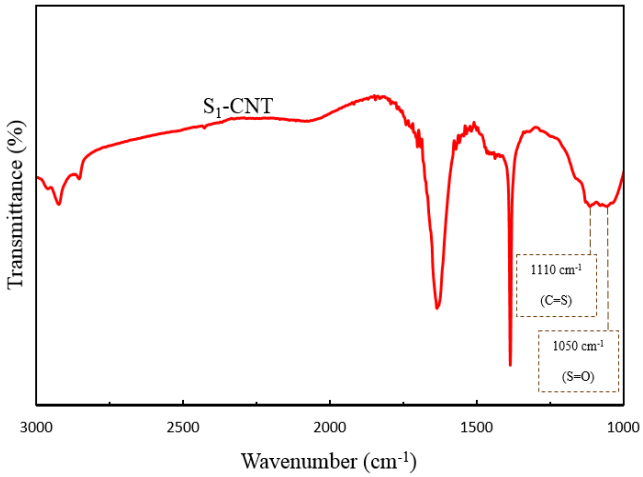

Figure 4.26 IR spectrum of sulphur$_1$ doped multi-walled carbon nanotubes.

4.2.5.8 Results obtained by XPS

The XPS spectra of S_1-CNT supports have presented two results:

1. The chemical composition up to 99% and sp^3/sp^2 ratio as summarized in Table 4.15.

Table 4.15 Chemical composition and sp^3/sp^2 ratio from XPS spectra for S_1-CNT supports.

Support	Elements				sp^3/sp^2 ratio
	C%	O%	N%	S%	
S_1-CNT	91.4	5.2	0.0	2.8	0.5
S_1-CNT$_{HT}$	95.3	3.6	0.0	1.8	0.5

2. Sulphur species formed in S_1-CNT.

Sulphur species were found in sulphur$_1$ doped multi-walled carbon nanotubes: thiol compounds, sulfoxide compounds, thioether functional groups, and sulphur oxides. [2]

4.2.6 S_2-CNT and S_2-CNT_{HT} characterized by TEM, HRTEM, microanalysis, TGA, BET, Raman, XRPD, IR, and XPS

4.2.6.1 Results obtained by TEM

The TEM micrographs of sulphur$_2$ doped multi-walled carbon nanotubes have indeed showed unique characteristics due to sulphur doping as shown in Figure 4.27.

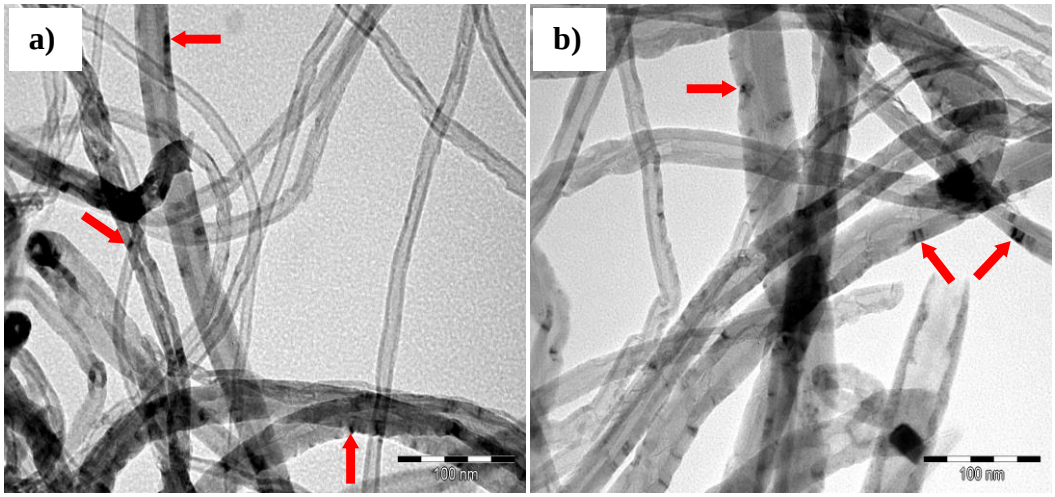

Figure 4.27 TEM micrographs of sulphur$_2$ doped multi-walled carbon nanotubes. a) S_2-CNT and b) S_2-CNT_{HT}.

4.2.6.2 Results obtained by HRTEM

The HRTEM micrograph of S_2-CNT support has clearly displayed its structural difference compared to pristine CNT support as shown in Figure 4.28.

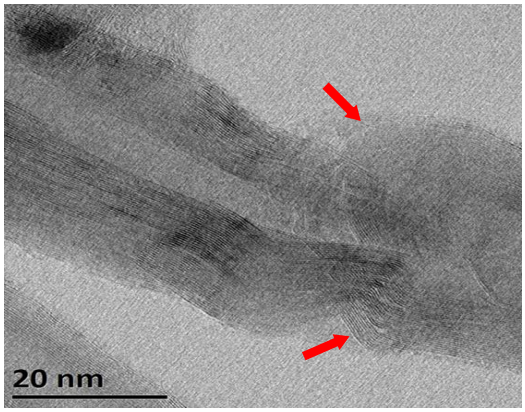

Figure 4.28 HRTEM micrograph of S_2-CNT support.

4.2.6.3 Results obtained by microanalysis

The microanalysis results of sulphur$_2$ doped multi-walled carbon nanotubes have presented carbon and sulphur percentages up to 77% and 4% respectively as summarized in Table 4.16.

Table 4.16 Microanalysis results of sulphur$_2$ doped multi-walled carbon nanotubes.

Support	Elements			
	C%	H%	N%	S%
S_2-CNT	78.6	0	0	5.0
S_2-CNT$_{HT}$	77.4	0	0	4.0

4.2.6.4 Results obtained by TGA

The TGA results of sulphur$_2$ doped multi-walled carbon nanotubes have revealed a similar tendency in their decomposition temperatures and purities up to 81 % as shown in Figure 4.29.

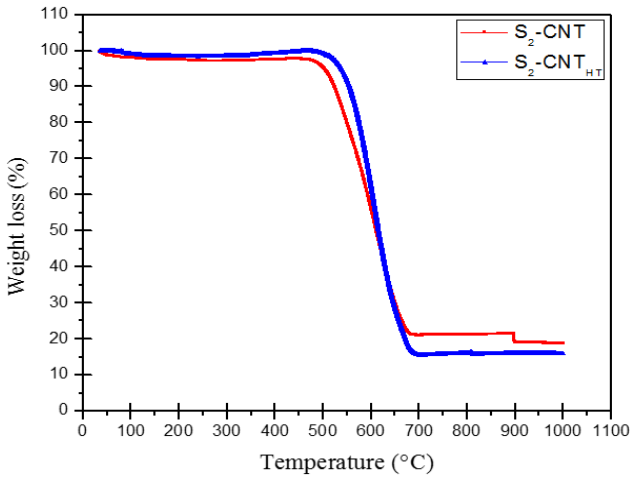

Figure 4.29 TGA analyses of sulphur$_2$ doped multi-walled carbon nanotubes.

4.2.6.5 Results obtained by BET

The BET results of sulphur$_2$ doped multi-walled carbon nanotubes have exposed low surface areas, small pore volumes, and mesopores in their structures as summarized in Table 4.17.

Table 4.17 BET results of sulphur$_2$ doped multi-walled carbon nanotubes.

Support	BET surface area ($m^2\ g^{-1}$)	Pore volume ($cm^3\ g^{-1}$)	Pore diameter (nm)
S_2-CNT	90	1.1	50.1
S_2-CNT$_{HT}$	116	0.6	19.4

4.2.6.6 Results obtained by Raman

The Raman spectra of sulphur$_2$ doped multi-walled carbon nanotubes exhibited a structural order acceptable as shown in Figure 4.30.

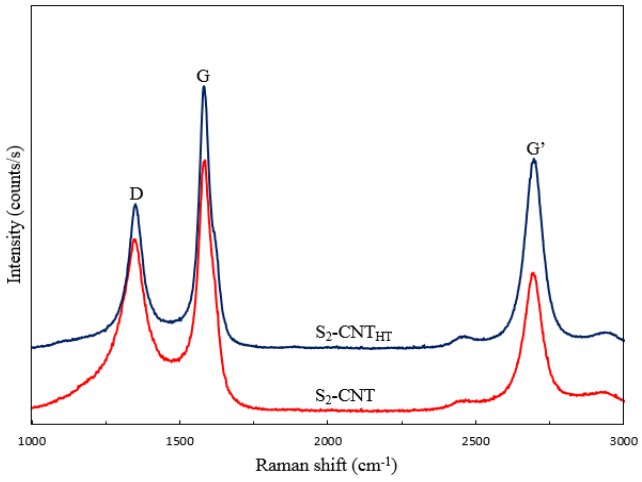

Figure 4.30 Raman spectra of sulphur$_2$ doped multi-walled carbon nanotubes.

4.2.6.7 Results obtained by XRPD

The XRD diffractograms of sulphur$_2$ doped multi-walled carbon nanotubes have indicated presence of metal traces from catalyst as shown in Figure 4.31.

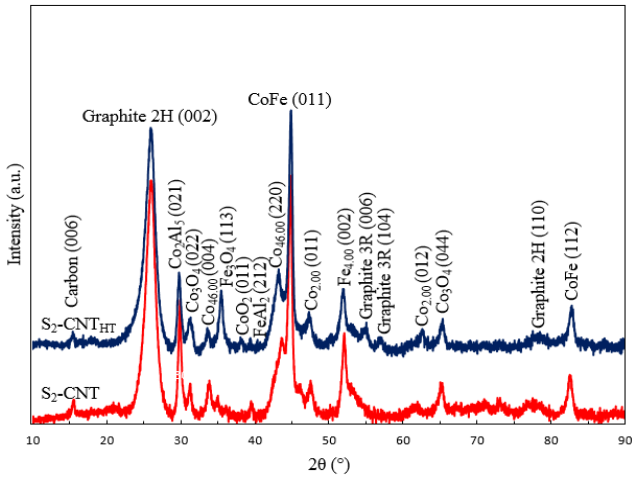

Figure 4.31 XRD diffractograms of sulphur$_2$ doped multi-walled carbon nanotubes.

4.2.6.8 Results obtained by IR

The IR spectrum of sulphur$_2$ doped multi-walled carbon nanotubes have clearly showed a C=S stretching and an S=O stretching from thiocarbonyl and sulfoxide compounds respectively as shown in Figure 4.32.

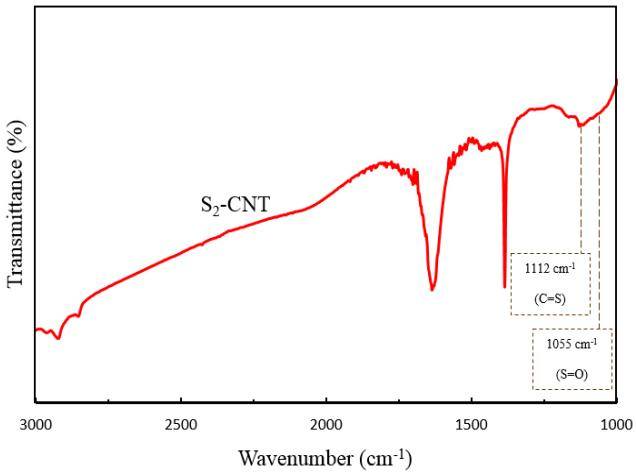

Figure 4.32 IR spectrum of sulphur$_2$ doped multi-walled carbon nanotubes.

4.2.6.9 Results obtained by XPS

The XPS spectra of S_2-CNT supports have presented two results:

1. The chemical composition up to 99 % and the sp^3/sp^2 ratio for all them as summarized in Table 4.18.

Table 4.18 Chemical composition and sp^3/sp^2 ratio from XPS spectra for S_2-CNT supports.

Support	Elements				sp^3/sp^2 ratio
	C%	O%	N%	S%	
S_2-CNT	95.6	2.8	0.0	1.3	0.4
S_2-CNT_{HT}	96.7	1.8	0.0	1.1	0.4

2. Sulphur species formed in S_2-CNT.

Sulphur species were found in $sulphur_2$ doped multi-walled carbon nanotubes: thiol compounds, sulfoxide compounds, thioether functional groups, and sulphur oxides. [2]

4.2.7 CNF, CNF_{-COOH}, CNF_{HT}, and $CNF_{-COOH\ HT}$ characterized by microanalysis, TEM, HRTEM, TGA, BET, Raman, XRPD, IR, and XPS

4.2.7.1 Results obtained by microanalysis

The microanalysis results of carbon nanofibers have presented carbon percentage up to 95 % as summarized in Table 4.19.

Table 4.19 Microanalysis results of carbon nanofibers.

Support	Elements			
	C%	H%	N%	S%
CNF	97.9	0	0	0
CNF_{-COOH}	95.7	0	0	0
CNF_{HT}	97.9	0	0	0
$CNF_{-COOH\ HT}$	98.4	0	0	0

4.2.7.2 Results obtained by TEM

The TEM micrographs of carbon nanofibers have showed no physical attrition due to the methods and/or treatments applied. But only morphological change anywhere as shown in Figure 4.33.

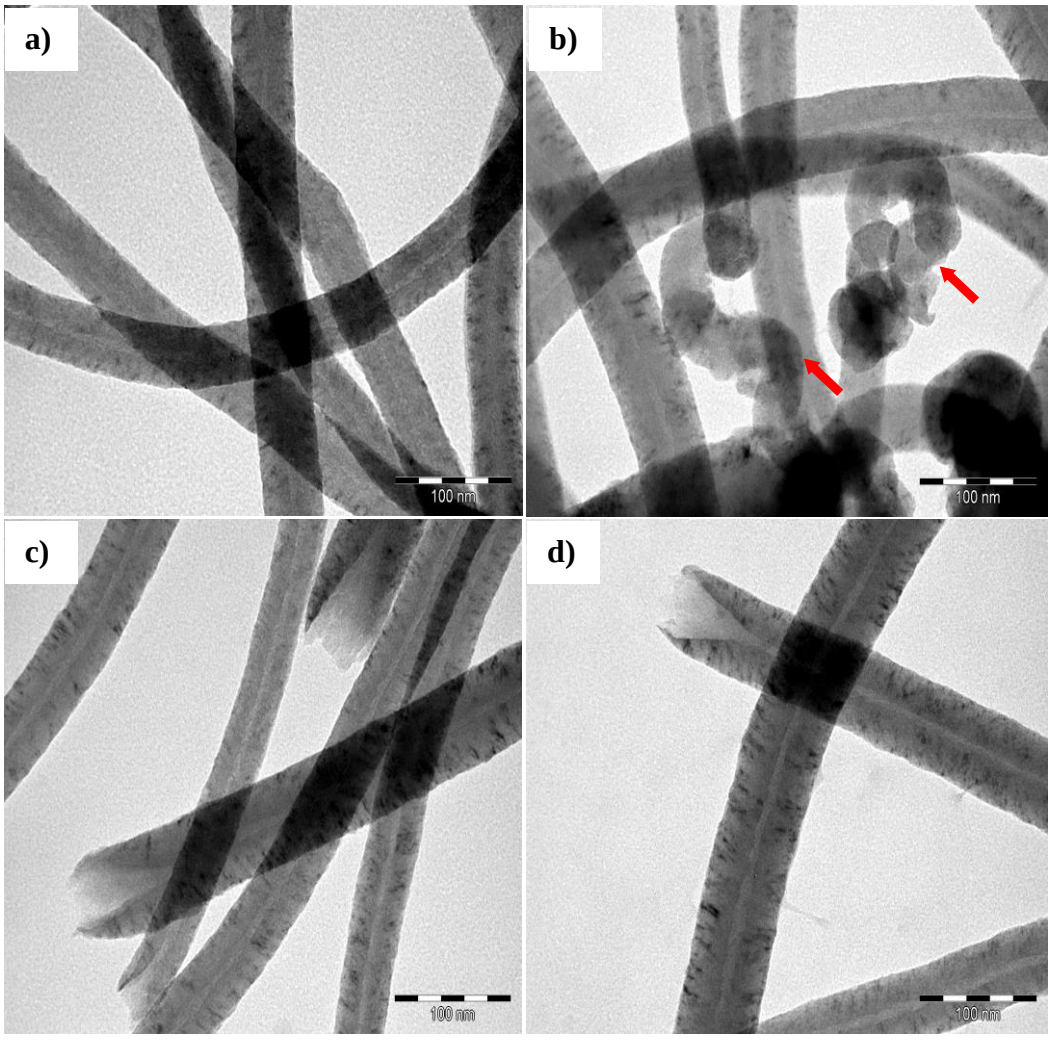

Figure 4.33 TEM micrographs of carbon nanofibers. a) CNF, b) CNF_{-COOH}, c) CNF_{HT}, and d) $CNF_{-COOH\ HT}$.

4.2.7.3 Results obtained by HRTEM

The HRTEM micrograph of CNF support has clearly displayed any morphological irregularities on the edge boundaries as shown in Figure 4.34.

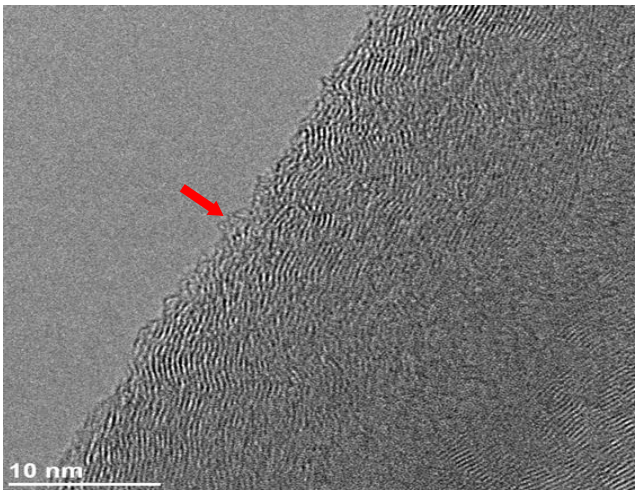

Figure 4.34 HRTEM micrograph of CNF support.

4.2.7.4 Results obtained by TGA

The TGA results of carbon nanofibers have revealed a similar tendency in their decomposition temperatures and purities up to 92 % as shown in Figure 4.35.

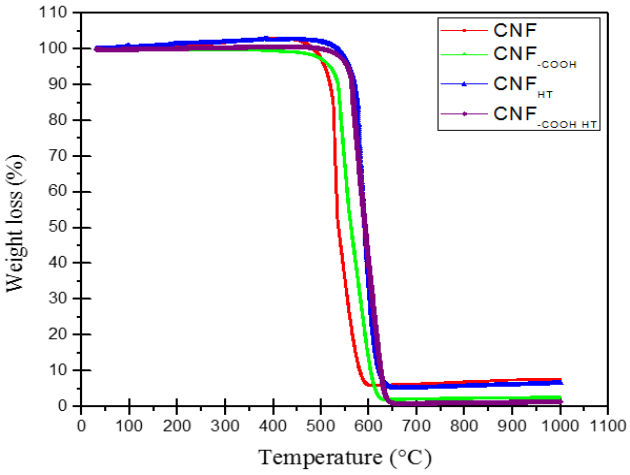

Figure 4.35 TGA analyses of carbon nanofibers.

4.2.7.5 Results obtained by BET

The BET results of carbon nanofibers have exposed low surface areas, small pore volumes, and mesopores in their structures as summarized in Table 4.20.

Table 4.20 BET results of carbon nanofibers.

Support	BET surface area ($m^2 g^{-1}$)	Pore volume ($cm^3 g^{-1}$)	Pore diameter (nm)
CNF	80	0.4	18.8
CNF_{-COOH}	70	0.3	17.1
CNF_{HT}	95	0.4	15.3
$CNF_{-COOH\ HT}$	82	0.3	16.6

4.2.7.6 Results obtained by Raman

The Raman spectra of carbon nanofibers exhibited a high structural disorder as shown in Figure 4.36.

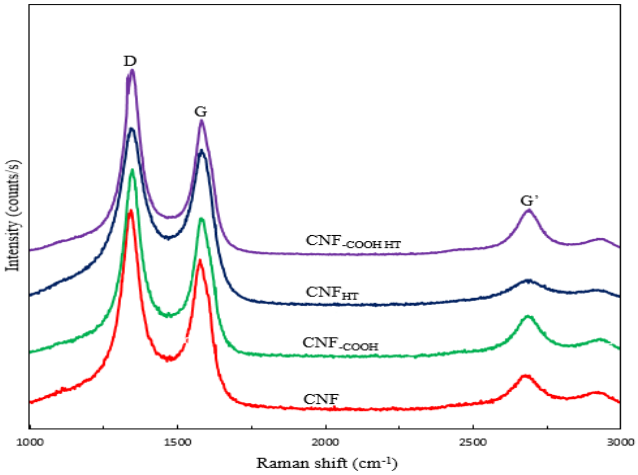

Figure 4.36 Raman spectra of carbon nanofibers.

4.2.7.7 Results obtained by XRPD

The XRD diffractograms of carbon nanofibers have indicated a define crystallinity no matter their preparation methods as shown in Figure 4.37.

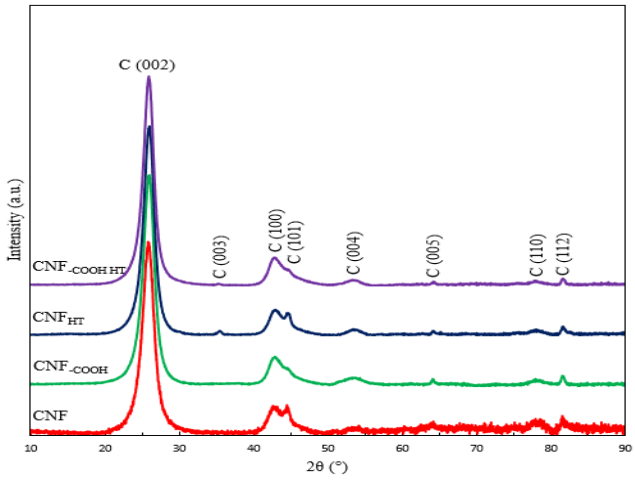

Figure 4.37 XRD diffractograms of carbon nanofibers.

4.2.7.8 Results obtained by IR

The IR spectra of carbon nanofibers have slightly showed for those treated supports the carbonyl group from carboxylic acid groups as shown in Figure 4.38.

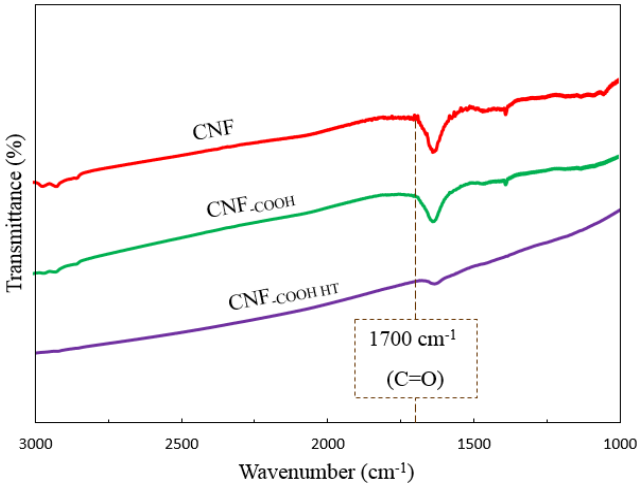

Figure 4.38 IR spectra of carbon nanofibers.

4.2.7.9 Results obtained by XPS

The XPS spectra of carbon nanofibers have presented the chemical composition equal to 100 % and the sp^3/sp^2 ratio for all them as summarized in Table 4.21.

Table 4.21 Chemical composition and sp^3/sp^2 ratio from XPS spectra for carbon nanofibers.

Support	Elements				sp^3/sp^2 ratio
	C%	O%	N%	S%	
CNF	98.5	1.5	0.0	0.0	0.5
CNF_{-COOH}	93.4	6.6	0.0	0.0	0.5
CNF_{HT}	97.7	2.3	0.0	0.0	0.5
$CNF_{-COOH\ HT}$	98.6	1.1	0.0	0.0	0.4

4.2.8 sCNF, $sCNF_{-COOH}$, $sCNF_{HT}$, and $sCNF_{-COOH\ HT}$ characterized by microanalysis, TEM, HRTEM, TGA, BET, Raman, XRPD, IR, and XPS

4.2.8.1 Results obtained by microanalysis

The microanalysis results of small carbon nanofibers have presented carbon percentage up to 87 % as summarized in Table 4.22.

Table 4.22 Microanalysis results of small carbon nanofibers.

Support	Elements			
	C%	H%	N%	S%
sCNF	92.7	0	0	0
$sCNF_{-COOH}$	87.2	0	0	0
$sCNF_{HT}$	95.8	0	0	0
$sCNF_{-COOH\ HT}$	96.6	0	0	0

4.2.8.2 Results obtained by TEM

The TEM micrographs of small carbon nanofibers have showed no physical attrition due to the methods and/or treatments applied as shown in Figure 4.39.

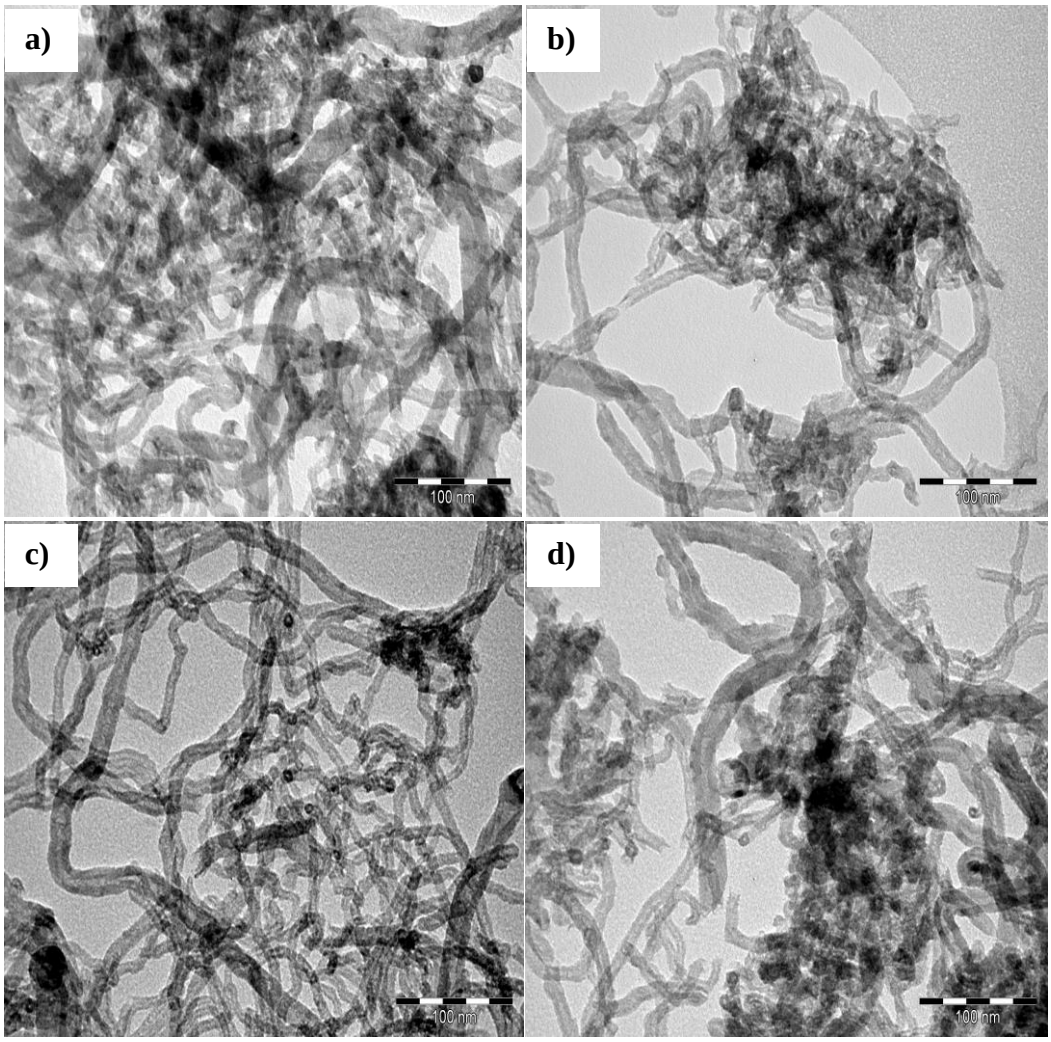

Figure 4.39 TEM micrographs of small carbon nanofibers. a) sCNF, b) $sCNF_{\text{-COOH}}$, c) $sCNF_{HT}$, and d) $sCNF_{\text{-COOH HT}}$.

4.2.8.3 Results obtained by HRTEM

The HRTEM micrograph of sCNF support has clearly displayed any morphological irregularities on the edge boundaries as shown in Figure 4.40.

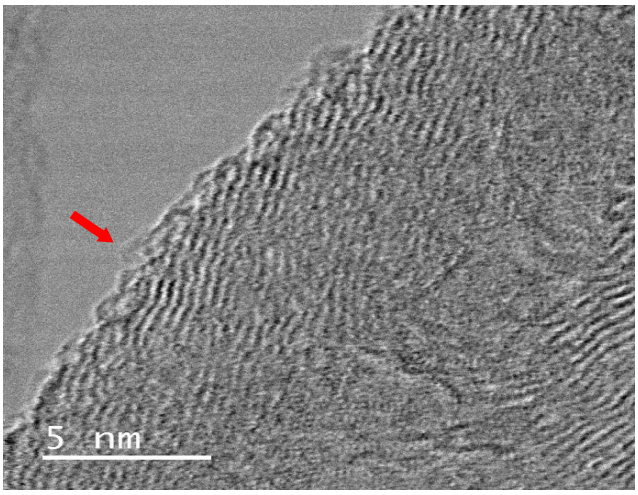

Figure 4.40 HRTEM micrograph of sCNF support.

4.2.8.4 Results obtained by TGA

The TGA results of small carbon nanofibers have revealed a similar tendency in their decomposition temperatures, purities up to 92 %, and the $sCNF_{HT}$ support exhibited remaining nickel, which is oxidized when finishing the analysis as shown in Figure 4.41.

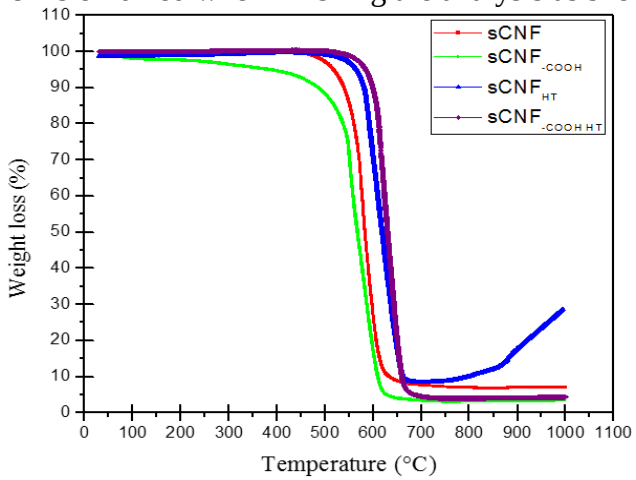

Figure 4.41 TGA analyses of small carbon nanofibers.

4.2.8.5 Results obtained by BET

The BET results of small carbon nanofibers have exposed high surface areas, medium pore volumes, and mesopores in their structures as summarized in Table 4.23.

Table 4.23 BET results of small carbon nanofibers.

Support	BET surface area ($m^2\ g^{-1}$)	Pore volume ($cm^3\ g^{-1}$)	Pore diameter (nm)
sCNF	299	1.0	14.1
$sCNF_{-COOH}$	296	1.0	13.1
$sCNF_{HT}$	204	0.8	15.7
$sCNF_{-COOH\ HT}$	296	1.2	16.3

4.2.8.6 Results obtained by Raman

The Raman spectra of small carbon nanofibers exhibited a high structural disorder as shown in Figure 4.42.

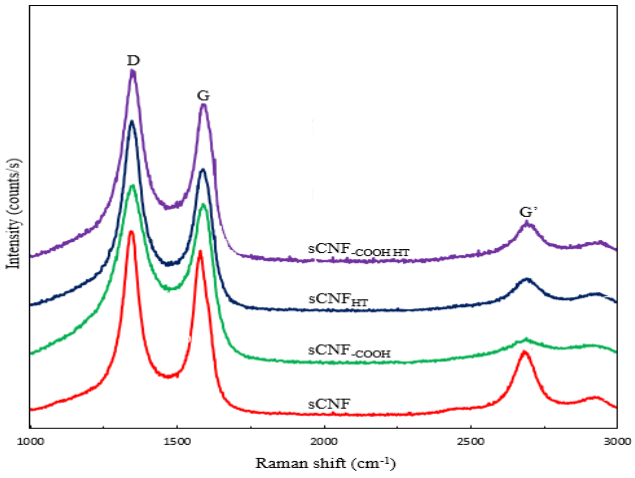

Figure 4.42 Raman spectra of small carbon nanofibers.

4.2.8.7 Results obtained by XRPD

The XRD diffractograms of small carbon nanofibers have indicated a define crystallinity no matter their preparation methods and the $sCNF_{HT}$ support exposed remaining nickel from catalyst (peak at 45°) as shown in Figure 4.43.

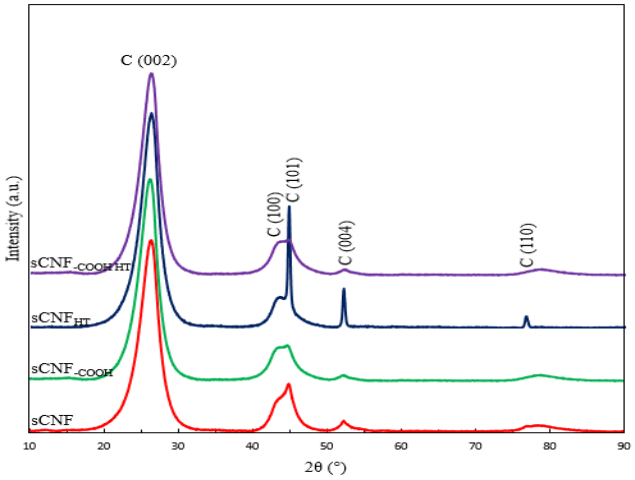

Figure 4.43 XRD diffractograms of small carbon nanofibers.

4.2.8.8 Results obtained by IR

The IR spectra of small carbon nanofibers have slightly showed for those treated supports the carbonyl group from carboxylic acid groups as shown in Figure 4.44.

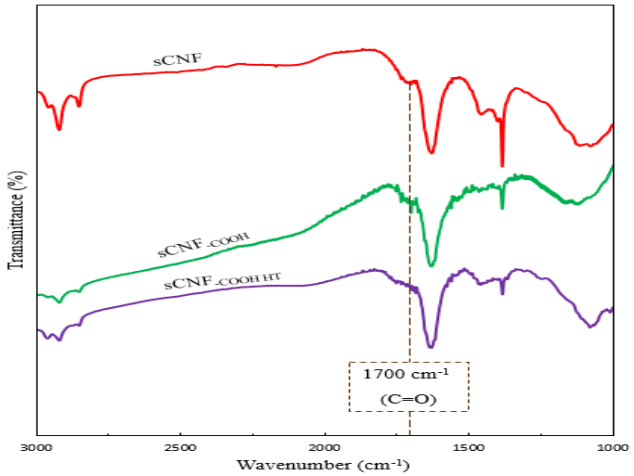

Figure 4.44 IR spectra of small carbon nanofibers.

4.2.8.9 Results obtained by XPS

The XPS spectra of small carbon nanofibers have presented the chemical composition equal to 100 % and the sp^3/sp^2 ratio for all them as summarized in Table 4.24.

Table 4.24 Chemical composition and sp^3/sp^2 ratio from XPS spectra for small carbon nanofibers.

Support	Elements				sp^3/sp^2 ratio
	C%	O%	N%	S%	
sCNF	98.5	1.5	0.0	0.0	0.4
$sCNF_{-COOH}$	93.8	6.2	0.0	0.0	0.5
$sCNF_{HT}$	99.2	0.8	0.0	0.0	0.4
$sCNF_{-COOH\ HT}$	98.6	1.4	0.0	0.0	0.4

4.2.9 FC, FC_{-COOH}, FC_{HT}, and $FC_{-COOH\ HT}$ characterized by microanalysis, TEM, HRTEM, TGA, BET, Raman, XRPD, IR, and XPS

4.2.9.1 Results obtained by microanalysis

The Microanalysis results of fibrous carbon supports have presented carbon percentage up to 86 % as summarized in Table 4.25.

Table 4.25 Microanalysis results of fibrous carbon supports.

Support	Elements			
	C%	H%	N%	S%
FC	97.2	0	0	0
FC_{-COOH}	86.3	0	0	0
FC_{HT}	97.2	0	0	0
$FC_{-COOH\ HT}$	96.3	0	0	0

4.2.9.2 Results obtained by TEM

The TEM micrographs of fibrous carbon supports have showed no physical attrition due to the methods and/or treatments applied as shown in Figure 4.45.

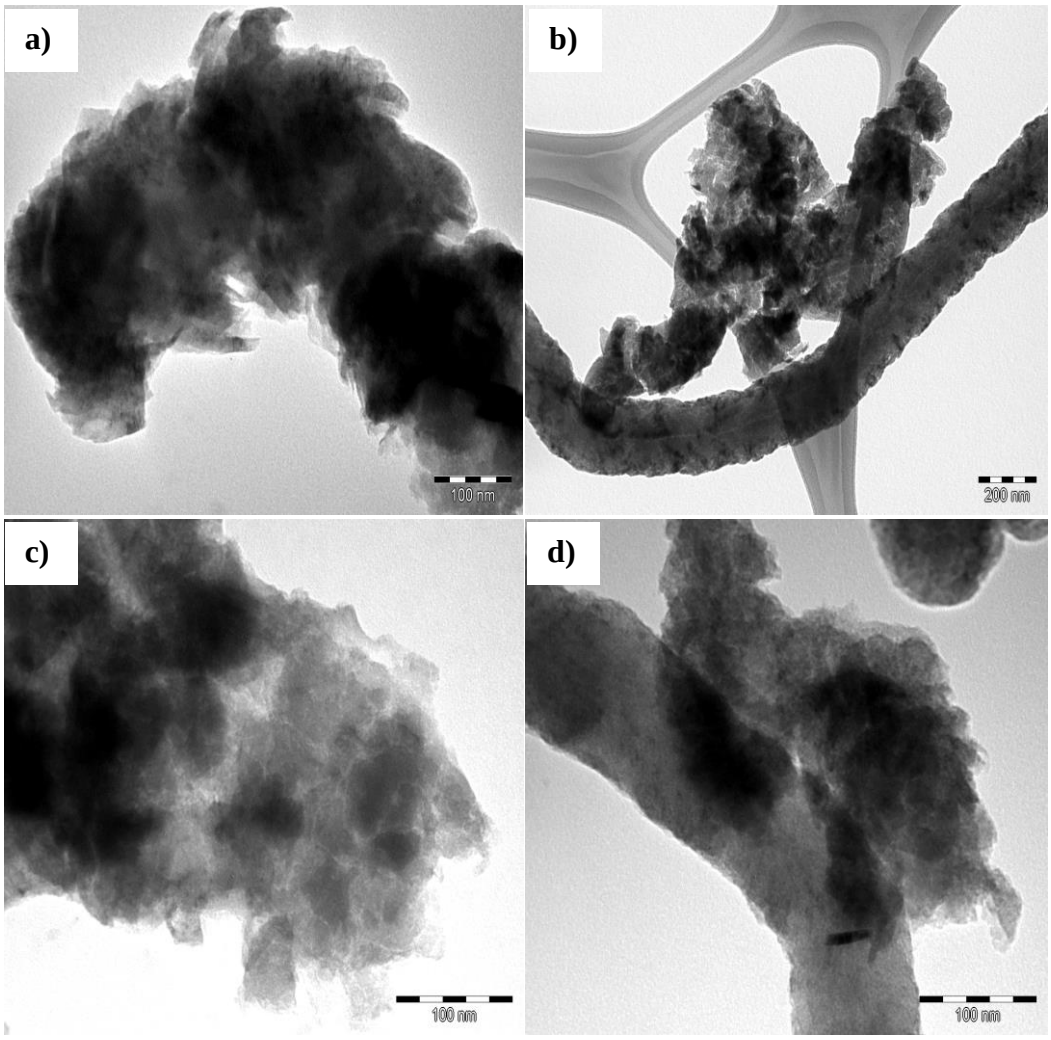

Figure 4.45 TEM micrographs of fibrous carbon supports. a) FC, b) $FC_{\text{-COOH}}$, c) FC_{HT}, and d) $FC_{\text{-COOH HT}}$.

4.2.9.3 Results obtained by HRTEM

The HRTEM micrograph of FC support has clearly displayed any morphological irregularities on the edge boundaries as shown in Figure 4.46.

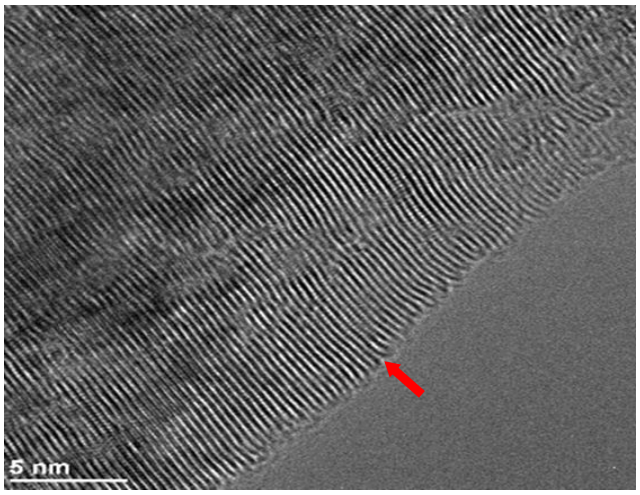

Figure 4.46 HRTEM micrograph of FC support.

4.2.9.4 Results obtained by TGA

The TGA results of fibrous carbon supports have revealed a similar tendency in their decomposition temperatures and purities up to 90 % as shown in Figure 4.47.

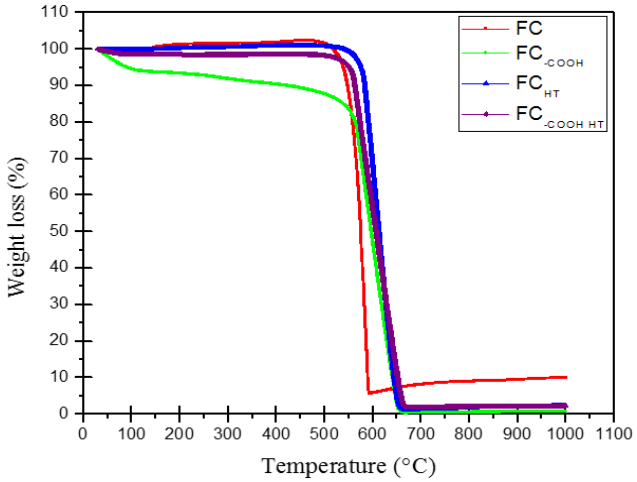

Figure 4.47 TGA analyses of fibrous carbon supports.

4.2.9.5 Results obtained by BET

The BET results of fibrous carbon supports have exposed high surface areas, small pore volumes, and mesopores in their structures as summarized in Table 4.26.

Table 4.26 BET results of fibrous carbon supports.

Support	BET surface area ($m^2 g^{-1}$)	Pore volume ($cm^3 g^{-1}$)	Pore diameter (nm)
FC	134	0.3	9.6
FC_{-COOH}	173	0.4	9.0
FC_{HT}	128	0.3	10.7
$FC_{-COOH\ HT}$	215	0.4	8.4

4.2.9.6 Results obtained by Raman

The Raman spectra of fibrous carbon supports exhibited a high structural disorder as shown in Figure 4.48.

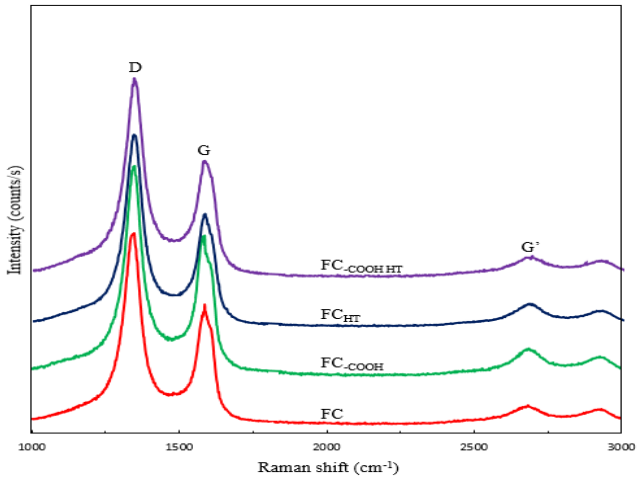

Figure 4.48 Raman spectra of fibrous carbon supports.

4.2.9.7 Results obtained by XRPD

The XRD diffractograms of fibrous carbon supports have indicated a define crystallinity no matter their preparation methods as shown in Figure 4.49.

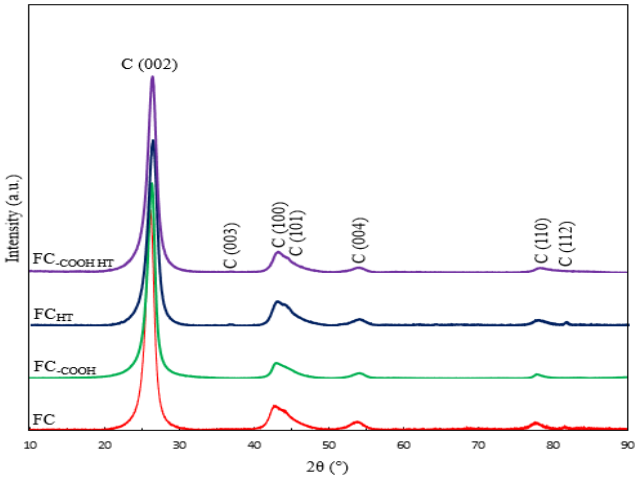

Figure 4.49 XRD diffractograms of fibrous carbon supports.

4.2.9.8 Results obtained by IR

The IR spectra of fibrous carbon supports have clearly showed for those treated supports the carbonyl group from carboxylic acid groups as shown in Figure 4.50.

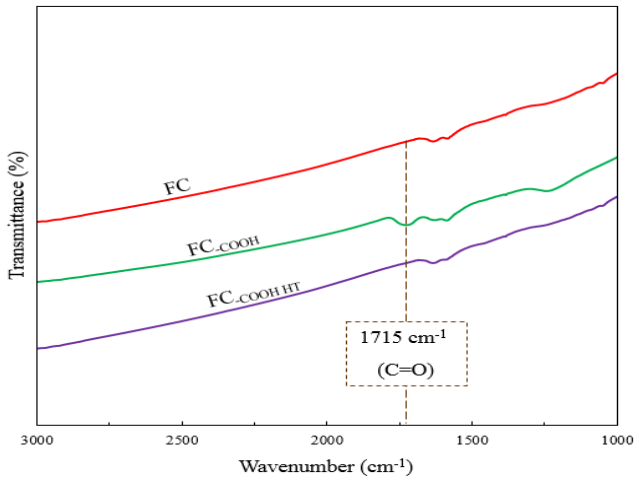

Figure 4.50 IR spectra of fibrous carbon supports.

4.2.9.9 Results obtained by XPS

The XPS spectra of fibrous carbon supports have presented the chemical composition equal to 100 % and the sp^3/sp^2 ratio for all them as summarized in Table 4.27.

Table 4.27 Chemical composition and sp^3/sp^2 ratio from XPS spectra for FC supports.

Support	Elements				sp^3/sp^2 ratio
	C%	O%	N%	S%	
FC	93.4	6.6	0.0	0.0	0.7
FC_{-COOH}	90.3	9.7	0.0	0.0	0.5
FC_{HT}	88.3	11.7	0.0	0.0	1.2
$FC_{-COOH\ HT}$	92.3	7.5	0.0	0.0	0.8

4.2.10 Characterization data of all carbon supports

As shown above, all carbon supports were characterized by using advanced characterization techniques, which have provided specific information that has allowed studying their physical and chemical properties. Thus, we have performed a detailed comparison of characterization data of carbon supports to clearly understand the influence of carbon nanomaterials before using them as catalyst supports. Chemical, textural, and crystallite properties of the carbon supports are summarized in Table 4.28.

Table 4.28 Chemical, textural and crystallite properties of the carbon supports.

Support	Elemental analysis			XPS analysis				Textural properties		Crystallite properties		TGA (°C)	TGA residue (%)
	C (%)	N (%)	S (%)	C (%)	O (%)	N (%)	S (%)	BET surface area (m^2 g^{-1})	Pore volume (cm^3 g^{-1})	d_{002} (nm)	$L_C(002)$ (nm)		
CNT	92.3			99.2	0.8			151	2.6	0.3444	4.20	628	6.6
CNT_{HT}	96.2			99.8	0.3			165	2.7	0.3446	4.57	663	5.5
CNT_{COOH}	90.4			94.3	5.7			220	1.2	0.3407	4.48	640	1.3
$CNT_{COOH-HT}$	97.6			99.2	0.8			251	2.7	0.3427	3.81	630	1.1
N-CNT	92.3	2.95		96.7	1.7	1.7		182	2.7	0.3436	4.25	542	7.4
$N\text{-}CNT_{HT}$	95.6	1.65		97.7	0.8	1.5		168	2.4	0.3379	4.14	505	6.6
S_1-CNT	64.1		12.3	91.4	5.2		2.8	48	4.1	0.3450	3.28	530	34.1
$S_1\text{-}CNT_{HT}$	67.1		9.55	95.3	3.6		1.8	79	0.4	0.3428	4.19	525	25.9
S_2-CNT	78.6		5.0	95.6	2.8		1.3	90	1.1	0.3422	5.75	610	18.7
$S_2\text{-}CNT_{HT}$	77.4		4.0	96.7	1.8		1.1	116	0.6	0.3423	5.23	614	15.9
FLG	98.8			99.1	0.9			41	0.2	0.3407	9.36	657	3.7
FLG_{HT}	98.6			99.2	0.8			74	0.3	0.3396	10.56	704	2.5
FLG_{COOH}	97.1			96.2	3.8			51	0.2	0.3393	10.34	724	2.5
$FLG_{COOH-HT}$	98.7			99.0	1.0			71	0.3	0.3396	10.48	719	1.3
FC	97.2			93.4	6.6			134	0.3	0.3401	6.38	577	9.9
FC_{HT}	97.2			88.3	11.7			128	0.3	0.3398	5.77	608	2.3
FC_{COOH}	86.3			90.3	9.7			215	0.4	0.3375	6.71	575	0.8
$FC_{COOH-HT}$	96.3			92.3	7.5			214	0.4	0.3361	5.81	595	2.3
CNF	97.9			98.5	1.5			80	0.4	0.3444	4.49	530	7.5
CNF_{HT}	97.9			97.7	2.3			95	0.4	0.3424	4.36	577	6.6
CNF_{COOH}	95.7			93.4	6.6			71	0.3	0.3434	4.64	538	2.5
$CNF_{COOH-HT}$	98.4			98.6	1.1			71	0.3	0.3446	5.00	566	1.4
sCNF	92.7			98.5	1.5			299	1.0	0.3384	2.83	579	7.0
$sCNF_{HT}$	95.8			99.2	0.8			204	0.8	0.3390	2.96	591	7.1
$sCNF_{COOH}$	87.2			93.8	6.2			296	1.0	0.3397	2.94	549	3.5
$sCNF_{COOH-HT}$	96.6			98.6	1.4			296	1.2	0.3402	2.93	614	4.4

Furthermore, XPS analyses carried out on the carbon supports have also provide particular information for C1s. Therefore, the assignments for the C1s peak from deconvolution are summarized in Table 4.29.

Table 4.29 C1s peak deconvolution assignments.

XPS analysis – C1s peak						
I	**II**	**III**	**IV**	**V**	**VI**	**VII**
Vacancies 283.5-283.9 eV	C=C (sp^2) 284.6 eV	C-C (sp^3) 285.1-285.2 eV	OH, C-O 286.0-286.2 eV	C=O 287.3-287.5 eV	COOH, lactone 288.4-289.2 eV	π-π* shake up 290.6-291.2 eV

Finally, XPS and Raman data of the carbon supports are summarized in Table 4.30.

Table 4.30 XPS (C1s peak) and Raman analyses of the carbon supports.

Supports	**Raman analysis**				**XPS analysis – C1s peak**							
	I_D/I_G	**$I_{G'}/I_G$**	**$I_{G'}/I_D$**	**L_D (nm)**	**FWHM (eV)**	**I**	**II**	**III**	**IV**	**V**	**VI**	**VII**
CNT	0.87	0.59	0.43	12.8	0.69	2.4	48.5	18.1	9.8	8.1	3.0	10.1
CNT_{HT}	0.79	0.79	0.67	13.5	0.69	1.5	50.5	17.7	11.1	6.6	3.4	9.3
CNT_{COOH}	1.01	0.83	0.59	11.9	0.69	1.3	45.9	20.0	10.5	7.9	5.5	8.9
$CNT_{COOH-HT}$	1.03	0.99	0.67	11.8	0.68	1.5	50.3	19.8	8.0	8.0	3.6	8.8
N-CNT	1.02	0.17	0.22	11.8	0.79	2.4	43.9	20.4	12.1	8.4	3.9	8.8
$N\text{-}CNT_{HT}$	0.95	0.19	0.23	12.3	0.82	1.5	45.6	20.3	12.0	7.6	3.5	9.4
S_1-CNT	1.12	0.07	0.15	11.3	0.80	1.3	47.7	18.3	10.7	7.6	4.6	7.6
$S_1\text{-}CNT_{HT}$	1.14	0.10	0.15	11.2	0.78	1.5	45.8	19.8	9.3	8.8	3.7	8.5
S_2-CNT	0.99	0.72	0.81	12.1	0.70	3.1	48.6	18.6	9.5	8.1	3.8	8.4
$S_2\text{-}CNT_{HT}$	0.58	1.04	1.30	15.8	0.71	2.3	49.5	18.7	9.2	7.8	4.0	8.7
FLG	0.61	1.17	1.21	15.4	0.66	1.1	54.1	15.5	10.3	6.5	4.0	8.3
FLG_{HT}	0.53	1.22	1.33	16.5	0.66	1.0	53.8	16.6	9.4	6.9	5.0	9.3
FLG_{COOH}	0.64	1.06	1.04	15.0	0.67	1.0	52.5	16.2	10.7	7.1	5.9	9.1
$FLG_{COOH-HT}$	0.63	1.00	1.01	14.9	0.65	1.0	53.6	16.6	10.0	6.8	4.1	8.1
FC	1.49	0.20	0.24	9.8	0.75	2.4	38.8	26.1	13.6	7.0	4.3	6.0
FC_{HT}	1.63	0.24	0.23	9.4	0.76	3.0	32.3	36.2	12.4	4.8	3.9	4.5
FC_{COOH}	1.41	0.27	0.26	10.1	0.74	1.7	44.3	20.2	10.4	8.3	5.8	9.2
$FC_{COOH-HT}$	1.65	0.18	0.28	9.3	0.76	1.6	38.5	30.7	10.8	6.4	5.8	6.9
CNF	1.30	0.32	0.13	10.5	0.76	4.8	46.3	18.7	9.4	8.4	4.0	8.3
CNF_{HT}	1.15	0.18	0.15	11.2	0.79	2.6	46.7	22.4	10.3	4.9	2.9	8.0
CNF_{COOH}	1.24	0.26	0.18	10.7	0.74	4.2	43.3	18.5	11.4	8.0	3.4	8.7
$CNF_{COOH-HT}$	1.26	0.45	0.14	10.7	0.77	2.9	48.6	18.3	10.0	7.6	3.7	8.5
sCNF	1.12	0.39	0.38	11.3	0.76	2.7	47.8	18.2	10.1	7.9	6.0	9.0
$sCNF_{HT}$	1.30	0.24	0.22	10.5	0.77	2.4	48.7	18.8	9.3	7.3	6.8	9.5
$sCNF_{COOH}$	1.10	0.12	0.23	11.4	0.76	2.0	44.3	19.2	11.5	8.2	6.0	9.0
$sCNF_{COOH-HT}$	1.20	0.31	0.27	10.9	0.75	2.5	48.9	17.3	12.7	2.9	5.0	9.9

4.2.11 Commercial SiO_2-Al_2O_3 and Al_2O_3 characterized by SEM, TEM and BET

4.2.11.1 Commercial alumina (Al_2O_3)

4.2.11.1.1 Results obtained by TEM

The TEM micrographs of alumina have shown a similar morphology everywhere in the sample as shown in Figure 4.51.

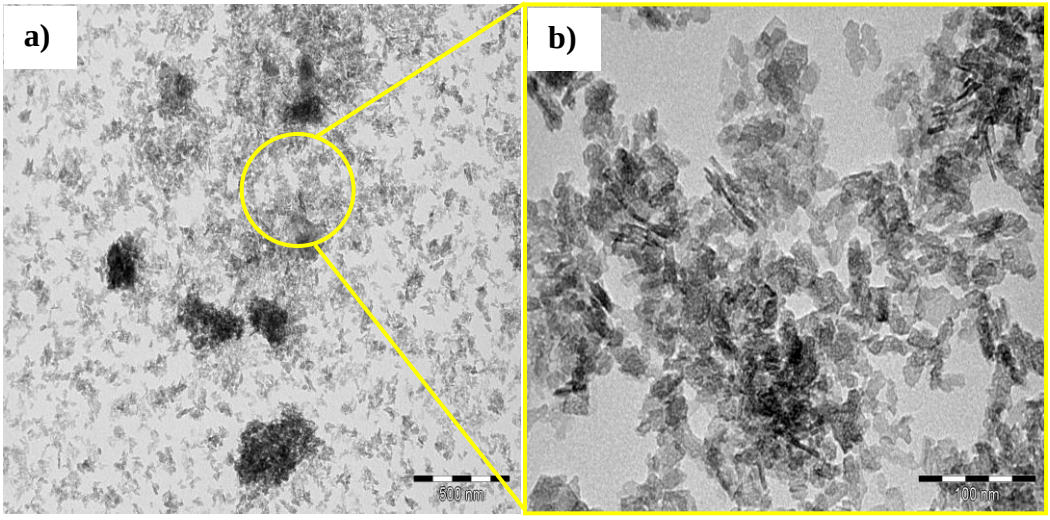

Figure 4.51 TEM micrographs of alumina. Scale bar: a) 500 nm and b) 100 nm.

4.2.11.1.2 Results obtained by BET

The BET results of alumina show high surface area, small pore volume, and mesopores in its structure as summarized in Table 4.31.

Table 4.31 BET results of alumina.

Support	BET surface area ($m^2\ g^{-1}$)	Pore volume ($cm^3\ g^{-1}$)	Pore diameter (nm)
Al_2O_3	194	0.4	7.7

4.2.11.2 Commercial silica-alumina (SiO_2-Al_2O_3)

4.2.11.2.1 Results obtained by SEM

The SEM micrographs of silica-alumina have shown a homogeneous morphology, forming spheres with different sizes as shown in Figure 4.52.

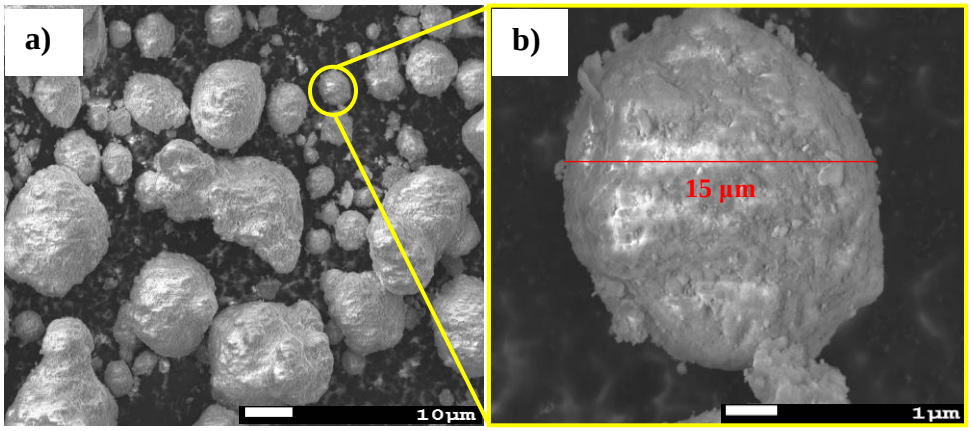

Figure 4.52 SEM micrographs of silica-alumina. Scale bar: a) 10 µm and b) 1 µm.

Furthermore, the contrasting analysis performed on various silica-alumina spheres has displayed no difference in chemical composition as shown in Figure 4.53.

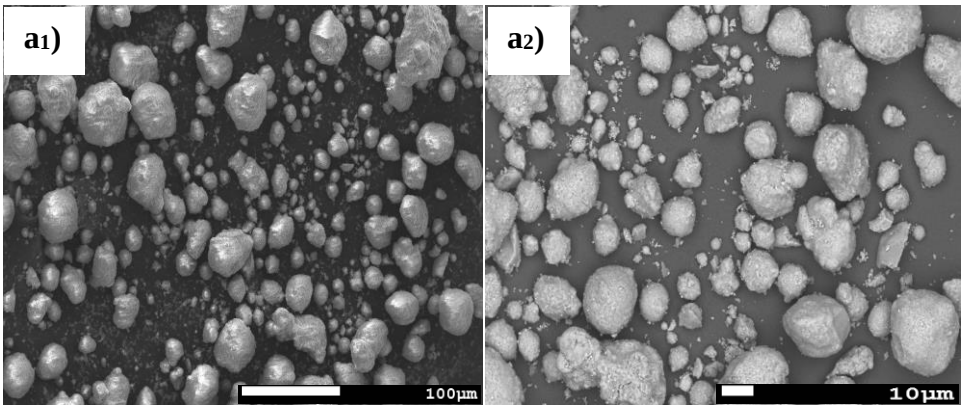

Figure 4.53 Contrasting analysis (a_2) of silica-alumina. a_1-a_2) SiO_2-Al_2O_3.

Finally, the EDX spectrum of silica-alumina has indeed presented the chemical composition and the mass percentage of each element according to its chemical formula as shown in Figure 4.54.

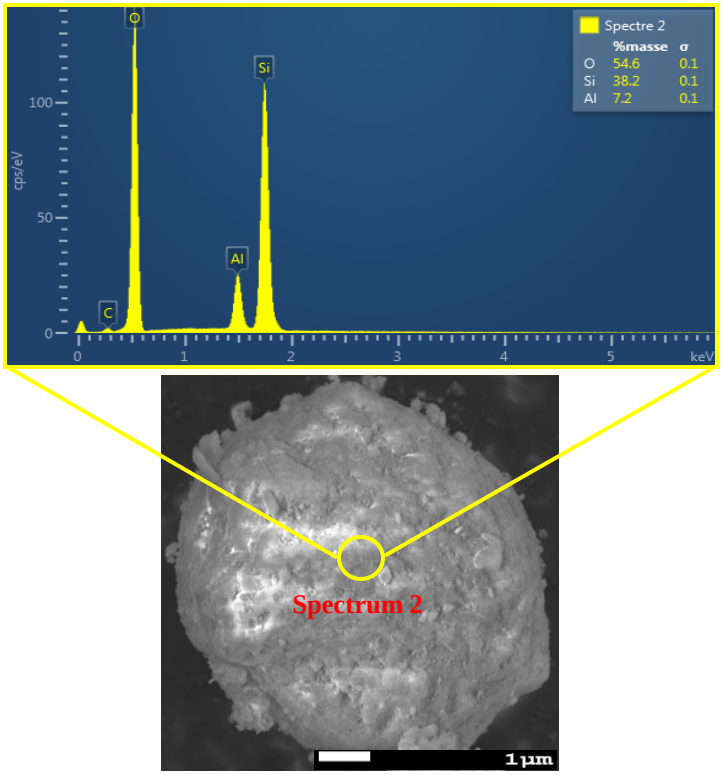

Figure 4.54 EDX spectrum of silica-alumina.

4.2.11.2.2 Results obtained by BET

The BET results of silica-alumina show high surface area, small pore volume, and mesopores in its structure as summarized in Table 4.32.

Table 4.32 BET results of silica-alumina.

Support	BET surface area ($m^2 g^{-1}$)	Pore volume ($cm^3 g^{-1}$)	Pore diameter (nm)
SiO_2-Al_2O_3	485	0.7	5.5

4.3 Characterization results of palladium catalysts

4.3.1 Palladium catalysts supported on FLG, FLG$_{\text{-COOH}}$, FLG$_{\text{HT}}$, and FLG$_{\text{-COOH HT}}$ characterized by TEM, XRPD, BET, and ICP-AES

4.3.1.1 Results obtained by TEM

The TEM micrographs of palladium catalysts supported on few layer graphene have showed a great palladium dispersion and a palladium particle size distribution ranging from 0.1 to 7.0 nm as shown in Figure 4.55.

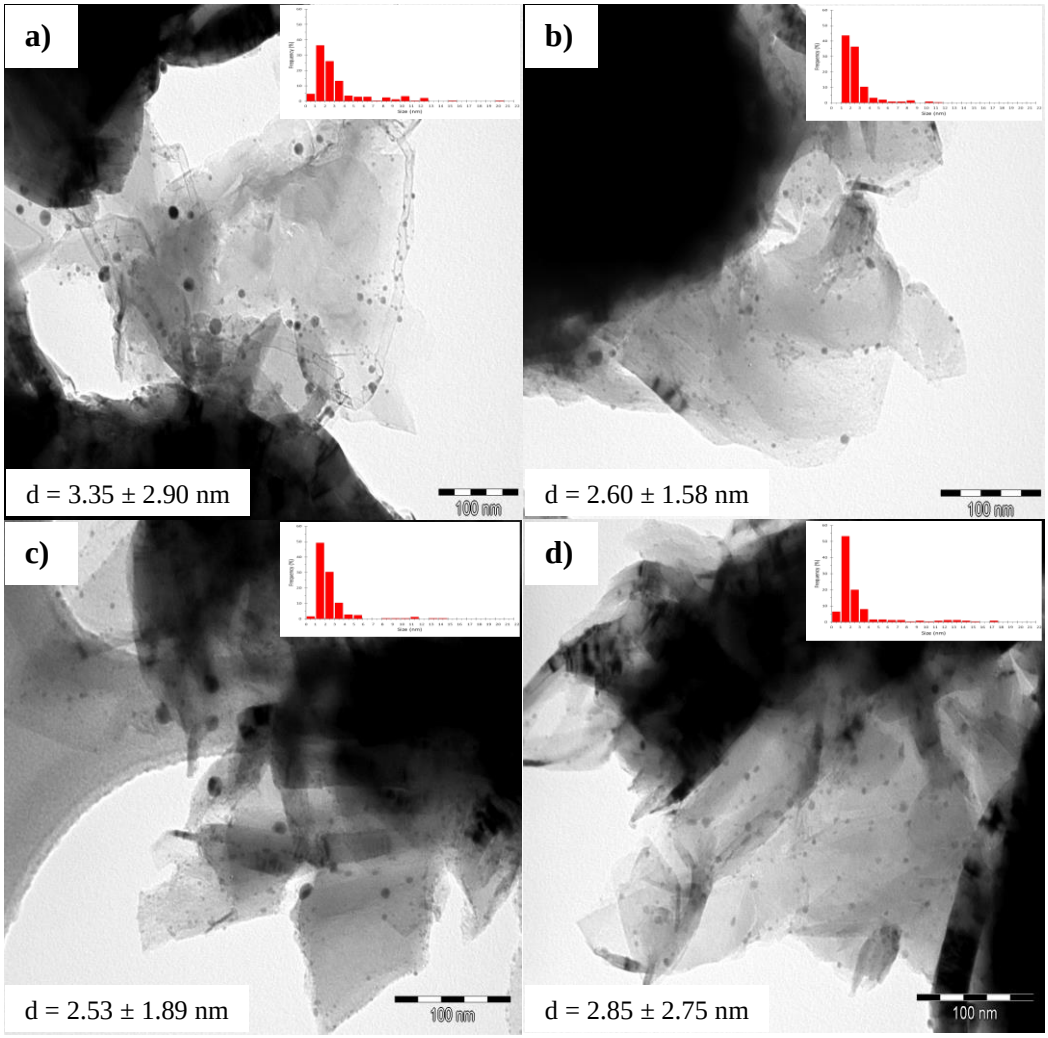

Figure 4.55 TEM micrographs of palladium catalysts supported on few layer graphene. a) Pd/FLG, b) Pd/FLG$_{\text{-COOH}}$, c) Pd/FLG$_{\text{HT}}$, and d) Pd/FLG$_{\text{-COOH HT}}$.

4.3.1.2 Results obtained by XRPD

The XRD diffractograms of palladium catalysts supported on few layer graphene have clearly indicated the presence of palladium metal as shown in Figure 4.56.

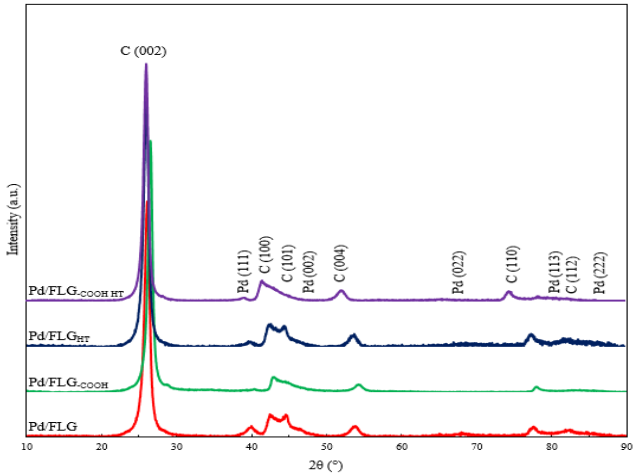

Figure 4.56 XRD diffractograms of palladium catalysts supported on few layer graphene.

4.3.1.3 Results obtained by BET

The BET results of palladium catalysts supported on few layer graphene show low surface areas, small pore volumes, and mesopores as summarized in Table 4.33.

Table 4.33 BET results of palladium catalysts supported on few layer graphene.

Catalyst	BET surface area ($m^2 g^{-1}$)	Pore volume ($cm^3 g^{-1}$)	Pore diameter (nm)
Pd/FLG	43	0.3	26.5
Pd/FLG_{-COOH}	54	0.3	20.2
Pd/FLG_{HT}	85	0.4	18.6
$Pd/FLG_{-COOH\ HT}$	80	0.4	20.2

4.3.1.4 Results obtained by ICP-AES

The ICP-AES results of palladium catalysts supported on few layer graphene have clearly exhibited a close ratio between theoretical and experimental percentages as summarized in Table 4.34.

Table 4.34 ICP-AES results of palladium catalysts supported on few layer graphene.

Catalyst	Element	Theoretical %	Experimental %
Pd/FLG	Pd	2	1.76
Pd/FLG$_{\text{-COOH}}$	Pd	2	1.87
Pd/FLG$_{\text{HT}}$	Pd	2	1.66
Pd/FLG$_{\text{-COOH HT}}$	Pd	2	1.51

4.3.2 Palladium catalysts supported on CNT, CNT_{-COOH}, CNT_{HT}, and $CNT_{-COOH\ HT}$ characterized by TEM, XRPD, BET, and ICP-AES

4.3.2.1 Results obtained by TEM

The TEM micrographs of palladium catalysts supported on multi-walled carbon nanotubes have showed a great palladium dispersion and a palladium particle size distribution ranging from 0.1 to 7.0 nm as shown in Figure 4.57.

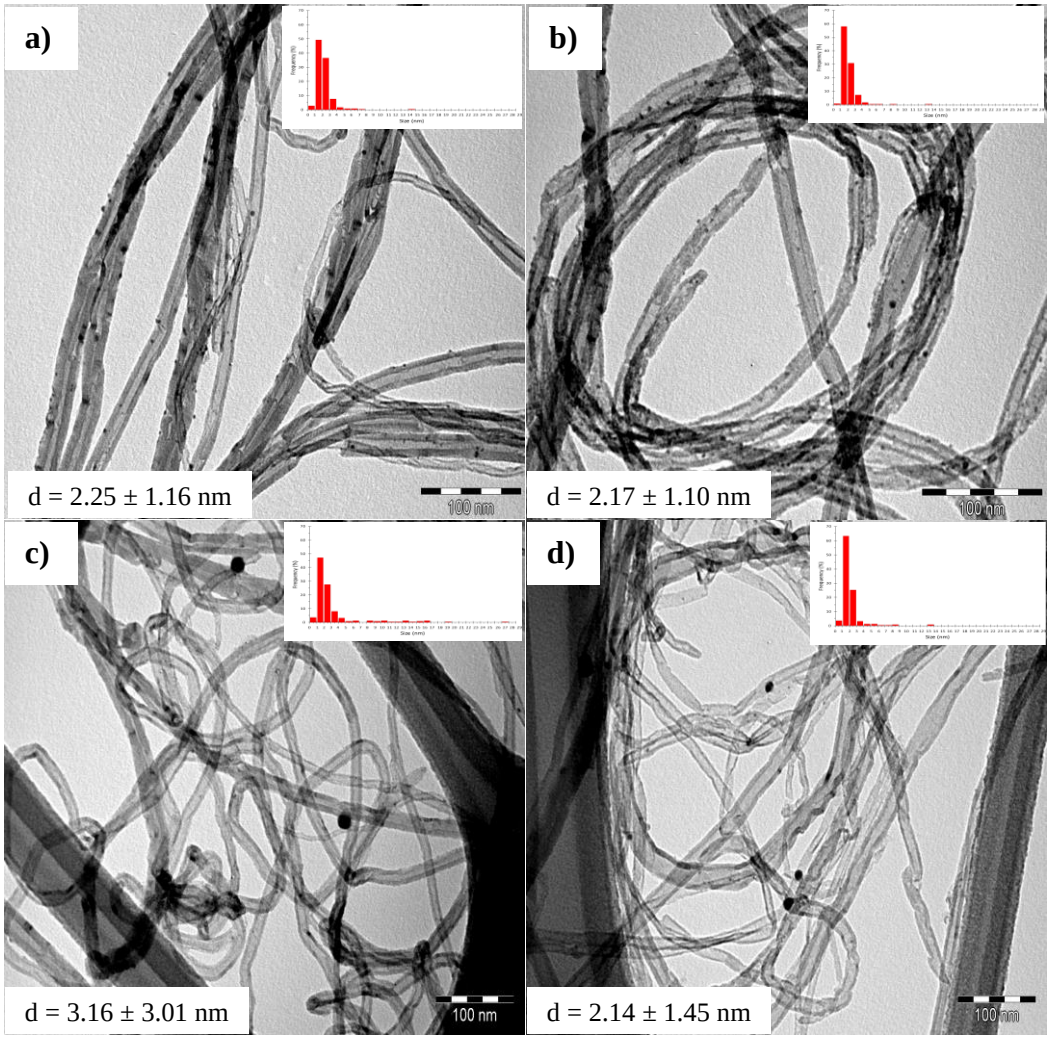

Figure 4.57 TEM micrographs of palladium catalysts supported on multi-walled carbon nanotubes. a) Pd/CNT, b) Pd/CNT_{-COOH}, c) Pd/CNT_{HT}, and d) $Pd/CNT_{-COOH\ HT}$.

4.3.2.2 Results obtained by XRPD

The XRD diffractograms of palladium catalysts supported on multi-walled carbon nanotubes have clearly indicated the presence of palladium metal and remaining CoFe from catalyst (peak at 44°) as shown in Figure 4.58.

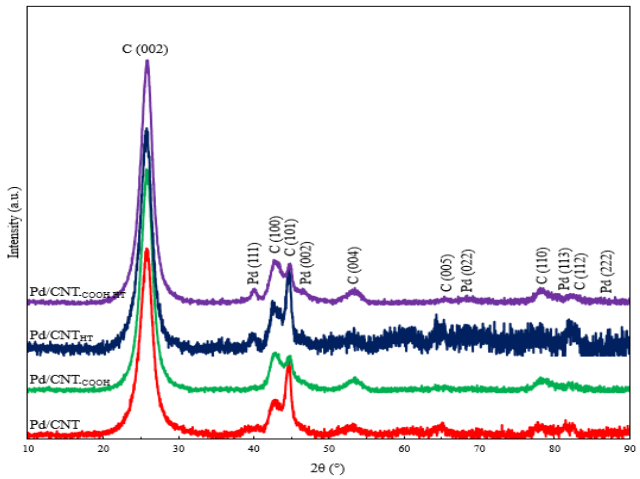

Figure 4.58 XRD diffractograms of palladium catalysts supported on multi-walled carbon nanotubes.

4.3.2.3 Results obtained by BET

The BET results of palladium catalysts supported on multi-walled carbon nanotubes have exposed high surface areas, large pore volumes, and macropores as summarized in Table 4.35.

Table 4.35 BET results of palladium catalysts supported on multi-walled carbon nanotubes.

Catalyst	BET surface area ($m^2 g^{-1}$)	Pore volume ($cm^3 g^{-1}$)	Pore diameter (nm)
Pd/CNT	158	2.8	71.9
Pd/CNT_{-COOH}	232	2.9	50.6
Pd/CNT_{HT}	146	2.8	75.7
$Pd/CNT_{-COOH\ HT}$	203	1.8	35.5

4.3.2.4 Results obtained by ICP-AES

The ICP-AES results of palladium catalysts supported on multi-walled carbon nanotubes have clearly exhibited a close ratio between theoretical and experimental percentages as summarized in Table 4.36.

Table 4.36 ICP-AES results of palladium catalysts supported on multi-walled carbon nanotubes.

Catalyst	Element	Theoretical %	Experimental %
Pd/CNT	Pd	2	1.60
Pd/CNT_{-COOH}	Pd	2	2.04
Pd/CNT_{HT}	Pd	2	1.60
$Pd/CNT_{-COOH\ HT}$	Pd	2	1.89

4.3.3 Palladium catalysts supported on N-CNT and N-CNT$_{HT}$ characterized by TEM, ICP-AES, XRPD, and BET

4.3.3.1 Results obtained by TEM

The TEM micrographs of palladium catalysts supported on nitrogen doped multi-walled carbon nanotubes have showed a great palladium dispersion and a palladium particle size distribution ranging from 0.1 to 4.0 nm as shown in Figure 4.59.

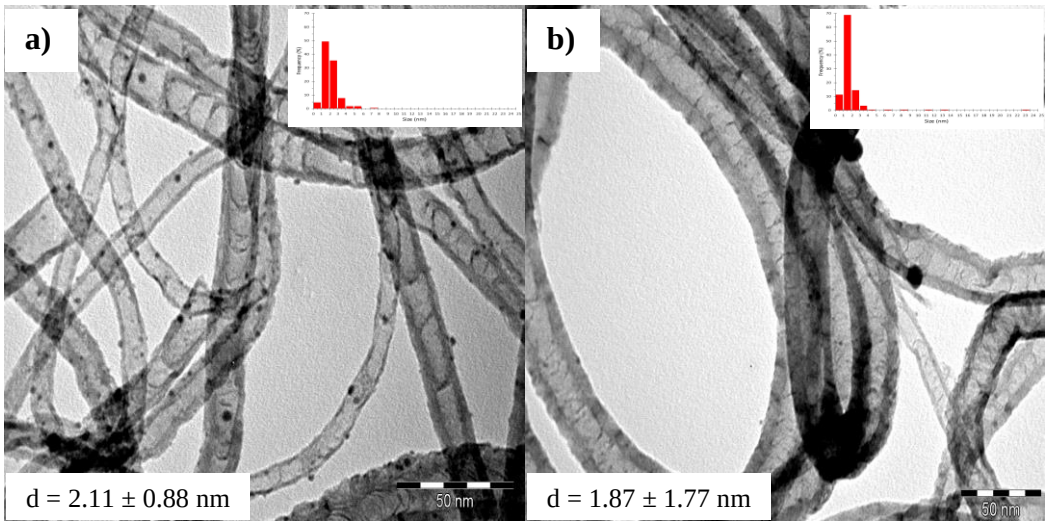

Figure 4.59 TEM micrographs of palladium catalysts supported on nitrogen doped multi-walled carbon nanotubes. a) Pd/N-CNT and b) Pd/N-CNT$_{HT}$.

4.3.3.2 Results obtained by ICP-AES

The ICP-AES results of palladium catalysts supported on nitrogen doped multi-walled carbon nanotubes have clearly exhibited a close ratio between theoretical and experimental percentages as summarized in Table 4.37.

Table 4.37 ICP-AES results of Pd/N-CNT catalysts.

Catalyst	Element	Theoretical %	Experimental %
Pd/N-CNT	Pd	2	1.81
Pd/N-CNT$_{HT}$	Pd	2	1.14

4.3.3.3 Results obtained by XRPD

The XRD diffractograms of palladium catalysts supported on nitrogen doped multi-walled carbon nanotubes have clearly indicated the presence of palladium metal as shown in Figure 4.60.

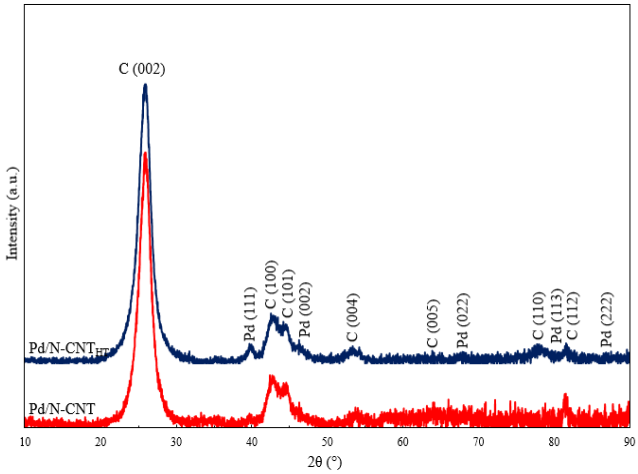

Figure 4.60 XRD diffractograms of palladium catalysts supported on nitrogen doped multi-walled carbon nanotubes.

4.3.3.4 Results obtained by BET

The BET results of palladium catalysts supported on nitrogen doped multi-walled carbon nanotubes have exposed high surface areas, large pore volumes, and macropores as summarized in Table 4.38.

Table 4.38 BET results of palladium catalysts supported on nitrogen doped multi-walled carbon nanotubes.

Catalyst	BET surface area ($m^2\ g^{-1}$)	Pore volume ($cm^3\ g^{-1}$)	Pore diameter (nm)
Pd/N-CNT	166	3.3	79.1
Pd/N-CNT$_{HT}$	195	3.1	63.9

4.3.4 Palladium catalysts supported on S_1-CNT and S_1-CNT_{HT} characterized by TEM, ICP-AES, XRPD, and BET

4.3.4.1 Results obtained by TEM

The TEM micrographs of palladium catalysts supported on sulphur$_1$ doped multi-walled carbon nanotubes have showed a great palladium dispersion and a palladium particle size distribution ranging from 0.1 to 6.0 nm as shown in Figure 4.61.

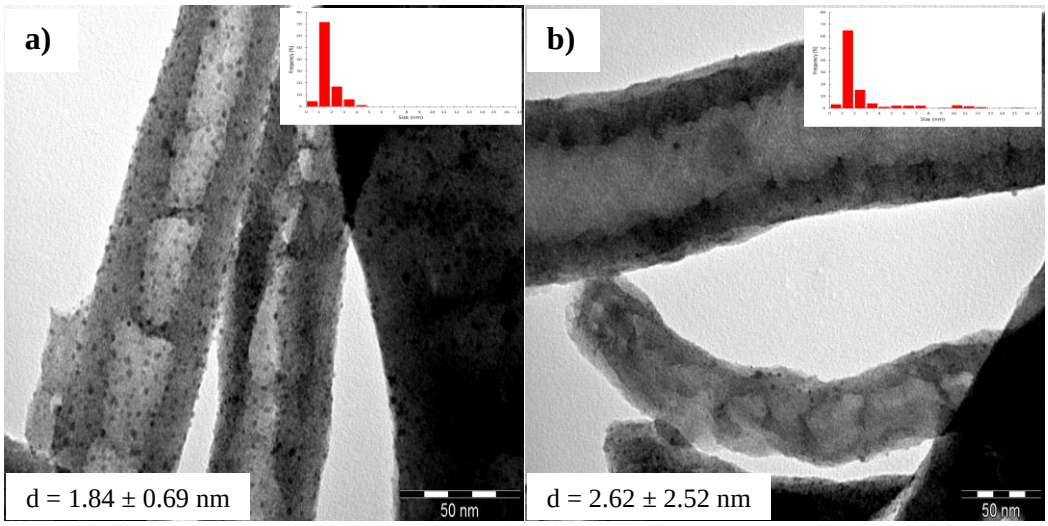

Figure 4.61 TEM micrographs of palladium catalysts supported on sulphur$_1$ doped multi-walled carbon nanotubes. a) Pd/S_1-CNT and b) Pd/S_1-CNT_{HT}.

4.3.4.2 Results obtained by ICP-AES

The ICP-AES results of palladium catalysts supported on sulphur$_1$ doped multi-walled carbon nanotubes have clearly exhibited a close ratio between theoretical and experimental percentages as summarized in Table 4.39.

Table 4.39 ICP-AES results of Pd/S_1-CNT catalysts.

Catalyst	Element	Theoretical %	Experimental %
Pd/S_1-CNT	Pd	2	1.82
Pd/S_1-CNT_{HT}	Pd	2	0.94

4.3.4.3 Results obtained by XRPD

The XRD diffractograms of palladium catalysts supported on sulphur$_1$ doped multi-walled carbon nanotubes have indicated metal traces from catalyst used as starting material and low palladium diffraction patterns as shown in Figure 4.62.

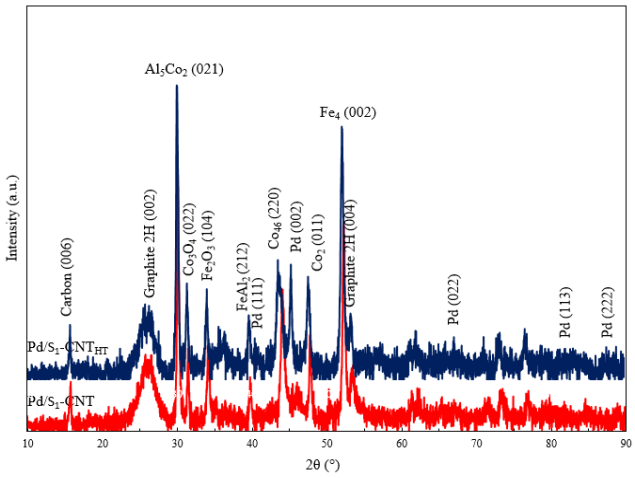

Figure 4.62 XRD diffractograms of palladium catalysts supported on sulphur$_1$ doped multi-walled carbon nanotubes.

4.3.4.4 Results obtained by BET

The BET results of palladium catalysts supported on sulphur$_1$ doped multi-walled carbon nanotubes have exposed low surface areas, small pore volumes, and mesopores as summarized in Table 4.40.

Table 4.40 BET results of palladium catalysts supported on sulphur$_1$ doped multi-walled carbon nanotubes.

Catalyst	BET surface area ($m^2\ g^{-1}$)	Pore volume ($cm^3\ g^{-1}$)	Pore diameter (nm)
Pd/S_1-CNT	50	0.2	20.3
Pd/S_1-CNT_{HT}	50	0.3	23.7

4.3.5 Palladium catalysts supported on S_2-CNT and S_2-CNT_{HT} characterized by TEM, ICP-AES, XRPD, and BET

4.3.5.1 Results obtained by TEM

The TEM micrographs of palladium catalysts supported on sulphur$_2$ doped multi-walled carbon nanotubes have showed a great palladium dispersion and a palladium particle size distribution ranging from 0.8 to 3.0 nm as shown in Figure 4.63.

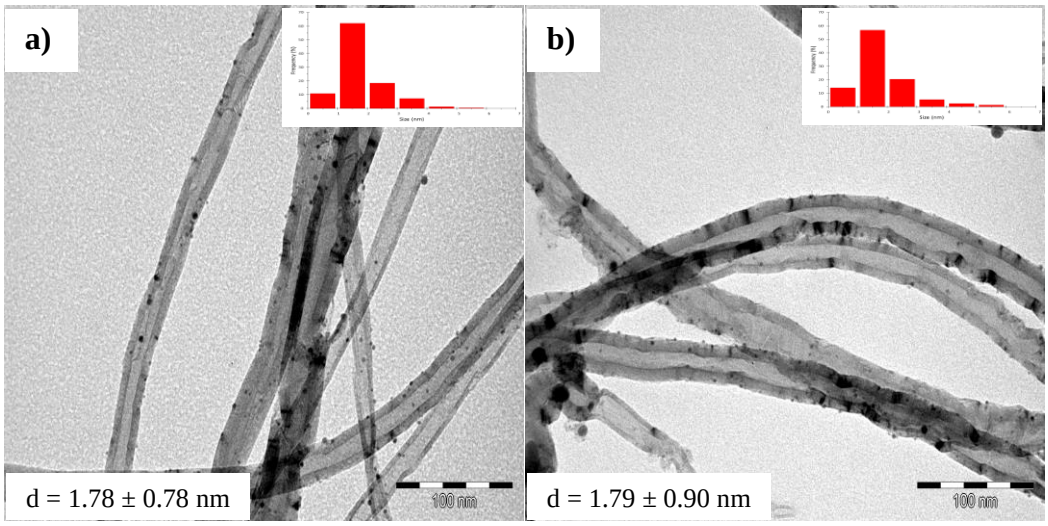

Figure 4.63 TEM micrographs of palladium catalysts supported on sulphur$_2$ doped multi-walled carbon nanotubes. a) Pd/S_2-CNT and b) Pd/S_2-CNT_{HT}.

4.3.5.2 Results obtained by ICP-AES

The ICP-AES results of palladium catalysts supported on sulphur$_2$ doped multi-walled carbon nanotubes have clearly exhibited a close ratio between theoretical and experimental percentages as summarized in Table 4.41.

Table 4.41 ICP-AES results of Pd/S_2-CNT catalysts.

Catalyst	Element	Theoretical %	Experimental %
Pd/S_2-CNT	Pd	2	1.70
Pd/S_2-CNT_{HT}	Pd	2	1.45

4.3.5.3 Results obtained by XRPD

The XRD diffractograms of palladium catalysts supported on sulphur$_2$ doped multi-walled carbon nanotubes have indicated metal traces from catalyst used as starting material and low palladium diffraction patterns as shown in Figure 4.64.

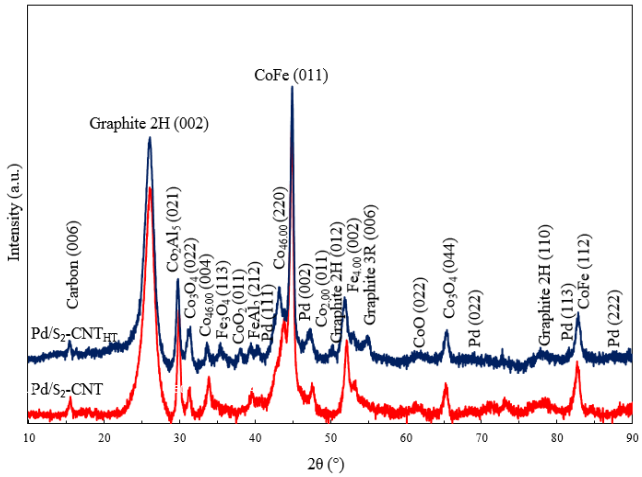

Figure 4.64 XRD diffractograms of palladium catalysts supported on sulphur$_2$ doped multi-walled carbon nanotubes.

4.3.5.4 Results obtained by BET

The BET results of palladium catalysts supported on sulphur$_2$ doped multi-walled carbon nanotubes have exposed low surface areas, small pore volumes, and mesopores as summarized in Table 4.42.

Table 4.42 BET results of palladium catalysts supported on sulphur$_2$ doped multi-walled carbon nanotubes.

Catalyst	BET surface area ($m^2\ g^{-1}$)	Pore volume ($cm^3\ g^{-1}$)	Pore diameter (nm)
Pd/S_2-CNT	97	1.3	52.9
Pd/S_2-CNT_{HT}	85	0.7	32.2

4.3.6 Palladium catalysts supported on CNF, CNF_{-COOH}, CNF_{HT}, and $CNF_{-COOH\ HT}$ characterized by TEM, XRPD, BET, and ICP-AES

4.3.6.1 Results obtained by TEM

The TEM micrographs of palladium catalysts supported on carbon nanofibers have showed a great palladium dispersion and a palladium particle size distribution ranging from 0.1 to 5.0 nm as shown in Figure 4.65.

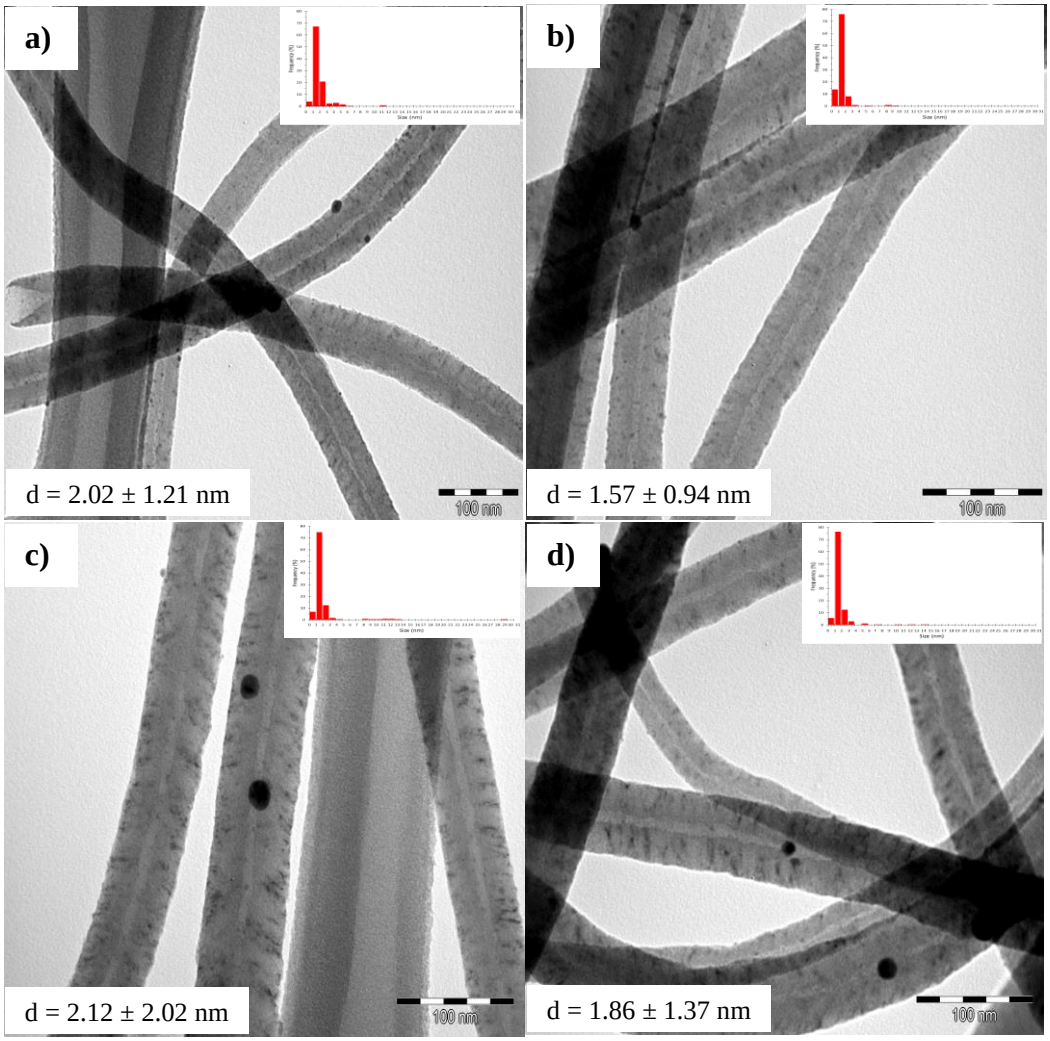

Figure 4.65 TEM micrographs of palladium catalysts supported on carbon nanofibers. a) Pd/CNF, b) Pd/CNF_{-COOH}, c) Pd/CNF_{HT}, and d) $Pd/CNF_{-COOH\ HT}$.

4.3.6.2 Results obtained by XRPD

The XRD diffractograms of palladium catalysts supported on carbon nanofibers have clearly indicated the presence of palladium metal as shown in Figure 4.66.

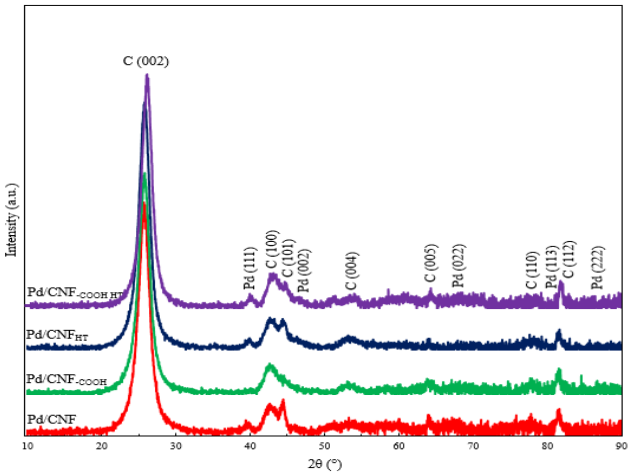

Figure 4.66 XRD diffractograms of palladium catalysts supported on carbon nanofibers.

4.3.6.3 Results obtained by BET

The BET results of palladium catalysts supported on carbon nanofibers have exposed low surface areas, small pore volumes, and mesopores as summarized in Table 4.43.

Table 4.43 BET results of palladium catalysts supported on carbon nanofibers.

Catalyst	BET surface area ($m^2\ g^{-1}$)	Pore volume ($cm^3\ g^{-1}$)	Pore diameter (nm)
Pd/CNF	104	0.4	17.4
Pd/CNF_{-COOH}	82	0.4	19.6
Pd/CNF_{HT}	67	0.4	25.5
$Pd/CNF_{-COOH\ HT}$	71	0.4	22.1

4.3.6.4 Results obtained by ICP-AES

The ICP-AES results of palladium catalysts supported on carbon nanofibers have clearly exhibited a close ratio between theoretical and experimental percentages as summarized in Table 4.44.

Table 4.44 ICP-AES results of palladium catalysts supported on carbon nanofibers.

Catalyst	Element	Theoretical %	Experimental %
Pd/CNF	Pd	2	1.65
Pd/CNF_{-COOH}	Pd	2	1.70
Pd/CNF_{HT}	Pd	2	1.18
$Pd/CNF_{-COOH\ HT}$	Pd	2	1.41

4.3.7 Palladium catalysts supported on sCNF, sCNF$_{-COOH}$, sCNF$_{HT}$, and sCNF$_{-COOH\ HT}$ characterized by TEM, XRPD, BET, and ICP-AES

4.3.7.1 Results obtained by TEM

The TEM micrographs of palladium catalysts supported on small carbon nanofibers have showed a great palladium dispersion and a palladium particle size distribution ranging from 0.1 to 5.0 nm as shown in Figure 4.67.

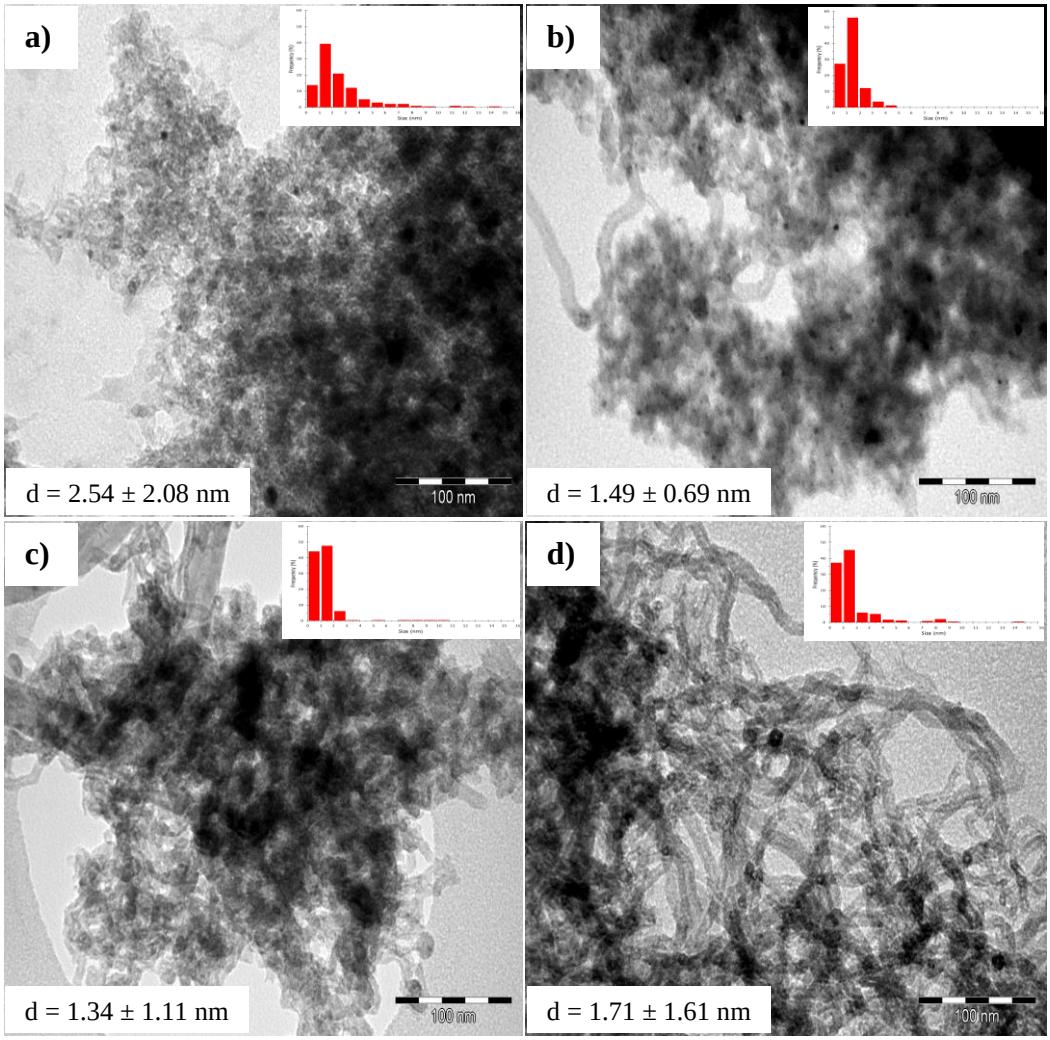

Figure 4.67 TEM micrographs of palladium catalysts supported on small carbon nanofibers. a) Pd/sCNF, b) Pd/sCNF$_{-COOH}$, c) Pd/sCNF$_{HT}$, and d) Pd/sCNF$_{-COOH\ HT}$.

4.3.7.2 Results obtained by XRPD

The XRD diffractograms of palladium catalysts supported on small carbon nanofibers have clearly indicated the presence of palladium metal and remaining nickel from catalyst (peak at 45°) as shown in Figure 4.68.

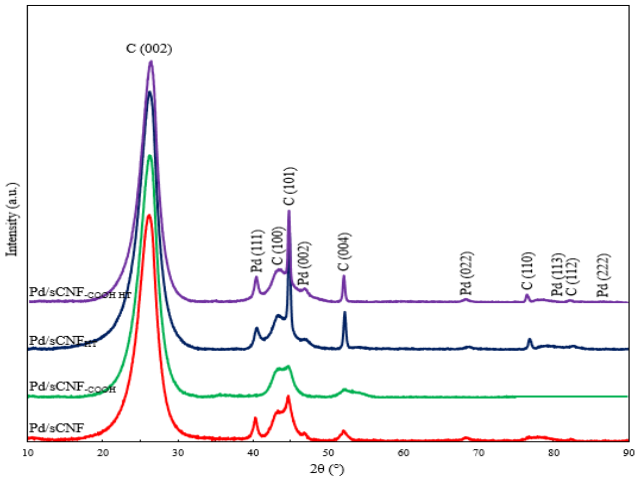

Figure 4.68 XRD diffractograms of palladium catalysts supported on small carbon nanofibers.

4.3.7.3 Results obtained by BET

The BET results of palladium catalysts supported on small carbon nanofibers have exposed high surface areas, medium pore volumes, and mesopores as summarized in Table 4.45.

Table 4.45 BET results of palladium catalysts supported on small carbon nanofibers.

Catalyst	BET surface area ($m^2\ g^{-1}$)	Pore volume ($cm^3\ g^{-1}$)	Pore diameter (nm)
Pd/sCNF	465	1.9	16.2
Pd/sCNF$_{-COOH}$	392	1.4	14.4
Pd/sCNF$_{HT}$	285	1.1	15.9
Pd/sCNF$_{-COOH\ HT}$	305	1.2	16.2

4.3.7.4 Results obtained by ICP-AES

The ICP-AES results of palladium catalysts supported on small carbon nanofibers have clearly exhibited a close ratio between theoretical and experimental percentages as summarized in Table 4.46.

Table 4.46 ICP-AES results of palladium catalysts supported on small carbon nanofibers.

Catalyst	Element	Theoretical %	Experimental %
Pd/sCNF	Pd	2	1.71
Pd/sCNF$_{\text{-COOH}}$	Pd	2	1.69
Pd/sCNF$_{\text{HT}}$	Pd	2	0.97
Pd/sCNF$_{\text{-COOH HT}}$	Pd	2	1.31

4.3.8 Palladium catalysts supported on FC, FC_{-COOH}, FC_{HT}, and $FC_{-COOH\ HT}$ characterized by TEM, XRPD, BET, and ICP-AES

4.3.8.1 Results obtained by TEM

The TEM micrographs of palladium catalysts supported on fibrous carbons have showed a great palladium dispersion and a palladium particle size distribution ranging from 0.1 to 8.0 nm as shown in Figure 4.69.

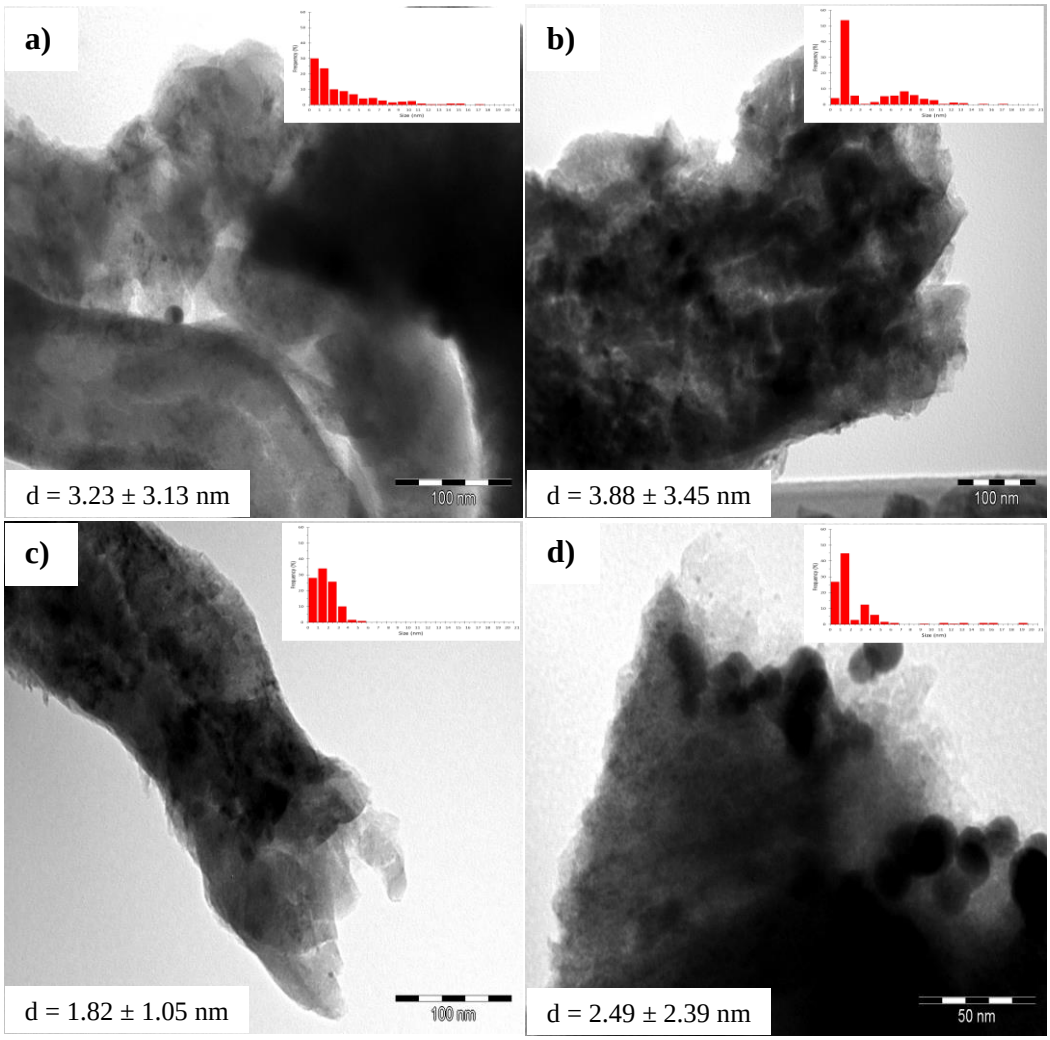

Figure 4.69 TEM micrographs of palladium catalysts supported on fibrous carbons. a) Pd/FC, b) Pd/FC_{-COOH}, c) Pd/FC_{HT}, and d) $Pd/FC_{-COOH\ HT}$.

4.3.8.2 Results obtained by XRPD

The XRD diffractograms of palladium catalysts supported on fibrous carbons have clearly indicated the presence of palladium metal as shown in Figure 4.70.

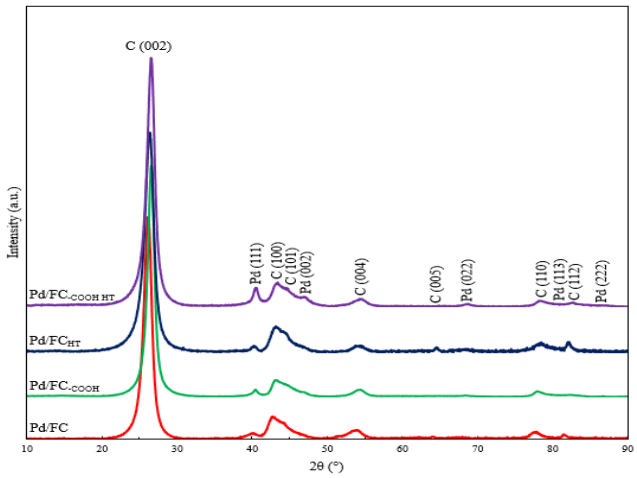

Figure 4.70 XRD diffractograms of palladium catalysts supported on fibrous carbons.

4.3.8.3 Results obtained by BET

The BET results of palladium catalysts supported on fibrous carbons have exposed high surface areas, small pore volumes, and mesopores as summarized in Table 4.47.

Table 4.47 BET results of palladium catalysts supported on fibrous carbons.

Catalyst	BET surface area ($m^2\ g^{-1}$)	Pore volume ($cm^3\ g^{-1}$)	Pore diameter (nm)
Pd/FC	140	0.4	11.7
Pd/FC_{-COOH}	186	0.4	9.6
Pd/FC_{HT}	138	0.5	13.8
$Pd/FC_{-COOH\ HT}$	232	0.5	9.3

4.3.8.4 Results obtained by ICP-AES

The ICP-AES results of palladium catalysts supported on fibrous carbons have clearly exhibited a close ratio between theoretical and experimental percentages as summarized in Table 4.48.

Table 4.48 ICP-AES results of palladium catalysts supported on fibrous carbons.

Catalyst	Element	Theoretical %	Experimental %
Pd/FC	Pd	2	1.50
Pd/FC_{-COOH}	Pd	2	2.05
Pd/FC_{HT}	Pd	2	1.49
$Pd/FC_{-COOH\ HT}$	Pd	2	1.61

4.3.9 Characterization data of all palladium catalysts

As shown above, all palladium catalysts were characterized by advanced characterization techniques, which have provided specific information that has allowed knowing the physical and chemical properties of palladium catalysts. Thus, we have performed a detailed comparison of characterization data of palladium catalysts to clearly understand the participation of palladium metal on carbon supports before using them as catalyst. Characterization data of palladium catalysts are summarized in Table 4.49.

Table 4.49 Characterization data of palladium catalysts.

Catalyst	Pd (%)	BET surface area ($m^2\ g^{-1}$)	Particle size[a)] (nm)	Particle size[e)] (nm)
Pd/CNT	1.60	158	2.2 ± 1.1	4.7
Pd/CNT_{HT}	1.60	146	3.1 ± 3.0	11.2
Pd/CNT_{-COOH}	2.04	232	2.2 ± 1.1	-
$Pd/CNT_{-COOH\ HT}$	1.89	203	2.1 ± 1.4	10.9
Pd/N-CNT	1.81	166	2.1 ± 0.9	-
$Pd/N\text{-}CNT_{HT}$	1.14	194	1.9 ± 1.8	12.0
$Pd/S_1\text{-}CNT$	1.82	50	1.8 ± 0.7	-
$Pd/S_1\text{-}CNT_{HT}$	0.94	50	2.6 ± 2.5	-
$Pd/S_2\text{-}CNT$	1.70	97	1.8 ± 0.8	-
$Pd/S_2\text{-}CNT_{HT}$	1.45	85	1.8 ± 0.9	-
Pd/FLG	1.76	43	3.3 ± 2.9	7.4
Pd/FLG_{HT}	1.66	84	2.5 ± 1.9	-
Pd/FLG_{-COOH}	1.87	50	2.6 ± 1.6	-
$Pd/FLG_{-COOH\ HT}$	1.51	79	2.8 ± 2.7	13.2
Pd/FC	1.50	140	3.2 ± 3.1[b)]	6.3
Pd/FC_{HT}	1.49	138	1.8 ± 1.0	-
Pd/FC_{-COOH}	2.05	186	3.9 ± 3.4[c)]	10.7
$Pd/FC_{-COOH\ HT}$	1.61	231	2.5 ± 2.4[d)]	9.4
Pd/CNF	1.65	104	2.0 ± 1.2	12.6
Pd/CNF_{HT}	1.18	67	2.1 ± 2.0	-
Pd/CNF_{-COOH}	1.70	82	1.6 ± 0.9	12.2
$Pd/CNF_{-COOH\ HT}$	1.41	71	1.9 ± 1.4	15.7
Pd/sCNF	1.71	465	2.5 ± 2.1	13.4
$Pd/sCNF_{HT}$	0.97	285	1.3 ± 1.1	12.1
$Pd/sCNF_{-COOH}$	1.69	392	1.5 ± 0.7	-
$Pd/sCNF_{-COOH\ HT}$	1.31	305	1.7 ± 1.6	12.6

a) From TEM. b) bimodal: 1.8 ± 1.2 and 8.7 ± 3.0 nm. c) bimodal: 1.5 ± 0.4 and 7.9 ± 2.4 nm.
d) bimodal: 1.2 ± 0.5 and 6.1 ± 4.3 nm. e) From XRD.

4.3.10 Palladium catalysts supported on SiO_2-Al_2O_3 characterized by ICP-AES, TEM, and BET

4.3.10.1 Results obtained by ICP-AES

The ICP-AES results of palladium catalysts supported on silica-alumina have clearly exhibited a close ratio between theoretical and experimental percentages as summarized in Table 4.50.

Table 4.50 ICP-AES results of palladium catalysts supported on silica-alumina.

Catalyst	Element	Theoretical %	Experimental %
Pd/SiO_2-$Al_2O_{3\ nc}$	Pd	2	1.91
Pd/SiO_2-$Al_2O_{3\ c}$	Pd	2	1.73

nc = no calcination. c = calcination (In air at 430 °C for 2 h).

4.3.10.2 Results obtained by TEM

The TEM micrographs of palladium catalysts supported on silica-alumina have showed a great palladium dispersion and a palladium particle size distribution ranging from 5 to 13 nm as shown in Figure 4.71.

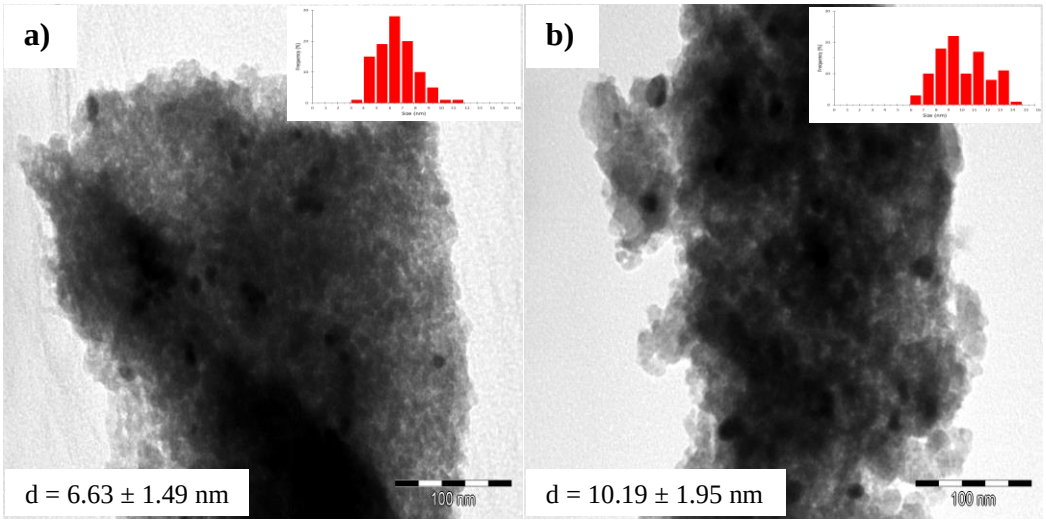

Figure 4.71 TEM micrographs of palladium catalysts supported on silica-alumina. a)Pd/SiO_2-$Al_2O_{3\ nc}$ and b)Pd/SiO_2-$Al_2O_{3\ c}$. nc = no calcination. c = calcination (In air at 430 °C for 2 h).

4.3.10.3 Results obtained by BET

The BET results of palladium catalysts supported on silica-alumina have exposed high surface areas, small pore volumes, and mesopores as summarized in Table 4.51.

Table 4.51 BET results of palladium catalysts supported on silica-alumina.

Catalyst	BET surface area ($m^2 g^{-1}$)	Pore volume ($cm^3 g^{-1}$)	Pore diameter (nm)
Pd/SiO_2-$Al_2O_{3\ nc}$	495	0.7	5.7
Pd/SiO_2-$Al_2O_{3\ c}$	558	0.8	5.8

nc = no calcination. c = calcination (In air at 430 °C for 2 h).

4.3.11 Nickel catalyst supported on Al_2O_3 characterized by ICP-AES, TEM, and BET

4.3.11.1 Results obtained by ICP-AES

The ICP-AES results of nickel catalyst supported on alumina has clearly exhibited a close ratio between theoretical and experimental percentages as summarized in Table 4.52.

Table 4.52 ICP-AES results of nickel catalyst supported on alumina.

Catalyst	Element	Theoretical %	Experimental %
Ni/Al_2O_3	Pd	10	6.15

4.3.11.2 Results obtained by TEM

The TEM micrographs of nickel catalyst supported on alumina have showed a great nickel dispersion as shown in Figure 4.72.

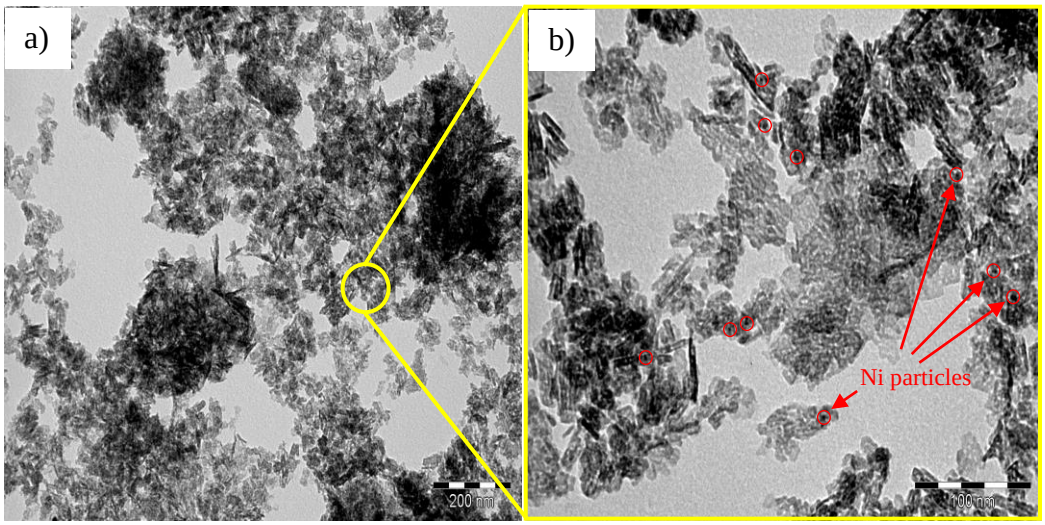

Figure 4.72 TEM micrographs of nickel catalyst supported on alumina. Scale bar: a) 200 nm and b) 100 nm.

4.3.11.3 Results obtained by BET

The BET results of nickel catalyst supported on alumina has exposed high surface area, small pore volumes, and mesopores as summarized in Table 4.53.

Table 4.53 BET results of nickel catalyst supported on alumina.

Catalyst	BET surface area ($m^2\ g^{-1}$)	Pore volume ($cm^3\ g^{-1}$)	Pore diameter (nm)
Ni/Al_2O_3	186	0.3	6.9

4.4 Summary

In this chapter, all characterization data for carbon supports and palladium catalysts are summarized. Various advanced characterization techniques were used to clearly understand the role of carbon supports and/or palladium catalysts before using them as catalyst supports and/or catalysts, respectively. All information obtained of carbon supports and/or palladium catalysts is an important resource before taking some decisions such as choice of the best catalyst, selection of the chemical reaction, and optimization of the reaction conditions using the best catalyst.

4.5 References

[1] A. Benyounes, M. Kacimi, M. Ziyad, P. Serp, Chinese Journal of Catalysis 35 (**2014**) 970-978.

[2] S. Louisia, R. Castro Contreras, M. Heitzmann, M. R. Axet, P.-A. Jacques, P. Serp, Catalysis Communications 109 (**2018**) 65-70.

CHAPTER V

Discussion

5.1 Introduction

The need to understand the catalyst behavior during its preparation and application is a very important issue for the catalytic community. In heterogeneous catalysis, the catalyst plays a significant role in a chemical reaction, being the heart of the catalytic process. High activity and selectivity towards the main product will depend on the catalyst up to 90 %. According to that, we have performed a detailed comparison of all results obtained of our carbon supports and palladium catalysts by using advanced characterization techniques. Therefore, the best catalyst will be selected through its physicochemical properties such as porosity, surface area, pore volume, active phase loading and dispersion, metal particle size, and attrition resistance.

To clearly understand the structural order of this Chapter V: Discussion, the main issues are summarized in Table 5.1.

Table 5.1 Main issues of Chapter V.

Issues
5.2 Understanding the surface chemistry of carbon materials
5.3 Understanding the metal-support interaction of palladium catalysts
5.4 Summary
5.5 References

5.2 Understanding the surface chemistry of carbon materials

5.2.1 Morphology, elemental distribution, and chemical composition of unsupported catalysts by SEM

The results obtained by SEM, have provided important information about the unsupported catalysts. According to that, the contrasting analyses (see Figure 4.2) performed on $AlCoFeO_4$, $NiFe_2O_4$, $CoFe_2O_4$, and $Cu_{0.1}Ni_{0.9}Co_2O_4$ catalysts, have revealed the same chemical composition everywhere for all them.

5.2.2 Morphology of carbon materials by HRTEM and LRTEM

Carbon nanomaterials are clearly observed by using transmission electron microscopy (TEM). High and low resolution have allowed making a detailed study on the morphological characteristics of the carbon nanomaterials, which present differences between them. These structural changes such as arrangement of the graphene layers, particular markings, surface damages, and kind of edges, are mainly originated by the preparation method. The detailed study performed on the carbon nanomaterials has provided a broad knowledge of the morphological characteristics, allowing their identification under certain parameters such as dimensions (width, length, and height), shape (square, rectangle, or cylinder), graphene layer angle with respect to the filament axis (from 0 to 90 °), and edges (open, close or mixed open-close). But, this identification is only possible reading TEM micrographs of high and low resolution as shown in next paragraphs.

TEM micrographs of carbon materials are shown in Figure 5.1. Carbon materials can be distinguished according to their morphology. The graphene layers are oriented in different ways to originate unique carbon structures depending on some parameters such as kind of catalyst using as starting material and reaction temperature during the synthesis.

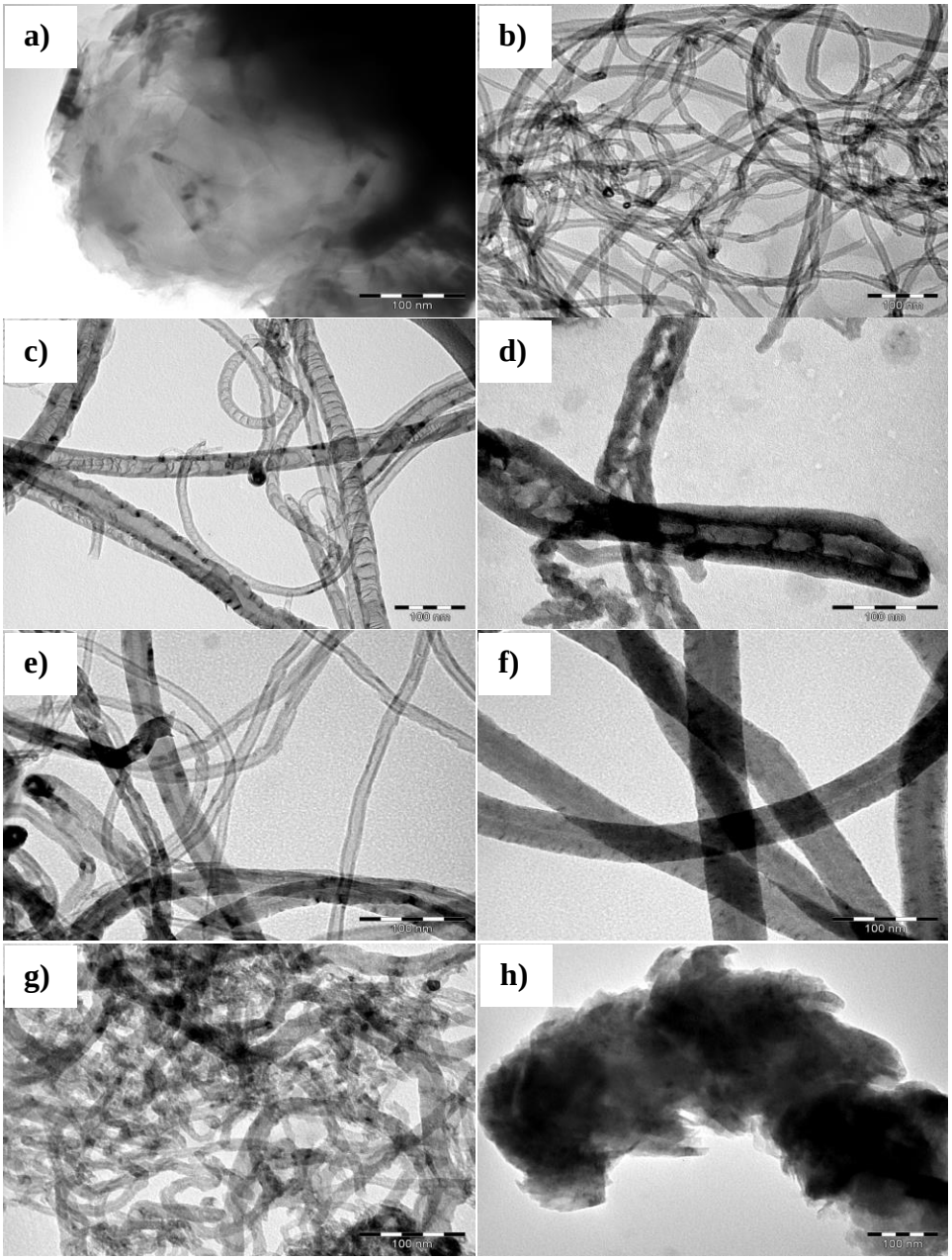

Figure 5.1 TEM micrographs of carbon materials. a) FLG, b) CNT, c) N-CNT, d) S_1-CNT, e) S_2-CNT, f) CNF, g) sCNF, and h) FC. Scale bar for all micrographs: 100 nm.

Besides, HRTEM micrographs of carbon materials have revealed unique characteristics, which allow identifying to carbon materials depending on the arrangement of their graphene layers. According to that, the filamentous carbon materials such as CNT and S_2-CNT present graphene layers parallel to the filament axis, and N-CNT, CNF, sCNF, and FC present an angle between filament axis and graphene layers. The average angle with respect to the filament axis is different, 20°, 26°, 40° and 90° for N-CNT, CNF, sCNF and FC, respectively. These structural arrangements are showed in Figure 5.2

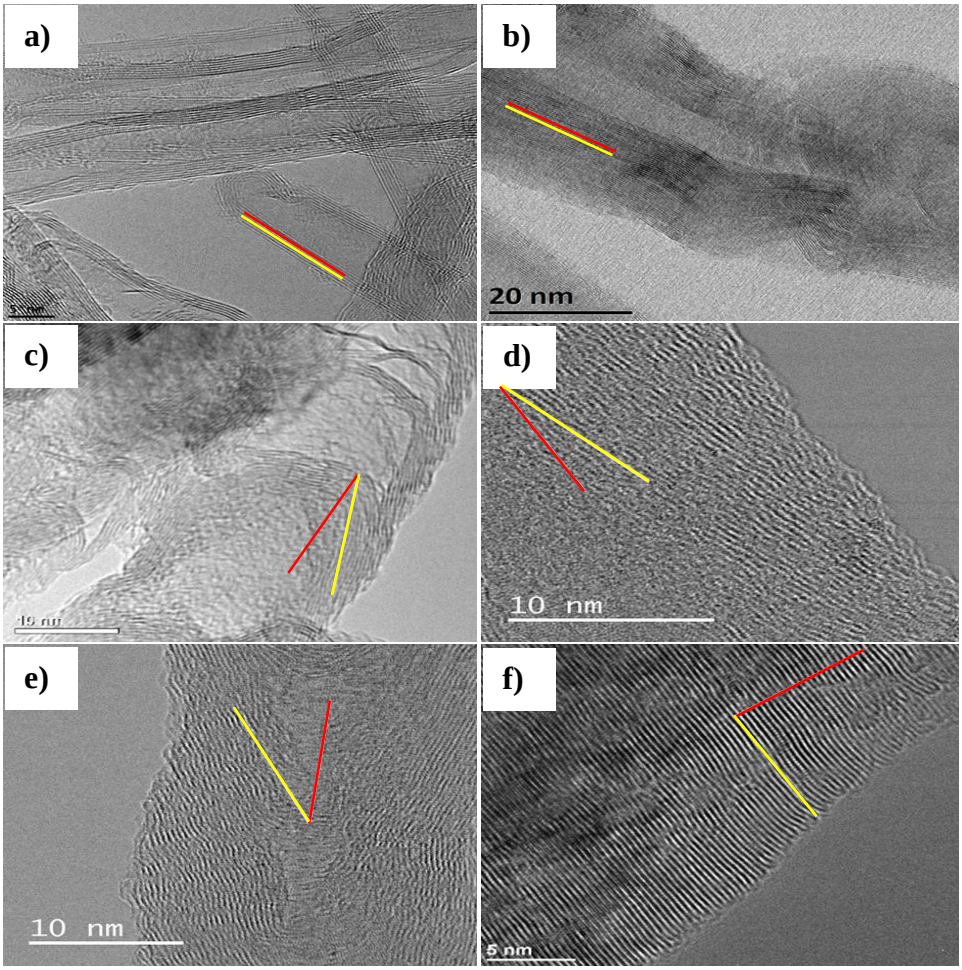

Figure 5.2 HRTEM micrographs of carbon materials. a) CNT (scale bar 5 nm), b) S_2-CNT (scale bar 20 nm), c) N-CNT (scale bar 10 nm), d) CNF (scale bar 10 nm), e) sCNF (scale bar 10 nm), and f) FC (scale bar 5 nm). Red line: filament axis. Yellow line: graphene layer.

Also, the N-CNT (bamboo structures), S_1-CNT (branched tube structures), and S_2-CNT (bulbous segments) compared to pristine CNT (tube structures) present differences between them, being possible the identification of each one as shown in Figure 5.3.

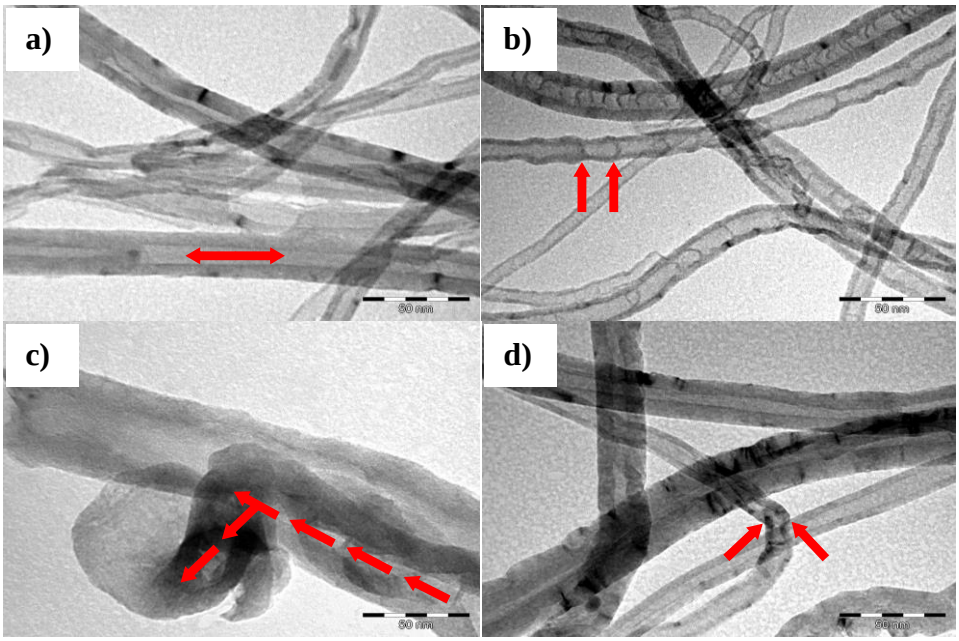

Figure 5.3 TEM micrographs of carbon materials. a) CNT, b) N-CNT, c) S_1-CNT, and d) S_2-CNT. Scale bar of all micrographs: 50 nm.

After the purification treatment of carbon materials, we independently checked that the post-treatments have no significant effect on the general morphology of these carbon materials, at the exception of HNO_3 treatment that creates some surface damages, particularly for small diameter CNT. These surface damages on CNT_{-COOH} are showed in Figure 5.4.

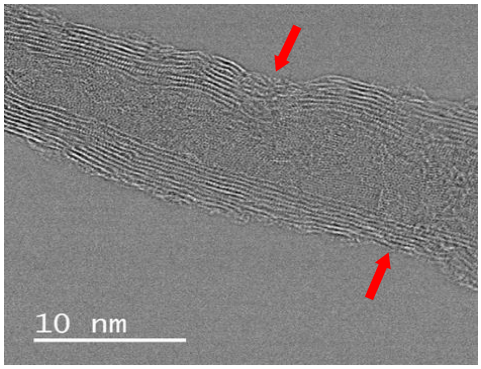

Figure 5.4 HRTEM micrograph of CNT_{-COOH}. Scale bar: 10 nm.

Furthermore, for some carbon materials as FC, the surface is mainly composed of edges. Therefore, it is reasonable to propose that some of the graphene edges are likely to be closed. For open edges, they may be easily terminated by -OH or -COOH under ambient conditions, or more likely by –H. Both close and open edges are shown in Figure 5.5.

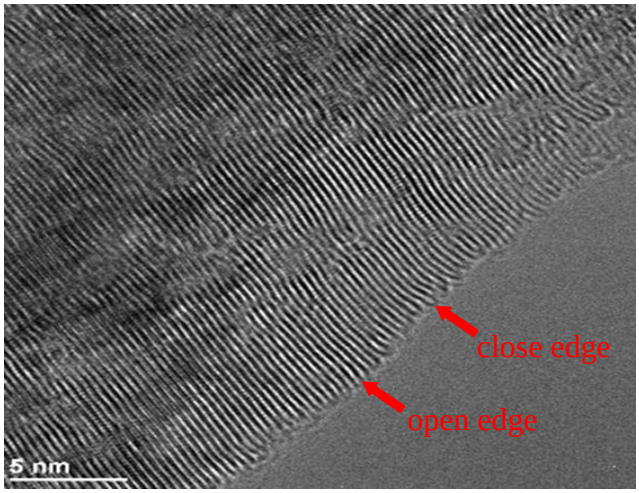

Figure 5.5 HRTEM micrograph of close and open edges of fibrous carbon. Scale bar: 5 nm.

Considering the structure of these carbon materials, it is very likely that the carbon edges end in CH_2/CH_3 or aromatic C-H groups. [3]

In the case of CNF, disordered carbon can also be seen at their surface. The surface of this support is composed by a mixture of edges and disordered carbon (curved surfaces [4]). This structure is similar to the one of the hollow vapor grown CNF from Pyrograf Products that shows a dual-wall structure. In that industrial material, the core layer is a catalytically-grown hollow fishbone-type carbon fiber, whereas the outer layer consists of disordered, pyrolytically grown walls, parallel to the main axis of the fiber. [5] The CNF surfaces with or without a dual-wall structure are shown in Figure 5.6.

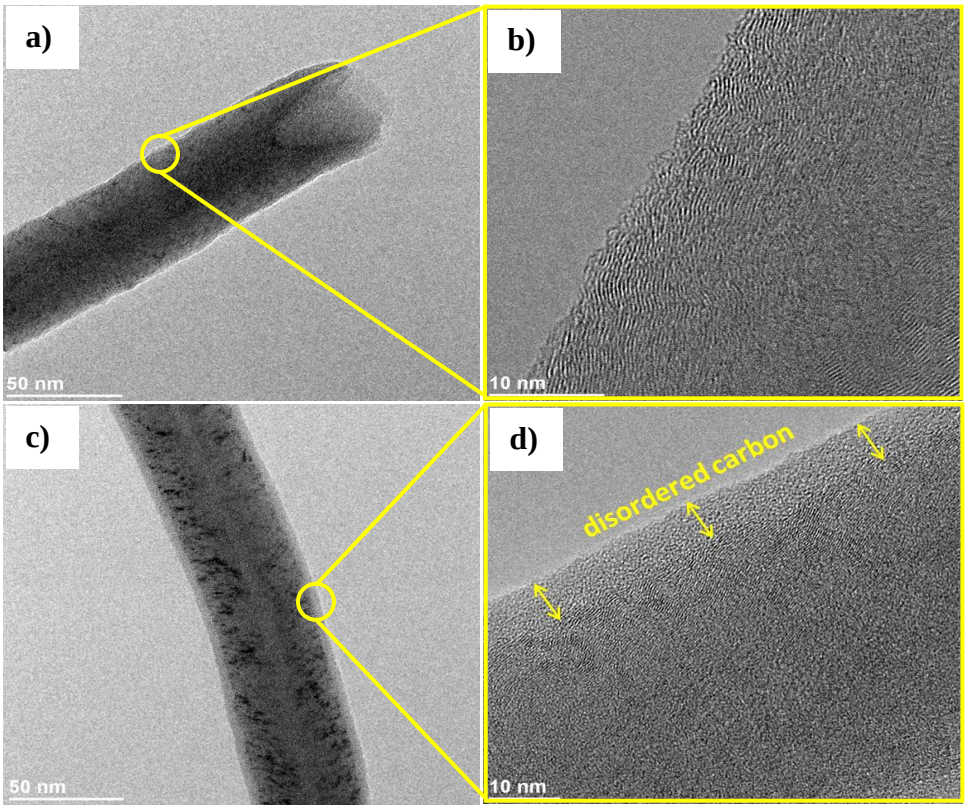

Figure 5.6 TEM micrographs of a) CNF without a dual-wall structure (scale bar 50 nm), b) CNF without a dual-wall structure (scale bar 10 nm), c) CNF with a dual-wall structure (scale bar 50 nm), and d) CNF with a dual-wall structure (scale bar 10 nm).

The mean external diameter of CNF is 50 nm, and their mean inner diameter 6 nm. The CNT are multi-walled CNT, with an average external diameter of 15 nm and an internal diameter of 7 nm. The tubes are made up of 5-10 graphene layers. N-CNT, [6] S_1-CNT and S_2-CNT [7] have mean external diameters of 18, 15, and 50 nm, respectively. The different diameters between S_1-CNT and S_2-CNT come from their preparation method (see Chapter III: Methodology, sections: 3.7.2.1.1.2 and 3.7.2.1.1.3). The FC shows a quite broad diameter size distribution, ranging from 50 to 400 nm with an average diameter of about 100 nm. The FLG consists in graphitic flakes of turbostratic carbon of around 1 μm^2; the number of graphene layers ranged between 5 and 20. [8]

5.2.3 Elemental composition of carbon materials by elemental analysis

According to the elemental analyses, high levels of purity are achieved for all carbon materials (see Tables 4.4, 4.7, 4.10, 4.19, 4.22, and 4.25), at the exception of S_1-CNT and S_2-CNT (see Tables 4.13 and 4.16), which contain significant amounts of residual catalyst. This should be connected to the slow growth of these kinds of nanotubes. [7]

5.2.4 Effect of nitric acid oxidation in carbon materials by TGA and XPS analyses

The treatment with nitric acid, for a given type of material, allows decreasing the amount of residual catalyst, as shown by the TGA analyses, where a decrease of the residue amount is notices after this treatment. This decrease of residual catalyst is shown in Figure 5.7.

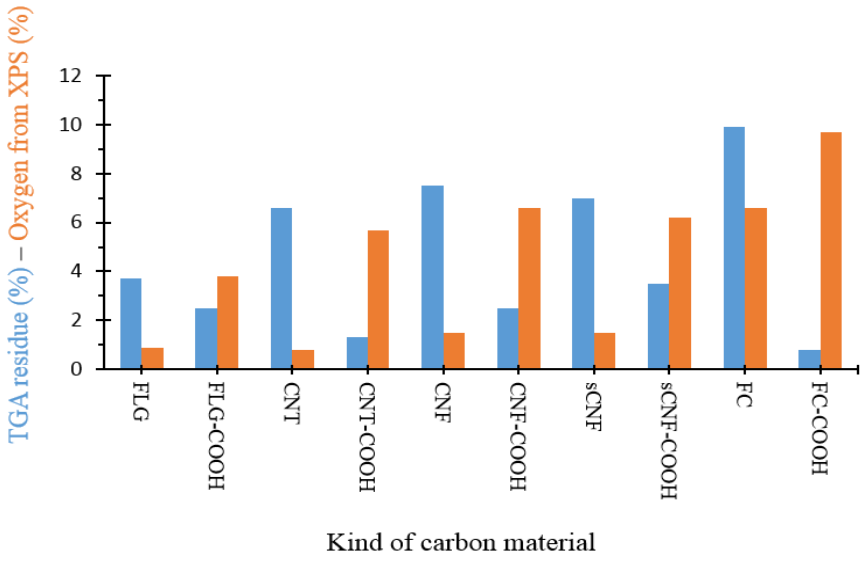

Figure 5.7 Evolution of the amount of catalyst residue (from TGA) and the percentage of surface oxygen (from XPS) with the nitric acid treatment. Blue bars: TGA residue. Orange bars: oxygen from XPS.

Another effect of the HNO_3 treatment is to significantly increase the amount of surface oxygen, as revealed by XPS (see Table 4.28 and Figure 5.7). This does not significantly affect the temperature of decomposition of these carbon materials (see Figures 4.6, 4.12, 4.35, 4.41, and 4.47).

The introduction of N or S in the carbon structure via doping, results in its part to a higher reactivity of the materials towards air oxidation; as shown by the TGA results (see Table 4.28 and Figures 4.18, 4.23, and 4.29).

The XPS analysis has also shown that, as expected, the high temperature treatment allows decreasing significantly the amount of surface heteroatoms (O, N or S). For the non-functionalized supports (FLG, CNT, CNF, sCNF and FC), this treatment also results in an increased stability of the materials, as shown by the TGA analyses. This increased stability of the materials is shown in Figure 5.8.

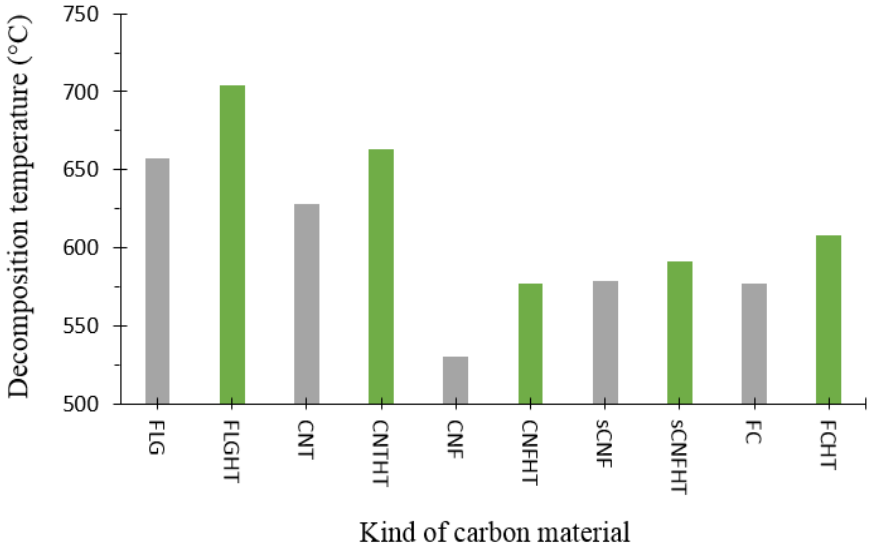

Figure 5.8 Decomposition temperature (from TGA) of pristine and heat-treated carbon materials. Gray bars: pristine carbon materials. Green bars: heat-treated carbon materials.

In that case, this treatment results in a surface reconstruction that produces a less reactive surface. The same phenomenon is not systematically observed for the functionalized carbons (oxidized materials and S- or N-doped CNTs); so for these materials the surface reconstruction does not provide a less reactive surface.

5.2.5 BET surface area and pore volume of carbon materials by physisorption analysis

The textural properties of the supports have been evaluated from the nitrogen adsorption/desorption isotherms. These carbon materials present pore volumes of 0.2-4.1 $cm^3.g^{-1}$ and are predominantly mesoporous (see Table 4.28). For the filamentous carbons, the pores are arising from interstices between entangled fibers or tubes. The specific surface area of the supports ranged between 40 and 300 $m^2\ g^{-1}$ (see Table 4.28). Their N_2 adsorption isotherms are typical of IV. The lowest surface area was measured for FLG (40 $m^2\ g^{-1}$), and the highest for $sCNF_{-COOH}$ (296 $m^2\ g^{-1}$). At the exception of CNF, the HNO_3 treatment generally results in an increase of the S_{BET}. A little change in surface area was also observed by Pittman *et al*. by N_2 BET for vapor-grown carbon nanofibers, [9] confirming our findings. For CNTs, S_{BET} increases after HNO_3 treatments have already been reported, which are associate to tube tips opening. [10] The high temperature treatment induces different effects on the S_{BET}, according to the materials. For CNTs, FLG, and CNF a slight increase in S_{BET} is generally observed after the heat treatment. Such a phenomenon has already been observed for CNT, and has been attributed to the removal of surface functional groups during the heat-treatment that could create some porosity. [11] Interestingly, materials such as CNF, sCNF and FC, for which surface is mainly composed from edges, behave differently.

In that case, the heat-treatment induces a significant decrease of the S_{BET} for the pristine materials, and has no effect on the oxidized materials. It has been shown that the graphitization of CNF does not affect their morphology, but contributes to the formation of loops to connect the edges of the graphene sheets. [12-14] A decrease of CNF S_{BET} after heat-treatment has already been observed, [15, 16] which could be associated with the increase of the degree of structural order as a consequence of the removal of the structural defects.

5.2.6 Correlation between TGA and BET results and XRD analysis

The d_{002} graphene interlayer distance and the average stacking height parallel to the fiber axis, L_c, as found from XRD are shown in Table 4.28. The highest intensity of the graphite (002) peak ($2\theta = 26°$) and thereby d_{002} values close to the value for graphite (0.335 nm) was seen for the FLG, FC and sCNF samples. The higher amount of macro-sized defects indicated by a lower L_c can be correlated with a higher S_{BET} and a higher reactivity (lower decomposition temperature in air oxidation) of the materials (see Figure 5.9). Similar tendencies were reported for carbon blacks [17] and carbon fibers. [18]

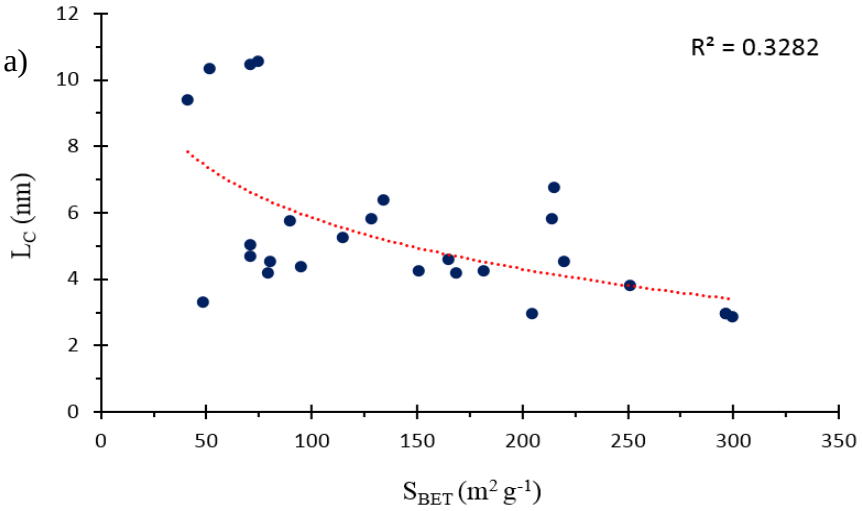

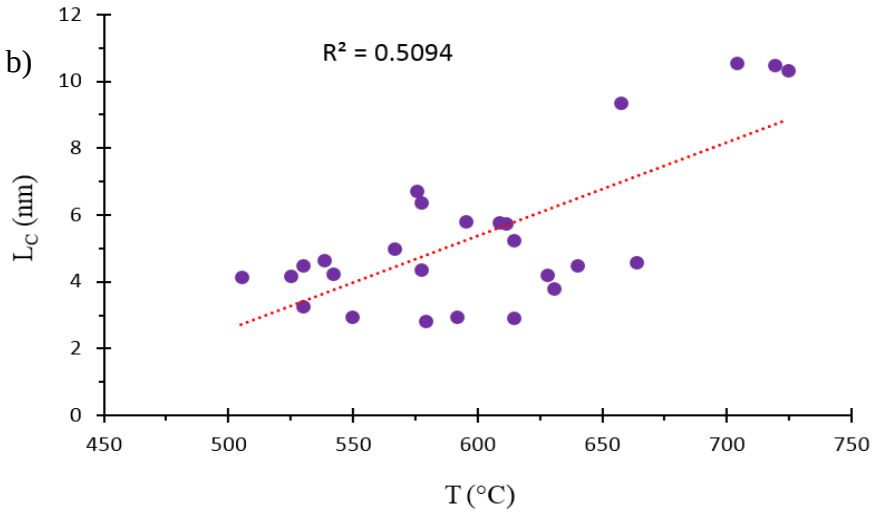

Figure 5.9 Evolution of: a) S_{BET} and b) Decomposition temperature (from TGA) for the carbon materials with the L_c value (from XRD).

5.2.7 Correlation between Raman parameters and XPS and XRD analyses

The XPS and Raman characterizations of the carbon materials are reported in Tables 4.29, 4.30, and 4.49. Raman spectroscopy is extensively used for investigating, and quantitatively and qualitatively measuring structural disorder in carbonaceous materials. [19, 20] In spite of these advantages, Raman spectroscopy has certain inherent limitations in detecting in these materials defects such as charged impurities, perfect zigzag edges, intercalants, uniaxial and biaxial strain, as they do not manifest as defect band (D band). Furthermore, the defects caused by surface functional groups also do not leave any significant footprints in Raman spectra. XPS, in addition to ascertain chemical composition and bonding environment, can also provide useful information about defects and disorder in carbonaceous materials. [21] The presence of defects and functional groups in these materials introduce new peaks and alter the peak position and line width of C1s peak.

The best fit for the main C1s spectrum was obtained by deconvoluting the profile into seven Gaussian line shapes and their respective parameters are given in Table 4.29. The peak I at around 283.7 eV is attributed to the presence of point defects, which could arise from C vacancies, pentagon and heptagon rings, Stone-Wales defects, or formation of fullerene like structures. [22-24] The peak II at 284.6 eV, represents sp^2 C−C bonds in the regions containing only unmodified C rings at the surface or in subsurface layers. The peak III at 285.1-285.2 eV was assigned to sp^3 carbon species. [25] The peaks at 286.0-286.2 (IV), 287.3-287.5 (V) and 288.4-289.2 eV (VI), correspond to carbon atoms attached to different oxygen-containing moieties. [26, 27] Finally, the π–π∗ transition loss peak was detected at 290.6-291.2 eV; it typically comprised 15-18 % of the total sp^2 signal. The full width at half-maximum (FWHM) of the C1s peak has been used to assess the graphitic nature of carbons, with a larger FWHM corresponding to a more disordered structure. [28]

A reasonable correlation was observed between the L_c (from XRD) and the FWHM as shown in Figure 5.10.

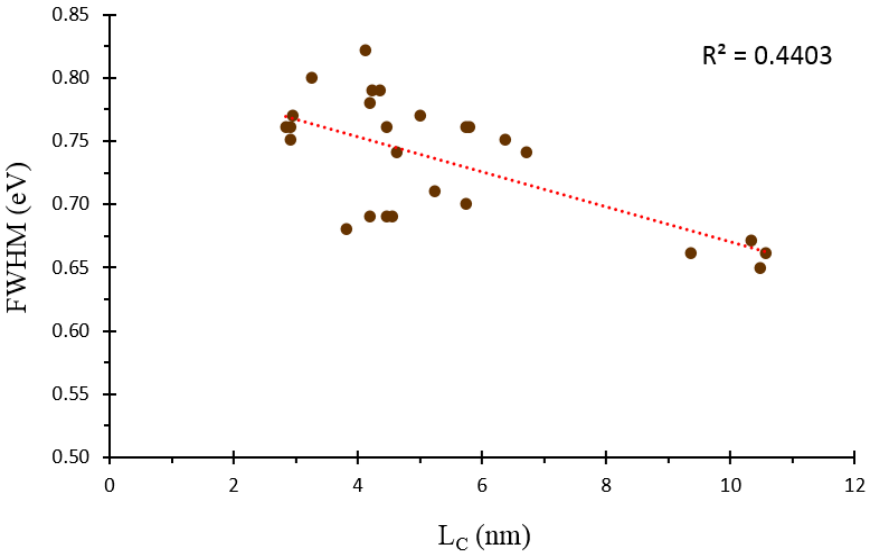

Figure 5.10 Evolution of the FWHM from XPS C1s peak and the L_c from XRD.

Raman spectroscopy was also used to evaluate the degree of structural order of the different carbon materials. It is complementary to XRD although it has the advantage of surface specificity, thus allowing the study of very heterogeneous materials. The most important parameter calculated with this technique is the ratio of the integrated intensities of the D band (I_D) at ~1380 cm^{-1}, attributed to the defects of the graphitic structure, and the G band (I_G) at ~1580 cm^{-1}, which is ascribed to a graphitic (ordered) structure, both bands belonging to the first-order Raman spectrum for carbon materials. Obviously, the graphitic character will reduce the intensity of the D band, therefore decreasing the I_D/I_G ratio. The degree of structural order estimated by this technique possesses a bi-dimensional character, being strongly dependent on the orientation of the crystallites, whereas in the case of XRD it has a three-dimensional nature.

Disorder is also responsible for the changes in the intensities of other bands, such as D′ and G′, and also affects the position and shape of the Raman peaks. The G' band is indicative of long-range order in a sample and arises from the two-phonon, second-order scattering process that results in the creation of an inelastic phonon. [29, 30] Finally, another parameter measurable by Raman spectroscopy, which is relevant to catalyst preparation is the L_D; L_D is a typical inter-defect distance, with the defect being a point-like (zero-dimensional) structure. [31] Correlations between the L_C and the Raman parameters are showed in Figure 5.11.

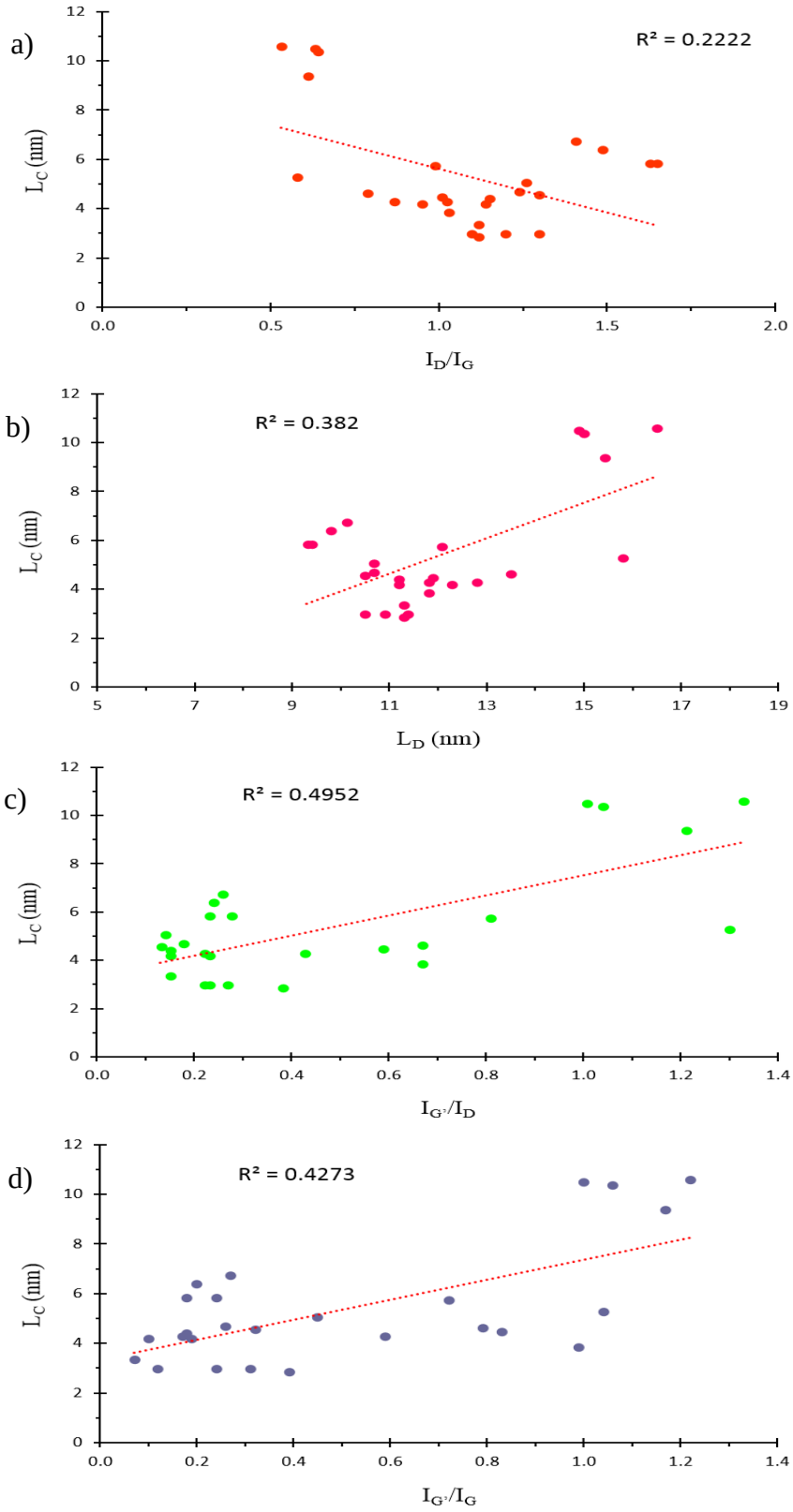

Figure 5.11 Evolution of L_c from XRD with Raman parameters: a) I_D/I_G, b) L_D, c) $I_{G'}/I_D$, and d) $I_{G'}/I_G$.

The best correlations were obtained based on L_D and $I_{G'}/I_G$. A comparative study on defect estimation using XPS and Raman spectroscopy in few layer nano-graphitic structures has shown nice correlations in estimating defect density between these two techniques, in general. [22] In our case, the best correlations were found between the $I_{G'}/I_G$ and the FWHM of the C1s peak of the sp^2 carbon as shown in Figure 5.12.

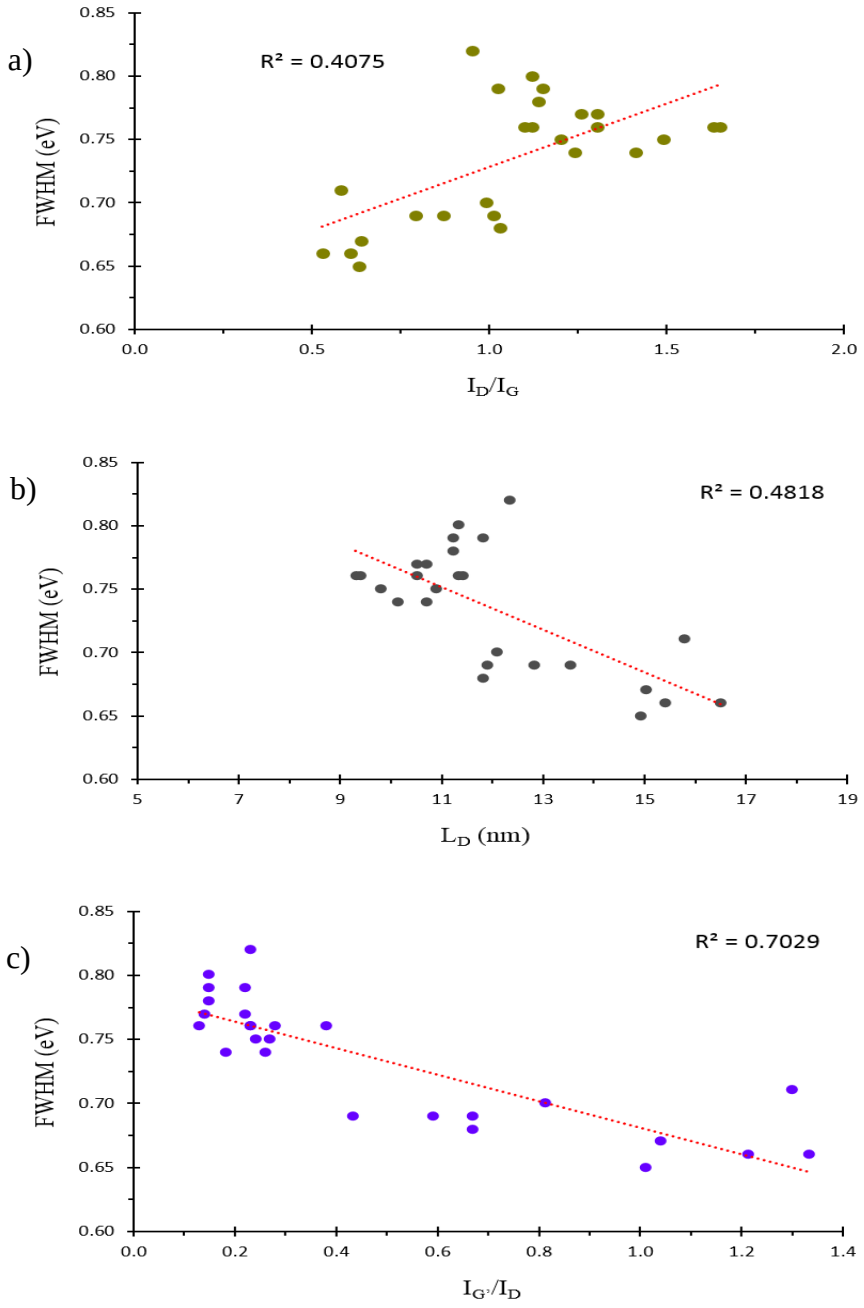

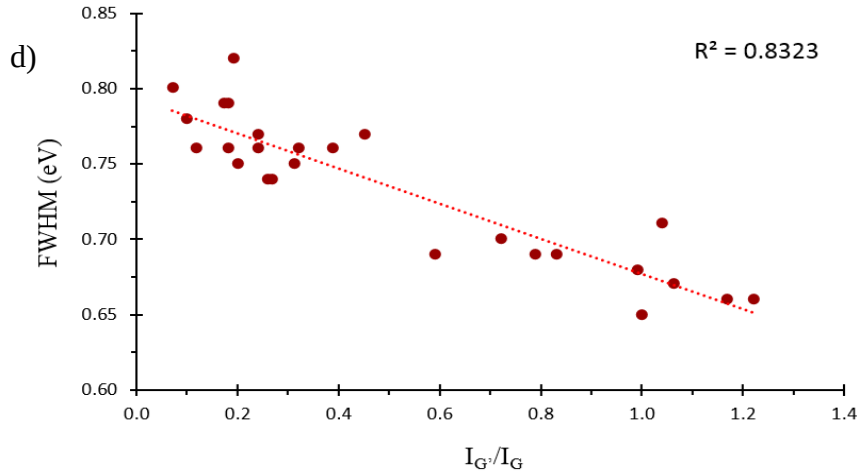

Figure 5.12 Evolution of the FWHM of the C1s sp^2 carbon peak from XPS with Raman parameters: a) I_D/I_G, b) L_D, c) $I_{G'}/I_D$, and d) $I_{G'}/I_G$.

The correlation between the I_D/I_G and the % of sp^2 carbon from XPS as shown in Figure 5.13.

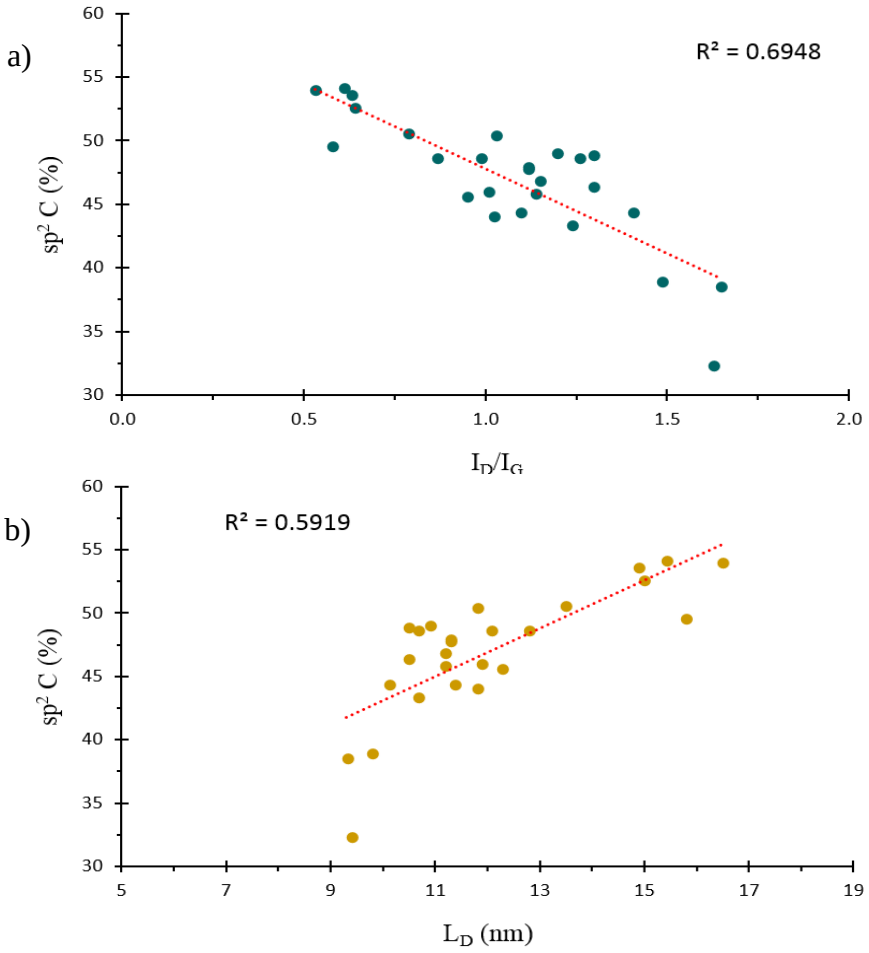

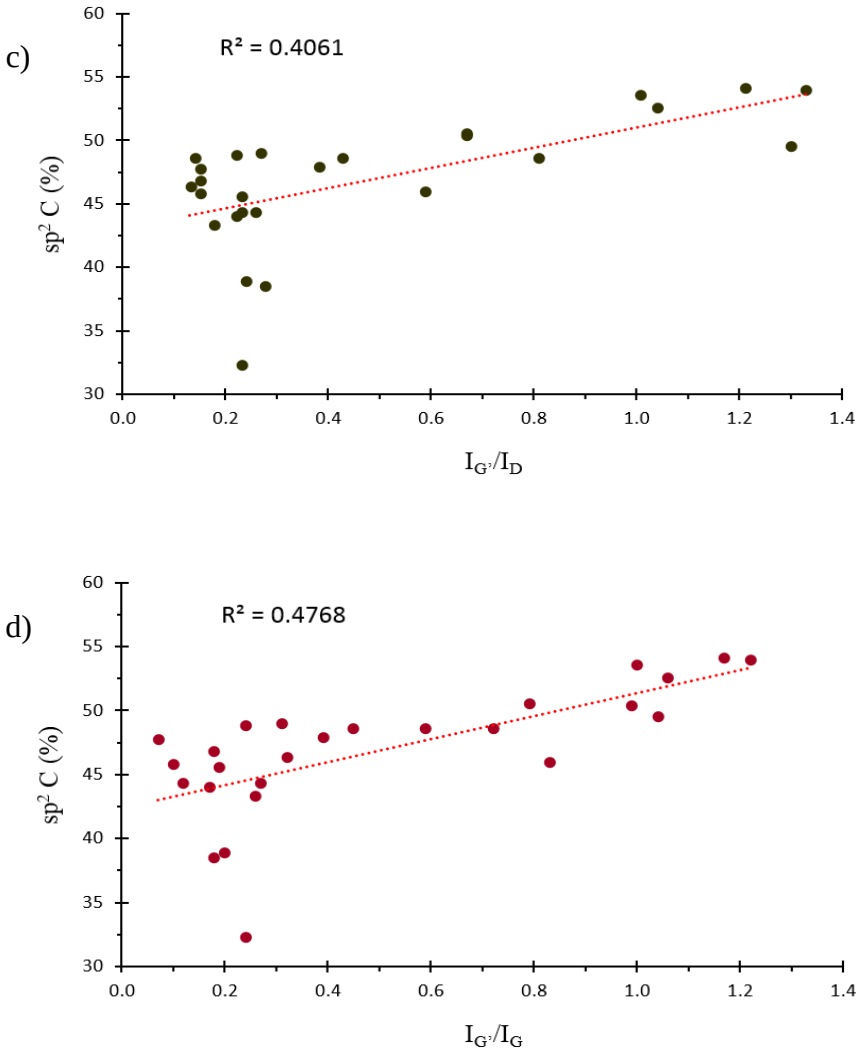

Figure 5.13 Evolution of the % of sp^2 carbon from XPS with Raman parameters: a) I_D/I_G, b) L_D, c) $I_{G'}/I_D$, and d) $I_{G'}/I_G$.

5.2.8 The best correlations of carbon materials by XPS, Raman, and TGA analyses

A comparison of Figures 5.11-5.13 shows that the best correlations were obtained between XPS and Raman analyses. Thus, we decide to use these two techniques to try to classify the numerous carbon materials investigated. Figure 5.14 shows the classification of the supports according to Raman and XPS parameters.

a)

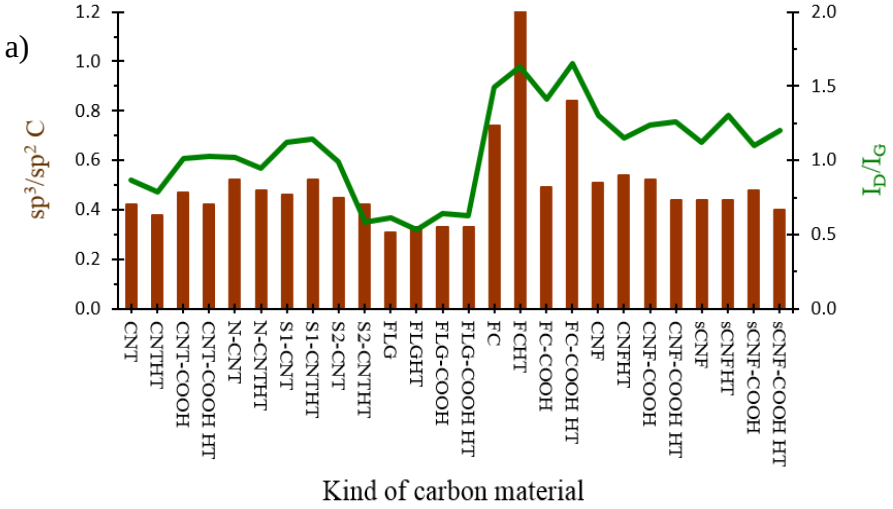
sp³/sp² C
I_D/I_G
Kind of carbon material
CNT
CNTHT
CNT-COOH
CNT-COOH HT
N-CNT
N-CNTHT
S1-CNT
S1-CNTHT
S2-CNT
S2-CNTHT
FLG
FLGHT
FLG-COOH
FLG-COOH HT
FC
FCHT
FC-COOH
FC-COOH HT
CNF
CNFHT
CNF-COOH
CNF-COOH HT
sCNF
sCNFHT
sCNF-COOH
sCNF-COOH HT

b)

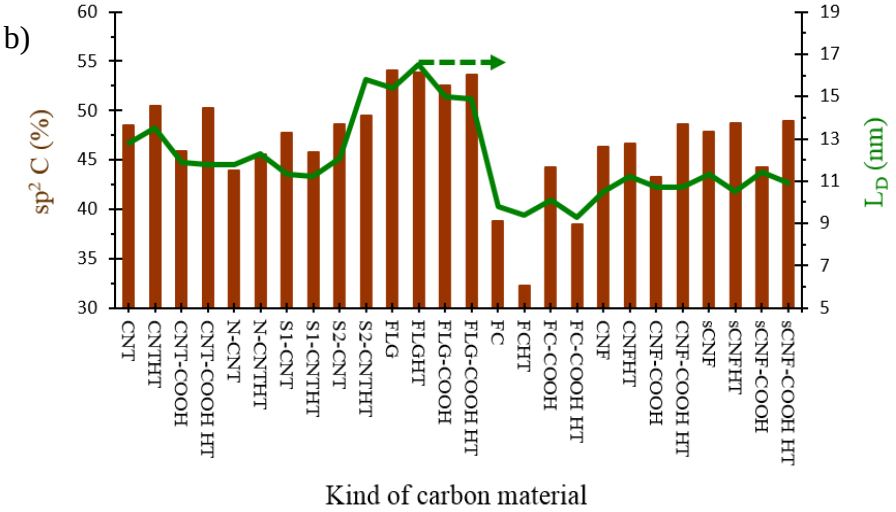
sp² C (%)
L_D (nm)
Kind of carbon material
CNT
CNTHT
CNT-COOH
CNT-COOH HT
N-CNT
N-CNTHT
S1-CNT
S1-CNTHT
S2-CNT
S2-CNTHT
FLG
FLGHT
FLG-COOH
FLG-COOH HT
FC
FCHT
FC-COOH
FC-COOH HT
CNF
CNFHT
CNF-COOH
CNF-COOH HT
sCNF
sCNFHT
sCNF-COOH
sCNF-COOH HT

c)

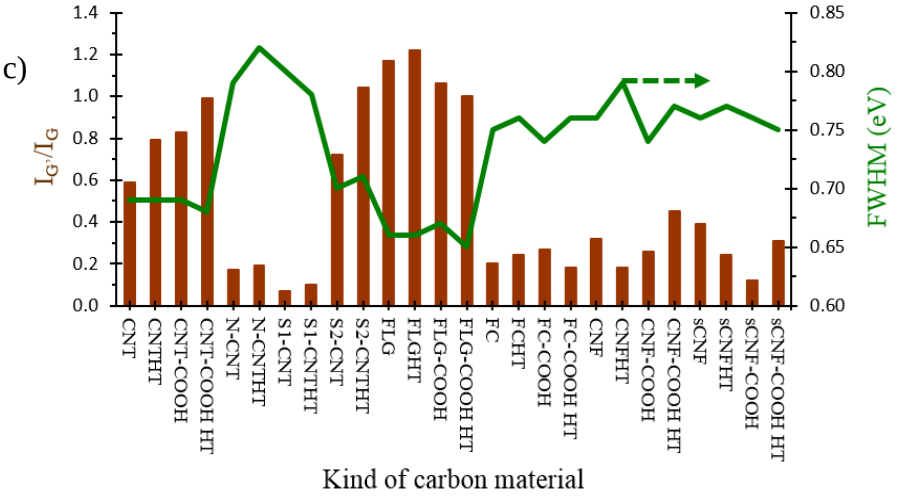
I_G'/I_G
FWHM (eV)
Kind of carbon material
CNT
CNTHT
CNT-COOH
CNT-COOH HT
N-CNT
N-CNTHT
S1-CNT
S1-CNTHT
S2-CNT
S2-CNTHT
FLG
FLGHT
FLG-COOH
FLG-COOH HT
FC
FCHT
FC-COOH
FC-COOH HT
CNF
CNFHT
CNF-COOH
CNF-COOH HT
sCNF
sCNFHT
sCNF-COOH
sCNF-COOH HT

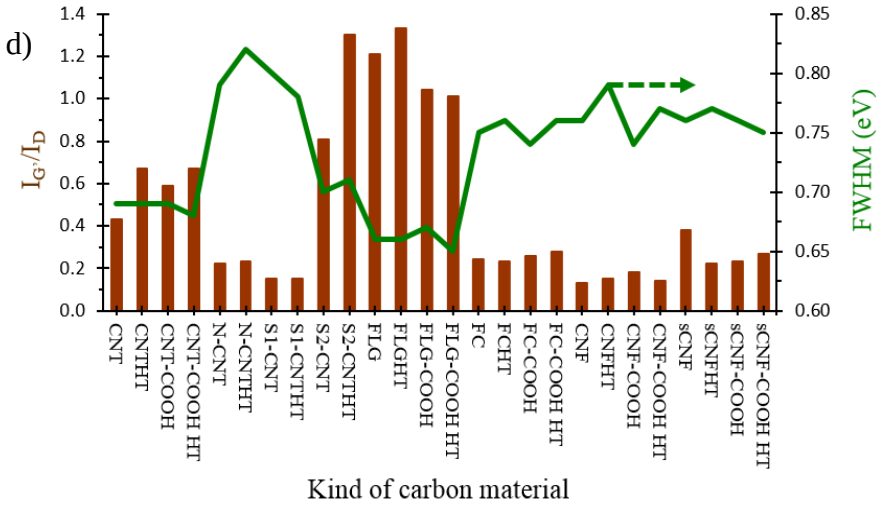

Figure 5.14 Carbon supports classified according to: a) sp^3/sp^2 carbon ratio from XPS and I_D/I_G from Raman, b) % of sp^2 carbon from XPS and L_D from Raman, c) $I_{G'}/I_G$ from Raman and the FWHM of the C1s peak from XPS, and d) $I_{G'}/I_D$ from Raman and the FWHM of the C1s peak from XPS. Brown bars: sp^3/sp^2 C, sp^2 C, $I_{G'}/I_G$, and $I_{G'}/I_D$. Green broken line: I_D/I_G, L_D, and FWHM.

From Figures 5.14a and 5.14b, two groups of materials present different characteristics, from one side FLG and CNT (pristine or doped with nitrogen or sulfur), which present less defects (low I_D/I_G or sp^3/sp^2 ratio) and a relatively large L_D, and on the other side the FC, CNF, and sCNF with opposite trends in their characteristics. However, the more interesting classification is seen on Figure 5.14c and 5.14d, where differences in long-range order appears more clearly with the $I_{G'}/I_G$ (or $I_{G'}/I_D$) and FWHM parameters. From this figure, it is clear that FLG, pristine CNT and S_2-CNT present very different characteristics than the other materials. On these carbon supports, significantly higher degree of long-range order is expected. This long-range order has a significant influence on the resistance of the materials towards air oxidation; indeed we find a very good correlation between the $I_{G'}/I_G$ (or $I_{G'}/I_D$) or FWHM values and the decomposition temperature obtained during the TGA experiments as shown in Figure 5.15.

a)

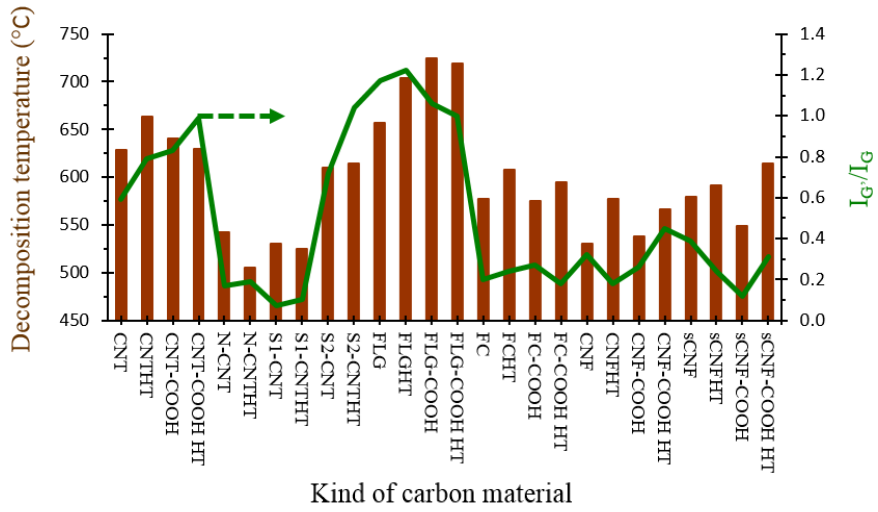
Decomposition temperature (°C)
$I_{G'}/I_G$
Kind of carbon material
CNT
CNTHT
CNT-COOH
CNT-COOH HT
N-CNT
N-CNTHT
S1-CNT
S1-CNTHT
S2-CNT
S2-CNTHT
FLG
FLGHT
FLG-COOH
FLG-COOH HT
FC
FCHT
FC-COOH
FC-COOH HT
CNF
CNFHT
CNF-COOH
CNF-COOH HT
sCNF
sCNFHT
sCNF-COOH
sCNF-COOH HT

b)

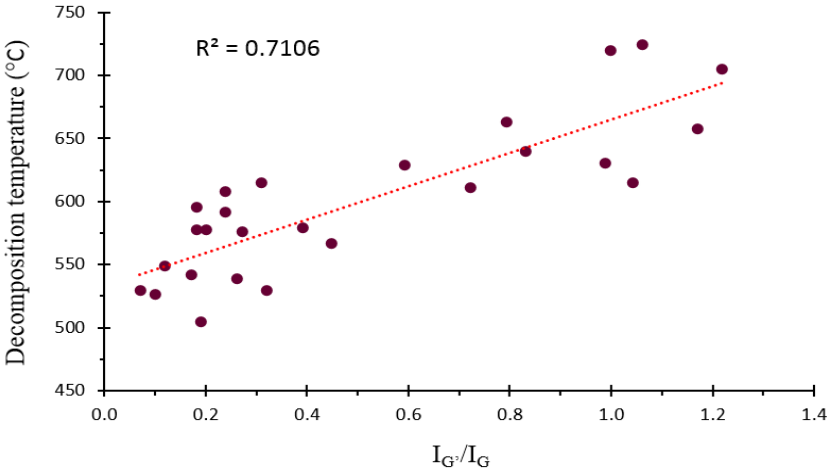
R² = 0.7106
Decomposition temperature (°C)
$I_{G'}/I_G$

c)

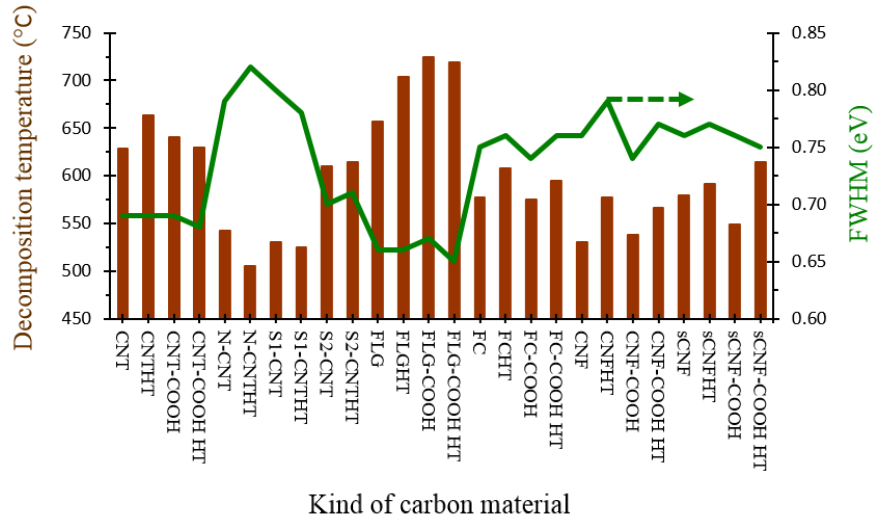
Decomposition temperature (°C)
FWHM (eV)
Kind of carbon material
CNT
CNTHT
CNT-COOH
CNT-COOH HT
N-CNT
N-CNTHT
S1-CNT
S1-CNTHT
S2-CNT
S2-CNTHT
FLG
FLGHT
FLG-COOH
FLG-COOH HT
FC
FCHT
FC-COOH
FC-COOH HT
CNF
CNFHT
CNF-COOH
CNF-COOH HT
sCNF
sCNFHT
sCNF-COOH
sCNF-COOH HT

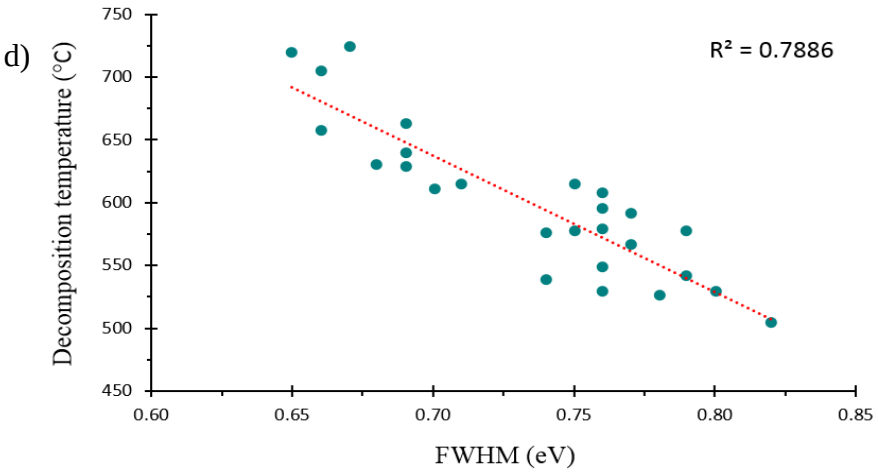

Figure 5.15 Evolution of the decomposition temperature of carbon materials (from TGA) with: a-b) the $I_{G'}/I_G$, and c-d) the FWHM of the C1s peak from XPS. Brown bars: decomposition temperature. Green broken line: $I_{G'}/I_G$ and FWHM.

Such correlations were not so good if we consider parameters such as the L_C (from XRD), the I_D/I_G or the L_D values as shown in Figure 5.16.

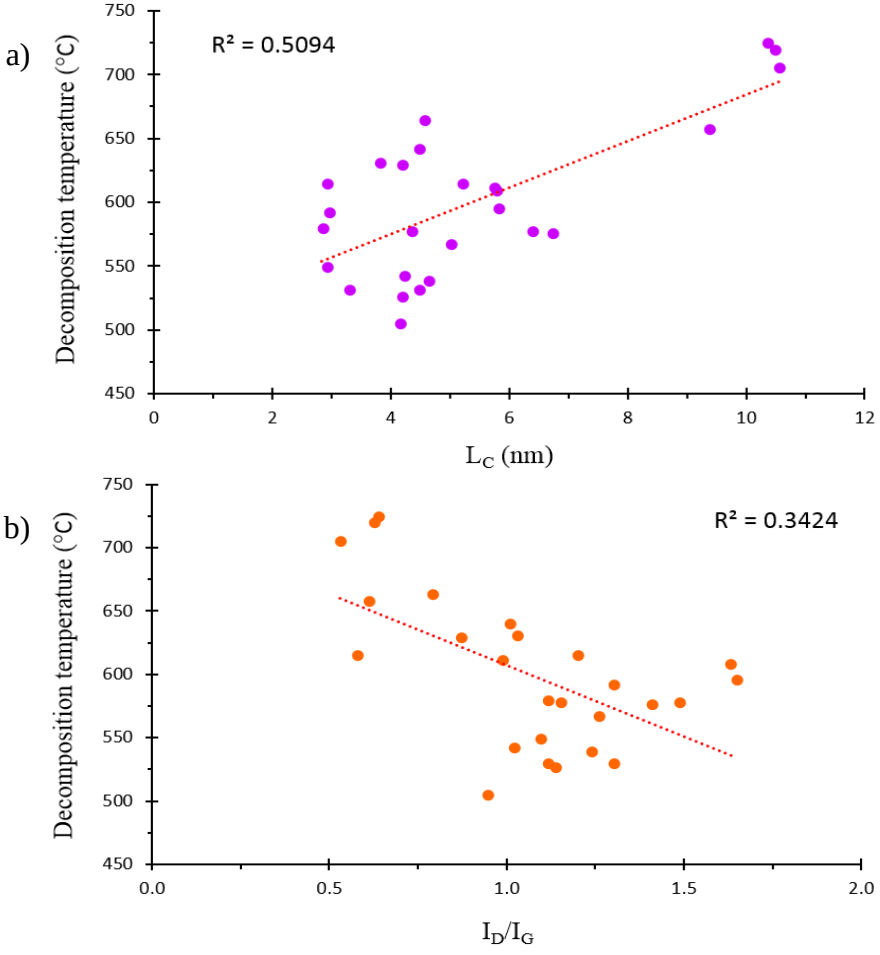

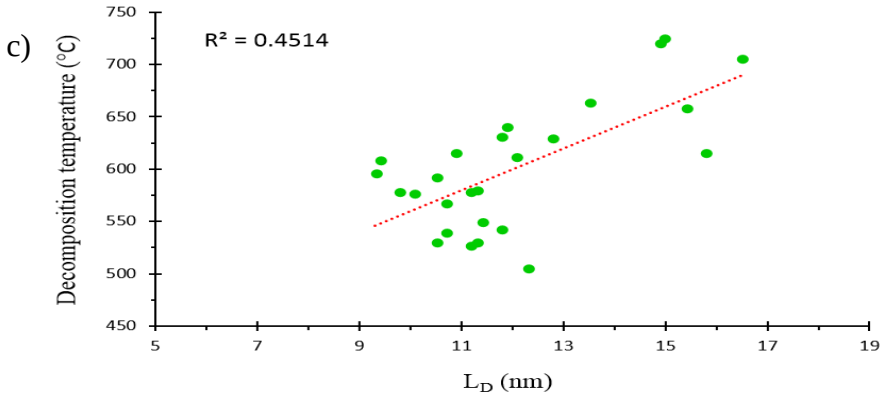

Figure 5.16 Evolution of the decomposition temperature of carbon materials (from TGA) with: a) the L_C, b) the I_D/I_G, and c) the L_D.

A significant higher degree of long-range order may also have a pronounced influence on the basicity of these materials. Indeed, it was pointed out that the π electrons of basal planes of graphene layers could act as Lewis bases. [28, 32, 33]

5.2.9 Effect of high temperature treatment in carbon materials by XPS and Raman analyses

We have already seen that one effect of the high temperature treatment is to significantly decrease the amount of surface heteroatoms (O, N or S). Another expected effect of this treatment is to decrease the number of defects in the materials. Figure 5.17 shows the effect of this treatment on structural parameters such as I_D/I_G, $I_{G'}/I_G$ or the amount of sp^2 carbon from XPS.

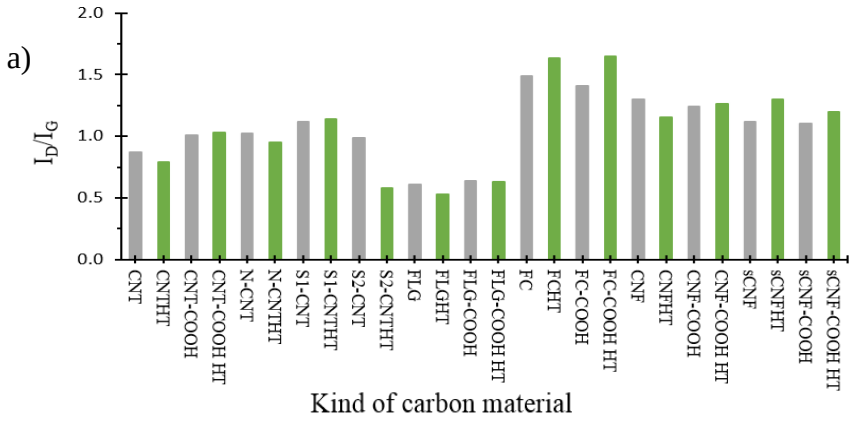

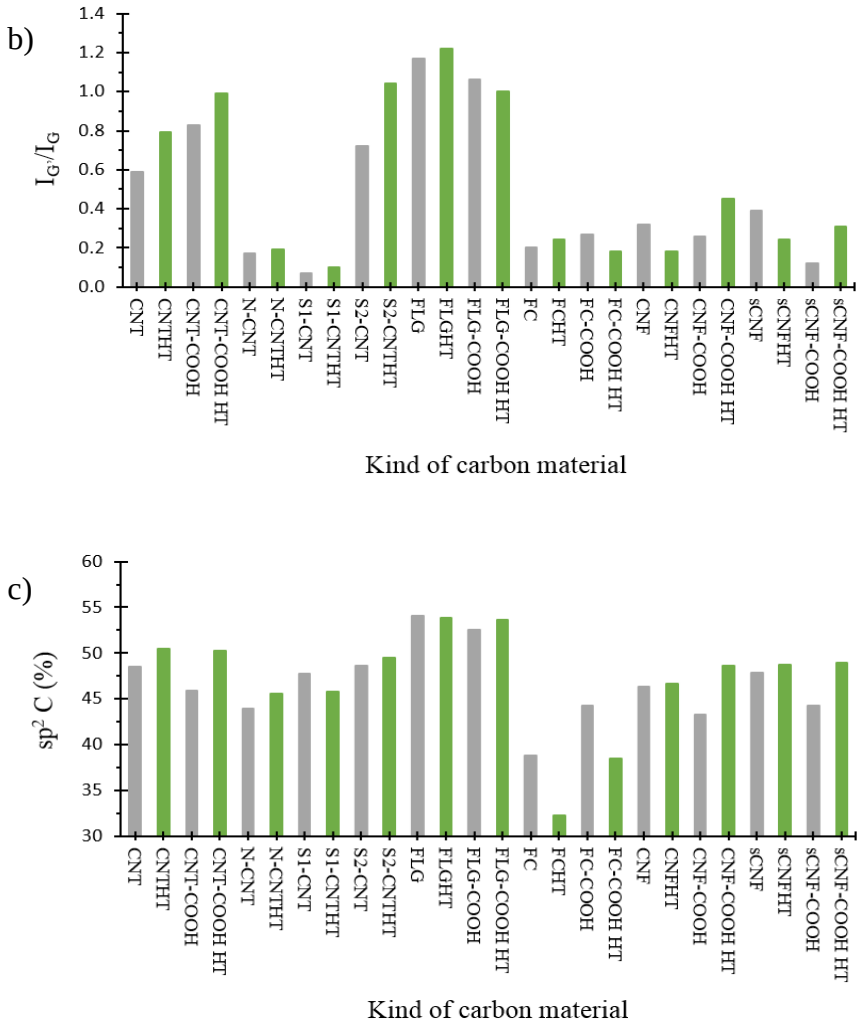

Figure 5.17 Influence of the high temperature treatment on: a) I_D/I_G, b) $I_{G'}/I_G$, and c) % of sp^2 carbon from XPS. Gray bars: no heat-treated carbon materials. Green bars: heat-treated carbon materials.

The general tendency is indeed a decrease of the I_D/I_G ratio and an increase of the amount of sp^2 carbon and long-range order ($I_{G'}/I_G$) after the heat-treatment. The clearest exception comes from fibrous carbon (FC) that presents edges with an angle of 90° with respect to the fiber axis. For this material the amount of sp^2 carbon detected by XPS decreases significantly after the heat-treatment, with a concomitant increase of the sp^3 carbon, and a I_D/I_G ratio increase as shown in Figure 5.18.

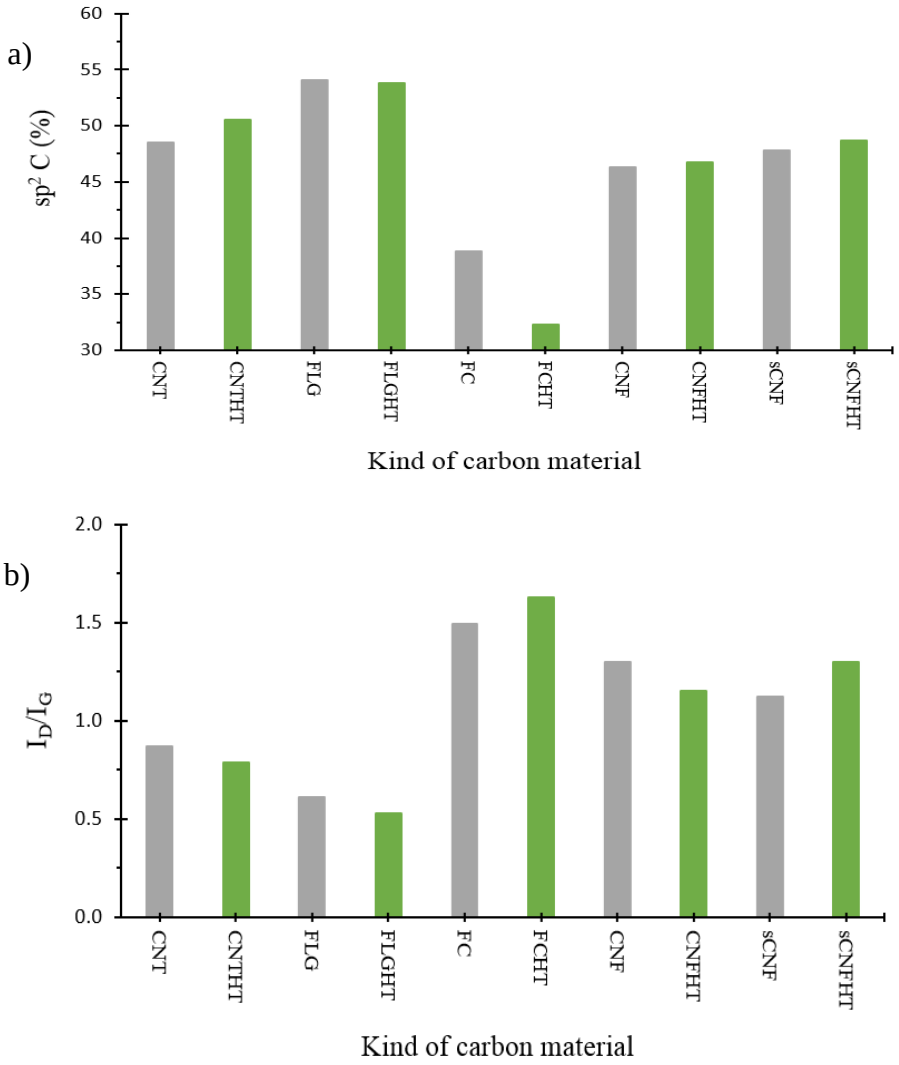

Figure 5.18 Influence of the high temperature treatment on: a) % of sp^2 carbon from XPS and b) I_D/I_G. Gray bars: pristine carbon materials. Green bars: heat-treated carbon materials.

We can tentatively attribute this phenomenon to the reactivity of the edges, which may have the tendency to easily form loops upon heating. The hybridization of carbon in these curved structures should be between sp^2 and sp^3, like in fullerene (C_{60}) for which a 2.28 hybridization has been estimated. [34] This phenomenon is less pronounced on sCNF, and not visible on CNF. This might be correlated to the average angle with respect to the filament axis that is different: 26°, 40° and 90° for CNF, sCNF, and FC, respectively.

The higher this angle, the higher is the propensity to form loops. A higher chemical reactivity (proton affinity) has already been proposed by Chen *et al*. for CNFs presenting different average angle with respect to the filament axis; there also, the higher this angle is, the higher is the reactivity. [1]

5.2.10 Effect of nitric acid oxidation in carbon materials by XPS and Raman analyses

An important effect of nitric acid oxidation, which is regularly performed on carbon nanomaterials to improve metal adhesion, is to increase the amount of surface oxygen, and particularly the carboxylic groups. For CNT, FLG and FC, an increase of peak VI (carboxylic acid and lactone groups) from the C1s XPS spectra is indeed observed after HNO_3 oxidation (see Figure 5.19a); but this is not the case for CNF and sCNF. For this latter supports it is mainly the intensity of peak IV from the C1s XPS spectra (OH, C-O containing groups) that increases. The nitric acid functionalization of CNF has already been studied in the literature. [35, 36] Upon treatment at room temperature, an increase of the carboxylic groups has been reported; [35] whereas with increasing temperature and process duration, the yield of functionalization products decreases, and their concentration ("solubility") in the aqueous dispersion increases. [36] It can thus be anticipated that in our case this treatment should not have a significant impact on palladium loading on carbon nanofibers. The introduction of oxygenated surface groups in carbon nanomaterials is generally associated to an increase of disorder. For CNT and FLG, we indeed measured an increase of the I_D/I_G values and a decrease of the L_D values, which is consistent with an increase of the disorder in these materials upon oxidation (see Figures 5.19b-c). Such a phenomenon has already been reported in the literature. [2, 37]

An opposite evolution was observed for the supports showing a low basal- to "non-basal-plane" ratio. A decrease of the I_D/I_G ratio upon nitric acid oxidation of CNF has already been reported. [38]

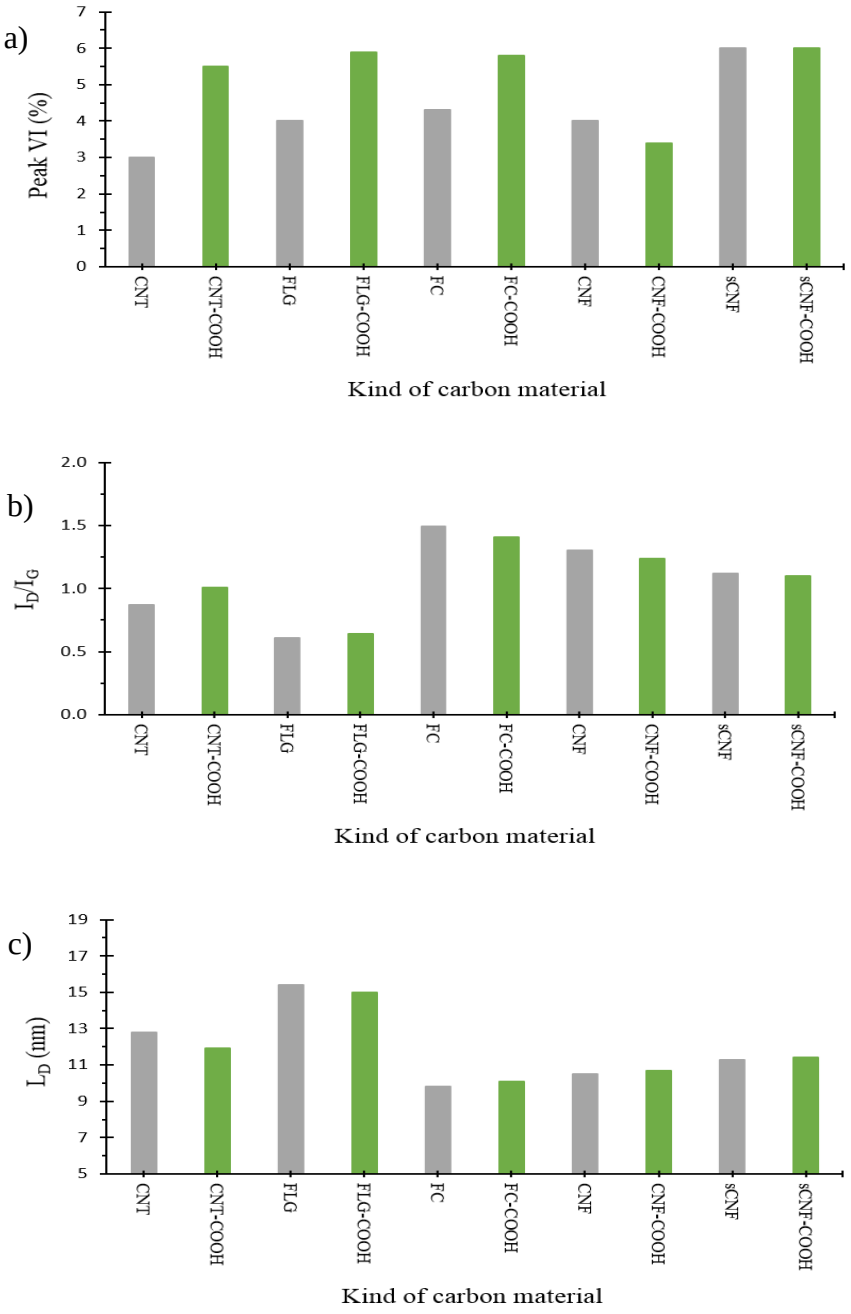

Figure 5.19 Influence of the nitric acid oxidation on: a) the peak VI of the C1s XPS spectrum (carboxylic acid and lactone groups), b) I_D/I_G, and c) L_D. Gray bars: pristine carbon materials. Green bars: acid-treated carbon materials.

The authors proposed that the small amount of amorphous carbon that is deposited on the CNF during their synthesis is almost completely removed through the oxidization process. It is also possible that the acidic oxidation cuts off the closed loop ends on the surface of CNF, consequently improving the overall alignment of hexagonal planes. [39]

The investigated supports reflect the broad spectrum of carbon nanomaterials used for Pd/C catalyst preparation. They are characterized by a different surface chemistry, arising from: i) the presence or not of oxygen, sulfur or nitrogen bearing surface groups, which can contribute to the stabilization of the metal precursor or metallic nanoparticles, ii) different concentration of defects illustrated by different I_D/I_G ratio, different inter-defect distances (L_D) or different long-range order illustrated by different $I_{G'}/I_G$ ratio, which can also affect metal deposition, and iii) different orientations of the graphene layers, which allow metal deposition either on the flat (FLG) or curved (CNT) graphitic shell, or on the edges (CNF and FC). These supports were also characterized by Physisorption (BET surface area). The specific surface area is also an important parameter that could affect metal dispersion, as discussed in next paragraphs.

5.3 Understanding the metal-support interaction of palladium catalysts

In the preparation method of a catalyst, certain experimental conditions play a very important role. In our case, the wetness impregnation method was employed to prepare all palladium catalysts (see Chapter III: Methodology, section: 3.9.1). This method uses a solvent to bring in contact the metal precursor salt and the solid carbon support. The choice of solvent thus affects affecting the final dispersion state of the metallic particles on the carbon support.

Considering the solubility of the metal precursor salt and the hydrophobic character of the carbon support, we used acetone as a solvent instead of water (solvent commonly used). Palladium nitrate was also preferred over other salts as its reduction yields palladium particles free of any impurities. The catalysts were characterized by ICP (palladium loading), TEM (palladium particle size), and physisorption (BET surface area).

5.3.1 Dependence of palladium loading, palladium particle size, and specific surface area on the carbon support characteristics

The surface chemistry of a support plays a fundamental role in the metal amount deposited on the support. In our case, different methods and/or treatments were applied to the carbon supports to improve their surface chemistry, in order to achieve a high palladium loading.

As already mentioned, 2 wt% of palladium was introduced in the carbon support suspension (see Chapter III: Methodology, section: 3.9.1). Figure 5.20a shows the palladium loading variation between all catalysts. Among the catalysts with a higher palladium loading, we identified palladium catalysts for which their carbon support was previously treated. Besides, as expected, the previously treated carbon supports allowed a higher palladium loading compared to the catalysts supported on pristine carbon.

It is well-known that the metal particle size is also an important parameter in heterogeneous catalysis. Thus, a small particle size leads to high activity and selectivity (see Chapter I: Introduction, section 1.5). In our case, we obtained palladium particle sizes ranging from 1 to 3 nm (see Figure 5.20b).

In those catalysts in which their carbon support was previously treated before introducing the palladium metal, smaller particle sizes were measured compared to the catalysts in which their carbon support was not previously treated. This means that as expected the methods and/or treatments applied to activate the carbon support surface lead to small particle sizes.

Along with the palladium loading and the palladium particle size, the specific surface area of the support is another very important parameter to include into the study of a catalyst. It is known that porous materials possess high specific surface areas compared to the non-porous materials. Carbon materials are considered as porous materials. Our carbon supports provide acceptable specific surface areas. But, these specific surface areas significantly vary between all them. One of the most important characteristics of carbon supports for considering in the final calculation of specific surface area, is the arrangement of graphene layers and the surface chemistry of carbon support, which account for the high specific surface areas. The specific surface area of palladium-containing catalysts did not change significantly compared to the bare supports, except for the sCNF supports for which a significant increase of the specific surface area was measured for the palladium catalysts (see Table 4.28 and Figure 5.20c).

a)

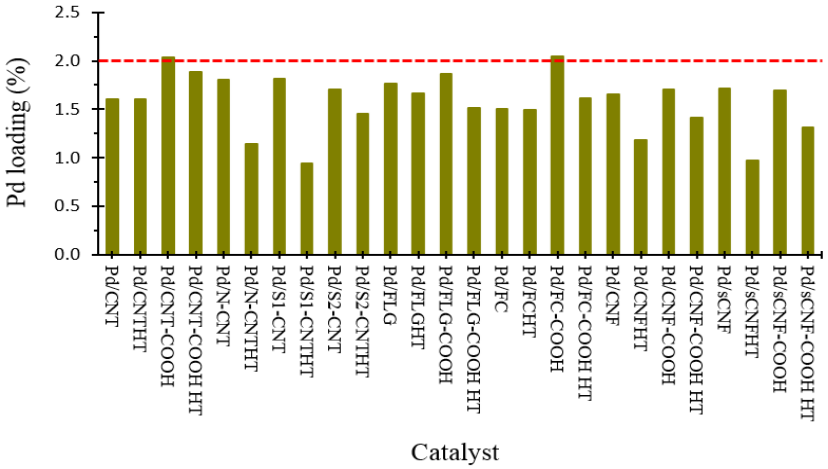

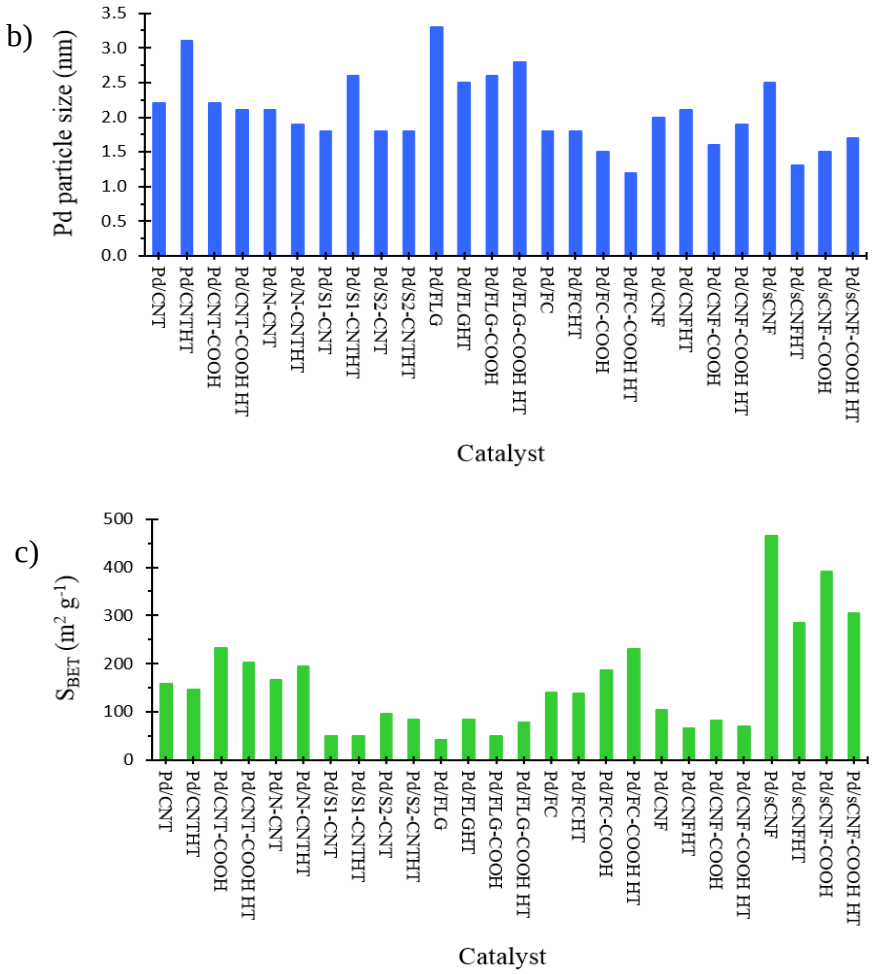

Figure 5.20 Influence of the surface chemistry on: a) the palladium loading (from ICP), b) the palladium particle size (from TEM), and c) the BET surface area (from physisorption) for the catalysts.

5.3.2 Influence of nitric acid oxidation on palladium loading, palladium particle size, and specific surface area for the catalysts

Figure 5.21a shows the positive effect in the palladium catalysts supported on functionalized carbon materials (nitric acid oxidation) compared to the palladium catalysts supported on pristine carbon materials. Indeed, palladium catalysts supported on functionalized carbon materials present a higher palladium loading compared to the palladium catalysts supported on pristine carbon materials for all them.

Palladium catalysts supported on functionalized carbon materials have exhibited palladium particle sizes smaller than palladium catalysts supported on pristine carbon materials (see Figure 5.21b). Thus, palladium catalysts supported on functionalized carbon materials with smaller palladium particle sizes, should promote their catalytic activity.

The higher specific surface area of the palladium catalysts supported on functionalized carbon materials compared to the palladium catalysts supported on pristine carbon materials, are also expected to have a positive effect on catalytic activity. Exceptions are the Pd/CNF$_{-COOH}$ and Pd/sCNF$_{-COOH}$ catalysts, which have displayed lower specific surface areas compared to Pd/CNF and Pd/sCNF catalysts (see Figure 5.21c).

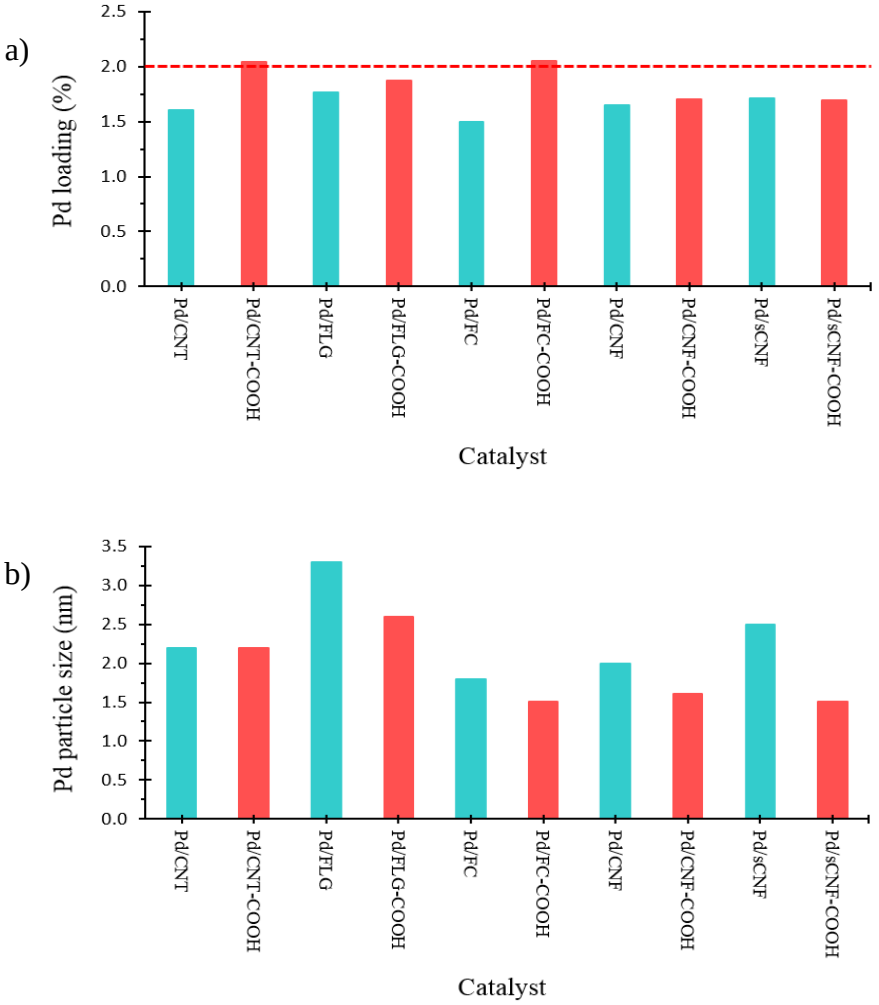

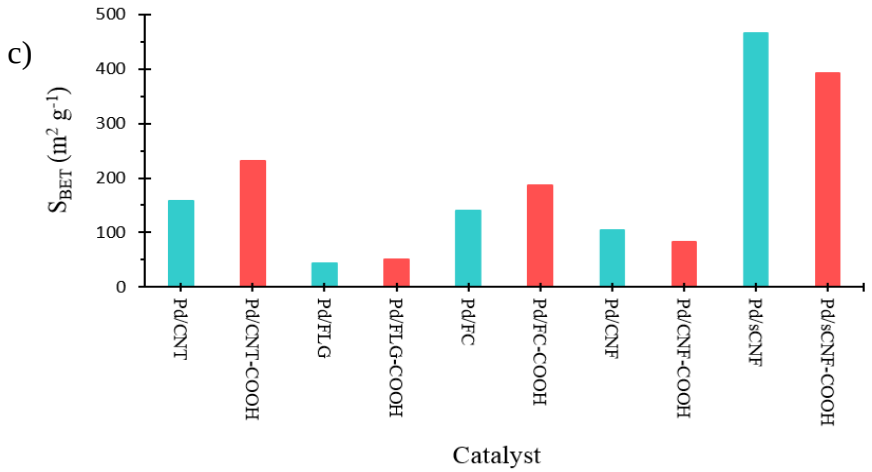

Figure 5.21 Influence of nitric acid oxidation on: a) the palladium loading (from ICP), b) the palladium particle size (from TEM), and c) the BET surface area (from physisorption) for the catalysts. Cyan bars: palladium catalysts supported on untreated carbon nanostructures. Red bars: palladium catalysts supported on acid-treated carbon nanostructures.

5.3.3 Influence of high temperature treatment on palladium loading, palladium particle size, and specific surface area for the catalysts

As already mentioned, another way to activate the support surface is using a thermal treatment. A high temperature treatment produces significant changes in the surface chemistry of support. In our case, the palladium catalysts supported on heat-treated carbon materials showed lower palladium loading compared to the palladium catalysts supported on pristine carbon materials (see Figure 5.22a). Indeed, this high temperature treatment performed on carbon supports before introducing the palladium metal, decreases the structural disorder, reducing the number of anchoring sites (see Figure 5.18b).

Thus, the palladium particle size is also affected by the high temperature treatment. Figure 5.22b shows the high temperature treatment effect in the palladium catalyst characteristics compared to the characteristics of palladium catalysts supported on pristine carbon materials.

It is shown that smaller palladium particle sizes were produced in those palladium catalysts supported on heat-treatment carbon materials, except for Pd/CNT_{HT} and Pd/CNF_{HT} catalysts, which present larger palladium particle sizes compared to Pd/CNT and Pd/CNF catalysts.

Finally, the specific surface area is also affected by the high temperature treatment. In our case, the palladium catalysts supported on heat-treated carbon materials exhibit lower specific surface areas compared to the palladium catalysts supported on pristine carbon materials, except for Pd/FLG_{HT} catalyst, which exposes a larger specific surface area compared to Pd/FLG catalyst as shown in Figure 5.22c.

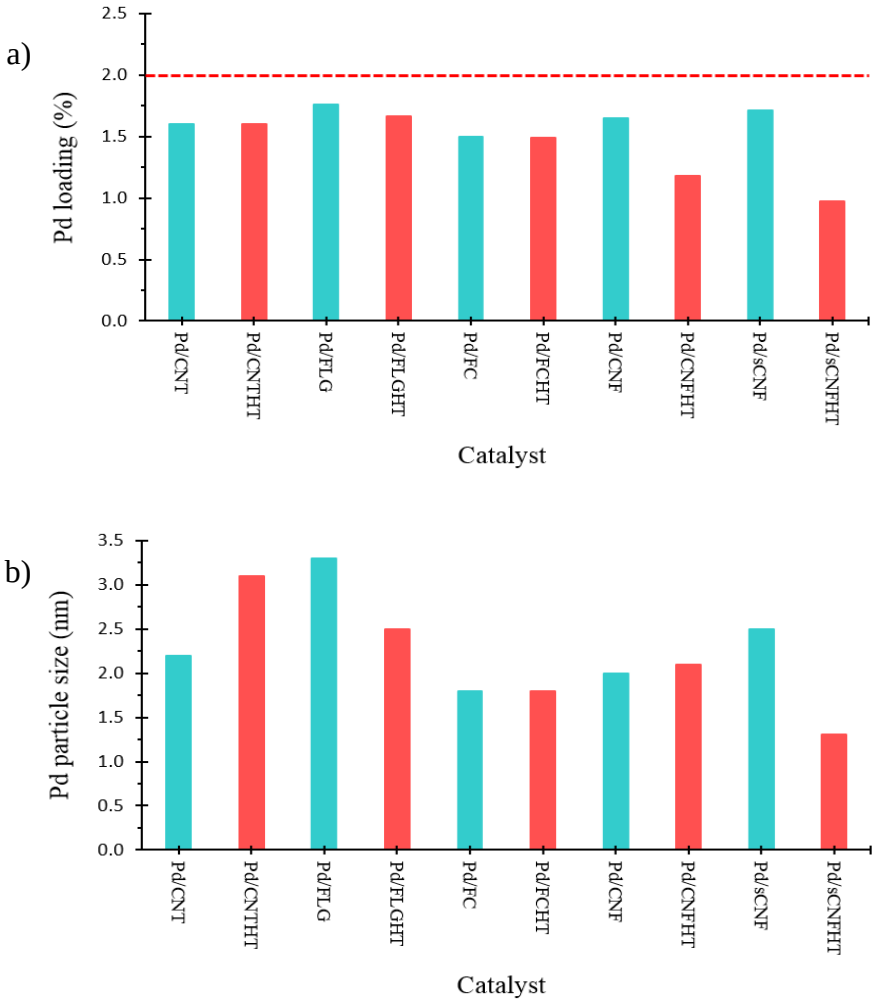

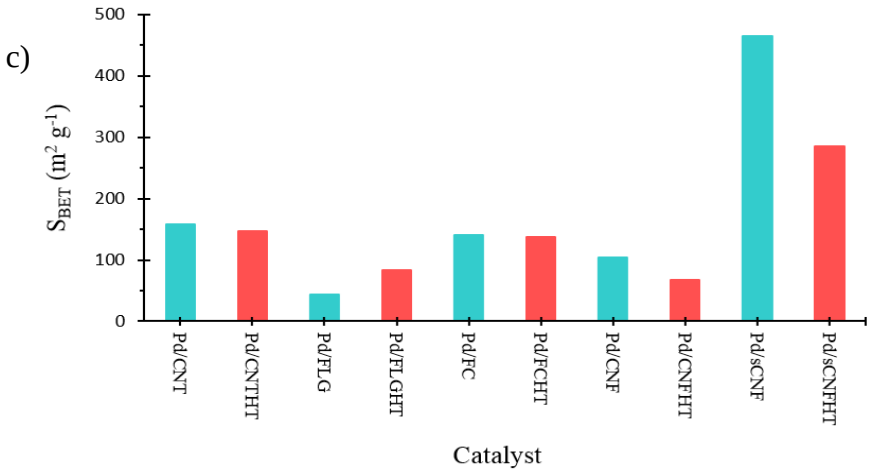

Figure 5.22 Influence of high temperature treatment on: a) the palladium loading (from ICP), b) the palladium particle size (from TEM), and c) the BET surface area (from physisorption) for the catalysts. Cyan bars: palladium catalysts supported on untreated carbon nanostructures. Red bars: palladium catalysts supported on heat-treated carbon nanostructures.

5.3.4 Influence of heteroatoms on palladium loading, palladium particle size, and specific surface area for the catalysts

In the doping process, the heteroatoms play a very important role in the surface chemistry of support. Nitrogen, sulphur or phosphorous are commonly used as heteroatoms. The incorporation of these heteroatoms in the carbon structure significantly improves the electronic properties of support. In our case, nitrogen and sulphur were used as heteroatoms during the doping process. Along with nitrogen and sulphur, oxygen was also used as heteroatom, which was added by nitric acid oxidation. The doping process was only performed in the multi-walled carbon nanotubes. Hence, a higher palladium loading is observed in the palladium catalysts supported on doped multi-walled carbon nanotubes compared to that palladium catalyst supported on pristine multi-walled carbon nanotubes. This means that the incorporation of heteroatoms modifies the surface chemistry of support, improving the palladium loading (see Figure 5.23a).

Figure 5.23b shows a positive influence of the doping in the palladium particle size. The palladium catalysts supported on doped multi-walled carbon nanotubes exhibit smaller palladium particle sizes compared to the palladium catalyst supported on pristine multi-walled carbon nanotubes.

Finally, the specific surface area is also modified by a doping process. Palladium catalysts supported on doped multi-walled carbon nanotubes present specific surface areas higher than palladium catalyst supported on pristine multi-walled carbon nanotubes, except for Pd/S_1-CNT and Pd/S_2-CNT catalysts (see Figure 5.23c).

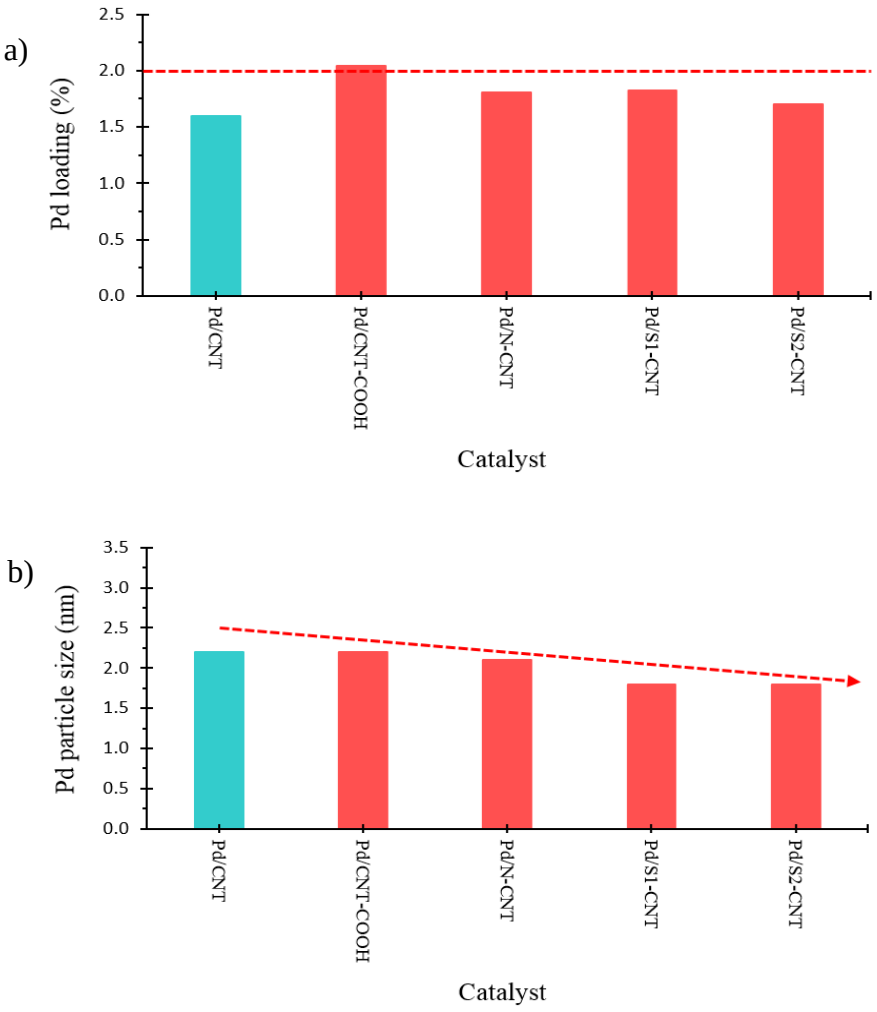

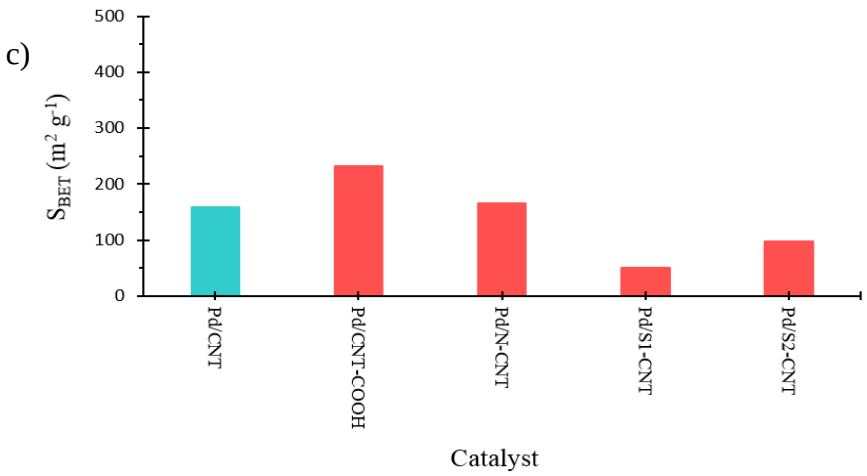

Figure 5.23 Influence of heteroatoms on: a) the palladium loading (from ICP), b) the palladium particle size (from TEM), and c) the BET surface area (from physisorption) for the catalysts. Cyan bar: palladium catalyst supported on pristine multi-walled carbon nanotubes. Red bars: palladium catalysts supported on doped multi-walled carbon nanotubes.

5.3.5 Influence of edges (defects) on palladium loading, palladium particle size, and specific surface area for the catalysts

In contrast to nitric acid oxidation, thermal treatment, and doping of heteroatoms are post-synthesis treatments. The edges are produced during the support synthesis, affecting positively the subsequent palladium loading, the palladium particle size, and the specific surface area. Although the level of defects between carbon supports considerably varies, a similar tendency on the palladium loading is observed for all catalysts, except for Pd/FLG catalyst, which shows the highest palladium loading compared to other ones (see Figure 5.24a).

Figure 5.24b shows that the palladium particle size significantly varies between all catalysts. The Pd/FLG catalyst presents the largest palladium particle size compared to the other ones.

The specific surface area of palladium catalysts supported on pristine carbon materials considerably varies, being the Pd/FLG catalyst, the one with the lowest specific surface area compared to the other ones as shown in Figure 5.24c.

The edge defects of the materials could be controlled, but it has not been possible to completely eliminate them. We propose that a low specific surface area and a low level of defect produce large palladium particle sizes as shown in the Pd/FLG catalyst (see Figures 5.24b-c and 5.26).

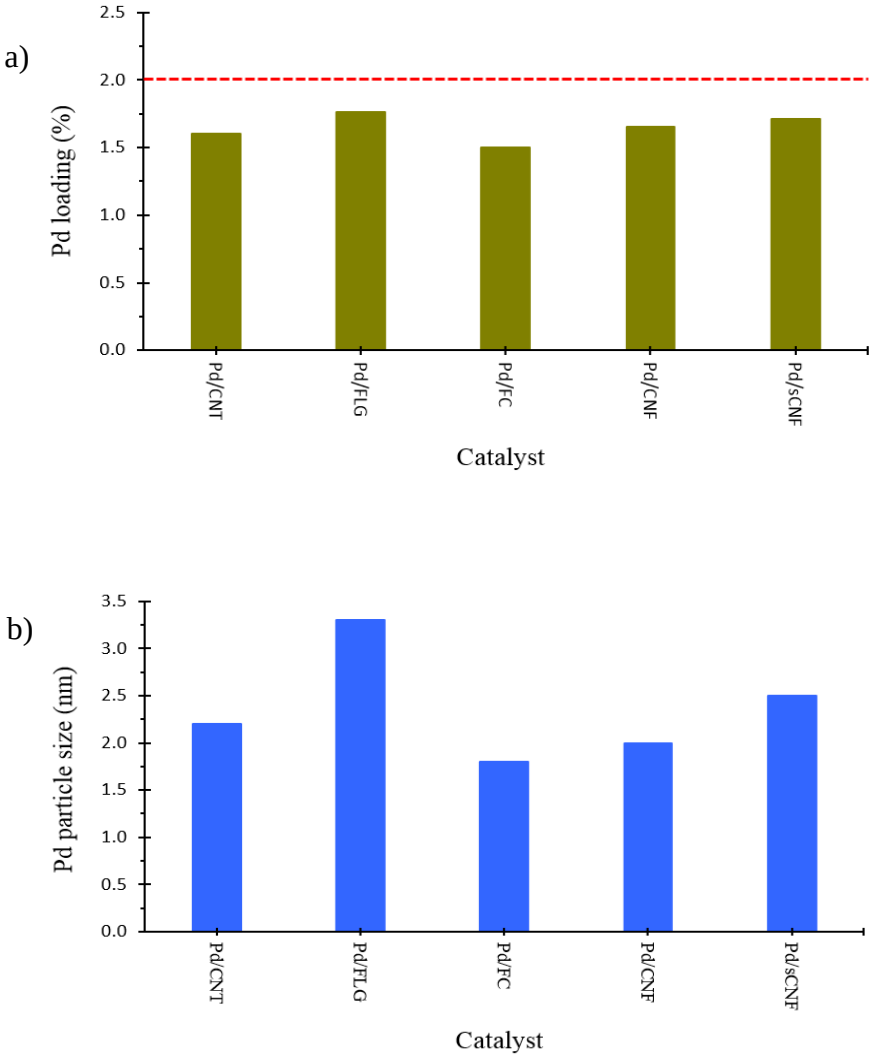

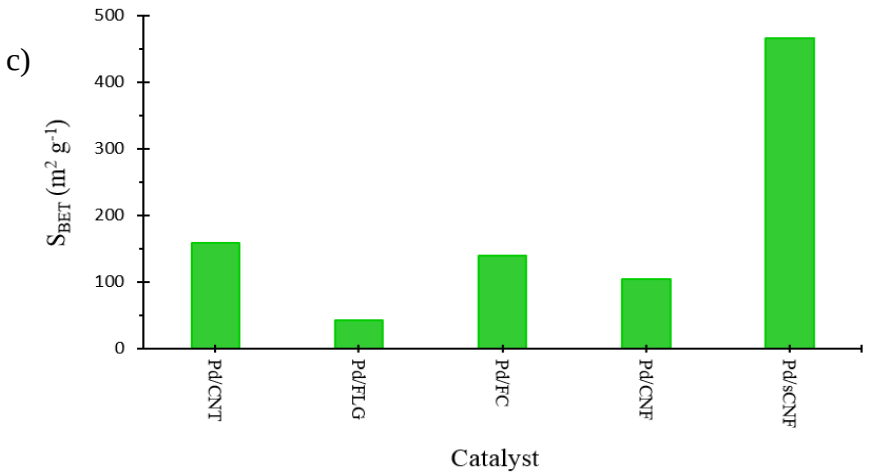

Figure 5.24 Influence of edges (defects) on: a) the palladium loading (from ICP), b) the palladium particle size (from TEM), and c) the BET surface area (from physisorption) for the catalysts.

5.3.6 Influence of specific surface area on palladium loading for the catalysts

Both specific surface area and palladium loading significantly vary between all catalysts. Figure 5.25 shows a comparison between specific surface area and palladium loading for all catalysts, wherever a tendency is observed. Thus, high specific surface areas are associated to high palladium loading.

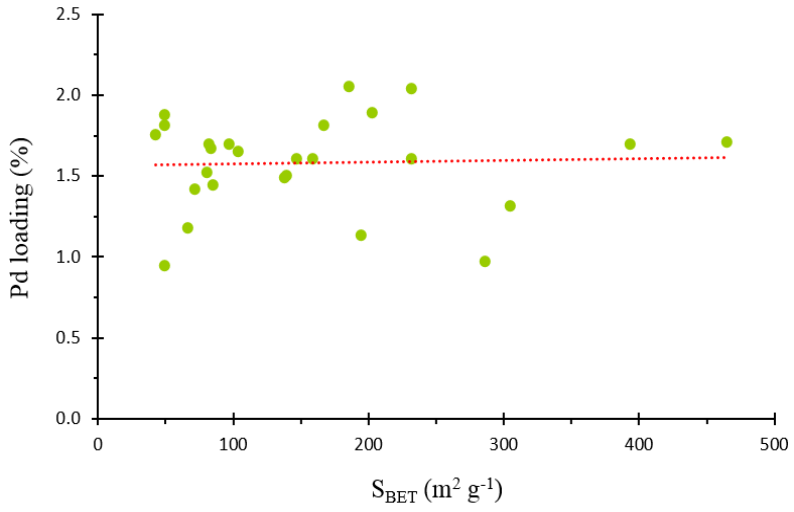

Figure 5.25 Evolution of BET surface area (from physisorption) for the palladium catalysts with the palladium loading (from ICP).

5.3.7 Influence of specific surface area on palladium particle size for the catalysts

Along with the specific surface area, the palladium particle size considerably varies between all catalysts. Figure 5.26 shows a comparison between specific surface area and palladium particle size for all catalysts. High specific surface areas induce the formation of small palladium particle sizes.

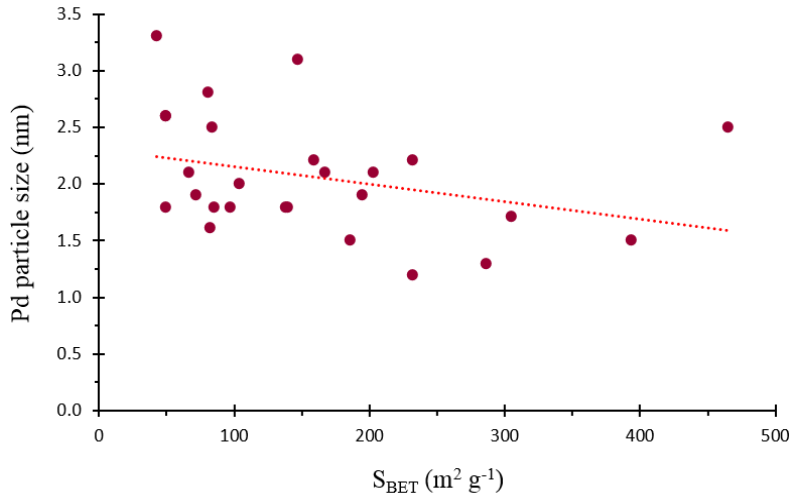

Figure 5.26 Evolution of BET surface area (from physisorption) for the palladium catalysts with the palladium particle size (from TEM).

5.3.8 Palladium loading, palladium particle size, and specific surface area on the catalysts: A detailed study

Metal loading, metal particle size, and specific surface area are important parameters to be taken into account for the selection of the best catalyst.

Figure 5.27 shows palladium loading, palladium particle size, and specific surface area for all catalysts. Thus, it is possible to determine the best catalyst. A high palladium loading, a small palladium particle size to allow sufficient loading, and a large specific surface area, should be the characteristics corresponding to the most promising catalyst.

According to what has been presented before, the Pd/CNT$_{\text{-COOH}}$, Pd/FC$_{\text{-COOH}}$, and Pd/sCNF$_{\text{-COOH}}$ catalysts exhibit high palladium loading, moderate palladium particle sizes, and large specific surface areas.

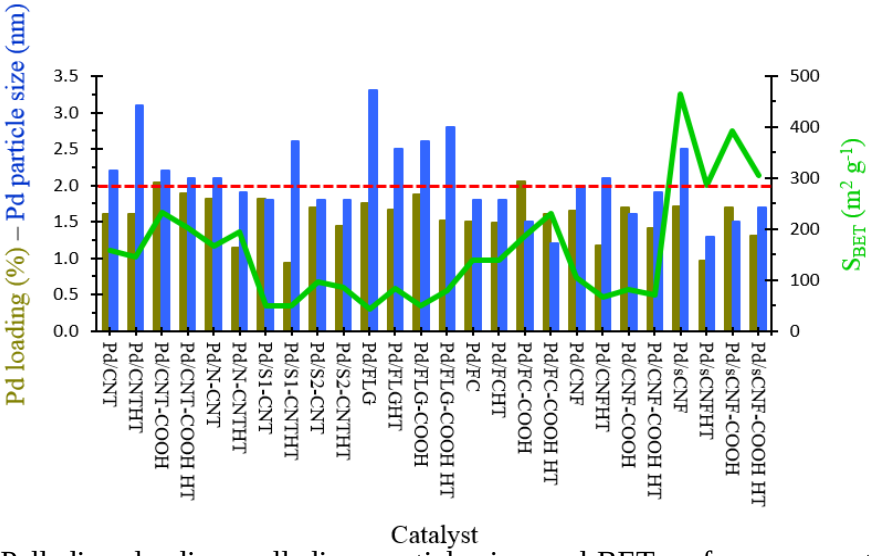

Figure 5.27 Palladium loading, palladium particle size, and BET surface area on the catalysts. Olive bars: Pd loading. Blue bars: Pd particle size. Green broken line: BET surface area.

Considering the selected palladium catalysts, HRTEM analyses were performed. HRTEM micrographs made on the Pd/CNT$_{\text{-COOH}}$, Pd/FC$_{\text{-COOH}}$, and Pd/sCNF$_{\text{-COOH}}$ catalysts show great palladium dispersion and moderate palladium particle sizes (see Figure 5.28).

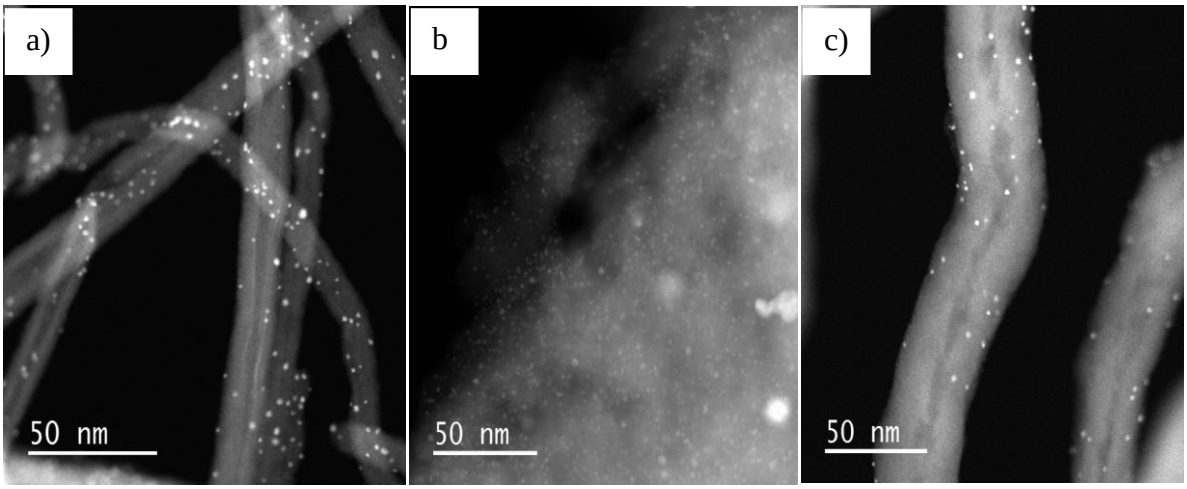

Figure 5.28 HRTEM micrographs performed on: a) Pd/CNT$_{\text{-COOH}}$, b) Pd/FC$_{\text{-COOH}}$, and c) Pd/sCNF$_{\text{-COOH}}$. Scale bar for all micrographs: 50 nm.

5.4 Summary

The detailed study performed on the carbon supports and palladium catalysts allowed identifying the most important characteristics by using different characterization techniques. This study has given important information on the surface chemistry of carbon supports. The best carbon support was selected for its large specific surface area and high concentration in edges and heteroatoms. In addition, the palladium loading, palladium particle size and specific surface area measurements allowed selecting the most promising palladium catalysts, which will be employed in the selected chemical reaction in order to determine the best reaction conditions and then evaluate all palladium catalysts under these conditions as discussed next Chapter VI: Catalytic tests.

5.5 References

[1] J. Zhu, A. Holmen, D. Chen, Carbon Nanomaterials in Catalysis: Proton Affinity, Chemical and Electronic Properties, and their Catalytic Consequences, ChemCatChem, 5 (**2013**) 378-401.

[2] I. Gerber, M. Oubenali, R. Bacsa, J. Durand, A. Gonçalves, M.F.R. Pereira, F. Jolibois, L. Perrin, R. Poteau, P. Serp, Theoretical and Experimental Studies on the Carbon-Nanotube Surface Oxidation by Nitric Acid: Interplay between Functionalization and Vacancy Enlargement, Chemistry – A European Journal, 17 (**2011**) 11467-11477.

[3] T.G. Ros, A.J. van Dillen, J.W. Geus, D.C. Koningsberger, Surface Structure of Untreated Parallel and Fishbone Carbon Nanofibres: An Infrared Study, ChemPhysChem, 3 (**2002**) 209-214.

[4] J.F.H. Peter, L. Zheng, S. Kazu, Imaging the atomic structure of activated carbon, Journal of Physics: Condensed Matter, 20 (**2008**) 362201.

[5] J.-P. Tessonnier, D. Rosenthal, T.W. Hansen, C. Hess, M.E. Schuster, R. Blume, F. Girgsdies, N. Pfänder, O. Timpe, D.S. Su, R. Schlögl, Analysis of the structure and chemical properties of some commercial carbon nanostructures, Carbon, 47 (**2009**) 1779-1798.

[6] A.D. Purceno, B.F. Machado, A.P.C. Teixeira, T.V. Medeiros, A. Benyounes, J. Beausoleil, H.C. Menezes, Z.L. Cardeal, R.M. Lago, P. Serp, Magnetic amphiphilic hybrid carbon nanotubes containing N-doped and undoped sections: powerful tensioactive nanostructures, Nanoscale, 7 (**2015**) 294-300.

[7] S. Louisia, R.C. Contreras, M. Heitzmann, M. Rosa Axet, P.-A. Jacques, P. Serp, Sequential catalytic growth of sulfur-doped carbon nanotubes and their use as catalyst support, Catalysis Communications, 109 (**2018**) 65-70.

[8] R.R. Bacsa, I. Cameán, A. Ramos, A.B. Garcia, V. Tishkova, W.S. Bacsa, J.R. Gallagher, J.T. Miller, H. Navas, V. Jourdain, M. Girleanu, O. Ersen, P. Serp, Few layer graphene synthesis on transition metal ferrite catalysts, Carbon, 89 (**2015**) 350-360.

[9] P.V. Lakshminarayanan, H. Toghiani, C.U. Pittman, Nitric acid oxidation of vapor grown carbon nanofibers, Carbon, 42 (**2004**) 2433-2442.

[10] A. Solhy, B.F. Machado, J. Beausoleil, Y. Kihn, F. Gonçalves, M.F.R. Pereira, J.J.M. Órfão, J.L. Figueiredo, J.L. Faria, P. Serp, MWCNT activation and its influence on the catalytic performance of Pt/MWCNT catalysts for selective hydrogenation, Carbon, 46 (**2008**) 1194-1207.

[11] S.A. Carabineiro, M.F. Pereira, J.N. Pereira, C. Caparros, V. Sencadas, S. Lanceros-Mendez, Effect of the carbon nanotube surface characteristics on the conductivity and dielectric constant of carbon nanotube/poly(vinylidene fluoride) composites, Nanoscale Research Letters, 6 (**2011**) 302.

[12] S.-H. Yoon, C.-W. Park, H. Yang, Y. Korai, I. Mochida, R.T.K. Baker, N.M. Rodriguez, Novel carbon nanofibers of high graphitization as anodic materials for lithium ion secondary batteries, Carbon, 42 (**2004**) 21-32.

[13] A. Ramos, I. Cameán, A.B. García, Graphitization thermal treatment of carbon nanofibers, Carbon, 59 (**2013**) 2-32.

[14] S.-H. Yoon, S. Lim, S.-h. Hong, W. Qiao, D.D. Whitehurst, I. Mochida, B. An, K. Yokogawa, A conceptual model for the structure of catalytically grown carbon nano-fibers, Carbon, 43 (**2005**) 1828-1838.

[15] A.B. Garcia, I. Cameán, I. Suelves, J.L. Pinilla, M.J. Lázaro, J.M. Palacios, R. Moliner, The graphitization of carbon nanofibers produced by the catalytic decomposition of natural gas, Carbon, 47 (**2009**) 2563-2570.

[16] G.G. Kuvshinov, I.S. Chukanov, Y.L. Krutsky, V.V. Ochkov, V.I. Zaikovskii, D.G. Kuvshinov, Changes in the properties of fibrous nanocarbons during high temperature heat treatment, Carbon, 47 (**2009**) 215-225.

[17] L. Pahalagedara, H. Sharma, C.-H. Kuo, S. Dharmarathna, A. Joshi, S.L. Suib, A.B. Mhadeshwar, Structure and Oxidation Activity Correlations for Carbon Blacks and Diesel Soot, Energy & Fuels, 26 (**2012**) 6757-6764.

[18] D.-H.K. Kim, Bo-Hye; Yang, Kap-Seung; Bang, Yun-Hyuk; Kim, Sung-Ryong; Im, Hun-Kook, Analysis of the Microstructure and Oxidation Behavior of Some Commercial Carbon Fibers, Journal of the Korean Chemical Society, 55 (**2011**) 819-823.

[19] M.S. Dresselhaus, A. Jorio, R.Saito, Characterizing Graphene, Graphite, and Carbon Nanotubes by Raman Spectroscopy, Annual Review of Condensed Matter Physics, 1 (**2010**) 89-108.

[20] M.S. Dresselhaus, A. Jorio, M. Hofmann, G. Dresselhaus, R. Saito, Perspectives on Carbon Nanotubes and Graphene Raman Spectroscopy, Nano Letters, 10 (**2010**) 751-758.

[21] T. Susi, T. Pichler, P. Ayala, X-ray photoelectron spectroscopy of graphitic carbon nanomaterials doped with heteroatoms, Beilstein Journal of Nanotechnology, 6 (**2015**) 177-192.

[22] K. Ganesan, S. Ghosh, N. Gopala Krishna, S. Ilango, M. Kamruddin, A.K. Tyagi, A comparative study on defect estimation using XPS and Raman spectroscopy in few layer nanographitic structures, Physical Chemistry Chemical Physics, 18 (**2016**) 22160-22167.

[23] A. Barinov, O.B. Malcioğlu, S. Fabris, T. Sun, L. Gregoratti, M. Dalmiglio, M. Kiskinova, Initial Stages of Oxidation on Graphitic Surfaces: Photoemission Study and Density Functional Theory Calculations, The Journal of Physical Chemistry C, 113 (**2009**) 9009-9013.

[24] Y. Yamada, H. Yasuda, K. Murota, M. Nakamura, T. Sodesawa, S. Sato, Analysis of heat-treated graphite oxide by X-ray photoelectron spectroscopy, Journal of Materials Science, 48 (**2013**) 8171-8198.

[25] S.T. Jackson, R.G. Nuzzo, Determining hybridization differences for amorphous carbon from the XPS C 1s envelope, Applied Surface Science, 90 (**1995**) 195-203.

[26] H.P. Boehm, Surface oxides on carbon and their analysis: a critical assessment, Carbon, 40 (**2002**) 145-149.

[27] D. Yang, A. Velamakanni, G. Bozoklu, S. Park, M. Stoller, R.D. Piner, S. Stankovich, I. Jung, D.A. Field, C.A. Ventrice, R.S. Ruoff, Chemical analysis of graphene oxide films after heat and chemical treatments by X-ray photoelectron and Micro-Raman spectroscopy, Carbon, 47 (**2009**) 145-152.

[28] H. Darmstadt, C. Roy, Surface spectroscopic study of basic sites on carbon blacks, Carbon, 41 (**2003**) 2662-2665.

[29] R.A. DiLeo, B.J. Landi, R.P. Raffaelle, Purity assessment of multiwalled carbon nanotubes by Raman spectroscopy, Journal of Applied Physics, 101 (**2007**) 064307.

[30] R. Saito, A. Grüneis, G.S. Ge, V.W. Brar, G. Dresselhaus, M.S. Dresselhaus, A. Jorio, L.G. Cançado, C. Fantini, M.A. Pimenta, A.G.S. Filho, Double resonance Raman spectroscopy of single-wall carbon nanotubes, New Journal of Physics, 5 (**2003**) 157.

[31] L.G. Cançado, A. Jorio, E.H.M. Ferreira, F. Stavale, C.A. Achete, R.B. Capaz, M.V.O. Moutinho, A. Lombardo, T.S. Kulmala, A.C. Ferrari, Quantifying Defects in Graphene via Raman Spectroscopy at Different Excitation Energies, Nano Letters, 11 (**2011**) 3190-3196.

[32] H.P. Boehm, Some aspects of the surface chemistry of carbon blacks and other carbons, Carbon, 32 (**1994**) 759-769.

[33] E. Papirer, S. Li, J.-B. Donnet, Contribution to the study of basic surface groups on carbons, Carbon, 25 (**1987**) 243-247.

[34] R.C. Haddon, R.E. Palmer, H.W. Kroto, P.A. Sermon, The Fullerenes: Powerful Carbon-Based Electron Acceptors [and Discussion], Philosophical Transactions: Physical Sciences and Engineering, 343 (**1993**) 53-62.

[35] J.-H. Zhou, Z.-J. Sui, J. Zhu, P. Li, D. Chen, Y.-C. Dai, W.-K. Yuan, Characterization of surface oxygen complexes on carbon nanofibers by TPD, XPS and FT-IR, Carbon, 45 (**2007**) 785-796.

[36] N. T. Hung, N. M. Tuong, E. G. Rakov, Acid functionalization of carbon nanofibers, Inorganic Materials, 46 (**2010**) 1077-1083.

[37] S. Osswald, M. Havel, Y. Gogotsi, Monitoring oxidation of multiwalled carbon nanotubes by Raman spectroscopy, Journal of Raman Spectroscopy, 38 (**2007**) 728-736.

[38] M. Endo, Y.A. Kim, T. Takeda, S.H. Hong, T. Matusita, T. Hayashi, M.S. Dresselhaus, Structural characterization of carbon nanofibers obtained by hydrocarbon pyrolysis, Carbon, 39 (**2001**) 2003-2010.

[39] S. Lim, S.-H. Yoon, I. Mochida, J.-h. Chi, Surface Modification of Carbon Nanofiber with High Degree of Graphitization, The Journal of Physical Chemistry B, 108 (**2004**) 1533-1536.

CHAPTER VI

Catalytic tests

6.1 Introduction

After the preparation and characterization steps, the catalyst must be tested in a chemical reaction to evaluate its catalytic activity and selectivity towards the main product. In our case, all palladium catalysts were tested in the selected chemical reaction. Furthermore, three bimetallic catalysts were also prepared to be evaluated in the selected chemical reaction. Finally, recycling tests were performed using the best catalysts in both cases for the selected chemical reaction.

To clearly understand the structural order of this Chapter VI: Catalytic tests, the main issues are summarized in Table 6.1.

Table 6.1 Main issues of Chapter VI.

Issues
6.2 Reactants
6.3 Aerobic ethanol oxidation
6.4 Possible pathway and reaction mechanism for ethanol oxidation to acetic acid
6.5 Review of reaction conditions for ethanol oxidation to acetic acid
6.6 Equipment used in the catalytic tests
6.7 Optimization of reaction conditions
6.8 Results obtained of aerobic ethanol oxidation using all Pd catalysts
6.9 Recycling tests using the best Pd catalyst
6.10 Preparation and characterization of bimetallic catalysts
6.11 Results obtained of aerobic ethanol oxidation using the bimetallic catalysts
6.12 Recycling tests using the best bimetallic catalyst
6.13 Summary
6.14 References

6.2 Reactants

Many reactants were purchased from Sigma-Aldrich such as ethanol (99.8%, C_2H_6O), diethyl ether (>99.8%, $C_4H_{10}O$), ethyl acetate (>99.5, $C_4H_8O_2$), acetaldehyde (99.5%, C_2H_4O), acetic acid (>99.8%, $C_2H_4O_2$), acetonitrile (>99.9%, C_2H_3N), toluene (>99.7%, C_7H_8), acetone (>99.5%, C_3H_6O), palladium (II) nitrate dihydrate (~40% Pd basis, PdN_2O_6 $2H_2O$), gold (I) chloride (97%, AuCl), cobalt (II) nitrate hexahydrate (99%, CoN_2O_6 $6H_2O$), and ruthenium (III) nitrosyl nitrate, solution [1.5% Ru, $Ru(NO)(NO_3)_3$]. Nitrogen (99.999%, N_2), and hydrogen (99.999% H_2) were purchased from Air Liquide.

6.3 Aerobic ethanol oxidation

Among the most important reactions, the oxidation of alcohols is one of them. Aerobic ethanol oxidation to acetic acid is a useful route to produce carboxylic acids from oxidation of alcohols under aerobic conditions. Ethanol is a primary alcohol and renewable fuel used as starting material in different chemical reactions such as ester formation, dehydration, combustion, halogenation and/or oxidation. In our case, aerobic oxidation of ethanol to acetic acid is the selected chemical reaction to test all palladium catalysts.

Along with ethanol, acetic acid is a colourless liquid, weak acid, and the most important of the carboxilic acids. Acetic acid is widely used for different uses and applications such as acidic component of vinegar, acidity regulator in foods, household cleaner for windows and mirrors, chemical reagent to produce vinyl acetate, and precursor to photographic films, inks, dyes, and synthetic fibers.

Presently, 75% of acetic acid is formed *via* methanol carbonylation using fossil resources, and 25% by other processes, including classical fermentation. [1] Gold, [2] ruthenium, [3] and palladium [4] supported catalysts are active for aerobic ethanol oxidation.

6.4 Possible pathway and reaction mechanism for ethanol oxidation to acetic acid

A controlled ethanol oxidation reaction leads to acetic acid. In an incomplete reaction, by-products can be formed due to different parameters such as reaction temperature, oxidizing agent pressure, catalyst weight, solution volume, and ethanol concentration. The by-products commonly formed are acetaldehyde, ethyl acetate, and carbon dioxide, which result in different concentrations depending on the reaction conditions. The catalyst and the reaction time can control high ethanol conversion and high selectivity towards acetic acid. Parameters such as ethanol conversion, selectivity towards acetic acid, and reaction time are mainly used to determine the catalyst performances. Another very important parameter in liquid phase reactions is the solvent, which allows a good interaction between the reactant and the catalyst. After the chemical reaction, the main product separation from the solvent must be considered due to additional costs in this process.

Scheme 6.1 shows a possible pathway for ethanol oxidation to acetic acid. [5] The chemical equilibrium from ethanol to acetic acid is promoted when the stoichiometric ratio is achieved. A stoichiometric change on the ethanol oxidation reaction to acetic acid leads to undesired products and a different chemical equilibrium. Therefore, all parameters already mentioned above, play a very important role on the chemical reaction advancement.

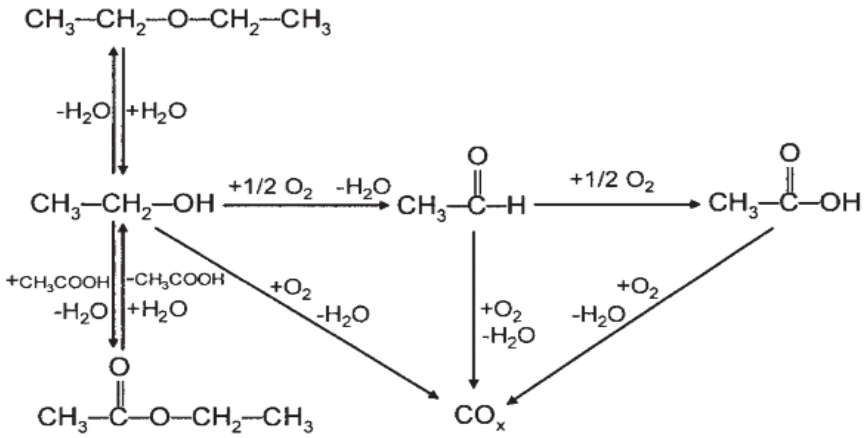

Scheme 6.1 A possible pathway for ethanol oxidation to acetic acid.

According to the possible pathway for ethanol oxidation to acetic acid, a reaction mechanism is proposed to clearly understand the ethanol oxidation reaction in presence of an oxidizing agent and in liquid phase as showed in scheme 6.2. An ethanol molecule is oxidized by 0.5 moles of molecular oxygen to form the acetaldehyde hydrate. If a water molecule is removed from the acetaldehyde hydrate, the acetaldehyde is formed; otherwise the acetaldehyde hydrate will newly be oxidized by 0.5 moles of molecular oxygen to form acetic acid when a second water molecule is removed.

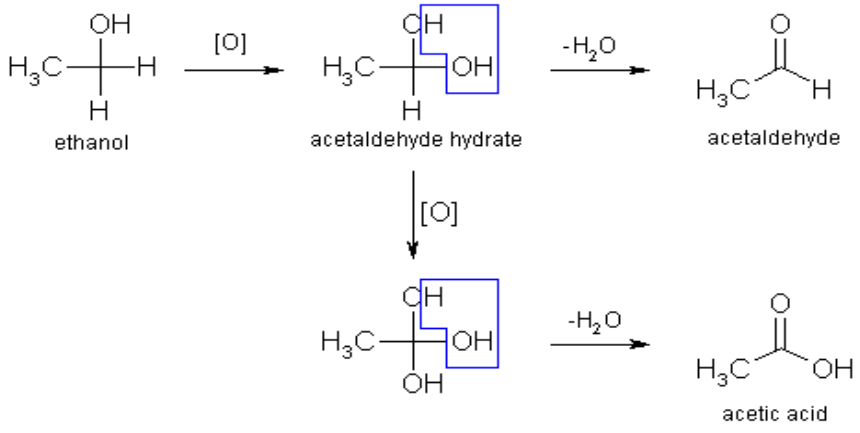

Scheme 6.2 A reaction mechanism for ethanol oxidation to acetic acid.

6.5 Review of reaction conditions for ethanol oxidation to acetic acid

A detailed review of reaction conditions for ethanol oxidation to acetic acid was performed before starting the catalytic tests. The following information allowed identifying the best reaction conditions to carry out the reaction catalyzed by our palladium catalysts.

In this study, ethanol concentrations of 5 % in water were used. Gold supported on titanium oxide or zinc oxide showed a high initial activity towards ethanol oxidation. Ethanol conversions of >90 % was achieved. After 10 h of reaction about 80 % of ethanol conversion was observed. An ethanol conversion of 93 % was observed when 1 % Au/TiO_2 was used in reactions conducted for longer than 20 h, at 150 °C, and 48 bar O_2. When a slight excess oxygen was used, an ethanol conversion of 99.4 %, with an acetic acid selectivity of 99.8 % were achieved. The activities seen when using 1 % Au/ZnO and 1 % Au/TiO_2 were similar. TEM images were used to confirm the presence of gold in the catalysts. [6] The gold particle size distributions seen with Au/TiO_2 and Au/ZnO were very narrow with most of the particles being in the range of 2 to 3 nm.

The conversion of ethanol was observed to decrease with increasing ethanol concentration at a given time. Ethanol conversion of 93 % was achieved in all reactions with different initial ethanol concentration after the reactions had been run for 4 days. At high initial ethanol concentrations, the production of ethyl acetate becomes more apparent, as was reported by Christiansen *et al*. [7] At 40 wt% initial ethanol concentration, ethyl acetate is the major product after 20 h. The yield of acetic acid using the Au/TiO_2 catalyst decreased from 75 to 19 % with increasing initial ethanol concentration in the range 5 – 40 wt%, respectively. [8]

Another study revealed that $MgAl_2O_4$-supported Pt and Pd catalysts have received attention as catalysts for ethanol oxidation.[9] The catalytic oxidation of alcohols with air has also attracted significant attention as a "green" reaction.[10] Among the heterogeneous catalysts, mainly Pd and Pt have shown promising results.[11, 12] A $MgAl_2O_4$-supported Au catalyst was also used in this study, it has exhibited similar or higher catalytic activity than Pt or Pd catalysts, and a significantly higher selectivity towards acetic acid than both of these well-known catalysts. The major by-product for the Au catalyst is CO_2, whereas the Pt and Pd catalysts also produce significant amounts of acetaldehyde. During the reaction, the solution became more and more acidic, but this did not influence the catalyst performance. It is seen that Au catalysts are indeed able to selectively oxidize ethanol to acetic acid in air at moderate temperatures and dioxygen pressures with very high yields. [13]

Another study showed highly selective and efficient aerobic oxidation of aqueous ethanol (2.5-50 wt%) to acetic acid with Al_2O_3-, CeO_2-, $MgAl_2O_4$-, and TiO_2-supported ruthenium hydroxide catalysts at elevated temperatures and oxygen pressures. Under the applied reaction conditions a change in ethanol concentration had only minor effect on the yields. However, a temperature of 125 °C or higher was needed to give high yield of acetic acid. At temperatures about 200 °C, over oxidation of the ethanol was observed leading to lower acetic acid selectivity and yields. The performance of catalysts based on different supports increased in the order $Ru(OH)_x/TiO_2$ < $Ru(OH)_x/Al_2O_3$ < $Ru(OH)_x/MgAl_2O_4$ < $Ru(OH)_x/CeO_2$ when applying identical reaction conditions. Furthermore, the activity of the CeO_2-supported $Ru(OH)_x$ catalyst was found to be dependent on the ruthenium species loaded on the surface of the support.

Increases in ruthenium loading gave larger particle sizes, as expected, and thereby lower catalytic activity. The optimal performance was found to occur with approximately 1 wt% $Ru(OH)_x$ loading with a particle size of 0.6-2 nm. Above this loading a decrease of the catalytic activity contributed by ruthenium species was found. Furthermore, calcination of the catalysts gave lower activity, which most likely was due to a combination of dehydration and sintering of the small Ru-containing particles. Quantitative yield of acetic acid was obtained with a 1.2 wt% $Ru(OH)_x/CeO_2$ catalyst at reaction conditions of 150 °C, 10 bar O_2 after 12 h of reaction time. [14]

Another study exposed that Pd nanoparticles supported on carbon nanotubes were used in the selective oxidation of ethanol in liquid phase. The characterization of the surface and bulk properties combined with the catalytic tests indicated the dissolution and redeposition of Pd under the reaction conditions. Nitrogen-doped carbon nanotubes were found to act as an excellent support for the Pd catalyst system by efficiently stabilizing and recapturing the Pd species, which resulted in high activity and selectivity to acetic acid. [15]

Finally, another study revealed that the main reason for specifically studying the ethanol oxidation is because the ethanol could be one of the future feedstocks of the chemical industry. The reaction mixture contained 0.1 g of Pd/N-CNT, 1 wt% of ethanol in 10 mL of toluene, 5 bar air, at 80 °C for 3 h. Ethanol conversion of 23 % and selectivity towards acetic acid of 95 % were achieved. [16]

Table 6.2 shows the reaction conditions according to the literature for ethanol oxidation reaction to acetic acid. The work ranges for reaction conditions were identified before starting the catalytic tests.

Ethanol concentration ranging from 1 to 50 wt%, catalyst weight ranging from 0.03 to 0.21 g, air pressure ranging from 5 to 50 bar, temperature ranging from 80 to 250 °C, reaction time ranging from 3 to 20 h, stirring ranging from 400 to 500 rpm, solution volume for all cases 10 mL, water or toluene as solvent, metal percentage ranging from 1 to 2 %, and kind of catalyst depending on the metal (*e.g.*, Au, Pt, Ru, Pd) and the support (*e.g.*, metal oxides, carbon nanomaterials).

According to the work ranges, we selected those reaction conditions more used for ethanol oxidation reaction to acetic acid (see section 6.7)

Table 6.2 Comparison of the reaction conditions according to the literature for ethanol oxidation reaction to acetic acid.

Reaction conditions	S. M. Tembe *et al.* [7]	C. H. Christensen *et al.* [12]	Y. Y. Gorbanev *et al.* [13]	W. Dong *et al.* [14]	A. Benyounes *et al.* [15]
Ethanol concentration (wt%)	5 – 40	5	2.5 – 50	5	1
Catalyst weight (g)	0.15	0.15	0.21	0.03 - 0.12	0.1
Kind of catalyst	**Au/TiO_2*** Au/ZnO Au/Al_2O_3	**$Au/MgAl_2O_4$*** $Pt/MgAl_2O_4$ $Pd/MgAl_2O_4$	$Ru(OH)_X/TiO_2$ $Ru(OH)_X/Al_2O_3$ $Ru(OH)_X/MgAl_2O_4$ **$Ru(OH)_X/CeO_2$***	Pd/OCNT **Pd/NCNT-NH_3*** Pd/NCNT-G	Pd/CNT **Pd/N-CNT***
Air pressure (bar)	48	25 – 50	10 – 30	30	5
Temperature (°C)	150	100 – 200	125 – 250	80 – 180	80
Reaction time (h)	20	4	3	5	3
Stirring (rpm)	400	-	500	-	-
Volume (mL)	10	10	10	10	10
Solvent	Water	Water	Water	Water	Toluene
Metal percentage (%)	1	1	1	-	2
Ethanol conversion (%)	93	97	99	82	23
Acetic acid yield (%)	85	83	96	70	22
Acetic acid selectivity (%)	97	85	97	85	95
TOF (h^{-1})	94[a]	294[b]	73[c]	209[d]	26[e]

*Catalyst used to determine the ethanol conversion, the acetic acid yield, the selectivity towards acetic acid, and the TOF.
At [a]5, [b]4, [c]3, [d]5, and [e]3 h of reaction time, respectively.

6.6 Equipment used in the catalytic tests

All experiments were performed using a batch reactor, a Clarus 500 gas chromatograph, and a TitroLine KF trace titrator in those experiments in which toluene was used as solvent.

6.6.1 Batch reactor

The oxidation experiments were conducted in a 65 mL stainless steel autoclave reactor equipped with magnetic stirring, temperature controller, pressure controller, air pressurizer and heated in a silicone oil bath as shown in Figure 6.1.

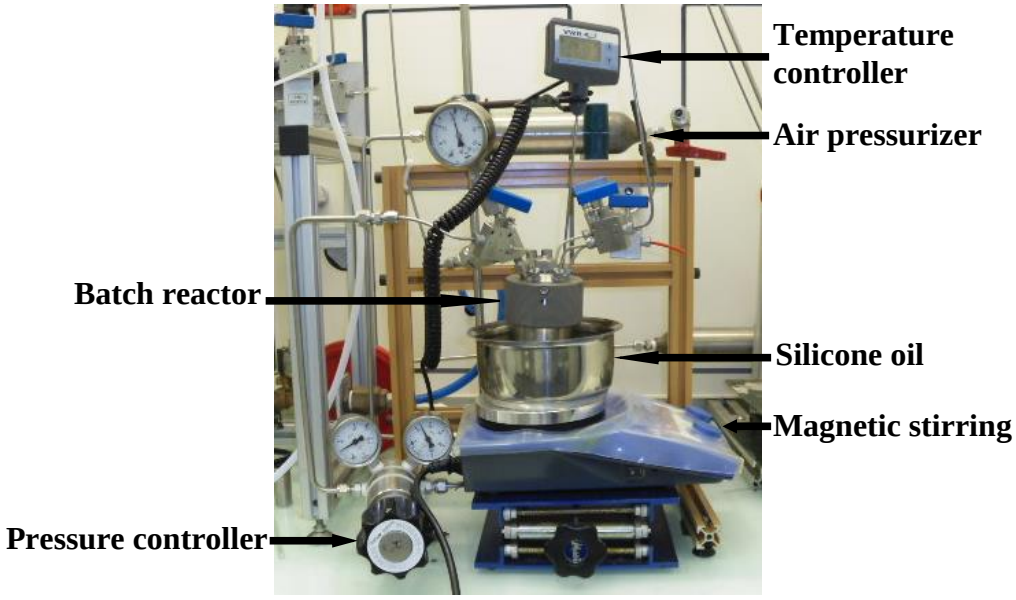

Figure 6.1 65 mL stainless steel autoclave reactor.

6.6.2 Clarus 500 gas chromatograph

The analyses were performed with a Clarus 500 gas chromatograph equipped with a split/splitless injector, a capillary column (Stabilwax®-DA Fused Silica 30 m, 0.25 mm i.d.) and a flame ionization detector (FID) as shown in Figure 6.2.

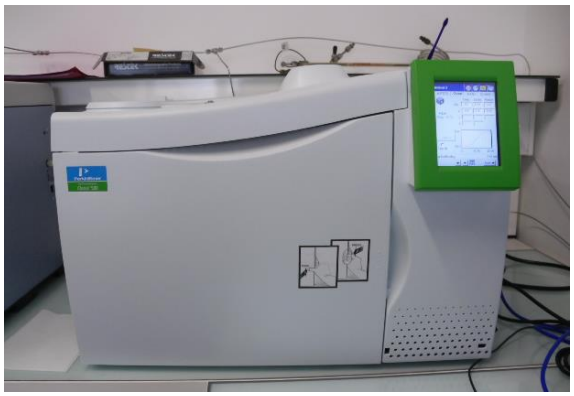

Figure 6.2 Clarus 500 gas chromatograph.

6.6.3 TitroLine KF trace titrator

The liquid reaction mixture was analyzed by Coulometry using a TitroLine KF trace titrator equipped with a magnetic stirrer and an electrode with diaphragm as shown in Figure 6.3.

Figure 6.3 TitroLine KF trace titrator.

6.7 Optimization of reaction conditions

According to Chapter V: Discussion, section 5.3.8, we selected between the best palladium catalysts, the Pd/FC_{-COOH} catalyst as the sacrificed catalyst to find the best reaction conditions.

The reactor was charged with 10 mL of 5 wt% ethanol in toluene and the desired Pd/FC_{-COOH} catalyst weight (0.05-0.15 g). The reactor was then closed and heated at 150 °C. The reactor was then pressurized with technical air (80 vol% N_2 and 20 vol% O_2) at 30 bar. The reaction was allowed to stir for 3 h. The stirring rate was kept constant at 400 rpm for all experiments. When the reaction was finished, the reactor was cooled with an ice-water mixture at a temperature below 5 °C, to ensure that the volatile products such as acetaldehyde remain in solution before analysis. [8] The analyses were performed with the Clarus 500 gas chromatograph. After the reaction, the catalyst was separated from the liquid reaction mixture by filtration and the liquid reaction mixture was analyzed by Coulometry to determine the water amount from ethanol oxidation reaction using the TitroLine KF trace titrator.

Table 6.3 shows the results obtained for ethanol oxidation reaction to acetic acid using the Pd/FC_{-COOH} catalyst at different catalyst weights. It is seen that the ethanol conversion and selectivity towards acetic acid (AcOH) increase when the catalyst weight is increased. This effect is also observed in the water (H_2O) amount formed during the reaction. In contrast, the acetaldehyde (AcH) amount decreases when employing higher catalyst weights. Ethyl acetate amount was perceived when using toluene as solvent in the reaction. Carbon dioxide (CO_2) formation was also detected as a result of total oxidation.

Therefore, a catalyst weight of 0.1 g was selected as the top extent to test all palladium catalysts (see Table 6.3, Entry 2).

Table 6.3 Main product distribution in the ethanol oxidation reaction using the Pd/FC_{-COOH} catalyst at different catalyst weights[a].

Entry	Catalyst weight (g)	Ethanol conversion (%)	Products selectivity (%)			H_2O (ppm)
			CO_2	AcH	AcOH	
1	0.05	50	0	10	90	403
2	0.10	58	5	7	88	490
3	0.15	65	6	3	91	571

[a]Reaction conditions: 10 mL of 5 wt% ethanol in toluene, 2 wt% Pd/FC_{-COOH}, 150 °C, 30 bar air, and 3 h of reaction time.

Once the catalyst weight was determined, we tested with 0.1 g Pd/FC_{-COOH} catalyst for all experiments to find the best reaction temperature and air pressure.

Thus, the reactor was newly charged with 10 mL of 5 wt% ethanol in toluene and 0.1 g Pd/FC_{-COOH} catalyst. The reactor was then closed and heated to the desired temperature (100-200 °C). The reactor was then pressurized with technical air (80 vol% N_2 and 20 vol% O_2) at desired pressure (10-50 bar). The reaction was allowed to stir for 3 h. The stirring rate was kept constant at 400 rpm for all experiments. When the reaction was finished, the reactor was cooled with an ice-water mixture at a temperature below 5 °C, to ensure that the volatile products such as acetaldehyde remain in solution before analysis. [8] The analyses were performed with the Clarus 500 gas chromatograph. After the reaction, the catalyst was separated from the liquid reaction mixture by filtration and the liquid reaction mixture was analyzed by Coulometry to determine the water amount from ethanol oxidation reaction using the TitroLine KF trace titrator.

Table 6.4 shows the results obtained for ethanol oxidation reaction to acetic acid using 0.1 g Pd/FC$_{-COOH}$ catalyst at different reaction temperatures and air pressures. It is seen that the ethanol conversion and selectivity towards acetic acid increase when the reaction temperature is increased, except for the ethanol conversion at 10 bar of air pressure, which decreases, but not its selectivity towards acetic acid. The acetaldehyde amount decreases when using higher reaction temperatures. In contrast, the ethanol conversion increases and the selectivity towards acetic acid decreases when the air pressure is increased. The acetaldehyde amount increases when employing higher air pressures. This effect is also detected in the carbon dioxide formed during the reaction. Ethyl acetate amount was newly perceived when using toluene as solvent in the reaction.

Therefore, a reaction temperature of 175 °C and an air pressure of 30 bar were selected as the top extents to test all palladium catalysts (see Table 6.4, Entry 9).

Table 6.4 Main product distribution in the ethanol oxidation reaction using the Pd/FC$_{-COOH}$ catalyst at different reaction temperatures and air pressures[a].

Entry	T (°C)	P (bar)	Ethanol conversion (%)	Products selectivity (%)			H_2O (ppm)
				CO_2	AcH	AcOH	
1	100	Air/10	33	64	12	24	434
2	125	Air/10	30	63	10	27	818
3	150	Air/10	54	8	2	90	573
4	175	Air/10	46	7	0	93	736
5	200	Air/10	38	8	0	92	439
6	100	Air/30	24	40	21	39	524
7	125	Air/30	41	1	19	80	684
8	150	Air/30	66	21	3	76	403
9	175	Air/30	75	15	0	85	464
10	200	Air/30	69	9	0	91	663
11	100	Air/50	36	58	14	28	534
12	125	Air/50	49	67	18	15	711
13	150	Air/50	69	23	9	68	506
14	175	Air/50	83	25	2	73	627
15	200	Air/50	86	19	0	81	845

[a]Reaction conditions: 10 mL of 5 wt% ethanol in toluene, 2 wt% Pd/FC$_{-COOH}$, 0.1 g of catalyst, and 3 h of reaction time.

The selected reaction conditions (*e.g.*, 0.1 g Pd/FC$_{-COOH}$ catalyst, 175 °C, and 30 bar air) as the top extents lead to high ethanol conversion and selectivity towards acetic acid, and low acetaldehyde amount, as expected.

Figure 6.4 shows the Pd/FC$_{-COOH}$ catalyst [a) fresh and b) spent] under the best reaction conditions (see Table 6.4, Entry 9). A small change on the palladium particle size was observed. Larger palladium particle sizes were measured on the spent Pd/FC$_{-COOH}$ catalyst compared to that fresh Pd/FC$_{-COOH}$ catalyst.

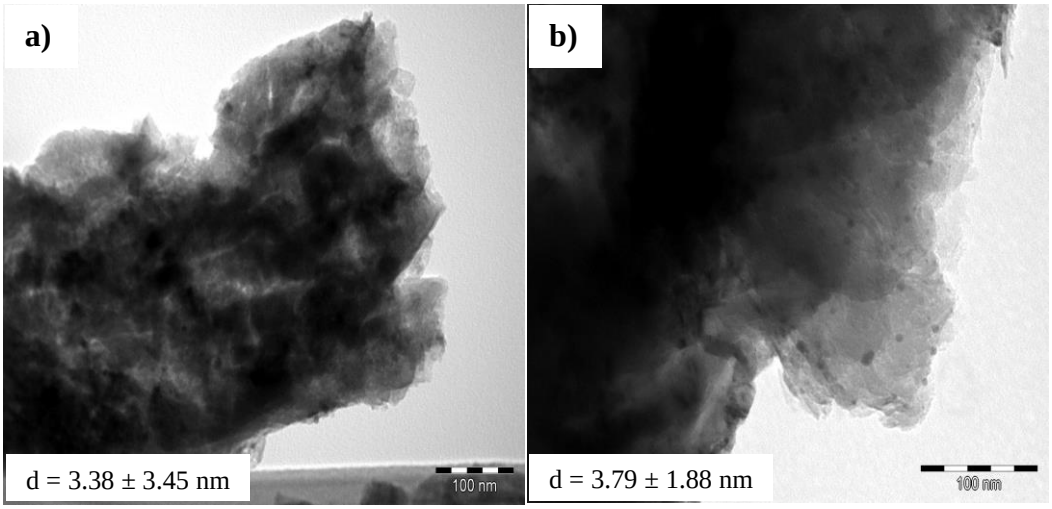

Figure 6.4 TEM micrographs of the Pd/FC$_{-COOH}$ catalyst. a) fresh and b) spent. Scale bar for all micrographs: 100 nm.

6.8 Results obtained of aerobic ethanol oxidation using all Pd catalysts

After the optimization of reaction conditions, all palladium catalysts were tested under the best reaction conditions.

6.8.1 Toluene as solvent

A very important parameter for a catalyzed chemical reaction in the liquid phase is the solvent, which allows the interaction between the reactant and the catalyst. This solvent must be friendly for both. Hence, we selected toluene as solvent to carry out the catalytic tests using all palladium catalysts.

Thus, the reactor was newly charged with 10 mL of 5 wt% ethanol in toluene and 0.1 g of the desired palladium catalyst (see Table 4.49). The reactor was then closed and heated at 175 °C. The reactor was then pressurized with technical air (80 vol% N_2 and 20 vol% O_2) at 30 bar. The reaction was allowed to stir for 3 h. The stirring rate was kept constant at 400 rpm for all experiments. When the reaction was finished, the reactor was cooled with an ice-water mixture at a temperature below 5 °C, to ensure that the volatile products such as acetaldehyde remain in solution before analysis. [8] The analyses were performed with the Clarus 500 gas chromatograph. After the reaction, the catalyst was separated from the liquid reaction mixture by filtration and the liquid reaction mixture was analyzed by Coulometry to determine the water amount from ethanol oxidation reaction using the TitroLine KF trace titrator.

Table 6.5 shows the results obtained for ethanol oxidation reaction to acetic acid using the desired palladium catalyst under the best reaction conditions. Reaction was observed in the absence of catalyst, but very low ethanol conversion and selectivity towards acetic acid were achieved. In contrast, high carbon dioxide formation was detected. It is seen that the TOF and selectivity towards acetic acid significantly vary between all palladium catalysts. This effect is also observed on the acetaldehyde and carbon dioxide amounts formed in the reaction. Ethyl acetate amount was newly perceived when using toluene as solvent in the reaction. Among ethanol conversion, selectivity towards acetic acid, acetaldehyde amount, carbon dioxide formed, and catalyst activity (TOF), a balance must be found to select the best palladium catalyst.

According to that, the Pd/S_2-CNT catalyst exhibited >95 % ethanol conversion, >98 % selectivity towards acetic acid, <2 % acetaldehyde produced, no carbon dioxide formed, and 218 h^{-1} TOF, therefore, it is considered as the best palladium catalyst (see Table 6.5, Entry 10). Furthermore, the palladium catalysts supported on commercial silica-alumina did not expose high catalytic activity compared to the palladium catalysts supported on carbon nanomaterials.

Table 6.5 Main product distribution in the ethanol oxidation reaction using all Pd catalysts[a].

Entry	Catalyst	Ethanol conversion (%)	Products selectivity (%)			H_2O (ppm)	TOF (h^{-1})[b]
			CO_2	AcH	AcOH		AcOH
1	without catalyst	37	92	3	5	3487	-
2	Pd/CNT	92	8	1	91	527	296
3	Pd/CNT_{-COOH}	98	6	0	94	560	174
4	Pd/CNT_{HT}	97	2	0	98	561	229
5	Pd/$CNT_{-COOH\ HT}$	96	12	0	88	566	172
6	Pd/N:CNT	96	15	0	85	724	174
7	Pd/N:CNT_{HT}	87	9	2	89	606	261
8	Pd/S_1-CNT	97	1	0	99	737	203
9	Pd/S_1-CNT_{HT}	80	11	1	88	600	288
10	Pd/S_2-CNT	96	1	0	99	889	218
11	Pd/S_2-CNT_{HT}	91	4	0	96	902	232
12	Pd/FLG	95	30	1	69	450	143
13	Pd/FLG_{-COOH}	96	3	0	97	523	192
14	Pd/FLG_{HT}	96	16	0	84	570	187
15	Pd/$FLG_{-COOH\ HT}$	93	15	1	84	452	199
16	Pd/CNF	94	16	0	84	441	184
17	Pd/CNF_{-COOH}	97	5	0	95	509	209
18	Pd/CNF_{HT}	89	4	2	94	408	273
19	Pd/$CNF_{-COOH\ HT}$	94	5	0	95	650	244
20	Pd/FC	88	23	0	77	387	174
21	Pd/FC_{-COOH}	75	15	0	85	464	120
22	Pd/FC_{HT}	89	1	0	99	420	228
23	Pd/$FC_{-COOH\ HT}$	78	29	4	67	540	125
24	Pd/SiO_2-Al_2O_3 (n/c)	73	23	8	69	1555	102
25	Pd/SiO_2-Al_2O_3 (c)	80	36	1	63	1150	112

[a]Reaction conditions: 10 mL of 5 wt% ethanol in toluene, 2 wt% Pd, 0.1 g of catalyst, 30 bar air, 175 °C, and 3 h of reaction time.

[b]$mol_{AcOH\ produced}/(mol_{Pd}\ time)$, at 3 h.

Figure 6.5 shows the Pd/S_2-CNT catalyst [a) fresh and b) spent] under the best reaction conditions (see Table 6.5, Entry 10). A significant change on the palladium particle size was observed. Larger palladium particle sizes were measured on the spent Pd/S_2-CNT catalyst compared to that fresh Pd/S_2-CNT catalyst.

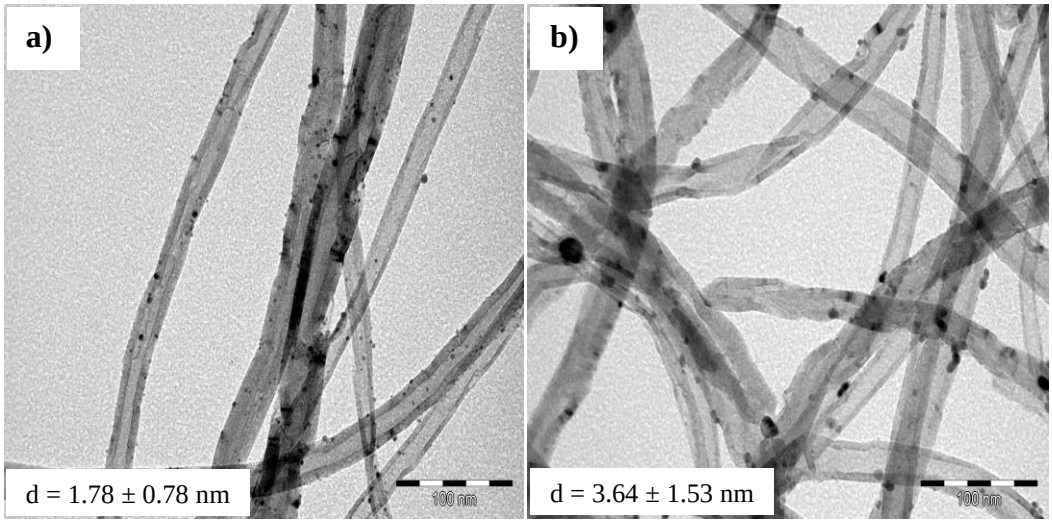

Figure 6.5 TEM micrographs of the Pd/S_2-CNT catalyst. a) fresh and b) spent. Scale bar for all micrographs: 100 nm.

6.8.2 Water as solvent

Among the most important reaction parameters, the solvent is one of them. We used water instead toluene as solvent to observe the influence of a polar media compared to a non-polar media. Besides, the use of water as solvent decreases costs and environmental damages. Therefore, the reactor was newly charged with 10 mL of 5 wt% aqueous ethanol and 0.1 g of the desired palladium catalyst (see Table 4.49). The reactor was then closed and heated at 175 °C. The reactor was then pressurized with technical air (80 vol% N_2 and 20 vol% O_2) at 30 bar. The reaction was allowed to stir for 3 h. The stirring rate was kept constant at 400 rpm for all experiments.

When the reaction was finished, the reactor was cooled with an ice-water mixture at a temperature below 5 °C, to ensure that the volatile products such as acetaldehyde remain in solution before analysis. [8] The analyses were performed with the Clarus 500 gas chromatograph. After the reaction, the catalyst was separated from the liquid reaction mixture by filtration.

Table 6.6 shows the results obtained for ethanol oxidation reaction to acetic acid using the desired palladium catalyst under the best reaction conditions. It is seen that the ethanol conversion and selectivity towards acetic acid significantly vary between all palladium catalysts. An effect is also observed on the acetaldehyde and carbon dioxide amounts formed in the reaction. No ethyl acetate amount was perceived when using water as solvent in the reaction. Among ethanol conversion, selectivity towards acetic acid, acetaldehyde amount, carbon dioxide formed, and catalyst activity (TOF), a balance must be found to select the best palladium catalyst. According to that, the $Pd/CNF_{-COOH\ HT}$ catalyst exhibited >87 % ethanol conversion, >94 % selectivity towards acetic acid, <4 % acetaldehyde produced, <3 % carbon dioxide formed, and 228 h^{-1} TOF, therefore, it is considered as the best palladium catalyst (see Table 6.6, Entry 16).

Furthermore, the palladium catalysts supported on high temperature treated carbon nanomaterials were not used for aerobic ethanol oxidation to acetic acid when using water as solvent due to their high hydrophobic character.

No reaction was observed in the absence of catalyst. This means that the reaction does not work without catalyst in aqueous media. But, the reaction works when using a non-aqueous media (*e.g.*, in toluene).

Table 6.6 Main product distribution in the ethanol oxidation reaction using all Pd catalysts[a].

Entry	Catalyst	Ethanol conversion (%)	Products selectivity (%)			TOF (h^{-1})[b]
			CO_2	AcH	AcOH	AcOH
1	without catalyst	0	0	0	0	-
2	Pd/CNT	74	0	7	93	243
3	Pd/CNT_{-COOH}	63	1	21	78	93
4	$Pd/CNT_{-COOH\ HT}$	43	1	20	79	69
5	Pd/N:CNT	98	13	8	79	165
6	$Pd/N:CNT_{HT}$	55	0	35	65	121
7	Pd/S_1-CNT	83	8	5	87	153
8	Pd/S_1-CNT_{HT}	68	35	6	59	164
9	Pd/S_2-CNT	80	0	11	89	163
10	Pd/S_2-CNT_{HT}	71	0	23	77	145
11	Pd/FLG	92	0	10	90	181
12	Pd/FLG_{-COOH}	87	0	5	95	170
13	$Pd/FLG_{-COOH\ HT}$	74	0	3	97	183
14	Pd/CNF	75	1	4	95	166
15	Pd/CNF_{-COOH}	75	0	11	89	151
16	$Pd/CNF_{-COOH\ HT}$	88	2	3	95	228
17	Pd/sCNF	55	0	9	91	113
18	$Pd/sCNF_{-COOH}$	91	1	5	94	196
19	$Pd/sCNF_{-COOH\ HT}$	58	16	7	77	131
20	Pd/FC	48	0	25	75	92
21	Pd/FC_{-COOH}	83	0	7	93	145
22	$Pd/FC_{-COOH\ HT}$	68	0	4	96	156

[a]Reaction conditions: 10 mL of 5 wt% aqueous ethanol, 2 wt% Pd, 0.1 g of catalyst, 30 bar air, 175 °C, and 3 h of reaction time.
[b]$mol_{AcOH\ produced}/(mol_{Pd}\ time)$, at 3 h.

For some selected catalysts, we also calculated the palladium dispersion from a universal mathematical relation between the mean relative size of metallic crystallites and their dispersion. [17] Palladium catalyst particle size and dispersions are given in Table 6.7. We then used these values of the dispersion to calculate the TOF by mole of surface palladium (see Table 6.7).

Table 6.7 Palladium loading, palladium particle size, palladium dispersion, and TOF on the catalysts.

Catalyst	Pd loading[a] (%)	Pd particle size[b] (nm)	Pd dispersion (%)	TOF[c] (h^{-1})
Pd/CNT	1.60	2.2 ± 1.2	49	1010.9
Pd/CNT_{COOH}	2.04	2.2 ± 1.1	36	374.9
Pd/$CNT_{COOH\ HT}$	1.89	2.1 ± 1.4	49	277.0
Pd/N-CNT	1.81	2.1 ± 0.9	51	650.1
Pd/N-CNT_{HT}	1.14	1.9 ± 1.9	51	432.2
Pd/S_1-CNT	1.82	1.8 ± 0.8	56	525.0
Pd/S_1-CNT_{HT}	0.94	2.6 ± 2.5	58	772.9
Pd/FLG	1.76	3.3 ± 2.9	43	1041.4
Pd/FLG_{COOH}	1.87	2.6 ± 1.6	35	796.1
Pd/$FLG_{COOH\ HT}$	1.51	2.8 ± 3.0	44	923.2
Pd/FC	1.50	3.2 ± 3.3	43	633.2
Pd/FC_{COOH}	2.05	2.4	41	662.8
Pd/$FC_{COOH\ HT}$	1.61	2.5 ± 3.0	36	812.6
Pd/CNF	1.65	2.0 ± 1.2	58	517.7
Pd/CNF_{COOH}	1.70	1.5 ± 0.9	46	583.5
Pd/$CNF_{COOH\ HT}$	1.41	1.9 ± 1.4	44	436.7
Pd/sCNF	1.71	2.5 ± 2.1	53	318.8
Pd/$sCNF_{COOH}$	1.69	1.5 ± 0.7	51	636.6
Pd/$sCNF_{COOH\ HT}$	1.31	1.7 ± 1.7	67	402.9

[a]From ICP. [b]From TEM.
[c]$mol_{AcOH\ produced}$/($mol_{Pd\text{-}surf}$ time), at 3 h.

We find a general tendency for the activity of the catalysts according to the palladium particle size: the lower the particle size, the lower the TOF (see Figure 6.6). A gold nano-size effect in Au/SiO_2 catalysts was already evidenced for ethanol oxidation to acetic acid. [18] In that case, Au particles with an average diameter of 5 nm showed an activity that was about three times that of 3 nm particles. It is important to note that in our case it is a rough tendency, which strongly depends also on the nature of the support, and maybe of its surface chemistry.

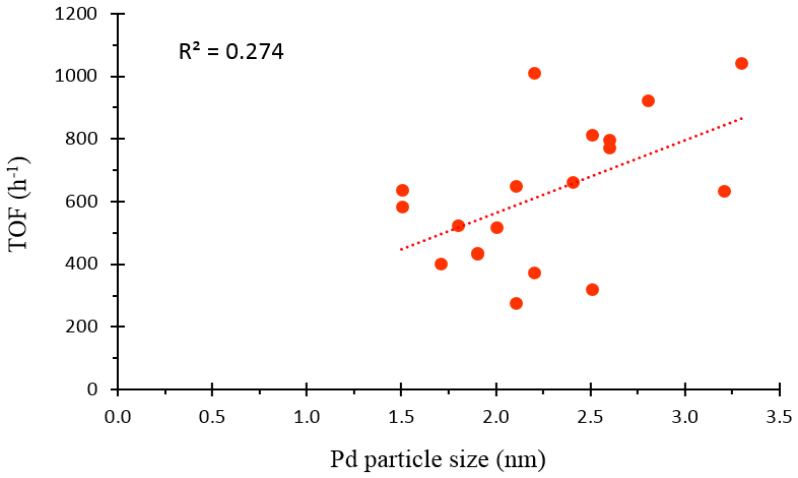

Figure 6.6 Influence of palladium particle size on the TOF.

Indeed, if very good correlations were found for FLG, S-CNT, and N-CNT supports (see Figure 6.7), no correlations exist for CNF and sCNF (see Figure 6.7).

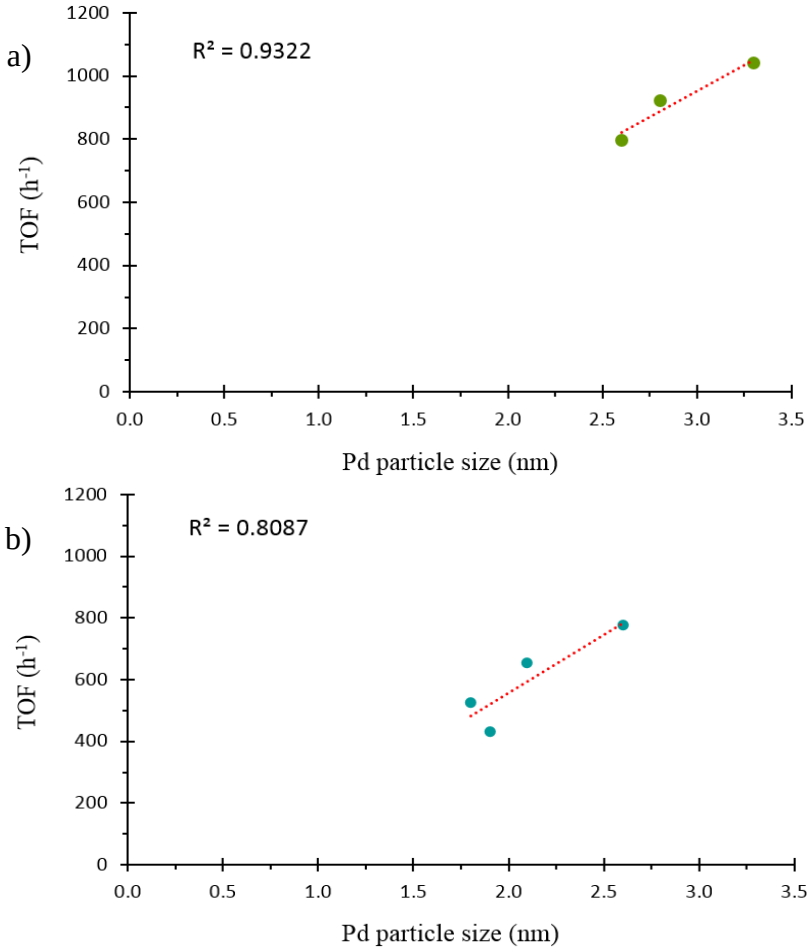

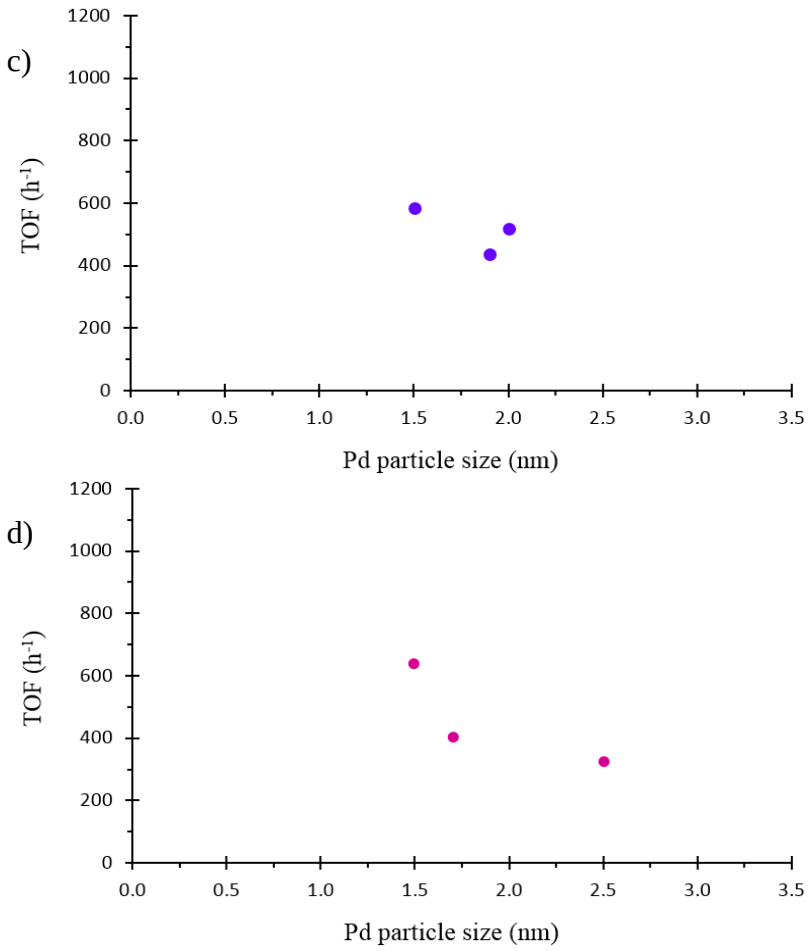

Figure 6.7 Influence of palladium particle size on the TOF for: a) FLG, b) N-CNT and S-CNT, c) CNF, and d) sCNF.

No specific influence of the palladium particle size on AcOH selectivity was noticed (see Figure 6.8).

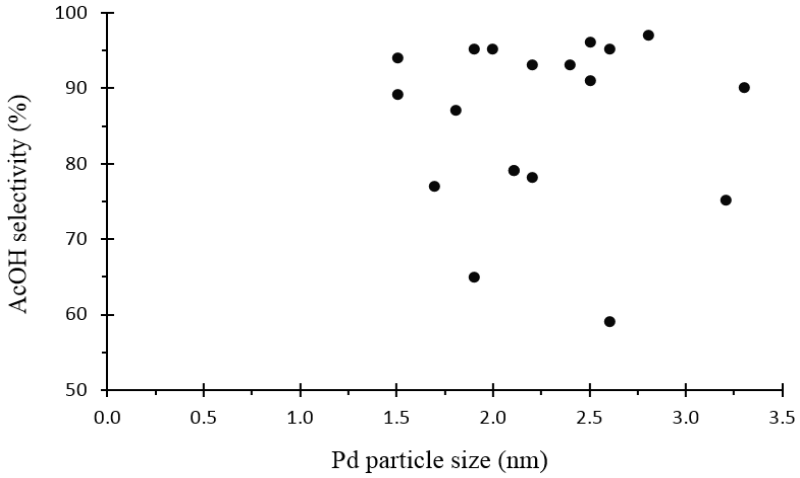

Figure 6.8 Influence of palladium particle size on AcOH selectivity.

Figure 6.9 shows the Pd/CNF$_{\text{-COOH HT}}$ catalyst [a) fresh and b) spent] under the best reaction conditions (see Table 6.6, Entry 16). A significant change on the palladium particle size was observed. Larger palladium particle sizes were measured on the spent Pd/CNF$_{\text{-COOH HT}}$ catalyst compared to the fresh Pd/CNF$_{\text{-COOH HT}}$ catalyst.

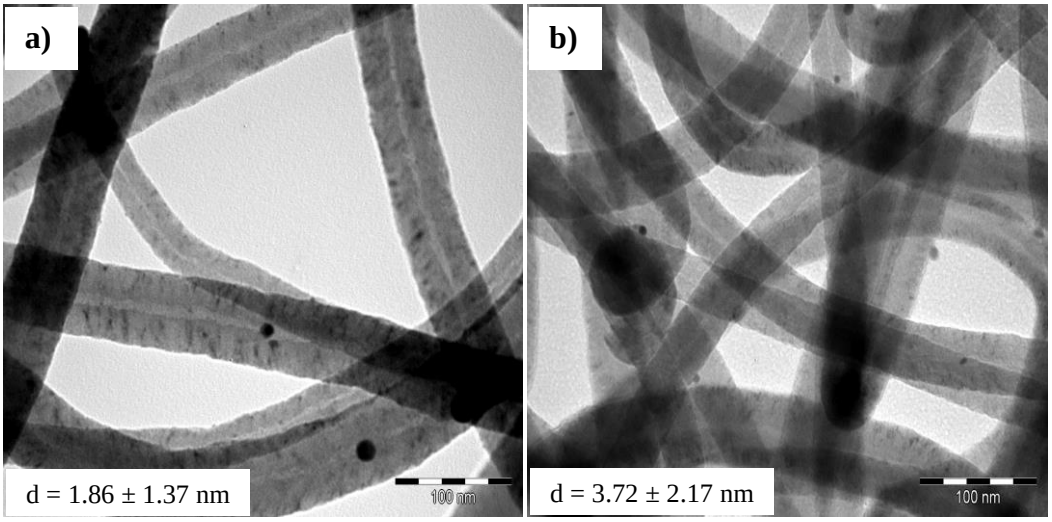

Figure 6.9 TEM micrographs of the Pd/CNF$_{\text{-COOH HT}}$ catalyst. a) fresh and b) spent. Scale bar for all micrographs: 100 nm.

Moreover, we compared the ethanol conversion, the selectivity towards acetic acid and the TOF from Table 6.2 with our results obtained by the Pd/S_2-CNT (see Table 6.5, Entry 10) and Pd/CNF$_{\text{-COOH HT}}$ (see Table 6.6, Entry 16) catalysts, which are considered as the best palladium catalysts for our study. The comparison revealed that the ethanol conversion and selectivity towards acetic acid obtained by using our palladium catalysts were much higher than the ethanol conversion and selectivity towards acetic acid from Table 6.2 for 3 h of reaction time. Both the TOFs from Table 6.2 and our TOFs exhibited similar catalytic activities, considering reaction times between 3 and 5 h.

6.9 Recycling tests using the best Pd catalyst (Pd/CNF$_{\text{-COOH HT}}$)

Among all palladium catalysts, the Pd/CNF$_{\text{-COOH HT}}$ catalyst was selected as the best catalyst for aerobic ethanol oxidation to acetic acid in an aqueous media. Due to its high ethanol conversion, high selectivity towards acetic acid, low acetaldehyde produced, low carbon dioxide formed, and high catalytic activity compared to all the other ones. Recycling tests were performed to evaluate the stability of the Pd/CNF$_{\text{-COOH HT}}$ catalyst.

Thus, the reactor was newly charged with 10 mL of 5 wt% aqueous ethanol and 0.1 g Pd/CNF$_{\text{-COOH HT}}$ catalyst. The reactor was then closed and heated at 175 °C. The reactor was then pressurized with technical air (80 vol% N_2 and 20 vol% O_2) at 30 bar. The reaction was allowed to stir for 3 h. The stirring rate was kept constant at 400 rpm. When the reaction was finished, the reactor was cooled with an ice-water mixture at a temperature below 5 °C, to ensure that the volatile products such as acetaldehyde remain in solution before analysis. [8] The analyses were performed with the Clarus 500 gas chromatograph. After the reaction, the catalyst was separated from the liquid reaction mixture by filtration and then transferred to next test. Table 6.8 shows the results obtained in the recycling tests using the Pd/CNF$_{\text{-COOH HT}}$ catalyst for ethanol oxidation reaction to acetic acid. It is seen that the ethanol conversion and selectivity towards acetic acid significantly decreased after each recycling test. In contrast, the acetaldehyde amount increased.

Table 6.8 Recycling tests in the ethanol oxidation reaction using the Pd/CNF$_{\text{-COOH HT}}$ catalyst[a].

Entry	Reaction cycles	Ethanol conversion (%)	Products selectivity (%)			TOF (h^{-1})[b]
			CO_2	AcH	AcOH	AcOH
1	Test 1	88	2	3	95	228[c]
2	Recycle 1	49	2	10	88	135[d]
3	Recycle 2	28	0	22	78	81[e]
4	Recycle 3	26	4	27	69	80[f]

[a]Reaction conditions: 10 mL of 5 wt% aqueous ethanol, 2 wt% Pd, 0.1 g of Pd/CNF$_{\text{-COOH HT}}$ catalyst, 30 bar air, 175 °C, and 3 h of reaction time. TOF calculated on: [c]100, [d]87, [e]74, and [f]61 mg of catalyst weight, respectively.
[b]$mol_{AcOH\ produced}/(mol_{Pd}\ time)$, at 3 h.

Among the entries 1 and 2, the ethanol conversion decreased up to 44 % and 42 % between the entries 2 and 3 as shown in Figure 6.10.

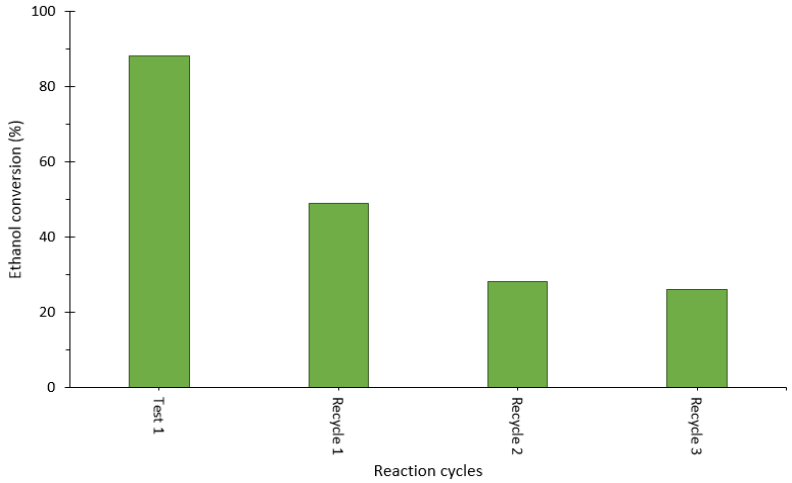

Figure 6.10 Evolution of ethanol conversion on the recycling tests.

Among the entries 1 and 2, the selectivity towards acetic acid also decreased up to 7 % and 11 % between the entries 2 and 3 as shown in Figure 6.11.

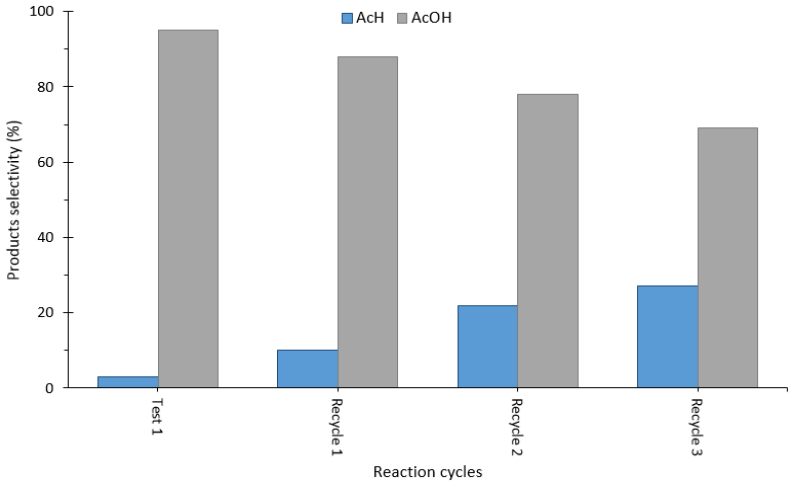

Figure 6.11 Evolution of selectivity towards acetic acid on the recycling tests.

In summary, ethanol conversion and selectivity towards acetic acid lower than the first test could be attributed to a catalyst deactivation by blockage of the surface through strongly adsorbed molecules (*e.g.*, oxygen), reaction products (*e.g.*, acetaldehyde, ethyl acetate, acetic acid, or carbon dioxide), and/or leaching of metal (*e.g.*, palladium) into the liquid reaction mixture.

Figure 6.12 shows the Pd/CNF$_{\text{-COOH HT}}$ catalyst [a) fresh and b) spent after third recycle] under the best reaction conditions (see Table 6.8, Entry 4). A significant change on the palladium particle size was observed. Larger palladium particle sizes were measured and surface damages were also found on the Pd/CNF$_{\text{-COOH HT}}$ catalyst spent after third recycle compared to the fresh Pd/CNF$_{\text{-COOH HT}}$ catalyst.

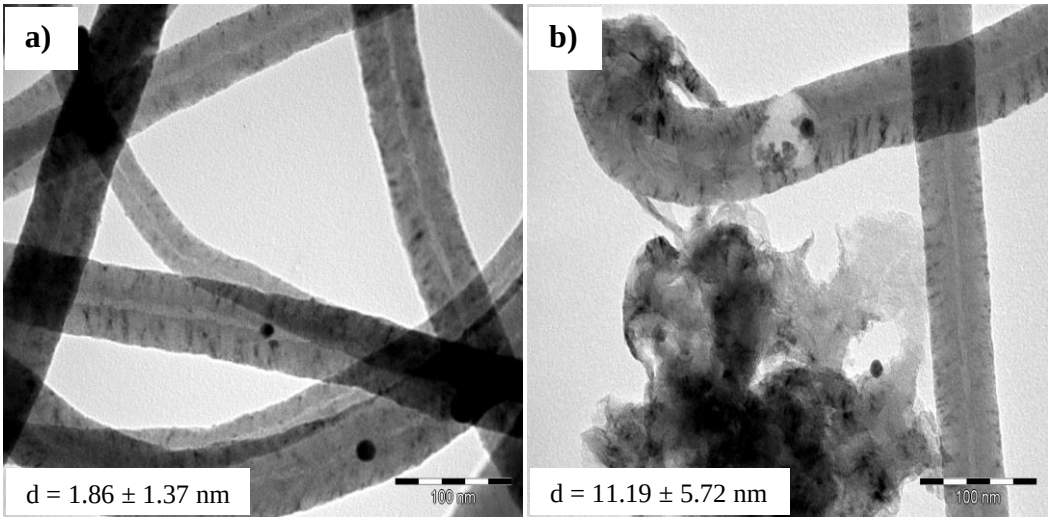

Figure 6.12 TEM micrographs of the Pd/CNF$_{\text{-COOH HT}}$ catalyst. a) fresh and b) spent after third recycle. Scale bar for all micrographs: 100 nm.

Moreover, the liquid reaction mixtures obtained by filtration after the recycling tests did not show significant colour from palladium leaching in the solution (see Figure 6.13).

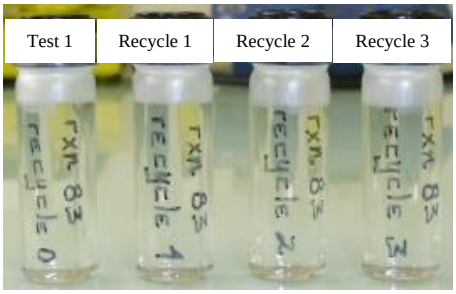

Figure 6.13 Liquid reaction mixtures obtained by filtration after the recycling tests. Reaction time for all cases: 3 h.

Therefore, the recycling tests revealed that the Pd/CNF$_{\text{-COOH HT}}$ catalyst can only be used once, and still maintain high ethanol conversion and selectivity towards acetic acid of 88 % and 95 %, respectively.

6.10 Preparation and characterization of bimetallic catalysts

The incorporation of a second metal on the best monometallic catalyst may increase the activity and selectivity towards main product due to a larger amount of active sites. As already mentioned in section 6.3, certain metals such as gold and ruthenium are often used as active phase for ethanol oxidation to acetic acid. According to that previously mentioned, we selected gold, cobalt, and ruthenium as second metals.

6.10.1 Preparation of bimetallic catalysts

Along with palladium (Pd), gold (Au), cobalt (Co), and ruthenium (Ru), were introduced on the $CNF_{-COOH\ HT}$ support, so as to prepare three bimetallic catalysts such as $Au\text{-}Pd/CNF_{-COOH\ HT}$, $Co\text{-}Pd/CNF_{-COOH\ HT}$, and $Ru\text{-}Pd/CNF_{-COOH\ HT}$. A simple synthesis method was employed to prepare the three bimetallic catalysts.

6.10.1.1 Wetness impregnation method

A wetness impregnation method was used to prepare the bimetallic catalysts supported on $CNF_{-COOH\ HT}$. The desired amount of metal precursors was added to an acetone solution (100 mL) containing 1 g of $CNF_{-COOH\ HT}$, so as to introduce 2 wt% Pd and 1 wt% of second metal (Au, Co, or Ru). The solution was then sonicated at room temperature for 1 h and magnetically stirred at room temperature overnight. The solution was then filtered and washed with acetone. The resulting solid was then dried in an oven at 120 °C overnight. Finally, the catalyst was then reduced in a horizontal tube oven under a nitrogen and hydrogen flow (20 vol% H_2) at 300 °C for 2 h. [19] All bimetallic catalysts are shown in Figure 6.14.

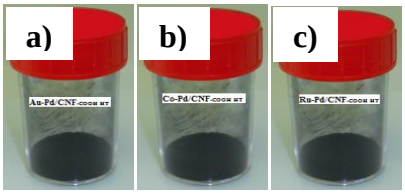

Figure 6.14 Bimetallic catalysts supported on $CNF_{-COOH\ HT}$. a) $Au\text{-}Pd/CNF_{-COOH\ HT}$, b) $Co\text{-}Pd/CNF_{-COOH\ HT}$, and c) $Ru\text{-}Pd/CNF_{-COOH\ HT}$.

6.10.2 Characterization results of bimetallic catalysts

6.10.2.1 Bimetallic catalysts supported on $CNF_{-COOH\ HT}$ were characterized by TEM, XRPD, BET, and ICP-AES

6.10.2.1.1 Results obtained by TEM

The TEM micrographs of bimetallic catalysts supported on high temperature treated functionalized carbon nanofibers have showed an excellent dispersion of both metals and a particle size distribution on both metals ranging from 0.3 to 3.8 nm for all cases as shown in Figure 6.15.

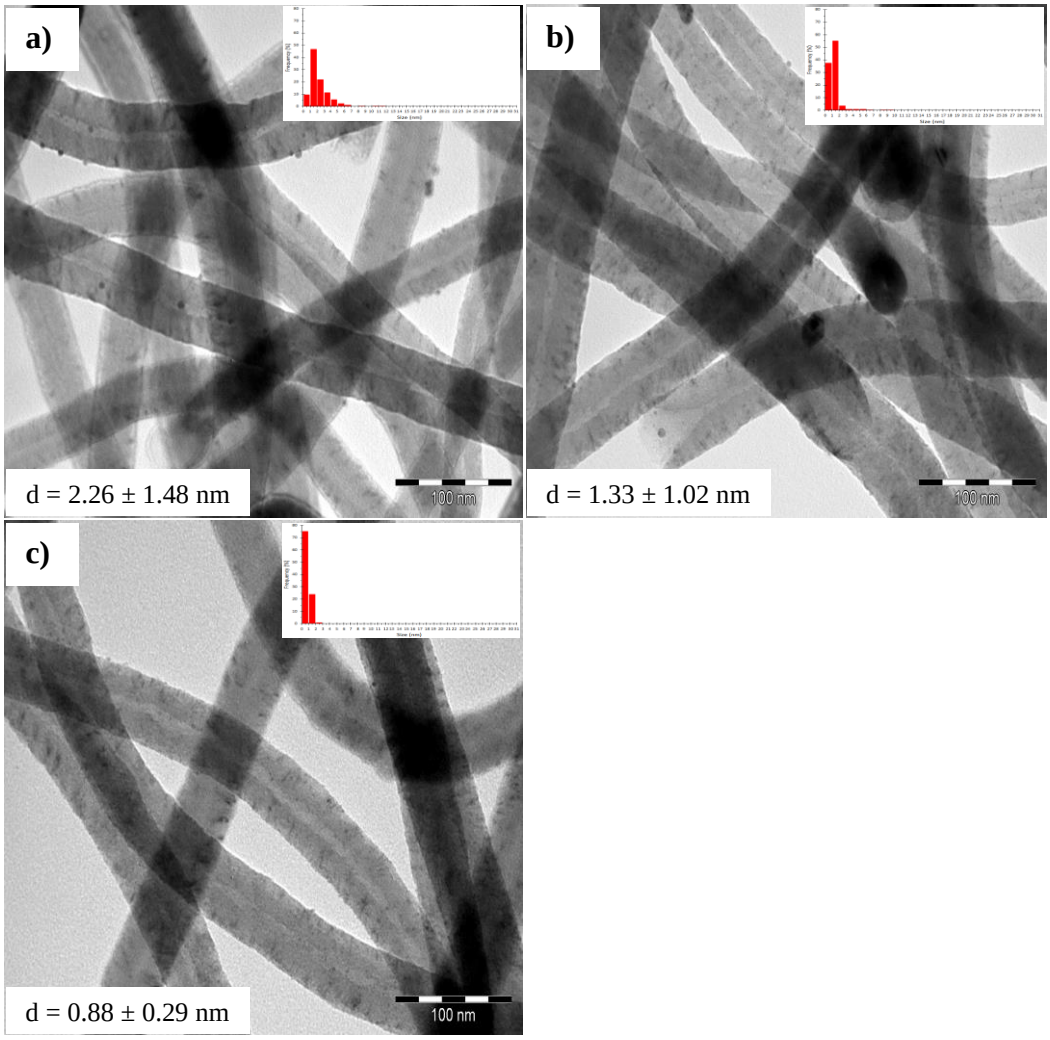

Figure 6.15 TEM micrographs of bimetallic catalysts supported on $CNF_{-COOH\ HT}$. a) $Au\text{-}Pd/CNF_{-COOH\ HT}$, b) $Co\text{-}Pd/CNF_{-COOH\ HT}$, and c) $Ru\text{-}Pd/CNF_{-COOH\ HT}$. Scale bar for all micrographs: 100 nm.

6.10.2.1.2 Results obtained by XRPD

The XRD diffractograms of bimetallic catalysts supported on high temperature treated functionalized carbon nanofibers have clearly indicated the presence of gold-palladium, cobalt-palladium, and ruthenium-palladium metals as shown in Figure 6.16.

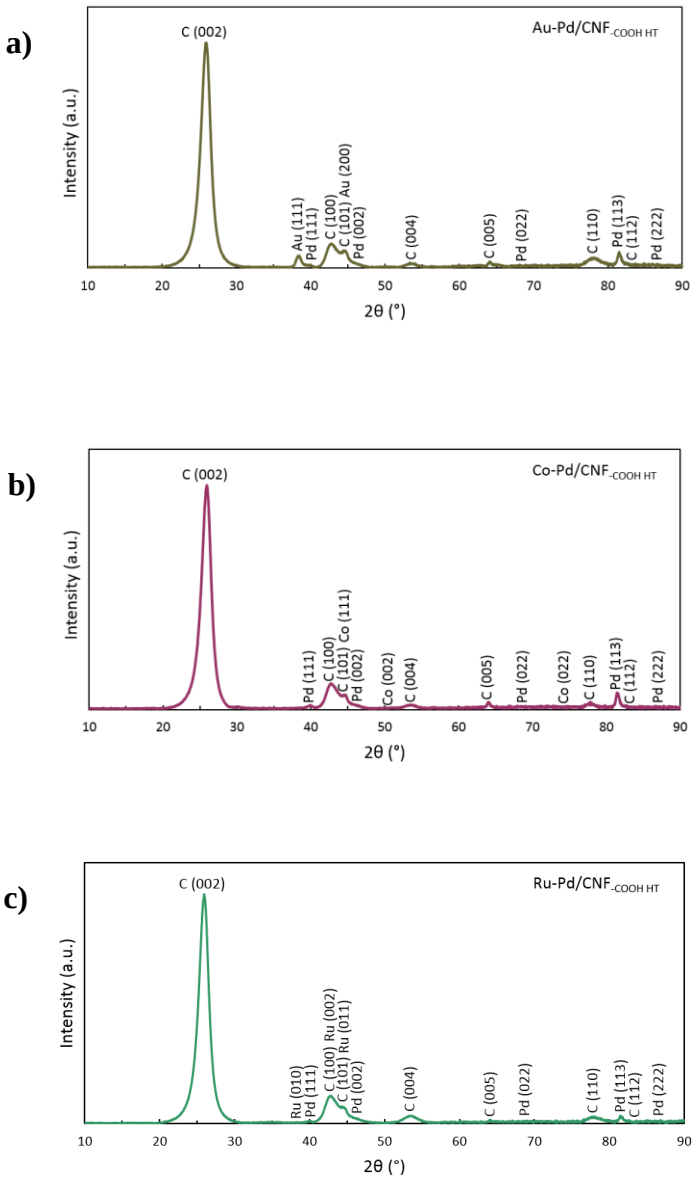

Figure 6.16 XRD diffractograms of bimetallic catalysts supported on $CNF_{\text{-COOH HT}}$. a) $Au\text{-}Pd/CNF_{\text{-COOH HT}}$, b) $Co\text{-}Pd/CNF_{\text{-COOH HT}}$, and c) $Ru\text{-}Pd/CNF_{\text{-COOH HT}}$.

6.10.2.1.3 Results obtained by BET

The BET results of bimetallic catalysts supported on high temperature treated functionalized carbon nanofibers have exposed high surface areas, small pore volumes, and mesopores, except the Ru-Pd/CNF$_{\text{-COOH HT}}$ catalyst, which exhibited high surface area, large pore volume and macropores as summarized in Table 6.9.

Table 6.9 BET results of bimetallic catalysts supported on CNF$_{\text{-COOH HT}}$.

Catalyst	BET surface area ($m^2\ g^{-1}$)	Pore volume ($cm^3\ g^{-1}$)	Pore diameter (nm)
Au-Pd/CNF$_{\text{-COOH HT}}$	139	0.6	17.2
Co-Pd/CNF$_{\text{-COOH HT}}$	103	0.7	27.6
Ru-Pd/CNF$_{\text{-COOH HT}}$	148	3.9	105.7

6.10.2.1.4 Results obtained by ICP-AES

The ICP-AES results of bimetallic catalysts supported on high temperature treated functionalized carbon nanofibers did not present a close ratio between theoretical and experimental percentages as summarized in Table 6.10.

Table 6.10 ICP-AES results of bimetallic catalysts supported on CNF$_{\text{-COOH HT}}$.

Catalyst	Element	Theoretical %	Experimental %
Au-Pd/CNF$_{\text{-COOH HT}}$	Au	1	0.14
	Pd	2	1.64
Co-Pd/CNF$_{\text{-COOH HT}}$	Co	1	0.12
	Pd	2	1.20
Ru-Pd/CNF$_{\text{-COOH HT}}$	Ru	1	1.40
	Pd	2	0.65

6.11 Results obtained of aerobic ethanol oxidation using the bimetallic catalysts

After the preparation and characterization steps, all bimetallic catalysts were tested under the best reaction conditions, which were previously employed for the monometallic catalysts.

6.11.1 Water as solvent

Along with the monometallic catalysts, water was also used as solvent with the bimetallic catalysts for aerobic ethanol oxidation to acetic acid.

Thus, the reactor was newly charged with 10 mL of 5 wt% aqueous ethanol and 0.1 g of the desired bimetallic catalyst (see Figure 6.15 and Tables 6.9-6.10). The reactor was then closed and heated at 175 °C. The reactor was then pressurized with technical air (80 vol% N_2 and 20 vol% O_2) at 30 bar. The reaction was allowed to stir for 3 h. The stirring rate was kept constant at 400 rpm for all experiments. When the reaction was finished, the reactor was cooled with an ice-water mixture at a temperature below 5 °C, to ensure that the volatile products such as acetaldehyde remain in solution before analysis. [7] The analyses were performed with the Clarus 500 gas chromatograph. After the reaction, the catalyst was separated from the liquid reaction mixture by filtration.

Table 6.11 shows the results obtained using the desired bimetallic catalyst for aerobic ethanol oxidation to acetic acid under the best reaction conditions. It is seen that the ethanol conversion and selectivity towards acetic acid significantly vary between all bimetallic catalysts. This effect is also observed on the acetaldehyde amount produced in the reaction. No carbon dioxide formed for all cases.

Among all results obtained using all bimetallic catalysts for aerobic ethanol oxidation to acetic acid, the Au-Pd/$CNF_{-COOH\ HT}$ catalyst revealed the higher ethanol conversion and selectivity towards acetic acid compared to the other ones. Moreover, the Au-Pd/$CNF_{-COOH\ HT}$ catalyst exposed ethanol conversion and selectivity towards acetic acid higher than the best monometallic catalyst (Pd/$CNF_{-COOH\ HT}$). According to that, the Au-Pd/$CNF_{-COOH\ HT}$ catalyst exhibited >94 % ethanol conversion, >97 % selectivity towards acetic acid, <3 % acetaldehyde produced, no carbon dioxide formed, and 209 h^{-1} TOF, being considered as the best bimetallic catalyst (see Table 6.11, Entry 1).

Table 6.11 Main product distribution in the ethanol oxidation reaction using the bimetallic catalysts supported on $CNF_{-COOH\ HT}$[a].

Entry	Catalyst	Ethanol conversion (%)	Products selectivity (%)			TOF (h^{-1})[b]
			CO_2	AcH	AcOH	AcOH
1	1%Au2%Pd/$CNF_{-COOH\ HT}$	95	0	2	98	209
2	1%Co2%Pd/$CNF_{-COOH\ HT}$	62	0	8	92	155
3	1%Ru2%Pd/$CNF_{-COOH\ HT}$	83	0	43	57	86

[a]Reaction conditions: 10 mL of 5 wt% aqueous ethanol, 1 wt% Au - 2 wt% Pd (Entry 1), 1 wt% Co - 2 wt% Pd (Entry 2), 1 wt% Ru - 2 wt% Pd (Entry 3), 0.1 g of bimetallic catalyst, 175 °C, 30 bar air, and 3 h of reaction time.
[b]$mol_{AcOH\ produced}/(mol_{Pd}\ time)$, at 3 h.

Figure 6.17 shows the Au-Pd/$CNF_{-COOH\ HT}$ catalyst [a) fresh and b) spent] under the best reaction conditions (see Table 6.11, Entry 1). A significant change on the particle size of metals was observed. Larger metal particle sizes were measured on the spent Au-Pd/$CNF_{-COOH\ HT}$ catalyst compared to that fresh Au-Pd/$CNF_{-COOH\ HT}$ catalyst.

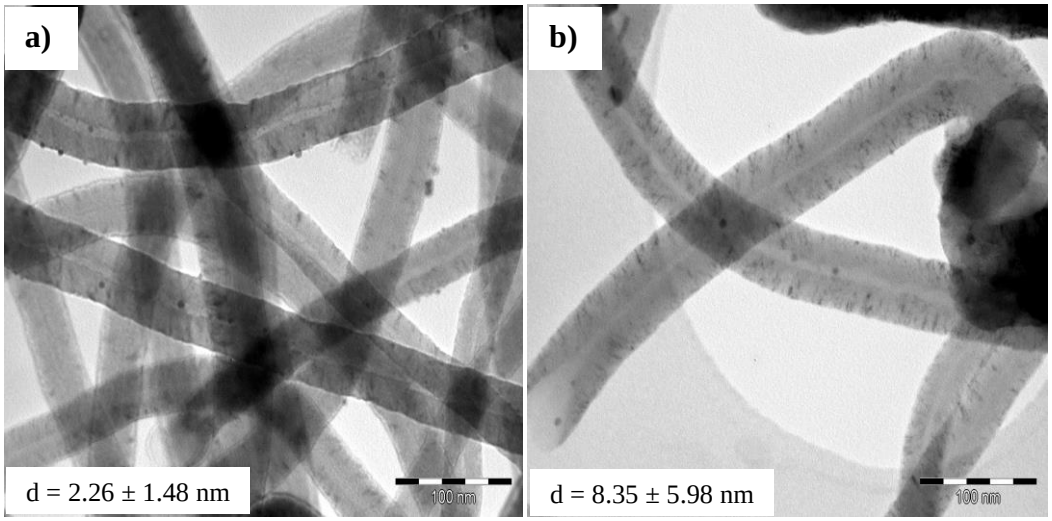

Figure 6.17 TEM micrographs of the Au-Pd/CNF$_{\text{-COOH HT}}$ catalyst. a) fresh and b) spent. Scale bar for all micrographs: 100 nm.

6.12 Recycling tests using the best bimetallic catalyst (Au-Pd/CNF$_{\text{-COOH HT}}$)

Among all bimetallic catalysts, the Au-Pd/CNF$_{\text{-COOH HT}}$ catalyst was selected as the best catalyst for aerobic ethanol oxidation to acetic acid in an aqueous media. Due to its high ethanol conversion, high selectivity towards acetic acid, low acetaldehyde produced, no carbon dioxide formed, and high catalytic activity compared to all the other ones. Recycling tests were performed to evaluate the catalytic stability of the Au-Pd/CNF$_{\text{-COOH HT}}$ catalyst.

Therefore, the reactor was newly charged with 10 mL of 5 wt% aqueous ethanol and 0.1 g Au-Pd/CNF$_{\text{-COOH HT}}$ catalyst. The reactor was then closed and heated at 175 °C. The reactor was then pressurized with technical air (80 vol% N_2 and 20 vol% O_2) at 30 bar. The reaction was allowed to stir for 3 h. The stirring rate was kept constant at 400 rpm. When the reaction was finished, the reactor was cooled with an ice-water mixture at a temperature below 5 °C, to ensure that the volatile products such as acetaldehyde remain in solution before analysis. [8]

The analyses were performed with the Clarus 500 gas chromatograph. After the reaction, the catalyst was separated from the liquid reaction mixture by filtration and then transferred to next test.

Table 6.12 shows the results obtained during the recycling tests using the Au-Pd/CNF$_{\text{-COOH HT}}$ catalyst for aerobic ethanol oxidation to acetic acid. It is seen that the ethanol conversion and selectivity towards acetic acid significantly decreased after each recycling test. In contrast, the acetaldehyde amount increased.

Table 6.12 Recycling tests in the ethanol oxidation using the Au-Pd/CNF$_{\text{-COOH HT}}$ catalyst[a].

Entry	Reaction cycles	Ethanol conversion (%)	Products selectivity (%)			TOF (h^{-1})[b]
			CO_2	AcH	AcOH	AcOH
1	Test 1	95	0	2	98	209[c]
2	Recycle 1	57	1	3	96	153[d]
3	Recycle 2	29	3	6	91	99[e]
4	Recycle 3	25	1	9	90	126[f]

[a]Reaction conditions: 10 mL of 5 wt% aqueous ethanol, 1 wt% Au - 2 wt% Pd, 0.1 g of Au-Pd/CNF$_{\text{-COOH HT}}$ catalyst, 30 bar air, 175 °C, and 3 h of reaction time. TOF calculated on: [c]100, [d]80, [e]60, and [f]40 mg of catalyst weight, respectively.
[b]$mol_{AcOH\ produced}/(mol_{Pd}\ time)$, at 3 h.

Among the entries 1 and 2, the ethanol conversion decreased up to 39 % and 49 % between the entries 2 and 3 as shown in Figure 6.18.

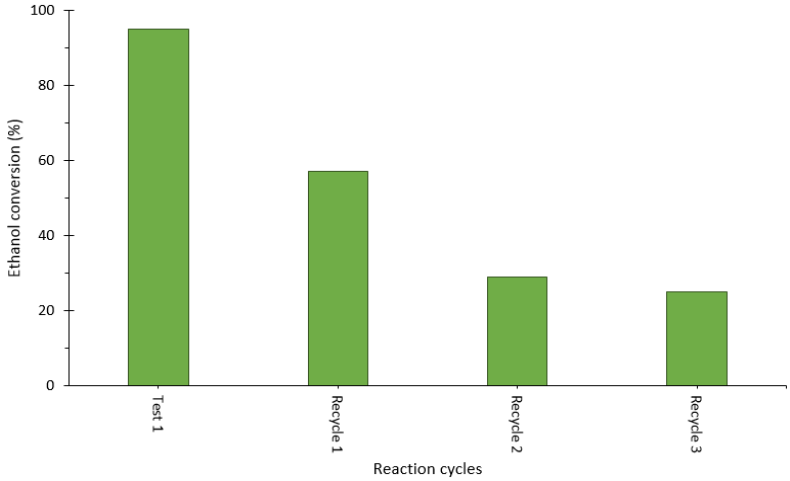

Figure 6.18 Evolution of ethanol conversion on the recycling tests.

Among the entries 1 and 2, the selectivity towards acetic acid also decreased up to 2 % and 5 % between the entries 2 and 3 as shown in Figure 6.19.

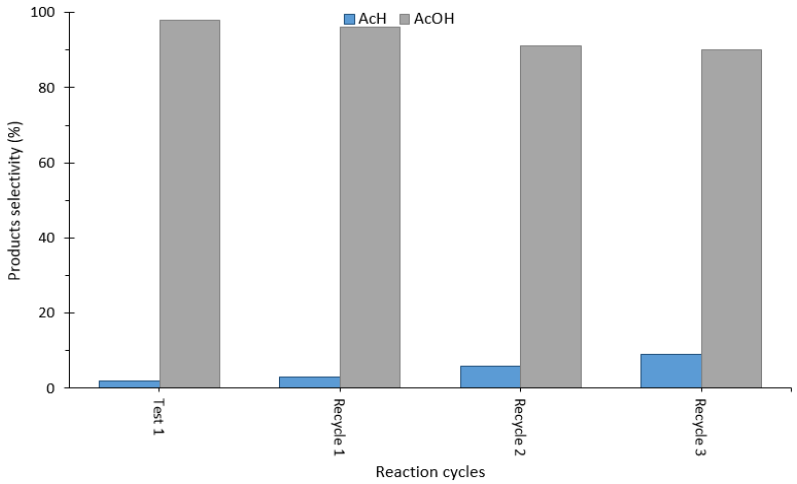

Figure 6.19 Evolution of selectivity towards acetic acid on the recycling tests.

In summary, ethanol conversion and selectivity towards acetic acid lower than during the first test could be attributed to a catalyst deactivation by blockage of the surface through strongly adsorbed molecules (*e.g.*, oxygen), reaction products (*e.g.*, acetaldehyde, ethyl acetate, acetic acid, or carbon dioxide), and/or leaching of metal (*e.g.*, gold and/or palladium) into the liquid reaction mixture.

Figure 6.20 shows the Au-Pd/CNF$_{\text{-COOH HT}}$ catalyst [a) fresh and b) spent after third recycle] under the best reaction conditions (see Table 6.12, Entry 4). A significant change on the particle size of metals was observed. Larger metal particle sizes were measured and surface damages were also found on the Au-Pd/CNF$_{\text{-COOH HT}}$ catalyst spent after third recycle compared to that fresh Au-Pd/CNF$_{\text{-COOH HT}}$ catalyst.

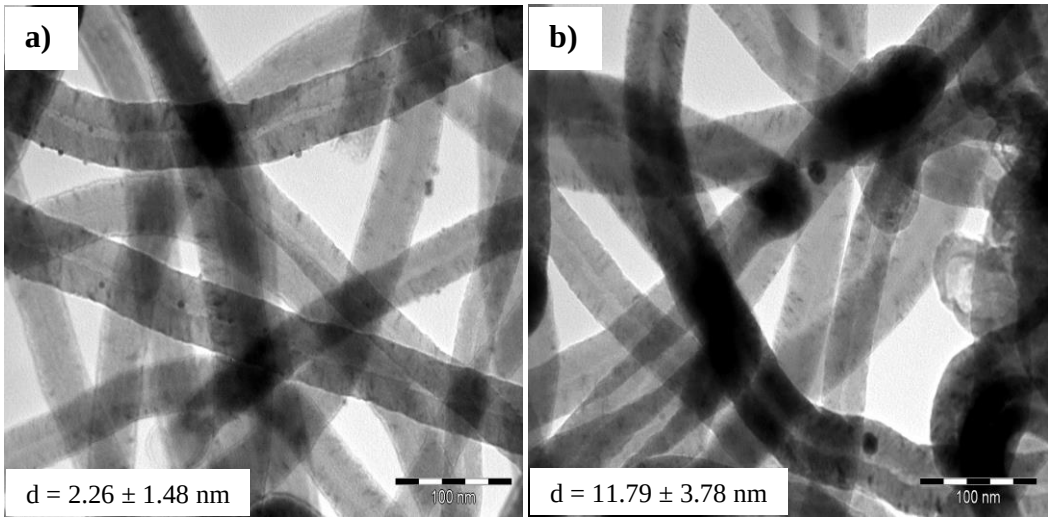

Figure 6.20 TEM micrographs of the Au-Pd/CNF$_{\text{-COOH HT}}$ catalyst. a) fresh and b) spent after third recycle. Scale bar for all micrographs: 100 nm.

Moreover, the liquid reaction mixtures obtained by filtration after the recycling tests did not show significant colour from gold-palladium leaching in the solution (see Figure 6.21).

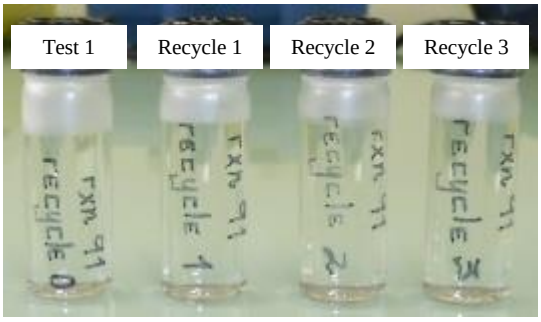

Figure 6.21 Liquid reaction mixtures obtained by filtration after the recycling tests. Reaction time for all cases: 3 h.

Therefore, the recycling tests revealed that the Au-Pd/CNF$_{\text{-COOH HT}}$ catalyst can only be used once, and still maintain high ethanol conversion and selectivity towards acetic acid of 95 % and 98 %, respectively.

6.13 Summary

Excellent catalytic results are commonly obtained through a good preparation and characterization of metal catalyst. According to that, the catalytic results obtained using the palladium catalysts for aerobic ethanol oxidation to acetic acid exhibited ethanol conversion and selectivity towards acetic acid higher than the metallic catalysts supported on metal oxides often used in catalysis. The best palladium catalysts (*e.g.*, Pd/FC$_{\text{-COOH}}$, Pd/S$_2$-CNT, Pd/CNF$_{\text{-COOH HT}}$, and Au-Pd/CNF$_{\text{-COOH HT}}$) revealed ethanol conversion and selectivity towards acetic acid much higher than those of other palladium catalysts supported on carbon nanostructures and metallic catalysts supported on metal oxides already reported in the literature.

6.14 References

[1] C. Le Berre, P. Serp, P. Kalck, G.P. Torrence, Acetic acid, Ullmann's Encyclopedia of Industrial Chemistry, Wiley-VCH Verlag GmbH & Co. KGaA (**2000**).

[2] C.H. Christensen, B. Jørgensen, J. Rass-Hansen, K. Egeblad, R. Madsen, S.K. Klitgaard, S.M. Hansen, M.R. Hansen, H.C. Andersen, A. Riisager, Formation of acetic acid by aqueous-phase oxidation of ethanol with air in the presence of a heterogeneous gold catalyst, Angew. Chem. Int. Ed. 45 (**2006**) 4648–4651.

[3] Y.Y. Gorbanev, S. Kegnæs, C.W. Hanning, T.W. Hansen, A. Riisager, Acetic acid formation by selective aerobic oxidation of aqueous ethanol over heterogeneous ruthenium catalysts, ACS Catal. 2 (**2012**) 604–612.

[4] S. Letichevsky, P.C. Zonetti, P.P.P. Reis, J. Celnik, C.R.K. Rabello, A.B. Gaspar, L.G. Appel, The role of m-ZrO2 in the selective oxidation of ethanol to acetic acid employing PdO/m-ZrO, J. Mol. Catal. A Chem. 410 (**2015**) 177–183.

[5] X. Li and E. Iglesia, Selective Catalytic Oxidation of Ethanol to Acetic Acid on Dispersed Mo-V-Nb Mixed Oxides, Chem. Eur. J. 13 (**2007)** 9324-9330.

[6] S. M. Tembe, G. Patrick, M. S. Scurrell, Gold Bulletin, 42, 4 (**2009**) 321-327.

[7] B. Jørgensen, S. E. Christiansen, M. L. D. Thomsen, C. H. Christensen, Appl. Catal. A: Gen. 251 (**2007**) 332

[8] S. M. Tembe, G. Patrick, M. S. Scurrell, Gold Bulletin, 42, 4 (**2009**) 321-327.

[9] Y. Obana, H. Uchida, K.-i. Sano, US Patent 6, 867, 164, (**2005)**.

[10] G.-J. ten Brink, I. W. C. E. Arends, R. A. Sheldon, Science (**2000)**, *287*, 1636.

[11] K. Mori, T. Hara, T. Mizugaki, K. Ebitani, K. Kaneda, J. Am. Chem. Soc. (**2004)**, *126*, 10657.

[12] T. Nishimura, N. Kakiuchi, M. Inoue, S. Uemura, Chem. Commun. (**2000)** 1245.

[13] C. H. Christensen, B. Jørgensen, J. Rass-Hansen, K. Egeblad, R. Madsen, S. K. Klitgaard, S. M. Hansen, M. R. Hansen, H. C. Andersen, and A. Riisager, Angew. Chem. Int. Ed. 45 (**2006**) 4648-4651.

[14] Y. Y. Gorbanev, S. Kegnæs, C. W. Hanning, T. W. Hansen, A. Riisager, ACS Catal. 2 (**2012**) 604-612.

[15] W. Dong, P. Chen, W. Xia, P. Weide, H. Ruland, A. Kostka, K. Köhler, M. Muhler, ChemCatChem 8 (**2016**) 1269-1273.

[16] A. Benyounes, S. Louisia, R. Axet, Z. Mahfoud, M. Kacimi, P. Serp, Catalysis Today 249 (**2015**) 137-144.

[17] A. Borodziński, M. Bonarowska, Langmuir, 13 (**1997**) 5613-5620.

[18] K.-Q. Sun, S.-W. Luo, N. Xu, B.-Q. Xu, Catal Lett 124 (**2008**) 238-242.

[19] S. Louisia, R. Castro Contreras, M. Heitzmann, M. R. Axet, P.-A. Jacques, P. Serp, Catalysis Communications 109 (**2018**) 65-70.

CHAPTER VII

Conclusions and Future perspectives

7.1 Introduction

To clearly understand the structural order of this Chapter VII: Conclusions and Future perspectives, the main issues are summarized in Table 7.1.

Table 7.1 Main issues of Chapter VII.

Issues
7.2 Conclusions
7.3 Future perspectives

7.2 Conclusions

According to aims and results exposed in this PhD thesis, we can conclude the following claims:

- Well-defined carbon nanostructures were achieved through a controlled synthesis.

- Improved physicochemical properties were achieved on chemically treated carbon nanostructures compared to the pristine carbon nanostructures.

- Highly efficient catalyst supports such as few layer graphene, multi-walled carbon nanotubes, doped multi-walled carbon nanotubes, carbon nanofibers, and fibrous carbon were obtained by catalytic-chemical vapor deposition technique.

- Higher palladium loading and dispersion were generally observed on catalysts supported on chemically treated carbon nanostructures.

- Higher catalytic activities were generally obtained on chemically treated carbon nanostructures compared to the pristine carbon nanostructures.

- Higher ethanol conversion and selectivity towards acetic acid were achieved using palladium catalysts supported on chemically treated carbon nanostructures compared to the metallic catalysts supported on metal oxides commonly used.

- Higher ethanol conversion, selectivity towards acetic acid, and catalytic activity were reached using the best palladium catalysts compared with the results already reported in the literature.

- Much higher ethanol conversion and selectivity towards acetic acid were achieved when using bimetallic catalysts supported on carbon nanostructures.

Therefore, a controlled synthesis of carbon nanostructures, a suitable preparation method of palladium catalysts, and a detailed characterization of both support and catalyst allowed achieving higher ethanol conversion and selectivity towards acetic acid compared to the results already reported in the literature.

7.3 Future perspectives

According to catalytic tests and conclusions, we propose the following challenges:

- Previously used reaction conditions for aerobic ethanol oxidation to acetic acid might be changed to determine certain kinetic parameters such as order of reaction and activation energy, which are very important values for a catalyzed chemical reaction.

- A detailed study on the best palladium catalysts used in recycling tests may be carried out to clearly understand and then improve their catalytic stability.

- DFT calculations might be applied to widely understand the palladium-carbon interaction and thus increase the activity, selectivity, and stability of such catalysts.

- The palladium catalysts supported on carbon nanostructures may be tested in another chemical reaction, for example, hydrogenation reaction.

Attachments

A.1 Introduction

Many accumulated evidences which grant veracity to this PhD thesis are summarized in Table A.1.

Table A.1 Main evidences of this PhD thesis.

Evidences
A.2 INP-ENSIACET, LCC
A.3 Research collaboration
A.4 As co-author in a scientific article
A.5 As co-author in a presentation for an international congress
A.6 As first author in a scientific article (in process)

A.2 INP-ENSIACET, LCC

A.2.1 INP-ENSIACET

Figure A.1 École Nationale Supérieure des Ingénieurs en Arts Chimiques Et Technologiques (ENSIACET) in Toulouse, France.

A.2.2 LCC

Figure A.2 Supported catalysis laboratory in Toulouse, France.

A.2.3 Work team

Figure A.3 Work team of Institut National Polytechnique-École Nationale Supérieure des Ingénieurs en Arts Chimiques Et Technologiques, Laboratoire de Chimie de Coordination (INP-ENSIACET, LCC) in Toulouse, France.

A.3 Research collaboration

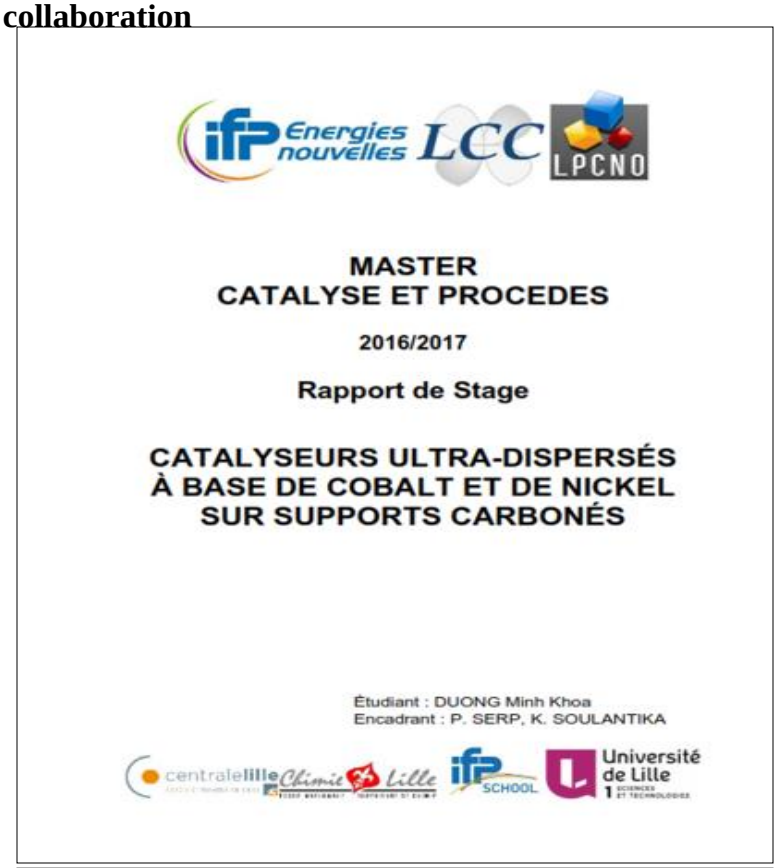

MASTER
CATALYSE ET PROCEDES

2016/2017

Rapport de Stage

CATALYSEURS ULTRA-DISPERSÉS À BASE DE COBALT ET DE NICKEL SUR SUPPORTS CARBONÉS

Étudiant : DUONG Minh Khoa
Encadrant : P. SERP, K. SOULANTIKA

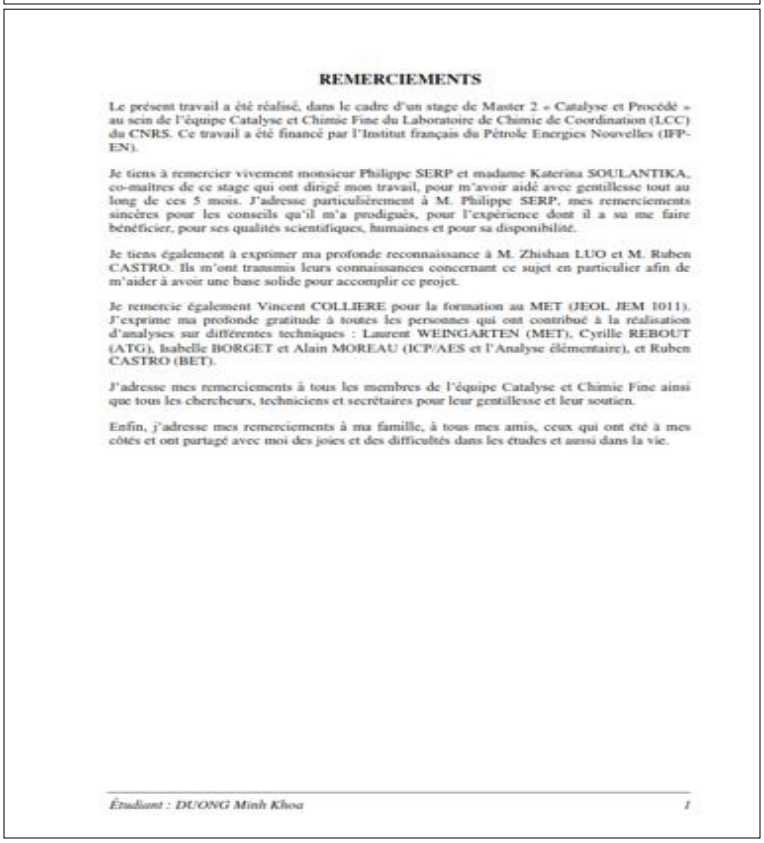

REMERCIEMENTS

Le présent travail a été réalisé, dans le cadre d'un stage de Master 2 « Catalyse et Procédé » au sein de l'équipe Catalyse et Chimie Fine du Laboratoire de Chimie de Coordination (LCC) du CNRS. Ce travail a été financé par l'Institut français du Pétrole Energies Nouvelles (IFP-EN).

Je tiens à remercier vivement monsieur Philippe SERP et madame Katerina SOULANTIKA, co-maîtres de ce stage qui ont dirigé mon travail, pour m'avoir aidé avec gentillesse tout au long de ces 5 mois. J'adresse particulièrement à M. Philippe SERP, mes remerciements sincères pour les conseils qu'il m'a prodigués, pour l'expérience dont il a su me faire bénéficier, pour ses qualités scientifiques, humaines et pour sa disponibilité.

Je tiens également à exprimer ma profonde reconnaissance à M. Zhishan LUO et M. Ruben CASTRO. Ils m'ont transmis leurs connaissances concernant ce sujet en particulier afin de m'aider à avoir une base solide pour accomplir ce projet.

Je remercie également Vincent COLLIERE pour la formation au MET (JEOL JEM 1011). J'exprime ma profonde gratitude à toutes les personnes qui ont contribué à la réalisation d'analyses sur différentes techniques : Laurent WEINGARTEN (MET), Cyrille REBOUT (ATG), Isabelle BORGET et Alain MOREAU (ICP/AES et l'Analyse élémentaire), et Ruben CASTRO (BET).

J'adresse mes remerciements à tous les membres de l'équipe Catalyse et Chimie Fine ainsi que tous les chercheurs, techniciens et secrétaires pour leur gentillesse et leur soutien.

Enfin, j'adresse mes remerciements à ma famille, à tous mes amis, ceux qui ont été à mes côtés et ont partagé avec moi des joies et des difficultés dans les études et aussi dans la vie.

A.4 As co-author in a scientific article

Contents lists available at ScienceDirect

Catalysis Communications

journal homepage: www.elsevier.com/locate/catcom

Short communication

Sequential catalytic growth of sulfur-doped carbon nanotubes and their use as catalyst support

Stéphane Louisia[a,b], Ruben Castro Contreras[a], Marie Heitzmann[b], M. Rosa Axet[a], Pierre-André Jacques[b,*], Philippe Serp[a,*]

[a] LCC, Université de Toulouse, CNRS, Toulouse, France
[b] Université Grenoble Alpes, CEA-LITEN/DEHT, 17 rue des martyrs, 38000 Grenoble, France

ARTICLE INFO

Keywords:
Carbon nanotubes
Sulfur
Palladium
Ethanol oxidation
Acetic acid

ABSTRACT

A sequential process has been developed to produce sulfur-doped carbon nanotubes (7% w/w sulfur) on iron supported catalysts. In this procedure it is necessary to first activate the iron catalyst to initiate the growth of all-carbon CNTs from ethylene, prior to growth sulfur doped CNTs from thiophene. The resulting sulfur-doped carbon nanotubes constitute an excellent support for the anchoring of very small (1.8 nm) palladium nanoparticles. This Pd based catalyst is very active for ethanol aerobic oxidation to acetic acid.

1. Introduction

It is known that the performances of carbon nanotubes (CNTs) can be improved by modifying the electronic properties of their sp^2 carbons, and a large number of developments have been carried out in this direction in recent years. This improvement is in particular obtained by insertion of heteroatoms, such as boron, nitrogen, phosphorous or sulfur, within the CNT structure, leading to substitutional doping [1]. These doped CNTs are proposed for various applications such as in the fields of catalysis, optoelectronics, solar panels, or even energy storage [2]. Many studies have attempted to produce B-, N-, or S-containing CNTs with the same methods to produce pristine CNTs. The morphology of the obtained materials differs notoriously from pure CNTs, which are tubular structures with hollow cores. For example, N-doping creates hollow sections separated by one to few graphitic layers (bamboo-like structures), and it was reported that S-doping produces branched morphologies [3]. Another approach to produce these doped-CNTs starts from pristine CNTs and involves costly post-synthesis treatment. The works describing the direct synthesis of S-CNTs are scarce compared to those concerning nitrogen doping. Denis et al. have shown by DFT calculation that it is possible to dope CNTs with sulfur [4]. The larger size of S atoms compared to the C ones and the longer C–S bond compared to the C–C bond should distort the structure, but they conclude that CVD could be an effective method to synthesize such structures. Zhou et al. describe a single step synthesis to obtain S-CNTs from dimethyl sulfide on a Co/MgO catalyst at 1273 K [5]. However, the material synthesized appear to be assemblages of CNTs covered with sulfur-containing sheaths, and not CNTs containing sulfur atoms within their structure. High temperatures were also used to prepare branched CNTs (Y-junction CNTs) from thiophene and nickel catalysts; however these structures contain only very small amounts of sulfur (< 1% at.) [6]. Additionally, it was shown that these structures exhibited a stacked-cone morphologies similar to the one obtained in carbon nanofibers. Small amounts of sulfur (0.7% w/w) were also obtained by decomposing carbon disulphide at 1173 K on iron catalysts [6]. Finally, it is interesting to note that the CNT synthesis by CVD in the presence of sulfur precursors does not necessarily lead to the synthesis of sulfur doped structures. Indeed, Lee et al. have shown that the presence of sulfur (they use in particular thiophene) during the synthesis by CVD at 1443 K makes it possible to decrease the catalyst sintering and to increase the purity of the CNTs produced [7]. The CNTs prepared have very regular walls and the sulfur is concentrated on the surface of the catalyst particles and not in CNT walls. It thus appears that the direct synthesis of S-CNTs containing significant amount of sulfur is still challenging.

We describe herein a simple sequential procedure to selectively produce at moderate temperature S-CNTs containing sound amounts (7% w/w) of sulfur in their structure, and their use as catalyst support for palladium deposition. The Pd/S-CNT catalyst have been used for ethanol aerobic oxidation to acetic acid, and compared to palladium catalysts deposited on undoped CNT, oxidized CNTs and nitrogen doped CNTs.

* Corresponding authors.
E-mail addresses: pierre-andre.jacques@cea.fr (P.-A. Jacques), philippe.serp@toulouse.inp.fr (P. Serp).

https://doi.org/10.1016/j.catcom.2018.02.024
Received 20 December 2017; Received in revised form 23 February 2018; Accepted 26 February 2018
Available online 27 February 2018
1566-7367/ © 2018 Published by Elsevier B.V.

2. Experimental

2.1. Materials

2.1.1. Nanotube synthesis

The multi-walled carbon nanotubes (CNT), nitrogen doped multi-walled carbon nanotubes (N-CNT), and sulfur doped multi-walled carbon nanotubes (S-CNT) were synthesized by a catalytic chemical vapor deposition process into a fluidized bed reactor using ethylene (C_2H_4) as a carbon source [8],acetonitrile (C_2H_3N) as a carbon and nitrogen source [9],and thiophene (C_4H_4S) as a carbon and sulfur source. The oxidized CNTs were obtained by nitric acid oxidation of the CNTs [10]. For S-CNT growth, the catalyst (Fe/Al_2O_3 or $AlFeCoO_x$) were reduced in a fluidized bed reactor under a nitrogen (225 mL·min^{-1} N_2) and hydrogen (150 mL·min^{-1} H_2) flow at 1023 K. After this reduction step the nitrogen and hydrogen flow was followed to ethylene for 3 min and then thiophene for 27 min to produce S-CNT. The S-CNT were recovered and then purified by aqueous solution (50 vol% H_2SO_4) under reflux at 413 K for 3 h. The product was then filtered and washed. The resulting solid was finally dried overnight at 393 K.

2.1.2. Palladium catalyst synthesis

A wet impregnation method was used to prepare the palladium catalysts supported on carbon nanotubes. The desired amount of palladium (II) nitrate dihydrate ($Pd(NO_3)_2.2H_2O$) was added to an acetone solution (100 mL) containing 1 g of carbon nanomaterial, so to introduce 2 wt% of metal phase. The solution was then sonicated at room temperature for 1 h followed by magnetic stirring at room temperature overnight. The solid was then filtered and washed with acetone. The resulting solid was then dried overnight in an oven at 393 K. Finally, the catalyst was reduced in a horizontal tube oven under a nitrogen and hydrogen flow (20 vol% H_2) at 573 K for 2 h.

2.1.3. Oxidation of ethanol

The oxidation experiments were conducted in a 65 mL stainless steel autoclave reactor equipped with magnetic stirring and heated in a silicone oil bath. The reactor was charged with 10 mL of 5wt% aqueous ethanol and 0.1 g of catalyst. The reactor was then closed and heated to the desired reaction temperature (373–473 K) and then pressurized with technical air (80 vol% N_2 and 20 vol% O_2) at a required pressure (10–30 bar) the reaction was allowed to stir for a required reaction time (3–25 h). The stirring rate was kept constant at 400 rpm for all experiments. When the reaction was finished, the reactor was cooled with an ice-water mixture at a temperature below 278 K, to ensure that the volatile products such as acetaldehyde remain in solution before analysis [6]. The analyses were performed in a Clarus 500 gas chromatograph, equipped with a split/splitless injector, a capillary column (Stabilwax®-DA Fused Silica 30 m, 0.25 mm I.d.) and a flame ionization detector (FID). At the end of each experiment, the catalyst was separated from the liquid reaction mixture by filtration and the liquid reaction mixture was analyzed by Coulometry to determine the water amount from ethanol oxidation reaction using a Titrator TitroLine KF trace.

2.2. Methods

TEM micrographs were taken with a JEOL JEM 1011 microscope operating at 100 kV. The high resolution analyses were conducted using a JEOL JEM2100F microscope equipped with a Field Emission Gun (FEG) operating at 200 kV with a point resolution of 2.3 Å and a JEOL JEM-ARM200F Cold FEG microscope operating at 200 kV with a point resolution of > 1.9 Å. The approximation of the particle mean size was made through a manual analysis of enlarged micrographs by measuring at least 250 particles on a given grid. The Brunauer–Emmett–Teller (BET) analyses by N_2 adsorption isotherms at 77 K (Quantachrome instrument) were performed to give the specific surface area and pore volume and pore size distribution. XRD diffractograms were obtained at room temperature with a Panalytical X'PERT PRO diffractometer, employing Cu Kα radiation (λ = = 1.54 Å) and a parabolic MPD-mirror for Cu radiation. The diffractograms were acquired in 2θ range from 5° to 90°, using a continuous scan mode with an acquisition step size of 0.0170° and a counting time of 299.72 s. Raman spectra were obtained in a micro Raman Spectrometer HR 800 Jobin Yvon Horiba using a laser of 633 nm wavelength as an excitation source. The thermograms were acquired in a temperature range from 303 to 1273 K at 10 K·min^{-1} under air atmosphere using a TG/DTA Shimadzu. The elemental results were obtained using a CHN Perkin-Elmer elemental analyzer. The palladium percentage were measured using an ICAP 6300 ICP Spectrometer. The X-ray photoelectron spectroscopy was performed on XPS K-alpha Thermoscientific apparatus, which operated with a non chromatized Mg K source (1253.6 eV).

3. Results and discussion

Sulfur is known to be a source of poisoning for metal catalysts. A complex mechanism of poisoning has been proposed, which comprises site-blocking, and a change of the number of active sites driven by temperature [11]. It is also known that sulfur plays an important role to promote or inhibit the CNT growth [12]. At low concentration, optimized CNT yields can be obtained, whereas high concentration of sulfur inhibit the growth of CNTs [12,13]. The positive role of sulfur has been explained through the formation of a layer on the surface of the catalyst particles that plays a role in encouraging nanotube growth by surface diffusion [14]. Interesting comparison can be made with the Fischer-Tropsch synthesis on iron catalysts. In this reaction, sulfur is also considered as a severe poison [15], even if addition of low amounts of this heteroelement can, in some specific cases, improve the performances [16–18]. In that case, monolayer surface sulfides are formed on the iron catalysts at H_2S concentrations below 2 ppm, while bulk sulfides are formed at higher sulfur concentrations [19]. In the Fischer-Tropsch synthesis [20], as for CNT growth [21], both metallic iron and iron carbides are suspected to be the active phases. Interestingly, it has been shown that, for the Fischer-Tropsch reaction, iron carbides are more resistant to poisoning by sulfur than metallic iron [18]. Since iron carbide(s) should be present during CNT growth we investigate the possibility to grow S-CNTs from a sequential process; in which the iron catalyst will be activated via the initial growth of all-carbon CNTs. During this phase, iron carbide should be at the surface of the catalyst particles; so that if the thiophene is introduced these particles should be less prone to deactivation. We have recently shown that it was possible to grow hybrid CNT@N-CNT structures containing undoped and N-doped sections on the same tube by using a sequential approach [9]. We have followed a similar approach to initiate the growth of S-CNTs. Indeed, the direct approach, i. e. direct decomposition of thiophene on 5% Fe/Al_2O_3 (C1) or $AlCoFeO_x$ (C2) catalysts did not lead to S-CNT, but to a poorly defined material (see SI.1) with a low yield (0.45 $g_C \cdot g_{cat(C)}^{-1}$, and 2.2 $g_C \cdot g_{cat(C2}^{-1}$), and with a low surface area (47 $m^2 \cdot g^{-1}$) and a high sulfur content (12.7%). In the first sequence (the activation step), an ethylene/Ar/H_2 mixture is introduced for a short duration (1 to 3 min) to initiate the CNT growth. Then, for the second sequence, the ethylene/Ar/H_2 mixture is switched-off and replaced by a thiophene/Ar/H_2 mixture. At 1023 K, this procedure allows the production of S-CNTs with yields of 0.23 $g_C \cdot g_{cat(C1}^{-1}$ for C1 and of 3.0 $g_C \cdot g_{cat(C2}^{-1}$ for C2. The lower yields obtained compared to the synthesis of undoped CNTs (1.2 $g_C \cdot g_{Cat}^{-1}$(C1) and 9.8 $g_C \cdot g_{Cat}^{-1}$(C2), respectively) should be correlated to the fact that sulfur, as nitrogen [22], decreases the CNT growth rate.

After a purification step in boiling H_2SO_4 in order to remove the catalyst, the S-CNTs were characterized. TEM micrographs of S-CNT produced from C1 are shown in Fig. 1.

The S-CNT mean diameter is 13 nm. The S-CNT prepared from C2

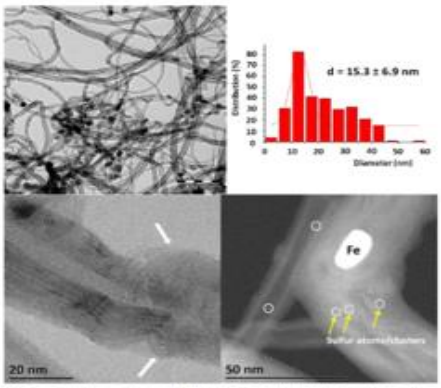

Fig. 1. TEM (scale bar: 200 nm) with histogram of diameters; HRTEM (scale bar: 20 nm); and STEM-HAADF (scale bar: 50 nm) micrographs of S-CNTs.

Table 1
Characterization of the S-CNTs produced from catalyst C1.

S_{BET} (m^2 g^{-1})	θ (nm)	S_{BET} (m^2 g^{-1})	V_p (cm^3 g^{-1})	I_D/I_G	Yield (wt/wt)^a	NH_{3max} (mmol/g)^b
0.339	15	338	2.1	0.66	7.7	3.6

^{a} From elemental analysis.
^{b} From XPS.

are similar (see SI.2). Compared to an undoped CNT, the structure of the S-doped CNT presents some alterations (bulbous segments, Fig. 1, white arrows), which are different than those observed for N-CNTs (bamboo structure). As in the case of N-CNTs, these alterations should be related to the growth process [3,20]. The size of S atoms may also have a profound effect. Indeed, S-doped into the graphitic carbon sticks out from the graphitic plane, inducing significant lattice distortions (see SI.3). Indeed, it has been shown that minute amounts of sulfur are sufficient to promote the formation of heptagons (negative curvature) and pentagons (positive curvature) [21]. Interestingly, in our case the S-CNT do not show a stacked-cone morphology. STEM-HAADF analyses (Fig. 1) allow showing, besides remaining iron catalyst nanoparticles, the presence of element heavier than carbon in the structure, as well as isolated sulfur atoms or clusters embedded in the CNT structure. The characterization of S-CNTs produced from catalyst C1 is summarized in Table 1. The XRD diagram of S-CNTs is shown in Fig. SI.4. It presents the four characteristic lines of the CNTs at $2\theta = 26.24°$, 43.07°, 53.71° and 78.39°, respectively corresponding to the (002), (100), (004) and (110) peaks of graphite. Considering the line at $2\theta = 26.24°$, the inter-planar distance d_{002} for S-CNTs is equal to 3.39 Å Table 1.

As shown in Fig. SI.5, the Brunauer-Emmett-Teller (BET) measurement suggests a mesoporous structure of the S-CNTs, as evidenced by the nitrogen adsorption/desorption isotherms of IV type. Based on the BET analysis, the specific surface area of the S-CNTs is calculated to be 338 m^2 g^{-1}. The most important features seen for Raman spectra of S-CNT (Fig. SI.6) are the disorder induced D band at 1320 cm^{-1}, its second harmonic D' at 1604 cm^{-1} (shoulder in G), and the tangential G band at 1580 cm^{-1}, which is related to the graphite tangential E_{2g} Raman active mode where the two atoms in graphene unit cell are vibrating tangentially one against the other. The ratio of the intensities of D and G bands is a good indicator of the quality of bulk samples. Similar intensities of these bands indicate a significant amount of structural defects, which is commonly observed for CVD-produced multi-walled CNTs. Studies have shown that the D' band feature depends on the number of defects in the CNT sidewall [24]. Thus a more intense D' band should appear in the Raman spectra as the disorder increases.

The sulfur content is 7.7% w/w as determined by elemental analysis, and the surface composition is 3.6% at. as determined by XPS, pointing the effectiveness of the sequential procedure to produce S-CNTs containing sound amounts of sulfur in the structure of the CNT. TG-DSC curve of the S-CNT sample in air presents a three-step weight loss of the carbon material (Fig. SI.7). The first weight loss of 6% between 493 and 593 K should correspond to the removal of some sulfate groups formed by reaction of oxygen with reactive sulfur atoms in thiol groups [25]. The largest weight loss of 53% appeared between 703 and 863 K; it can be due to oxidation of the less reactive S-CNT structure. Adams et al. by studying the decomposition of a CNT-SO_3H sample, distinguish also two sections: they attribute the first section to the decomposition of absorbed volatile compounds and the most fragile functions (between 313 K and 573 K) [26]. The second section

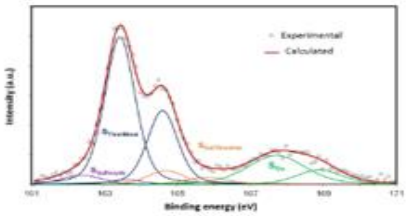

Fig. 2. High-resolution S_{2p} XPS spectrum for S-CNTs.

corresponds to the decomposition of the covalent bonds with the $-SO_3H$ groups (between 573 K and 833 K). The last weight loss of 35% has been observed between 863 and 953 K, probably corresponding to the oxidation of the undoped sections created during the activation step under ethylene. Indeed, this last weight loss corresponds well to the profile obtained with undoped CNTs (Fig. SI.7).

X-ray photoelectron spectroscopy was conducted to identify the chemical state of sulfur. The high resolution S2p spectrum is shown in Fig. 2. The fine-scanned high-resolution S 2p spectrum has a main S 2p1/2 and S 2p3/2 doublet detected at 164.6 eV and 163.4 eV spin-orbit levels with an energy separation of 1.0 eV and an intensity ratio of about 1:2.

These signals can be attributed to the formation of C=S and C S bonds, respectively, further confirming the doping of the graphene network by sulfur. The peaks at 167.7–168.2 eV corresponds to –C-SO_x-C– sulfur species [27]. The presence of oxidized sulfur species should arise from the sulfuric acid purification step.

Sulfur species are often used as the capping agents for metal nanoparticle (NP) stabilization. By using the high affinity of sulfur atoms towards heavy metals, we investigated the anchoring of palladium metal NPs on the S-CNTs (Pd/S-CNT), and compared the Pd dispersion with the ones obtained on pristine CNTs (CNT, $S_{BET} = 152\ m^2\ g^{-1}$), oxidized CNT (O-CNT, $S_{BET} = 220\ m^2\ g^{-1}$), and nitrogen doped CNTs (N-CNT, 3% N, $S_{BET} = 182\ m^2\ g^{-1}$). All the materials were prepared by incipient wetness impregnation in acetone of $[Pd(NO_3)_2{\cdot}2H_2O]$ to reach a theoretical Pd loading of 2% w/w. The resulting solids were then filtered, washed with acetone, dried in an oven at 393 K overnight, and then reduced under a N_2/H_2 flow (20 vol% H_2) at 573 K for 2 h. The characterization of the Pd based catalysts is summarized in Table 2. The heteroelement (O, N, or S) doping of CNT allows to increase the palladium loading compared to pristine CNTs. As far as Pd NP size is concerned, the best dispersion was obtained on the S-CNT support, with a mean particle size of 1.8 nm (Fig. 3).

This series of catalysts have been tested for the aerobic oxidation of ethanol to acetic acid. Ethanol has emerged as a fuel and a chemical feedstock available from biomass, and could provide alternative routes to produce chemicals, such as acetaldehyde and/or acetic acid. Currently, 75% of acetic acid is formed *via* methanol carbonylation utilizing fossil resources, and 25% by other processes, including classical fermentation [28]. Gold [29],ruthenium [30] and palladium [31] supported catalysts are active for this reaction. A recent study using CNTs as support for Pd deposition has shown that N-CNTs were more interesting than O-CNT for this reaction [32]. In this study, at 3 MPa and 453 K (EtOH/metal = 1500 mol/mol, 10 mL of 5 wt% aqueous EtOH, 5 h), the use of Pd/N-CNT catalyst allows a conversion of 77% *vs* 53% for the Pd/O-CNT one.

The acetic acid yields were 49% and 33% for the Pd/N-CNT and Pd/O-CNT catalysts, respectively. The supported Pd NPs had a mean diameter of approximately 3 nm regardless of the support. Small amounts of acetaldehyde and ethyl acetate were formed in the liquid phase. An unaccounted gap in the selectivity was probably due to the formation of CO_2 as a result of total oxidation. The selectivity towards acetic acid were 64% and 62% for the Pd/N-CNT and Pd/O-CNT catalysts, respectively.

The catalytic performances of the prepared Pd catalysts were evaluated in the aerobic ethanol oxidation under the following conditions: 10 mL of 5 wt% aqueous ethanol, 0.1 g of catalyst, 3.0 MPa, 448 K and 3 h of reaction time. The activity and selectivity of the catalysts are presented in Table 3. Under these conditions acetic acid was the major product of the reaction, the distribution of by-products (CO_2, acetaldehyde and ethyl acetate) is shown on Table S1. Our results confirmed that N-CNTs constitute a more interesting support for Pd than O-CNTs. A higher selectivity but a lower conversion are obtained on undoped CNTs. The best results in term of compromise between a high conversion and a high selectivity have been reached with the 2% Pd/S-CNT system. Under the studied conditions, this catalyst allows a conversion of 80% and a selectivity of 90%. Compared to the Pd/N-CNT the formation of CO_2 (12% for Pd/N-CNT) is completely suppressed on Pd/S-CNT. Noticeably, the reaction rate obtained with the Pd/S-CNT, 0.37 $g_{AcOH}.g_{cat}.h^{-1}$, is significantly higher than the one obtained with other palladium supported catalysts, 0.17–0.21 $g_{AcOH}.g_{cat}.h^{-1}$ [33].

Table 2
Characterization of the Pd-carbon nanotube materials.

Catalyst	S_{BET} (m^2 g^{-1})	Pd loading (%)	Pd NP size (nm)
Pd/CNT	156	1.39	2.25 ± 1.10
Pd/O-CNT	232	2.04	2.17 ± 1.10
Pd/N-CNT	187	1.81	2.21 ± 0.88
Pd/S-CNT	443	2.06	1.78 ± 0.76

4. Conclusion

In summary, a new type of sulfur-doped carbon nanotubes have been prepared by a sequential growth process on an iron based catalyst. This process includes a catalyst activation step under an ethylene atmosphere to initiate CNT growth, and a growth step during which ethylene is replaced by thiophene. The resulting S-CNTs contain up to

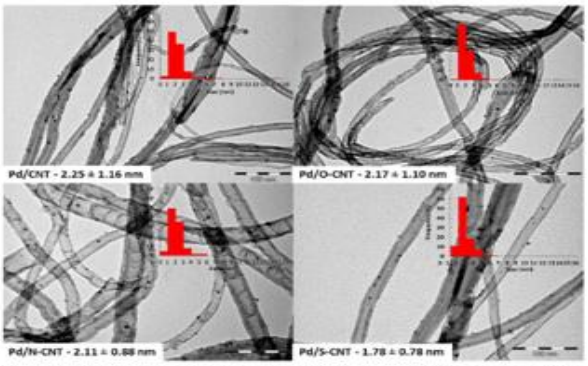

Fig. 5. TEM micrographs and Pd NP size distributions for Pd/CNT (scale bar = 100 nm), Pd/O-CNT (scale bar = 100 nm), Pd/N-CNT (scale bar = 50 nm), Pd/S-CNT (scale bar = 100 nm).

Table 3
Performances of the palladium supported catalysts in the selective oxidation of EtOH as a function of catalyst (10 mL of 5 wt% aqueous ethanol, ~0.1 g of catalyst, 5.0 MPa, 448 K and 5% of reaction time).

Catalyst	Conversion (%)	Selectivity[a] (%)	TOF (h^{-1})[b]
Pd/CNT	74	92	334
Pd/O-CNT	63	78	186
Pd/N-CNT	86	77	330
Pd/S-CNT	80	95	329

[a] At 50% conversion.
[b] $mol_{product}.mol_{Pd_{surface}}^{-1}.h^{-1}$.

7% w/w sulfur in their structure, present mainly in C=S and C–S bonds. We also demonstrate that the presence of sulfur in these structures allows to stabilize palladium NPs on their surface, opening the route to their use in catalysis. The as-prepared 2% Pd/S-CNT catalyst present excellent performances for the aerobic oxidation of ethanol to acetic acid with a productivity of 0.37 $g_{AcOH}.g_{cat}.h^{-1}$, significantly higher than the ones already reported for palladium-based catalysts.

Acknowledgement

The authors wish to thank the CEA LITEN, the CNRS and Région OCCITANIE for having funding the thesis in which most the results have been obtained.

Appendix A. Supplementary Data

Supplementary data to this article can be found online at https://

doi.org/10.1016/j.catcom.2018.02.024.

References

[1] L. Dreizler, Review of the doping of carbon nanotubes (multivalled and single walled), Carbon 40 (2002) 1751–1764.
[2] M. Rivallan, M. Ibrahi, M. Rosenzweig, Sulfur-doped porous carbons: synthesis and applications, Carbon 68 (2014) 1–32.
[3] J.M. Ramo-Herrera, R.G. Sumpter, N.A. Cabrio, H. Terrones, E. Cruz-Silva, O.J. Smith, V. Meunier, M. Terrones, An inelastic tunneling mechanism for carbon nanotube, sulfur as the triggering agent, Angew. Chem. 120 (2008) 2990–2995.
[4] P.A. Denis, R. Faccio, A.W. Mombrú, Is it possible to dope single-walled carbon nanotubes and graphene with sulfur? ChemPhysChem 10 (2009) 715–722.
[5] T. Zhou, Y. Hou, S. Liu, K. Li, H. Sun, Synthesis of sulfur-doped carbon nanotubes by liquid precursor, Mater. Focus 2 (2013) 64–67.
[6] D.A. Mendeleu, P., synthesis of carbon nanofibers and nanotubes using carbon disulfide as the precursor, Revista Mexicana de Física S3 (2007) 9–12.
[7] S.-H. Lee, J. Park, H.-B. Kim, J. Lee, K.-H. Lee, Synthesis of high-quality carbon nanotube fibers by controlling the effects of sulfur on the catalyst agglomeration during the direct spinning process, RSC Adv. 5 (2015) 41904–41909.
[8] M. Corrias, B. Caussat, A. Ayral, J. Durand, Y. Kihn, P. Kalck, P. Serp, Carbon nanotubes produced by fluidized bed catalytic CVD: first approach of the process, Chem. Eng. Sci. 58 (2003) 4475–4482.
[9] A.D. Pronina, R.F. Mazhalis, A.F.C. Tenneiu, T.V. Medvedeva, A. Benyoucef, J. Besnardeil, H.C. Mesnaoui, Z.L. Cardeal, R.M. Lago, P. Serp, Magnetic amalgam/polymer hybrid carbon nanotubes containing N-doped and undoped vertical graphene membranous nanostructures, Nanoscale 7 (2015) 394–399.
[10] J. Gerber, M. Oubenali, R. Backs, J. Durand, A. Gonçalves, M.F.R. Pereira, P. Jolibois, L. Perrin, H. Perrin, F. Serp, Theoretical and experimental studies on the carbon-nanotube surface oxidation by nitric acid: interplay between nanotube-acid and vacancy rearrangement, Chem. Nat. J. 17 (2011) 11467–11477.
[11] M. Skoglund, D. Moan-Ödeh, V. Sokhanvaz, P. Pitka, M. Pinkouba, Poisoning of iron catalyst by sulfur, Catal. Today 124 (2007) 45–48.
[12] C. R.S.J Tot, M. Chhowalla, M.J. Miller, Catalytic synthesis of carbon nanotubes and nanofibers, in: E. Nalwa (Ed.), Encyclopedia of Nanoscience and Nanotechnology, American Scientific Publishers, USA, Stevenson Ranch, CA, 2003, pp. 665–686.
[13] F. Ghiodi, T. Sugie, K. Ghosh, T. Endo, K. Kaneb, K. Hamiyama, T. Ando, effect of sulfur concentration on the morphology of carbon nanofibers produced from a benzene hydrocarbon, Nanoscale Res. Lett. 6 (2006) 641.
[14] M.S. Mehta, A. Mehrabi, I.A. Rashedi, A.M. Khalfa, The role of sulphur in the synthesis of carbon nanotubes by chemical vapour deposition at high temperature, J. Nanosci. Nanotechnol. 6 (2006) 2442–2446.
[15] E. de Smit, B.M. Weckhuysen, The renaissance of iron-based Fischer-Tropsch synthesis: on the multifaceted catalyst deactivation behaviour, Chem. Soc. Rev. 37 (2008) 2758–2781.
[16] H.M. Torres Galvis, A.C.J. Koeken, J.H. Bitter, T. Davidian, M. Ruitenbeek, A.I. Dugulan, K.P. de Jong, Effects of sodium and sulfur on catalytic performance of supported iron catalysts for the Fischer-Tropsch synthesis at lower alpha, J. Catal. 303 (2013) 22–30.
[17] B. Wu, L. Bai, H. Xiang, Y.-W. Li, Z. Zhang, B. Zhong, An active iron carbide containing sulfur for Fischer–Tropsch synthesis, Fuel 83 (2004) 205–212.
[18] R.J. Madon, H. Iglesia, Effect of sulfur on the Fischer-Tropsch synthesis, Catal. Rev. Sci. Eng. 19 (1977) 69–106.
[19] C.N. Rasmussen, A.M. Hvenmark, Initial poisoning of cobalt and iron Fischer-Tropsch catalysts, Appl. Catal. 32 (2006) 59–67.
[20] J. Zhang, M. Abbas, J. Chen, The evolution of Fe phases of a basalt iron catalyst during reduction and Fischer-Tropsch synthesis, Catal. Sci. & Technol. 7 (2017) 3626–3636.
[21] C.T. Wirth, R.C. Bowie, A.D. Gamubiei, S. Kaemmerspiegl, R.S. Weatherup, C. Ducati, C. Rudolf, J. Robertson, S. Hofmann, The phase of iron catalyst nanoparticles during carbon nanotube growth, Chem. Mater. 24 (2012) 4633–4640.
[22] J.W. Jang, C.E. Lee, S.C. Lyu, T.J. Lee, C.J. Lee, Structural study of nitrogen-doping effects in bamboo-shaped multiwalled carbon nanotubes, Appl. Phys. Lett. 84 (2004) 2877–2879.
[23] J.O. Sifkeen, S. Li, X.L.T. Jones, P.G. Thomas, J.S. Larsson, M.A. Morris, J.D. Holmes, Nitrogen-doped carbon nanotubes: growth, mechanism and structure, ChemPhysChem 12 (2011) 3689–3693.
[24] G. Lee, J. W. Feng, C.-H. Liu, Probing plasma-induced defect formation and vacancies in carbon nanotubes by Raman dispersion spectroscopy, Carbon 47 (2009) 3488–3497.
[25] D. Hao, W. Liu, S. Liu, T. Zhang, H. Wang, S. Chen, F. Cheng, S. Zhao, H. Yang, Rich sulfur doped porous carbon materials derived from ginkgo leaves for supercapacitor electrochemical energy storage devices, J. Mater. Chem. A 5 (2017) 2204–2214.
[26] L. Adams, A. Ohi, T. Grade, H. M-Whitmore, Z. Lee, Preparation and characterization of colloidal acid-functionalized single walled carbon nanotubes, Physica E: Low-dimensional Syst. and Nanostruct. 40 (2008) 723–728.
[27] L. Qie, W. Chen, X. Zhong, C. Wu, P. Xie, P. Hu, Y. Huang, Sulfur-doped carbon with enlarged interlayer distance as a high-performance anode material for sodium-ion batteries, Adv. Sci. 2 (2015) 1500195.
[28] C. La Berte, F. Imp, P. Kalck, G.P. Torrence, Acetic acid, Ullmann's Encyclopedia of Industrial Chemistry, Wiley-VCH Verlag GmbH & Co. KGaA, 2000.
[29] C.H. Christensen, B. Jørgensen, J. Rass-Hansen, K. Egeblad, R. Madsen, S.K. Klitgaard, S.M. Hansen, M.R. Hansen, H.C. Andersen, A. Riisager, Formation of acetic acid by aqueous-phase oxidation of ethanol with air in the presence of a heterogeneous gold catalyst, Angew. Chem. Int. Ed. 45 (2006) 4648–4651.
[30] T.T. Sonthaner, S. Kegnæs, C.W. Hansing, T.W. Hansen, A. Riisager, Acetic acid formation by selective aerobic oxidation of aqueous ethanol over heterogeneous cobaltone catalysts, ACS Catal. 2 (2012) 844–851.
[31] S. Lakshmanan, P.C. Zinnen, P.P.F. Reis, J. Gilsch, C.B.K. Rubella, A.K. Gurpur, L.G. Appel, The role of m-TiO2 in the selective oxidation of ethanol to acetic acid employing PdO-m-TiO$_2$, J. Mol. Catal. A Chem. 410 (2015) 177–183.
[32] W. Jiang, F. Chen, H. Xu, F. Wenda, H. Roland, A. Kunka, E. Ellert, M. Mohler, Palladium nanoparticles supported on nitrogen-doped carbon nanotube as a co-base-and-catch catalyst system in aerobic liquid-phase ethanol oxidation, ChemCatChem 8 (2016) 1369–1375.
[33] **FI. Ohsim, IK. Uchida, E.-I. Saito, Catalyst for Production of Acetic Acid or Acetic Acid and Ethyl Acetate, Process for its Production and Process for Production of Acetic Acid or Acetic Acid and Ethyl Acetate Using it. US9807534 B2.**

A.5 As co-author in a presentation for an international congress

ISCRE25 FLORENCE 2018 BRIDGING SCIENCE & TECHNOLOGY
The 25th International Symposium on Chemical Reaction Engineering
20-23 May 2018 Florence, Italy www.aidic.it/iscre25

Catalyst Support Effects and Development of a Compact Continuous Catalytic Reactor with Solid Foam Internals for the Hydrogenation of Terpenes

Boris Guicheret[1], Ruben Castro Contreras[2], Laurent Vanoye[1], Alain Favre-Réguillon[1], Valérie Meille[1], Claude de Bellefon[1], Philippe Serp[2] & Régis Philippe[1,*].

1 Laboratoire de Génie des Procédés Catalytiques, UMR 5285 CNRS-CPE Lyon-UCBL, Lyon (France);

2 Laboratoire de Chimie de Coordination, UPR 8241 CNRS-ENSIACET-UPS, Toulouse (France).

**Corresponding author: regis.philippe@lgpc.cpe.fr*

Highlights

- Pd /nanocarbons present high activities for the total hydrogenation of myrcene and squalene.
- Acidic pretreatment of the supports plays a crucial role in the catalyst activity.
- A compact continuous foam milli-reactor is optimized for the hydrogenation of neat terpenes.

The major uses for terpenes are in the flavour and fragrance industries, as a solvent, and in the manufacture of polymers and adhesives. Most of the terpenes are obtained as co-products of the paper or food processing industries. Recently, metabolic engineering has been successfully used to produce these valuable compounds in microbial hosts which enables their production on a larger scale [1] and for some of them opens the way for a potential use as a bio-fuel. Some applications of terpenes (e.g. cosmetics and fuel) require fully hydrogenated terpenes obtained with a complex network of exothermic catalytic reactions [2]. In the first part of this study, the development of new Pd catalysts supported on innovative carbon supports is presented. Several carbon supports were investigated including a screening of their pretreatments in order to identify the best catalytic material in comparison to reference Pd/Al_2O_3 and Ni/SiO_2–Al_2O_3 commercial catalysts. Myrcene was used as a model substrate because of the presence of conjugated double bonds that could lead to thermally activated by-products. Unsaturated all-*trans* squalene ($C_{30}H_{50}$) has also been studied as a strategic substrate. Squalane ($C_{30}H_{62}$), obtained by full hydrogenation of squalene, is a key ingredient in the cosmetic, neutraceutical and pharmaceutical industries. For both substrates, hydrogenation can be the subject of external and internal mass and heat transfer issues leading potentially to a decrease in selectivity, productivity and safety. Thus, the second part of this work is focused on the development of an intensified continuous reactor involving highly porous metallic foams. These internals, known for their low pressure loss and enhanced transfer capacities [3], are suitable to promote the highest apparent activity of the best identified catalysts in neat or concentrated media without alteration of the selectivity and/or safety.

Figure 1. TEM pictures of the carbonaceous supports investigated in this work (scale bar ca. 50 nm)

Four kinds of carbon materials were studied (Figure 1): carbon nanotubes (CNTs), nitrogen-doped carbon nanotubes (N-CNTs), filamentous carbon (FC) and few layer graphene (FLG). 4 pretreatments are also compared: no pretreatment (-), oxidation with nitric acid (-COOH); high temperature annealing (-HT) and a combination of nitric acid oxidation followed by high temperature annealing (-COOH-HT). All the catalysts are well characterized (TEM, SEM, XRD, BET, ICP, TGA, etc.) and present a Pd loading between 1-2 wt.% with mainly 2 nm well dispersed nanoparticles. The screening was conducted in a mechanically stirred tank reactor of 200 mL at 120°C under H_2 atmosphere at a constant pressure of 20 bar with a 1M substrate solution in heptane. Reaction course monitoring was done by following the H_2 consumption in a

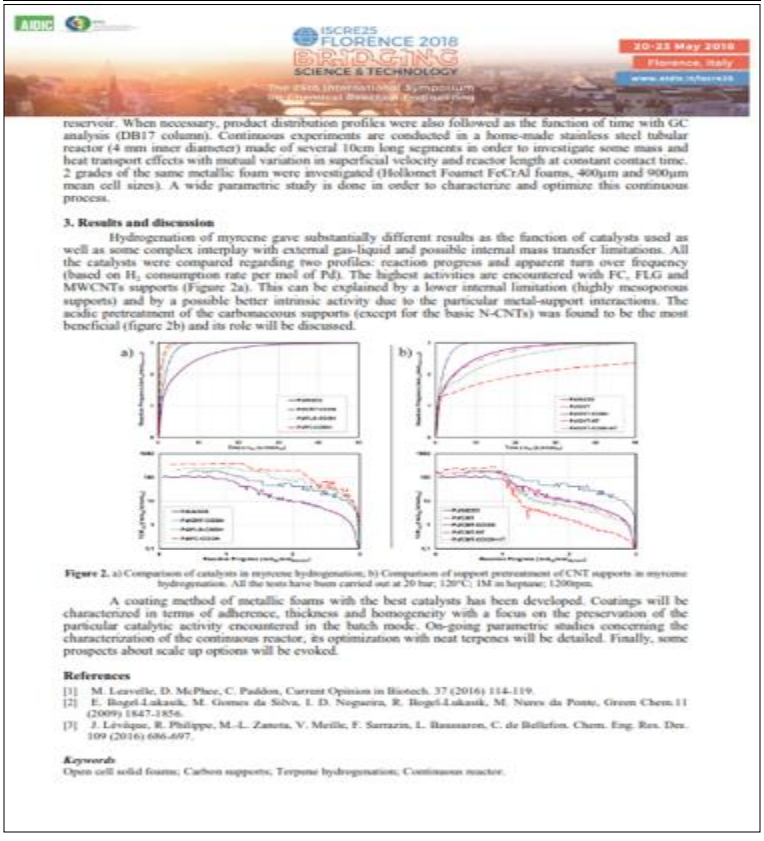

ISCRE25 FLORENCE 2018 BRIDGING SCIENCE & TECHNOLOGY
The 25th International Symposium on Chemical Reaction Engineering
20-23 May 2018 Florence, Italy www.aidic.it/iscre25

reservoir. When necessary, product distribution profiles were also followed as the function of time with GC analysis (DB17 column). Continuous experiments are conducted in a home-made stainless steel tubular reactor (4 mm inner diameter) made of several 10cm long segments in order to investigate some mass and heat transport effects with mutual variation in superficial velocity and reactor length at constant contact time. 2 grades of the same metallic foam were investigated (Holdercet Fourcet FeCrAl foams, 400µm and 900µm mean cell sizes). A wide parametric study is done in order to characterize and optimize this continuous process.

3. Results and discussion

Hydrogenation of myrcene gave substantially different results as the function of catalysts used as well as some complex interplay with external gas-liquid and possible internal mass transfer limitations. All the catalysts were compared regarding two profiles: reaction progress and apparent turn over frequency (based on H_2 consumption rate per mol of Pd). The highest activities are encountered with FC, FLG and MWCNTs supports (Figure 2a). This can be explained by a lower internal limitation (highly mesoporous supports) and by a possible better intrinsic activity due to the particular metal-support interactions. The acidic pretreatment of the carbonaceous supports (except for the basic N-CNTs) was found to be the most beneficial (figure 2b) and its role will be discussed.

Figure 2. a) Comparison of catalysts in myrcene hydrogenation; b) Comparison of support pretreatment of CNT supports in myrcene hydrogenation. All the tests have been carried out at 20 bar; 120°C; 1M in heptane; 1200rpm.

A coating method of metallic foams with the best catalysts has been developed. Coatings will be characterized in terms of adherence, thickness and homogeneity with a focus on the preservation of the particular catalytic activity encountered in the batch mode. On-going parametric studies concerning the characterization of the continuous reactor, its optimization with neat terpenes will be detailed. Finally, some prospects about scale up options will be evoked.

References

[1] M. Leavelle, D. McPhee, C. Paddon, Current Opinion in Biotech. 37 (2016) 114-119.
[2] E. Bogel-Lukasik, M. Gomes da Silva, I. D. Nogueira, R. Bogel-Lukasik, M. Nunes da Ponte, Green Chem.11 (2009) 1847-1856.
[3] J. Lévêque, R. Philippe, M.-L. Zanota, V. Meille, F. Sarrazin, L. Baussaron, C. de Bellefon. Chem. Eng. Res. Des. 109 (2016) 686-697.

Keywords
Open cell solid foams; Carbon supports; Terpene hydrogenation; Continuous reactor.

A.6 As first author in a scientific article (in process)

The broad spectrum of carbon nanomaterials for Pd/C catalyst preparation.

Part I. Influence of the support on Pd loading and dispersion

Part II. Involvement of Pd single atoms in Pd/C catalyzed myrcene hydrogenation

Part III. Direct coating of Pd/C on metallic foams for terpene hydrogenation

R. Castro Contreras,[a,b] B. Machado,[c] C. Rivera,[a] B. Guicheret,[d] M. A. Curiel Alvarez,[b] B. Valdez Salas,[b] M. Ruttert,[e] T. Placke,[e] R. Philippe,[d] P. Serp[a,*]

[a]LCC-CNRS, Université de Toulouse, CNRS, INPT, Toulouse, France

[b]Institute of Engineering, Autonomous University of Baja California, Benito Juarez Blvd. esc. Calle de la Normal, s/n, C. P. 21280 Mexicali, B. C., Mexico

[c]Laboratory of Separation and Reaction Engineering - Laboratory of Catalysis and Materials (LSRE-LCM), Departamento de Engenharia Química, Faculdade de Engenharia, Universidade do Porto, Rua Dr. Roberto Frias s/n, 4200-465 Porto, Portugal

[d]Laboratoire de Génie des Procédés Catalytiques, UMR 5285 CNRS - CPE Lyon – UCBL, France

[e]University of Muenster, MEET Battery Research Center, Institute of Physical Chemistry, Corrensstr. 46, 48149 Münster, Germany